Glacier-Climate Interactions: A Synoptic Approach

---

by

Tom Kenneth Roger Matthews

A Doctoral Thesis

Submitted in partial fulfilment of the requirements
for the award of
Doctor of Philosophy of Loughborough University

April 2013

Abstract

The reliance on freshwater released by mountain glaciers and ice caps demands that the effects of climate change on these thermally-sensitive systems are evaluated thoroughly. Coupling climate variability to processes of mass and energy exchange at the glacier scale is challenged, however, by a lack of climate data at an appropriately fine spatial resolution. The thesis addresses this challenge through attempting to reconcile this scale mismatch: glacier boundary-layer observations of meteorology and ablation at Vestari Hagafellsjökull, Iceland, and Storglaciären, Sweden, are related to synoptic-scale meteorological variability recorded in gridded, reanalysis data. Specific attention is directed toward synoptic controls on: i) near-surface air temperature lapse rates; ii) stationarity of temperature-index melt model parameters; and iii) glacier-surface ablation. A synoptic weather-typing procedure, which groups days of similar reanalysis meteorology into 'weather categories', forms the basis of the analytical approach adopted to achieve these aims.

Lapse rates at Vestari Hagafellsjökull were found to be shallowest during weather categories characterised by warm, cloud-free weather that encouraged katabatic drainage; steep lapse rates were encountered in weather categories associated with strong synoptic winds. Quantitatively, 26% to 38% of the daily lapse-rate variability could be explained by weather-category and regression-based models utilizing the reanalysis data: a level of skill sufficient to effect appreciable improvements in the accuracy of air temperatures extrapolated vertically over Vestari Hagafellsjökull. Weather categories also highlighted the dynamic nature of the temperature-ablation relationship. Notably, the sensitivity of ablation to changes in air temperature was observed to be non-stationary between weather categories, highlighting vulnerabilities of temperature-index models. An innovative solution to this limitation is suggested: the relationship between temperature and ablation can be varied as a function of weather-category membership. This flexibility leads to an overall improvement in the simulation of daily ablation compared to traditional temperature-index formulations (up to a 14% improvement in the amount of variance explained), without the need for additional meteorological data recorded in-situ. It is concluded that weather categories are highly appropriate for evaluating synoptic controls on glacier meteorology and surface energetics; significant improvements in the parameterization of boundary-layer meteorology and ablation rates are realised through their application.

Acknowledgements

I must first extend my thanks to my primary supervisor, Dr Richard Hodgkins, who has consistently provided me with timely and considered feedback on the research contained in this thesis. I am also grateful to Richard for the very considerable financial support he secured to facilitate the fieldwork component of this research; this not only enabled the collection of rich glacio-meteorological data, but also provided me with extended stays at Tarfala Research Station—an inspiring environment that nurtured my understanding of glacier boundary-layer processes.

My second supervisor, Professor Robert Wilby, is also thanked: critical reviews of key chapters greatly enhanced the quality of this research. Rob also ensured no city was too far, and no official funding source too small to preclude my attendance at international conferences. For this, I am sincerely grateful.

All staff of the Tarfala Research Station are acknowledged. Specific thanks are directed to Professor Peter Jansson, who provided valuable guidance over the use of meteorological instrumentation, loaned sensors, and who was *the* source of reference regarding the long-term meteorological measurement program at Tarfala. Henrik Törnberg, Andreas Bergström and Torbjörn Bergelv are also acknowledged for their generous logistical support.

I am also indebted to Sverrir Guðmundsson, Finnur Pálsson and Helgi Björnsson (Institute of Earth Sciences, Reykjavik) for the AWS data from Vestari Hagafellsjökull. Access to this resource broadened the scope of the research and enriched this thesis considerably,

My parents, Linda and Roger, receive my sincere gratitude: they have never faltered in their support of my academic ventures. I thank them for encouraging me to pursue my interests, and for enabling me to follow wherever these have led. I also thank my father for his conscientious reviewing of this thesis.

Lastly, I must thank Stefanie (L.P). Her editorial-eye for typographic oversights no-doubt improved the quality of this work. But more importantly, without her, the journey to completion of this work would have been immeasurably less fulfilling. I look forward to many new adventures with her by my side.

Table of Contents

List of Tables

List of Figures

1. Introduction

In their Fourth Assessment Report, the Intergovernmental Panel on Climate Change (IPCC) stated that warming of the climate system was unequivocal. It was also emphasised that continuation of such changes would have profound—and in some cases irreversible—consequences for many components of Earth's natural systems (IPCC, 2007). A concomitant result of this is the societal cost of climate change—from concerns over water scarcity, to rising sea levels—which is sufficient to demand the utmost attention of the international community's scientists and policy makers. Critically, rigorous research is required to understand better the complex response of the Earth system to a changing climate. The Fifth Assessment Report from the IPCC is currently in preparation. In this context, the cryosphere is conspicuous in its need for urgent assessment, and it is this area of research which is addressed in the thesis. Specifically, the research herein is concerned with synoptic aspects of glacier-climate interaction.

The purpose of the present chapter is to contextualise the research (sections 1.1 to 1.3), and to provide details of the specific aims and objectives which are addressed in this study. A summary of the thesis' structure is also provided (Section 1.4).

1.1. The Atmosphere

The energy available to the Earth-atmosphere system is principally determined by the planetary radiation balance. Gains to this system are in the form of solar (or shortwave) radiation, and losses result from thermal (or longwave) emissions. The turbulent fluxes (sensible and latent heat) redistribute energy. When averaged over the entire planet, and when the atmosphere is in a steady-state, the radiation fluxes cancel and the energy balance of the Earth remains unchanged (Lockwood, 1974). However, this global balance of net radiation belies appreciable spatial heterogeneity which results from differential solar heating of the Earth's surface.

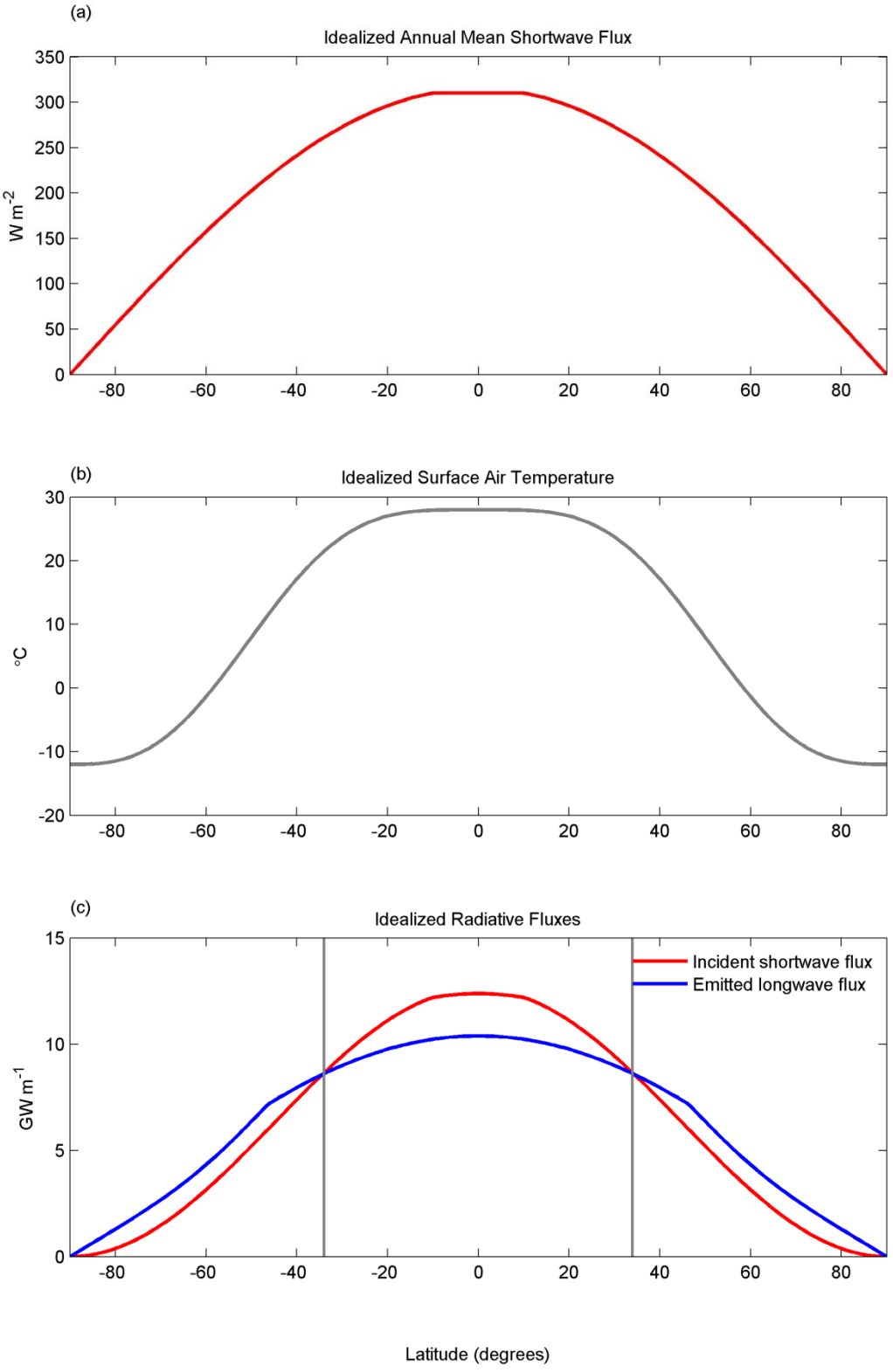

Figure 1.1. Idealized radiative and temperature profiles as a function of latitude. Curves are produced by applying the equations of Stull (2000, p224-227). In (c), the grey lines differentiate latitudes of net radiative energy gains and losses.

At high latitudes, the greater angle of incidence between the solar beam and the planet's surface reduces the flux density of shortwave radiation relative to that received at lower latitudes (Figure 1.1, a). Reflected shortwave radiation is also enhanced in the polar regions due to the higher planetary albedo which persists at these latitudes.

Spatial discrepancies in the amount of longwave heat energy emitted by the Earth are similarly apparent. The magnitude of this flux depends on the emissivity of the radiating surface and its temperature. Thus, its latitudinal variability can be idealised from a generalised global temperature distribution (Figure 1.1, b). Combining this information with knowledge of the incident solar radiation facilitates the deduction that radiative imbalances must persist (Figure 1.1, c). If this imbalance were not addressed, those regions of the Earth which observed a sustained gain of net radiation would warm, and those experiencing a deficit would cool; the fact that this is not observed demonstrates that redistribution of energy must occur within the Earth-atmosphere system. This is achieved through circulation of the planet's oceans and its atmosphere, which act ceaselessly to eliminate these energy gradients. It is with the atmosphere which the aims of this research are inextricably linked.

In the atmosphere, the redistribution of energy may be idealised as a three cell model. At low-latitudes, circulation persists in the form of a direct cell, termed the *Hadley Cell*. The rising limb of this cell is driven by the vigorous insolation at the Equator which forces convection. Having risen high in the troposphere, this air travels poleward in response to the latitudinal pressure gradient which is concomitant of the meridional temperature difference. The rotation of the Earth, and the tendency for angular momentum to be conserved, provides an easterly acceleration and impels the flow to change direction. An eventual balance is attained between the pressure-gradient force and the Coriolis force, to produce air-flow which is zonal, limiting the Hadley circulation to within ~30° of the Equator. The *Polar Cell* also redistributes energy in a direct circulation, with air subsiding and warming adiabatically over the poles to offset the radiation deficit which endures at high latitudes. Between these regions of direct circulation is the *Ferrel Cell*, in which energy is redistributed via atmospheric waves. At the northern limit of this cell, where thermal gradients are steepest, the Polar Front and accompanying jet stream are observed. Barotropic and baroclinic instabilities along this front promote meridional oscillation of the

predominantly zonal flow, and vorticity conservation results in an endless succession of cyclones and anticyclones being observed in the mid-latitudes (Stull, 2000). Day-to-day variability of the weather is therefore appreciable in the vicinity of the Polar Front. This has practical consequences when considering the behaviour of climatologically-sensitive environmental systems in these regions, particularly in the context of a changing climate.

1.2. Climate Change

Over time periods of several decades, the planet's incident shortwave flux remains essentially unchanged. However, at millennial resolution, appreciable, cyclical changes of the temporal and spatial distribution of insolation maxima are evident. Moreover, the *total* solar radiation received by the Earth is also subject to periodic variability (Berger, 1978). These changes have provoked substantial oscillations of the Earth's climate (e.g. Hays et al., 1976), as global temperatures have adjusted accordingly to effect a radiation balance. In particular, the palaeo-record highlights the importance of the 100ka eccentricity cycle of the Earth's orbit for pacing large-scale climate perturbations, and is seemingly responsible, therefore, for the repeated periods of *glacials* and *interglacials* which have formed the Quaternary (Imbrie and Imbrie, 1980).

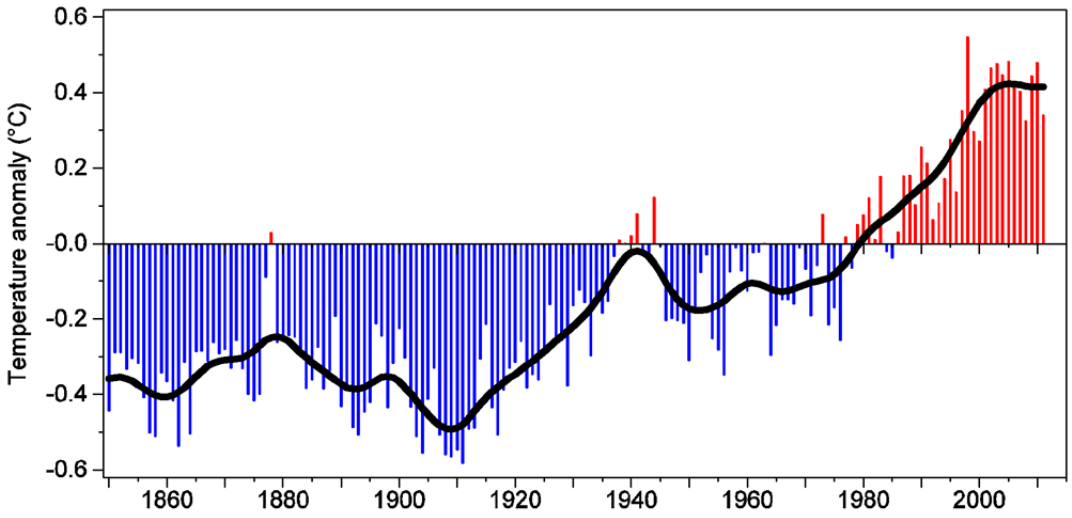

Figure 1.2.Global surface air temperature anomalies relative to the 1961-1990 mean. Figure produced by the Climatic Research Unit, UK. Details of observations are given in (Brohan et al., 2006).

Consideration of the effect that orbital modulation has on the Earth's equilibrium temperature suggests that global cooling should be anticipated over the coming millennia: Roberts (1998) explains that the planet is entering the latter part of the Holocene—the latest of the Quaternary interglacials—and suggests that a return to glacial conditions will occur ~25ka from now if the Earth's climate were to progress naturally. In this context, it is somewhat surprising that pronounced warming of the atmosphere has been observed during recent centuries (Figure 1.2.). The 100-year linear trend of this increase of surface air temperatures has been quantified by the IPCC (2007) as 0.74°C during the period preceding publication of the Fourth Assessment Report (FAR; 1906-2005); with an accelerated rate of warming observed during the last 50 years of this interval (1956-2005)—increasing at approximately twice the 100-year rate (0.13°C decade^{-1}).

The cause of the observed warming has been attributed largely to a decrease in the amount of planetary longwave radiation emitted into space. The atmosphere is mainly transparent to shortwave radiation, but opaque to thermal radiation. Specifically, methane, nitrous oxide, ozone, water vapour and carbon dioxide are constituents of the Earth's atmosphere which readily absorb terrestrially emitted longwave radiation (Oke, 1987). Of these, the concentration of atmospheric carbon dioxide has increased rapidly: the FAR reports its concentration had reached 135% of its preindustrial value by the year 2005 (IPCC, 2007). It also concluded that the most recent decade analysed (1995-2005) displayed the fastest increase of CO_2 emissions. Even more recently, observations have demonstrated that the rise in carbon dioxide concentration has continued unrelentingly (Figure 1.3, top). It is argued, therefore, that the increased atmospheric emissivity which this effects, provides a sufficient radiative forcing to account for the observed temperature increase (IPCC, 2007).

The degree of warming observed has not been spatially homogeneous, nor is it anticipated to be in the future (Gillett et al., 2012; Figure 1.3, bottom), as modelled scenarios of likely changes in air temperature suggest considerable variability, with warming concentrated at high latitudes due to important feedback processes (e.g. Serreze et al., 2009). It should also be emphasised that changes of the Earth's equilibrium temperature can produce substantial changes of the atmosphere's gross circulation. For example, during the last glacial period, when air temperatures were suppressed, palaeo-data and modelling studies suggest that the Polar Front and the

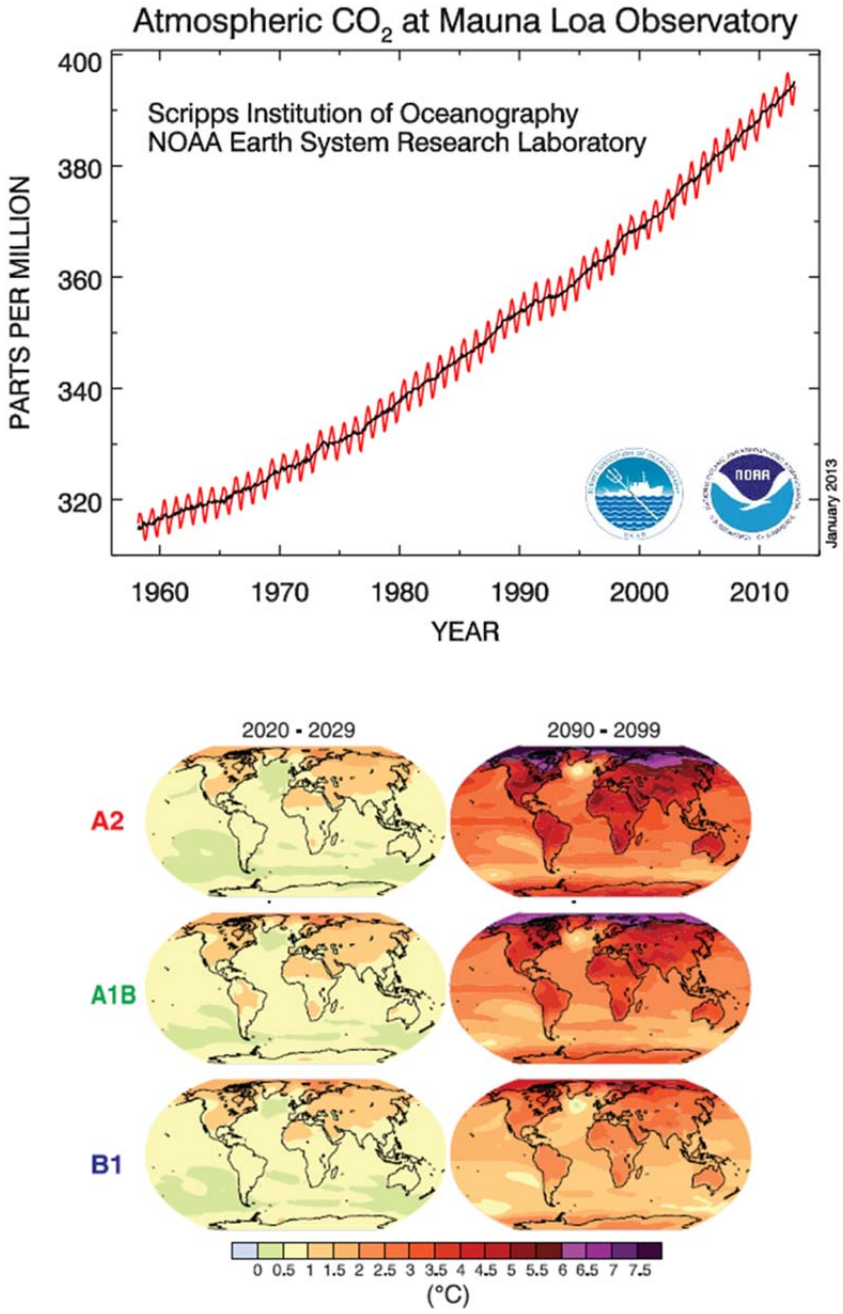

Figure 1.3. Top: Observations of carbon dioxide concentration at the Mauna Loa Observatory (courtesy of Dr. Pieter Tans, NOAA/ESRL (www.esrl.noaa.gov/gmd/ccgg/trends/) and Dr. Ralph Keeling, Scripps Institution of Oceanography (scrippsco2.ucsd.edu/). Bottom: projected change of surface air temperature (relative to 1980-1990 mean). Values shown are ensemble means from multiple, coupled, atmosphere-ocean circulation model runs. A2, A1B and B1 are different emission scenarios (IPCC, 2007).

Inter-Tropical Convergence Zone were located closer to the Equator (Wang et al., 2007; Asmerom et al., 2010), and that zonal circulation in the mid-latitudes was more vigorous (Bush and Philander, 1999). The resulting circulation changes that may occur from a positive perturbation of atmospheric heat energy therefore necessitates a judicious approach to determining regional responses of the climate system. Especially so, because it is at this finer spatial scale which people, cities, nations and physical environments are affected by climatic change (Mitchell and Hulme, 1999). It is the coupling between a physical component of the Earth-atmosphere system and climatic variability which is the focus of this research.

1.3. Glaciers and Climate Change

The cryosphere is comprised of frozen ground, river, lake and sea ice, snow, ice sheets, ice shelves, ice caps and glaciers; and within the Earth system, it is only exceeded in mass by the world's oceans (Lemke et al., 2007). Vulnerability of the cryosphere to climatic change has been acknowledged widely, as many of its components lie thermally proximate to the melting point (Watson et al., 1996). Such sensitivity is especially pertinent because how the cryosphere reacts to climate change is synergistically coupled to the evolution of atmospheric circulation. For example, declining snow- and ice-cover in the high latitudes is anticipated to reduce albedo considerably in these locations, altering the local energy balance and enhancing the rate of warming (e.g. Holland and Bitz, 2003). In turn, the modified meridional temperature gradient has the potential to affect atmospheric circulation, thereby influencing the global redistribution of momentum and heat. Rates of warming that exceed the global average have already been observed at the northern and southern extremes of the planet (ACIA, 2005; Vaughan et al., 2003).

The cryosphere is also of primary global significance as a source of freshwater, storing ~75% of the planet's resources and any release of this stored water to the hydrosphere has possibly serious implications: in terms of sea level rise, the mass of ice stored in the Greenland and Antarctic ice sheets has the potential to contribute ~7 and ~57m, respectively (Lemke et al., 2007). The scale of this change and the uneven concentration of populations into coastal environments therefore demand the effects of climate change on the cryosphere are closely monitored and researched; and, in particular, that the mass and energy budgets of terrestrial glaciers ice caps and ice

sheets be observed closely. This task is given greater urgency by the observation that glaciers and ice caps are already contributing appreciably to sea level rise (0.41 ±0.08 mm yr^{-1}: Jacob et al., 2012); and more recently, by the observation that the mass lost from the ice sheets is increasing greatly. According to some estimates, meltwater from the Greenland and Antarctic ice sheets is now responsible for the largest annual contribution to sea level rise (Rignot et al., 2011; Jacob et al., 2012).

Retreat of the world's glaciers and ice caps is also a pressing concern for resource planning. These ice masses are hydrologically important, acting as reservoirs and modulating water release to (often) populated catchments (Jansson et al., 2003). Their role in the water cycle is all the more important where distinct seasonality of precipitation occurs. The release of stored water during periods of no rainfall can reduce environmental stress in ecological systems, and provides an essential resource to human populations dependent on continuous supplies of freshwater for agricultural and domestic consumption (Vergara et al., 2007). Potential societal effects of changes in glacial runoff which may result from climate change are readily apparent when considering the number of people directly dependent on water released by ice and snow melt: it is estimated that over 1.4 billion people are reliant on the water of the Indus, Ganges, Brahmaputra and Yangtze rivers alone—all of which are nourished by snow and glacier melt runoff in the Himalaya (Immerzeel et al., 2010). Vuille et al. (2008a) highlight this dependency further, reporting that in the dry tropics and subtropics, over 80% of freshwater supplies originate from mountain catchments, and that much of this water is released by glaciers. Considering that over 99% of tropical glaciers are located in the tropical Andes (Kaser, 1999), the rapid (and accelerating) rate of ice loss which has recently been observed in this region is therefore additionally concerning (Rabatel et al., 2013). It must also be emphasised, that even in locations where water scarcity is less evident, pronounced changes in mountainous hydrological systems have immediate consequences for hazard mitigation (e.g. Carey et al., 2012) and industrial activities which are vulnerable to changes in the water cycle (Tangborn, 1984).

The observed retreat of the world's glaciers and ice caps, although almost universal, has been observed to be spatially variable (Jacob et al., 2012), which is a consequence of the complex regional manifestation of climate change. This variability, coupled to the significant societal and ecological impact which are likely to result, has prompted

modelling efforts to address the spatially-differentiated global consequences of likely future climate change on glacier mass balance (Raper and Braithwaite, 2006; Radić and Hock, 2011; Marzeion et al., 2012). These global estimates have sought to translate changes in air temperature and precipitation, predicted by General Circulation Models (GCMs) to the scale of individual glaciers. Whilst providing valuable insights into the probable changes to expect from the world's glaciers and ice caps, such studies are, by necessity, highly simplified: it is the totality of micro-climatic change which determines the mass balance of individual glaciers, and although air temperature and precipitation are important controls on glacier evolution, they are coarse metrics to summarise the entirety of meteorological change.

To evaluate likely future mass balance changes of the world's glaciers and ice caps in a way which is physically more complete, it is therefore necessary to consider micro-meteorological variability that will occur as the global climate warms. This is problematic, however, due to the considerable discrepancy that exists between the coarse spatial scales of GCMs—which typically have horizontal resolutions measured in the hundreds of kilometres—and the local, micro-meteorological information needed to deduce the rates of energy and mass exchange between glaciers and the atmosphere. These difficulties are all the more evident when the physically-complex nature of the glacier boundary layer is considered (discussed in Chapter 2), in which significant small-scale meteorological variability is often observed (Greuell et al., 1997; Strasser et al., 2004).

Scale mismatches between GCM output and that which is necessary to resolve important hydrological processes have long been acknowledged (Wilby et al., 1998), and downscaling techniques have seen frequent application in an attempt to reconcile these differences. Wilby and Wigley (1997) summarise that such techniques may be classified into four distinct approaches: regression-based methods, circulation-typing, stochastic weather generation, and limited area modelling. The latter of which is the only method to apply physical laws to produce higher resolution climate scenarios; the remaining methods use empirical-statistical techniques to couple local response variables to large-scale atmospheric processes. Downscaling not only facilitates the construction of high resolution meteorological time series in both space and time, but it also promotes enhanced physical understanding of how small-scale meteorological variability is coupled to gross atmospheric flow. This second capacity must be

regarded as particularly desirable and robust, because the predictive skill of downscaling methods is inextricably linked to the quality of the data with which it is driven. That is, if GCMs are deficient in simulating the future climate, then downscaled scenarios will be equally invalid (Mitchell and Hulme, 1999). Conversely, the empirical framework of statistical downscaling—which evaluates observed relationships between local responses and coarse atmospheric parameters—is of considerable utility in its own right, because it provides valuable insight as to how these scales are coupled. This knowledge can be used to provide a conceptual understanding of how gross changes in the atmosphere would manifest at the glacier-scale. Such benefit is independent from the present skill of GCMs, and some researchers have exploited this principle to elucidate connections between atmospheric parameters and the mass/energy balance of glaciers (discussed in Chapter 4).

It is argued that there is much to be gained in cryospheric research from exploring synoptic aspects of glacier-climate interactions further. During recent decades, many physical and empirical models have been developed, with the aim to understand spatial or temporal variability of mass balance components within the glacier boundary layer (Willis et al., 2002; Hock 2005). Similarly, investigations of the glacier meteorology have emphasised the boundary layer (Greuell et al., 1997; Strasser et al., 2004; Brock et al., 2010; Petersen and Pellicciotti, 2011). Yet, by comparison, the synoptic dimension of glacier-climate research has been afforded less attention. This is summarised in a comprehensive review by Hock (2005), who reports that relatively few studies have explicitly sought to link variations in glacier surface energetics observed at point locations on glaciers with wider-scale atmospheric processes. Thus, investigating how synoptic climatic variability drives processes at the glacier surface has been identified as a priority for future research.

1.4. Thesis Aims and Structure

The research in this thesis seeks to address this knowledge gap by contributing to the development of a better understanding of how synoptic climatological processes affect processes of energy exchange and mass loss within the glacier boundary layer. This aim is pursued through consideration of the following objectives, which aim to:

- gain insight into the variability of glacier surface meteorology and energy exchange at daily to interannual time scales;

- explore how spatial variability of near-surface air temperature is related to synoptic climatic variability;

- investigate further the utility of using air temperature as a means of translating the effects of synoptic climate variability to the glacier boundary layer for purposes of quantifying ablation;

- examine the possibility of developing practical, empirical models, which integrate synoptic climatological information to simulate ablation accurately.

The first of these objectives is addressed in order to acquire a detailed, quantitative knowledge of the glacier surface meteorology and resulting energy fluxes, which may subsequently be related to larger-scale atmospheric processes. An interannual, high resolution perspective is sought, so that information of how low- and high-frequency climatic variability manifest at the glacier scale may be obtained. Moreover, whilst glacier-meteorological research to date has emphasised the boundary layer, interannual studies are sparse (Hock, 2005). Obtaining an extended insight into glacier boundary-layer processes is therefore a valuable pursuit in its own right.

The second objective is targeted due to the ubiquity of air temperature in glacier mass- and energy-balance models: it is a driving variable required in all physical and nearly all empirical approaches to simulating ablation. However, the spatial distribution of near-surface air temperature has been observed to be highly variable over glaciers, which challenges application of such models for real-time modelling, forecasting or hindcasting. Considering that near-surface temperatures are affected by energy exchange with the underlying terrain, and by gross air mass characteristics, it

is reasoned that examination of the synoptic controls affecting near surface air temperatures should be undertaken.

The third objective investigates issues related to the use of air temperature as a variable for summarising the effect of climatological variability on glacier ablation. This is pursued because temperature-index methods are a well-established means of assessing the effect of climate warming on ice- and snow-melt, but it has been noted that the empirical relationship between air temperature and ablation is non-stationary in space and time, as a result of variable glacier surface conditions and changes in the prevailing meteorology. Because climate change is likely to result in additional meteorological changes other than a rise in air temperature, it is considered prudent to examine how synoptic-scale processes affect the temperature-index model.

The fourth objective addresses explicitly the problem of contrasting spatial scales when evaluating glacier surface energetics and mass loss. Specifically, it seeks to explore the utility of different physical and empirical methods of simulating ablation from spatially-coarse climate data. This is considered to be an essential contribution towards providing more robust, practical models to assist in determining the response of glaciers to a changing climate.

These objectives are developed in detail in the forthcoming chapters. Issues related to the first objective are the focus of chapters 2 and 3, in which the study sites are introduced and the meteorology and energy fluxes of the glacier surface explored. Chapter 4 progresses to the synoptic dimension of the research, by contextualising the thesis' contribution to glacier-climate research, and by developing a synoptic framework for analysis. The second, third and fourth objectives are then developed in chapters 5, 6 and 7, respectively, before Chapter 8 provides a synthesis of the research and draws conclusions. The format of the thesis is such that each chapter is somewhat self-contained, comprising introduction, methods, results and discussion sections where appropriate. This structure is favoured because the scope of the work undertaken is broad and draws on literature and methodologies from the fields of atmospheric and glaciological study. Presenting the thesis thematically is therefore considered as most appropriate to achieve continuity and clear communication of the research.

2. Meteorological Measurements and the Surface Energy Balance: Part I, Vestari Hagafellsjökull (Langjökull, Iceland)

2.1. Introduction and Aims

Ablation describes the processes by which mass, in the form of snow or ice, is removed from glaciers and manifests as surface melting, sublimation, or as iceberg-calving. Mass may also be lost from basal melting, but this is of negligible overall importance (Paterson, 1994). Calving represents the main mode of mass loss from the Antarctic ice sheet, and from some glaciers (e.g. Jacobs et al.,1992; Hagen et al., 2003; Rignot and Kanagaratnam, 2006); but processes which determine its rate are partly decoupled from climatic variations and are related to glacier dynamics in a complex way (Benn et al., 2007). Surface mass lost (hereafter simply ablation) on the other hand, through melting and/or sublimation, is more directly related to climate, and an extensive literature exists on i) models developed to simulate these process as a function of observed meteorology (e.g. Escher-Vetter, 1985; Munro, 1991; Greuell and Konzelmann, 1994; Van de Wal and Oerlemans, 1994; Arnold et al., 1996; Brock et al., 2000; Klok and Oerlemans, 2002; Hock and Holmgren, 2005; Pellicciotti et al., 2005); and ii) the likely future response of ice masses to future climate scenarios (e.g. Oerlemans et al., 1998; Braithwaite and Zhang, 1999; Radić and Hock, 2006; Raper and Braithwaite, 2006; Hock et al., 2007; Juen et al., 2007; Huss et al., 2008; Radić and Hock, 2011).

The physical processes which such modelling studies must explicitly or implicitly address are those of energy exchange, as it is the balance of energy at the glacier surface which determines the rate of ablation. For melting to occur, there must be a surplus of energy to provide the necessary latent heat to convert ice to liquid form (i.e.

the latent heat of fusion: 334 kJ kg^{-1}). Sublimation occurs when the latent heat flux is negative, and may be prolific in dry climates (e.g. Wagnon et al., 1999; Favier et al., 2004; Hock, 2005). In these settings, large discrepancies may exist between melt and ablation; and indeed, melt will actually be suppressed by the high latent energy consumption of the ice-vapour transition (the latent heat of vaporization: 2849 kJ kg^{-1}). The distinction between ablation and melt is of hydrological importance, as it is the melt component which may contribute to runoff and ultimately to streamflow.

The surface energy balance (SEB. Note that the equation is provided in Section 2.4), which determines ablation, is a function of the interaction between the glacier surface and the atmosphere. More specifically, it is dependent on energy fluxes between the glacier and the 'atmospheric boundary layer'—the lower level of the troposphere that is characterised by well-developed turbulence resulting from thermally- and frictionally-driven eddies transporting momentum, heat, moisture and pollutants (Oke, 1987). Turbulence transports energy directly to the glacier surface through the sensible and latent heat fluxes, whilst the spectral properties of the boundary layer (e.g. thermal emissivity and optical thickness) affect radiative energy transfer. The relationship between the boundary layer and the surface is synergistic, in the sense that both are modified by surface fluxes. On a macro-scale, this produces air masses and baroclinicity in the atmosphere (Stull, 1988); at a smaller scale, this interaction is responsible for the development of a distinct boundary layer, which forms over melting glaciers (e.g. Van den Broeke, 1997a, b; Oerlemans and Grisogono, 2002), and develops as a consequence of the limited maximum surface temperature which melting snow and ice surfaces can attain (0°C). Strong thermal gradients are therefore maintained between the surface and the boundary layer. Moisture gradients are also steep, due to the dependence of vapour pressure on temperature, and the thermal contrast results in negative buoyancy, stratification and the development of a low-level jet draining downhill under gravity (Stull, 2000). In turn, this 'glacier wind' amplifies the turbulent heat fluxes, by effectively generating turbulence through wind-shear (Van den Broeke, 1997a; Parmhed et al., 2004).

In addition to the formation of a glacier boundary layer, other properties of glaciers which are relevant for the surface energy balance are (Hock, 2005):

- high and variable albedo;
- penetration of shortwave radiation;
- high thermal emissivity;
- variable surface roughness.

Glacier surface albedo partly determines the shortwave energy balance, is highly variable, and has been found to be dependent on solar zenith angle, cloud cover, dust content, snow depth/density and grain size (Wiscombe and Warren, 1980; Warren and Wiscombe, 1980). Whilst some of these parameters are dependent on the prevailing weather (e.g. cloud cover), others are more strongly related to preceding conditions and time. For example, if melting persists, then snow grain-size may be determined explicitly as a function of age (Stephenson, 1967; Gow, 1969); similarly, if not removed by meltwater, dust and other absorptive particulates may concentrate with time to lower glacier-surface albedo. Shortwave radiation that is not reflected has the potential to penetrate the glacier to considerable depth, particularly if snow cover is absent (~10m); snow is less easily penetrated (~1m) (Hock, 2005), although this may still be sufficient to drive considerable sub-surface melting (La Chapelle, 1961; Föhn, 1973).

The thermal emissivity of snow and ice is close to unity (Mülller, 1985) and this can often contribute to making the longwave heat flux a net energy sink (e.g. Oerlemans and Klok, 2002; Konya et al., 2007). Nocturnal radiative budgets in particular may be strongly negative when the shortwave flux is negligible. For snow surfaces, this energy loss is not compensated adequately by conduction from the subsurface due to the low thermal conductivity of snow (Hock, 2005). Ice, on the other hand, transmits sensible heat more readily, and the effect of radiative cooling on the surface temperature is less pronounced.

The surface roughness lengths are important parameters for determination of the turbulent heat fluxes and a wide variety of values have been reported (e.g. Moore, 1983; Braithwaite, 1995a; Brock et al., 2006). This parameter can be highly variable between locations on the same glacier (Brock et al., 2000), and through time within the melt season (Grainger and Lister, 1966; Arnold and Rees, 2003). At the most

extreme, surface roughness lengths at a single location have been observed to vary by more than a factor of ten during a single ablation season (Smeets et al., 1999)—a magnitude which is sufficient to double the value of the turbulent heat fluxes (Munro, 1989; Brock et al., 2000). Many authors have reported marked changes in the roughness lengths between snow and ice surfaces (e.g. Bintanja and Van den Broeke, 1995; Hock and Holmgren, 1996; Greuell and Smeets, 2001; Arnold and Rees, 2003; Guo et al., 2011), but there is no clear consensus within the literature regarding which should be of greater magnitude (Hock and Holmgren, 2005).

The physical properties of glaciers, the dynamic, evolving nature of their surfaces, and the effect which this has on energy exchange make them challenging environments for energy-balance investigations. This is especially true when in-situ meteorological measurements within the glacier boundary layer are absent, because the strong modifying effect of glaciers on local climate may not be captured by spatially-coarse climate data. It is against this background that the analyses in this thesis are presented. Local weather, of the scale which affects the glacier boundary layer, manifests as a complex interaction between large- and small-scale processes; and for these to be physically resolved would require dynamical simulation to a resolution which is computationally unreasonable and impractical for most applications (e.g. Oerlemans and Grisogono, 2002; de Ruyter de Wildt et al., 2003). The challenge, therefore, is to examine how large-scale atmospheric processes manifest at the glacier-scale to affect surface energy exchange, in a way which is practical, and which affords understanding of the physical connections as to how these scales are related.

In order for this to be achieved, and before linkages may be sought with climatic processes at the larger scale, it is necessary to obtain a detailed process-based understanding of the SEB and ablation. Detailed knowledge of the meteorology within the glacier boundary layer is therefore required, which may be used to quantify the surface energetics; it is this requirement which the present chapter and Chapter 3 address. More specifically, the aim of this chapter is to outline one of the study sites used in this thesis, and to present details of the meteorological measurements conducted. A further aim is to use these data to simulate and explain variations in ablation caused by the SEB that occur through time and space. These data ultimately provide information about local processes which determine ablation, and will be

related to synoptic-scale climatic variability during subsequent analyses (chapters 4, 5 and 6).

The structure of this chapter is as follows: first, one of the study sites is introduced and details of the meteorological observation programme are given (sections 2.2 and 2.3); next, a SEB model used to simulate melt and ablation is introduced (Section 2.4), and the observed meteorology is then discussed (Section 2.5.1). Finally, the performance of the SEB model is evaluated, and the calculated energy fluxes are examined (Section 2.5.2).

2.2. Study Location

The research utilizes observational data from Vestari Hagafellsjökull, Iceland. This is a large outlet glacier (~157 km^2) of the Langjökull ice cap (Figure 2.1), which is the second largest of Iceland's ice caps at ~900 km^2 (as of 2000; Björnsson and Pálsson, 2008). Langjökull ranges in elevation from ~450 to 1450 metres above sea level, with an average altitude of around 900m and equilibrium line altitudes of ~1100 m and ~1200m for the southern and northern outlet glaciers, respectively (Guðmundsson et al., 2009). Like the rest of the glaciers in Iceland, Langjökull is warm-based or 'temperate' (Björnsson et al., 2003) and reacts rapidly to climatic change. Mass turnovers are also high at Langjökull, reaching ~0.8% of volume in a year of zero net balance (Björnsson and Pálsson, 2008).

Annual mass balance measurements have been performed at Langjökull since 1996/1997 (Guðmundsson et al., 2009), and through to 2005/2006 negative balances have persisted. This wastage is consistent with the retreat of other Icelandic glaciers since the end of the 19th century (Björnsson and Pálsson, 2008) and Langjökull is predicted to have disappeared completely within the next 200 years (Jóhannesson et al., 2007). Hydrologically, this will affect both the Hvítá River, which drains the ice cap, and groundwater supplies; the latter receives a substantial proportion of Langjökull's runoff (Sigurðsson, 1990).

From a climatological perspective, Iceland's position in the North Atlantic represents a key geographical area of atmospheric dynamics and of ocean-atmosphere interactions. This can be attributed to the relative proximity of the Greenland ice sheet, and the fact that the extratropical cyclone tracks frequently direct disturbances

in the polar front towards Iceland (Einarsson, 1984; Wang and Rogers, 2001). Indeed, a general characteristic of Iceland's climate is contrast: cold and warm ocean currents meet to the south-east and north-east of Iceland, as the warm Irminger Current (a branch of the North Atlantic Drift) meets the cold East Greenland Current. This frigid southerly flow may bring sea-ice to the north coast of Iceland, in which case, coastal locations can record appreciable negative temperature anomalies and a transition from maritime to continental-type climate can occur. Sharp temperature contrasts are also found in the atmosphere, due to the passage of both polar and tropical air masses (Einarsson, 1984).

Langjökull's location in the west of the Central Highlands means that it typically receives up to 3,500 mm of precipitation annually (Björnsson and Pálsson, 2008). In summer, clear weather in this location is often associated with the advection of northerly air, although due to the polar source, temperatures remain cool. Fair weather may also occur with easterly airflow. This condition is more common due to the proximity and persistence of the Icelandic Low, which means that airflow from southeast to northeast is most frequent. Favourable conditions resulting from anticyclones are usually caused by an extension of the Greenland High. Cyclones remain frequent but relatively subdued in summer (Serreze et al., 1997) and produce high wind speeds, frontal precipitation and rapid temperature changes (Einarsson, 1984). The dynamic climatological setting of Iceland, and in particular, of Langjökull, makes this location ideally suited for the investigation of synoptic aspects of glacier-climate interactions.

2.3. Meteorological Observations

To associate the processes that affect ablation with synoptic climatology, this study makes use of boundary-layer glacier climate data recorded by Automatic Weather Stations (AWSs) installed by the Institute of Earth Sciences, Reykjavik. Data were logged during the period 2001-2010 at two elevations on Vestari Hagafellsjökull (500 m and 1100 m). The period of operation and the location of the stations can be seen in Table 2.1 and Figure 2.1, respectively.

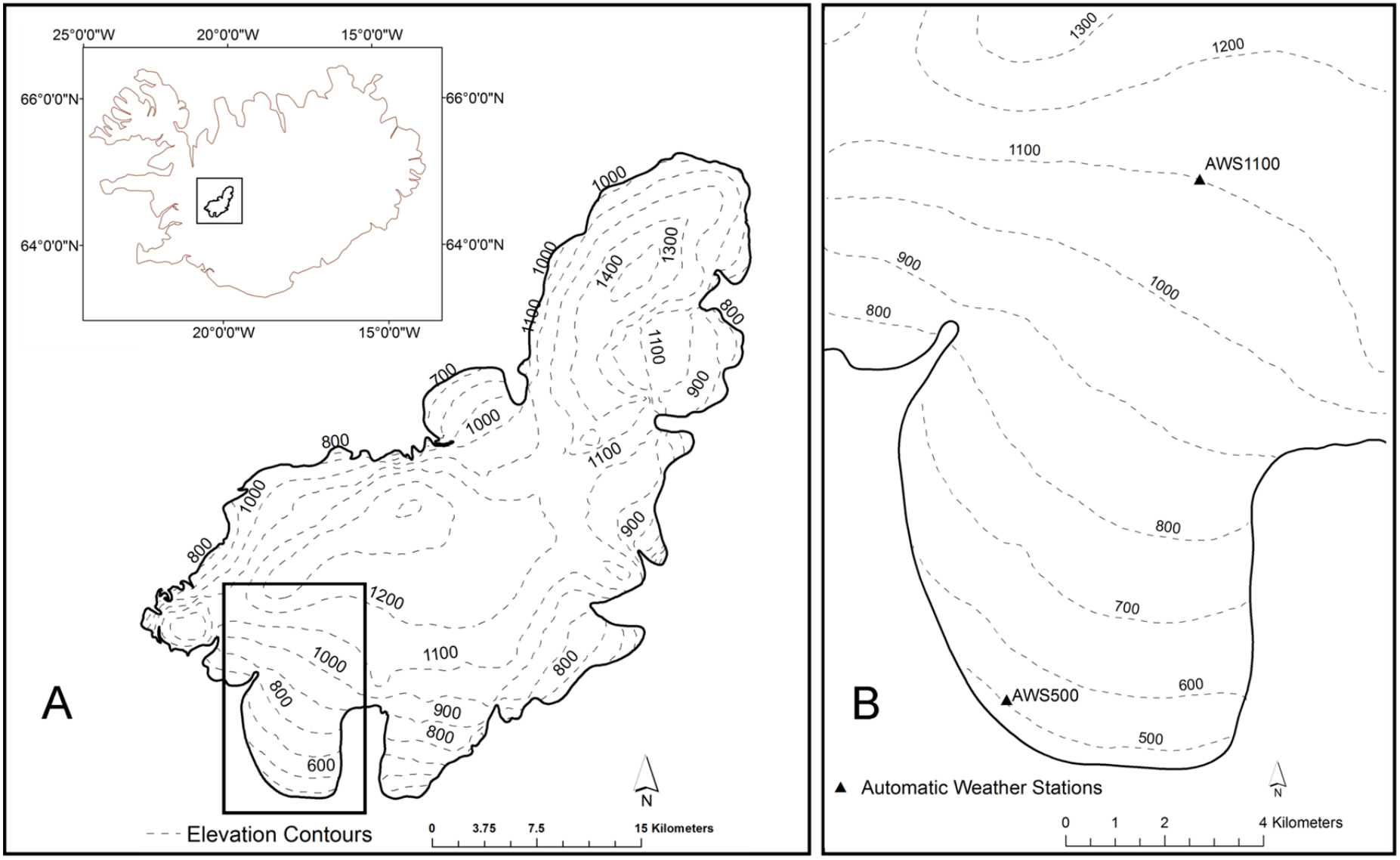

Figure 2.1. Location of study. A: Langjökull and its position in Iceland (inset). B: area indicated in 'A' enlarged, showing Vestari Hagafellsjökull and the location of the AWSs. Contoured maps produced from DEM provided by the Institute of Earth Sciences, Reykjavik.

Table 2.1. Periods of AWS observations. Dates are in day-of-year (Julian day) format. [a]See text for explanation.

Year	AWS 500 m	AWS 1100 m	UDG 500 m	UDG 1100 m
2001	110-278	109-359	[a]110-278	109-245
2002	117-304	117-288	116-304	117-288
2003	115-296	115-294	115-296	115-262
2004	129-297	130-258	-	-
2005	129-287	130-285	114-286	113-285
2006	137-325	137-291	191-325	136-291
2007	118-312	118-268	118-312	118-268
2008	110-326	110-326	110-326	110-235
2009	109-293	110-266	109-194	157-256
2010	107-193	107-277	107-193	107-277

Air pressure (P) is not measured at either AWS. Instead, its value at elevation (h) is approximated from synoptic weather stations at elevation (h_0), according to an empirical formula which has been applied successfully at locations on and around Vatnajökull (Guðmundsson et al., 2009):

$$P(h) = P(h_0)\left(1 - \frac{0.0065(h - h_0)}{T(h_0)}\right)^{5.25}, \quad 2.1$$

where T is the air temperature in Kelvin. P and T at h_0 are obtained from Hveravellir (a synoptic meteorological station maintained by the Icelandic Meteorological Office, and in close proximity to Langjökull). The AWS 'float' so that they lower as the glacier ablates. All instrumentation is therefore kept at a constant distance (2 metres) from the snow/ice surface. Radiation and wind speed sensors are mounted in a plane parallel with the surface. The full range of meteorological variables measured at each station is:

- air temperature;
- relative humidity;
- wind speed and direction ;
- incident and reflected shortwave radiation;
- incident and emitted longwave radiation;

Surface ablation and accumulation at each site were also recorded by ultrasonic depth gauges (UDGs). These instruments are mounted on frames drilled into the ice, which thus maintains a fixed reference height to determine relative surface elevation change.

Details of all the instrumentation, including the reported accuracies, are provided in Table 2.2. This setup has been described previously by Guðmundsson et al. (2009) and is illustrated schematically in Figure 2.2.

Table 2.2. Details of meteorological instrumentation.

Parameter	Sensor	Accuracy
Temperature	Vaisala HMP35	0.2°C
Relative humidity	Vaisala HMP35	2%
Wind speed	R.M. Young 05103	0.3 m s^{-1}
Wind direction	R.M. Young 05103	5°
Shortwave radiation	Kipp and Zonen CNR1-CM3	3% (±10% daily sums)
Longwave radiation	Kipp and Zonen CNR1-CG3	3% (±10% daily sums)
Accumulation/ablation	Cambell Scientific SR50	max(0.01m, 0.4%)

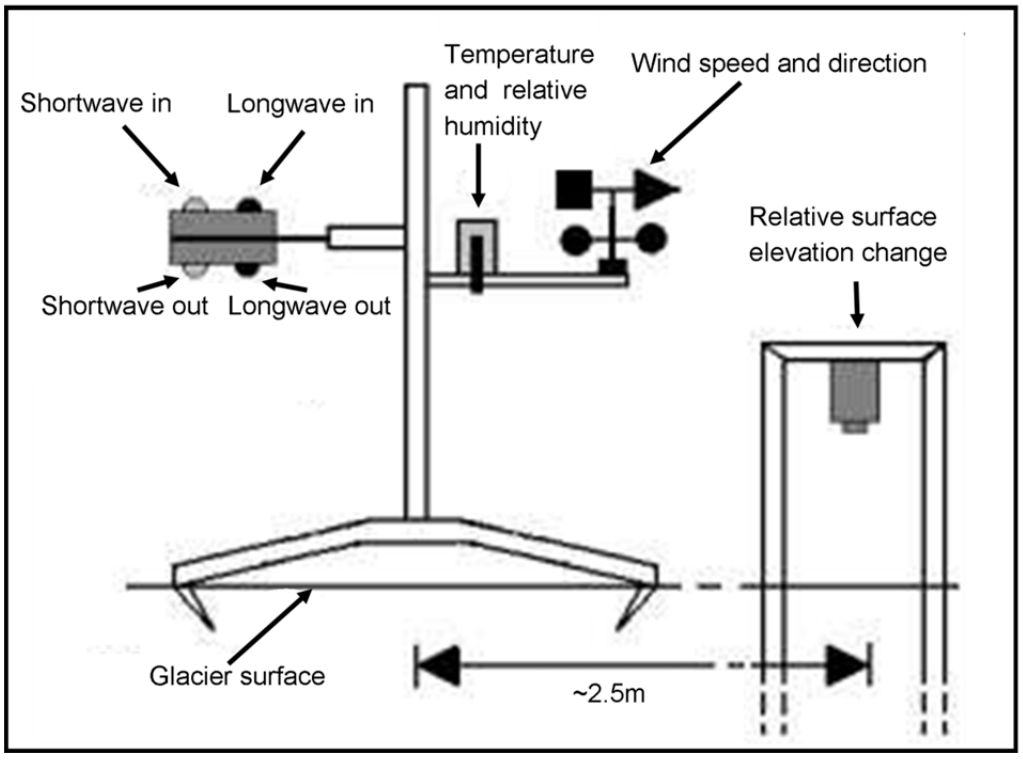

Figure 2.2. Schematic illustration of the AWS setup. Modified from Guðmundsson et al. (2009).

Instruments are calibrated each April and September in Reykjavik, and the AWSs were routinely monitored throughout the period of operation. Meteorological parameters were sampled every 10 minutes and averaged to hourly resolution. The UDGs measured at a 30 min interval prior to 2006, and a 10 min interval after. In 2001, UDGs failed at both elevations (in August at 500 m and in June at 1100 m). To

reconstruct surface elevation change during these periods, missing UDG data were linearly interpolated based on stake observations of total accumulated ablation at the end of the measurement period indicated in Table 2.1.

2.4. Energy Balance Modelling

The energy balance at a melting glacier surface can be written, e.g. Hock (2005):

$$Q_N + Q_H + Q_L + Q_G + Q_R + Q_M = 0 \ , \qquad 2.2$$

where Q_N is net radiation and the turbulent energy fluxes are given as Q_H (sensible) and Q_L (latent); Q_G refers to the ground heat flux and Q_R to the rain heat flux. Q_G may constitute a significant energy sink in the presence of a cold surface layer (e.g. Wheler and Flowers, 2011; Reijmer and Hock, 2008Pellicciotti et al., 2009). However, on temperate glaciers, during melt conditions, Q_G can be assumed to be zero (e.g. Oerlemans, 2000; Brock and Arnold, 2000), and is consequently ignored in this study. Similarly, the rain heat flux (Q_R) is not calculated, as only in exceptional circumstances does rain constitute a significant energy source (e.g. Hay and Fitzharris, 1988; Hock, 2005).

Q_N is a function of the net shortwave (S) and longwave (L) energy components:

$$Q_N = S_i \ (1 - \alpha) + L_i - L_o \ , \qquad 2.3$$

in which the subscripts i and o denote the incident and outgoing radiative fluxes, respectively and the albedo is given by α. All these terms are measured directly, in situ (Table 2.2). The turbulent fluxes are calculated from air temperature, relative humidity and wind speed data recorded at one measurement height, z (2 metres) above the surface using the bulk aerodynamic method (e.g. Ambach and Kirchlechner, 1986; Oke, 1987; Braithwaite et al., 1998a):

$$Q_H = \rho_v c_p \frac{k^2}{[\ln\left(\frac{z}{z_{0w}}\right) - \Psi_{\mathrm{M}}(\frac{\mathrm{z}}{\mathrm{L}})]\,[\ln\left(\frac{\mathrm{z}}{\mathrm{z}_{0T}}\right) - \Psi_{\mathrm{H}}\left(\frac{\mathrm{z}}{\mathrm{L}}\right)]} U_z(T_z - T_0) \ , \qquad 2.4$$

$$Q_L = Lv\frac{0.623\rho_v}{P} \frac{k^2}{[\ln\left(\frac{z}{z_{0w}}\right) - \Psi_{\mathrm{M}}(\frac{\mathrm{z}}{\mathrm{L}})]\,[\ln\left(\frac{\mathrm{z}}{\mathrm{z}_{0e}}\right) - \Psi_{\mathrm{E}}\left(\frac{\mathrm{z}}{\mathrm{L}}\right)]} U_z\,(e_z - e_0) \ , \qquad 2.5$$

where ρ_v is the variable air density given by $\rho_0(P/P_0)$ with ρ_0 as the density of air at standard pressure, P_0 (1.29 kg m^{-3} at 1.013×10^5 Pa, respectively (Paterson, 1994)) and P being the air pressure as determined by Equation 2.1 (Guðmundsson et al., 2003); k is the Von Karman constant (0.40) and c_p is the specific heat capacity of air under constant pressure (1010 J kg^{-1}); Lv is set to the specific latent heat of evaporation (2.514×10^6 J kg^{-1}), or sublimation (2.849×10^6 J kg^{-1}), as appropriate; z is the measurement height; and z_{0w}, z_{0T} and z_{0e} are the roughness lengths for wind speed, temperature and water vapour, respectively; U is wind speed; T is temperature; and e is vapour pressure (the subscripts refer to values at the measurement height (z: 2 m, and the surface: 0 m); Ψ_M, Ψ_H and Ψ_E are stability functions and L is the Monin-Obukhov Length. The stability functions are incorporated to correct for deviations from the neutral logarithmic boundary-layer profiles of wind speed, temperature and water vapour. This correction is applied because the turbulent fluxes are likely to be overestimated considerably during stable conditions and low wind speeds (Brock and Arnold, 2000; Munro, 1989; Braithwaite, 1995a).

Vapour pressure for a melting glacier surface (e_0) is constrained to 610.8 Pa; e_z is obtained from $e_s\ Rh/100$ where Rh is relative humidity (%) and e_s is the saturation vapour pressure, which is given by Oerlemans (2000) as:

$$e_s = 610.8 \exp[19.85\left(1 - \frac{273.15}{T_k}\right)] \ , \qquad 2.6$$

in which T_k is temperature in Kelvin. To determine the stability corrections (Ψ_M, Ψ_H and Ψ_E) for stable conditions, the corrections are parameterized according to Beljaars and Holtslag (1991):

$$-\Psi_M = \frac{az}{L} + b\left(\frac{z}{L} - \frac{c}{d}\right)\exp\left(-d\frac{z}{L}\right) + \frac{bc}{d} \ , \qquad 2.7$$

$$-\Psi_H = \left(1 + \frac{2}{3}\frac{az}{L}\right)^{\frac{3}{2}} + b\left(\frac{z}{L} - \frac{c}{d}\right)\exp\left(-d\frac{z}{L}\right) + \frac{bc}{d} - 1 \ . \qquad 2.8$$

The coefficients for these equations are assigned as: a = 1, b = 0.667, c = 5 and d is 0.35. For unstable conditions (when $T_0 > T_z$), which are encountered less frequently, the stability functions of Paulson (1970) and Dyer (1974) are preferred, as recommended by Högstrom (1988):

$$\Psi_{\mathrm{M}} = 2\ln[(1+\mathrm{x})/2] + \ln[(1+\mathrm{x}^2)/2] - 2tan^{-1}(x) + \pi/2\,, \qquad 2.9$$

$$\Psi_{\mathrm{H}} = 2\ln[(1+\mathrm{x}^2)/2]\,, \qquad 2.10$$

where x is given by $(1-16z/L)^{1/4}$. For both stable and unstable cases, it is assumed that $\Psi_{\mathrm{H}} = \Psi_{\mathrm{E}}$.

The Monin-Obukhov Length is determined from:

$$\mathrm{L} = \frac{\rho_v c p {u_*}^3 T_a}{kgQ_H}\,, \qquad 2.11$$

in which g is the acceleration due to gravity (9.81 m s^{-2}), T_a is the mean temperature (K) between the surface and the measurement height and u_* is friction velocity, given by:

$$u_* = \frac{kU_z}{\ln\left(\frac{z}{z_{0w}}\right) - \Psi_{\mathrm{M}}}\,. \qquad 2.12$$

The stability functions require L, which in turn depends on knowledge of Q_H and u_*. This introduces circularity, which is dealt with by means of an iterative loop (Munro, 1989; Brock and Arnold, 2000; Hock and Holmgren 2005; Wheler and Flowers, 2011): Q_H and u_* are calculated for the neutral case and the stability functions = 0. These initial estimates are used to estimate L. The stability functions are then re-calculated, and the iteration continues until the change in Q_H is small. In this study, the iteration is terminated when the change in Q_H is less than or equal to 0.05W m^{-2}, or 1% of Q_H. This is frequently achieved after ~5 iterations, with the bulk of the correction applied during the second loop (Munro, 1989).

Values for the roughness lengths of temperature and water vapour are provided by a polynomial of the form suggested by Andreas (1987):

$$\ln\left(\frac{Z_s}{z_{0w}}\right) = f_0 + f_1 \ln Re^* + f_2(\ln Re^*)^2\,, \qquad 2.13$$

where Z_s is Z_{0e} or Z_{0T} .The coefficients (f_n—see Table 2.3 for values) are dependent on the roughness Reynolds number (Re^*), given by: $u_*\ z_0$/v where v is the kinematic viscosity of air (1.461 × 10^{-5} m^2 s^{-1}). Through use of Equation 2.13, it is necessary to

prescribe only the roughness length for wind speed. Values for this parameter vary substantially depending on the physical properties of the glacier surface, with published values ranging over three and five orders of magnitude for low and high latitude glaciers respectively (Brock et al., 2006). Values adopted for this study (Table 2.4), are taken from Guðmundsson et al. (2009), and are based on detailed energy budget studies on Vatnajökull, during 1996-2000. The calculated heat fluxes are defined as positive when directed towards the surface.

Table 2.3. Coefficients for parameterization of the temperature and vapour roughness lengths.

	Smooth	**Transition**	**Rough**
	$\boldsymbol{Re}^* \leq 0.135$	$0.135 < \boldsymbol{Re}^* < 2.5$	$2.5 \leq \boldsymbol{Re}^* \leq 1000$
Temperature (z_{0T})			
$\boldsymbol{f_0}$	1.250	0.149	0.317
$\boldsymbol{f_1}$	-	-0.550	-0.565
$\boldsymbol{f_2}$	-	-	-0.183
Water vapour (z_{0e})			
$\boldsymbol{f_0}$	1.610	0.351	0.396
$\boldsymbol{f}$	-	-0.628	-0.512
$\boldsymbol{f_2}$	-	-	-0.180

The surface types determining which value of z_{0w} to apply were identified from the near-surface density of the glacier: at 500 m, the roughness length for ice was used when near-surface density was $\geq 8.3 \times 10^2$ kg m^{-3}, and that of new snow for densities below 4×10^2 kg m^{-3}. Otherwise, the roughness length for firn/melting snow was applied (e.g. Paterson, 1994). At 1100 m, the choice of roughness lengths is between those for new snow and firn, as ice is not exposed in the summer at this elevation (Guðmundsson et al., 2009); the same threshold of 4×10^2 kg m^{-3} is used to differentiate between these surface types.

Table 2.4. Roughness lengths of momentum applied in this study after Guðmundsson et al. (2009).

	$\boldsymbol{z_{0w}}$ **(mm)**	$\boldsymbol{\ln(z_{0w})}$
New snow	0.1	-9.2
Firn/melting snow	2	-6.2
Ice	10	-4.6

Surface density is also required to validate the melt model through comparison with the UDG record, and is parameterized following Hodgkins et al. (2012a), by solving the equation of Greuell and Konzelmann (1994) for ρ_1, the near surface density:

$$\alpha = \alpha_i + (\rho_1 - \rho_i)\frac{(\alpha_s - \alpha_i)}{(\rho_s - \rho_i)} + 0.05(n - 0.5) \ , \qquad 2.14$$

where α is the surface albedo, and ρ is the near-surface density; the subscripts *s* and *i* refer to ice and snow respectively. This parameterization utilizes albedo changes caused by varying grain size and surface roughness to infer density. The last term on the right-hand side is included to incorporate the rise in albedo with increasing cloud cover (n) (Grenfell, 1979). As no observations of cloud cover are made automatically on the ice cap, cloud cover was derived from ERA-interim reanalysis data, downloaded for the *c.*110 × 50km grid cell in which Vestari-Hagafellsjökull is located (http://data-portal.ecmwf.int/data/d/interim_daily). 6-hourly data were obtained and then averaged to daily resolution. The ERA-interim reanalysis covers the period 1979 to present, using T255 horizontal resolution, boundary forcing fields from ECMWF operations and a 12 hour, 4D-Var data assimilation system (ECMWF, 2006, 2007, 2008). Daily average albedo was used to prescribe α, and the density time-series produced by Equation 2.14 was smoothed with a moving average to more realistically capture the low-frequency evolution of near-surface density.

Measured ablation (A_{meas}: in mm w.e.) is then obtained by correcting the raw UDG measured change (Δh_{meas}) according to the ratio of p_1 to the density of water (p_w:10 × 10^2 kg m^{-3}). For purposes of validation, the UDG record is truncated when snowfall is frequent at the beginning and end of the ablation season. The model is validated at daily resolution and periods of net accumulation at the surface are treated as missing data; these days are differentiated from instances when no ablation takes place according to:

$$A_{meas} = \begin{cases} \frac{p_1}{p_w}\,\Delta h_{meas} & , \Delta h_{meas} \geq 0 \\ 'missing' & , \text{otherwise} \end{cases} . \qquad 2.15$$

And, for comparison, ablation simulated by the model (A_{mod}: also in mm w.e.) is given by:

$$A_{\mathrm{mod}} = \begin{cases} \max\left(0, \frac{Q_m}{L_f}\right) & , Q_L \geq 0 \\ \max\left(0, \frac{Q_m}{Q_L}\right) - \frac{Q_L}{L_s} & , Q_L < 0 \end{cases}, \qquad 2.16$$

where L_f is the specific latent heat of melting and L_s is the latent heat of sublimation. It is therefore assumed that when the latent heat flux is negative, mass may be lost through sublimation. When the latent heat flux is positive, however, runoff, rather than re-sublimation occurs, because it is assumed the surface is at the melting point throughout the simulation. Comparisons of the modelled and observed ablation series defined according to equations 2.15 and 2.16 are performed at daily resolution.

Although glacier observations are available for a range of months over the measurement period (Table 2.1), energy balance computations are only performed for the summer months of June, July and August (JJA). This decision is taken because the focus of this research is on processes which determine ablation—the majority of which takes place during the summer months; and whilst September is regarded as part of the summer in Iceland (Hanna et al., 2004), it is more of a transitional month on the ice cap, with temperatures hovering around the freezing point (Björnsson and Pálsson, 2008; Hodgkins et al., 2012b). Moreover, measurements of ablation (and accumulation) from the UDGs do not extend to the end of September in five of the ten years of observations at 1100 m and validation of simulated ablation is therefore limited during this month.

Additional restrictions on the SEB modelling are: at 500 m, energy balance computations are not performed after 2007, due to uncertainty surrounding the calibration coefficient of the CNR1 for the period 2008-2010 at this elevation (Guðmundsson, personal communication); and at 1100 m, validation of the SEB model is avoided in 2010, due to the eruption of the Eyjafjallajökull volcano, which greatly affected the albedo of Langjökull (Guðmundsson, personal communication), thereby eliminating the utility of Equation 2.14 to parameterize the near-surface density. SEB calculations are, however, still performed for 2010, and because the prescription of the roughness lengths is based on the observed albedo/density, the

effect of the tephra-layer must still be considered. This was dealt with by manually assigning roughness lengths after examination of the albedo record. Differentiating between new snow and firn was readily achieved, as snowfall buries the tephra and greatly increases the albedo.

2.5. Results

This section presents results of the meteorological observations on the ice cap during the measurement period (Section 2.5.1), before evaluating the ability of the energy balance model to simulate observed ablation (Section 2.5.2). Finally, temporal and spatial variability of the observed energy balance on the ice cap is discussed (Section 2.5.2.1).

2.5.1. Meteorological observations

The JJA period clearly exhibits the highest air temperatures at both elevations on the ice cap, and the warmest month is July. This pattern is consistent with the climate regime of most of Iceland, as only on the north and east coasts is August typically the warmest month (Einarsson, 1984). Days on which the mean daily air temperature falls below zero are rare during this three-month interval at 1100 m (~10% of days) and even more so at 500 m (<1% of days) (Figure 2.3). Outside JJA, freezing temperatures are more common, although the average monthly temperature remains positive for all observations at the 500 m station (Table 2.5: page 39). There is also appreciable spatial coherence in air temperature between the two elevations, as shown by the hourly and daily correlation coefficients (0.68 and 0.78, respectively for the JJA period).

Although temperatures are evidently warmer lower on the glacier, the magnitude of this difference is relatively muted: mean temperatures for JJA were 4.9°C and 1.7°C at 500 m and 1100 m, respectively, corresponding to a mean lapse rate of -0.53°C 100 m^{-1}—appreciably lower than the Environmental Lapse Rate (ELR) of -0.65°C 100 m^{-1}. Subdued lapse rates over glaciers during the summer have been observed previously (Greuell et al., 1997; Marshall et al., 2007; Gardner et al., 2009; Hodgkins et al., 2012b), and are attributed to the cooling effect of the melting glacier surface, which remains limited to a maximum of 0°C (Greuell and Böhm, 1998).

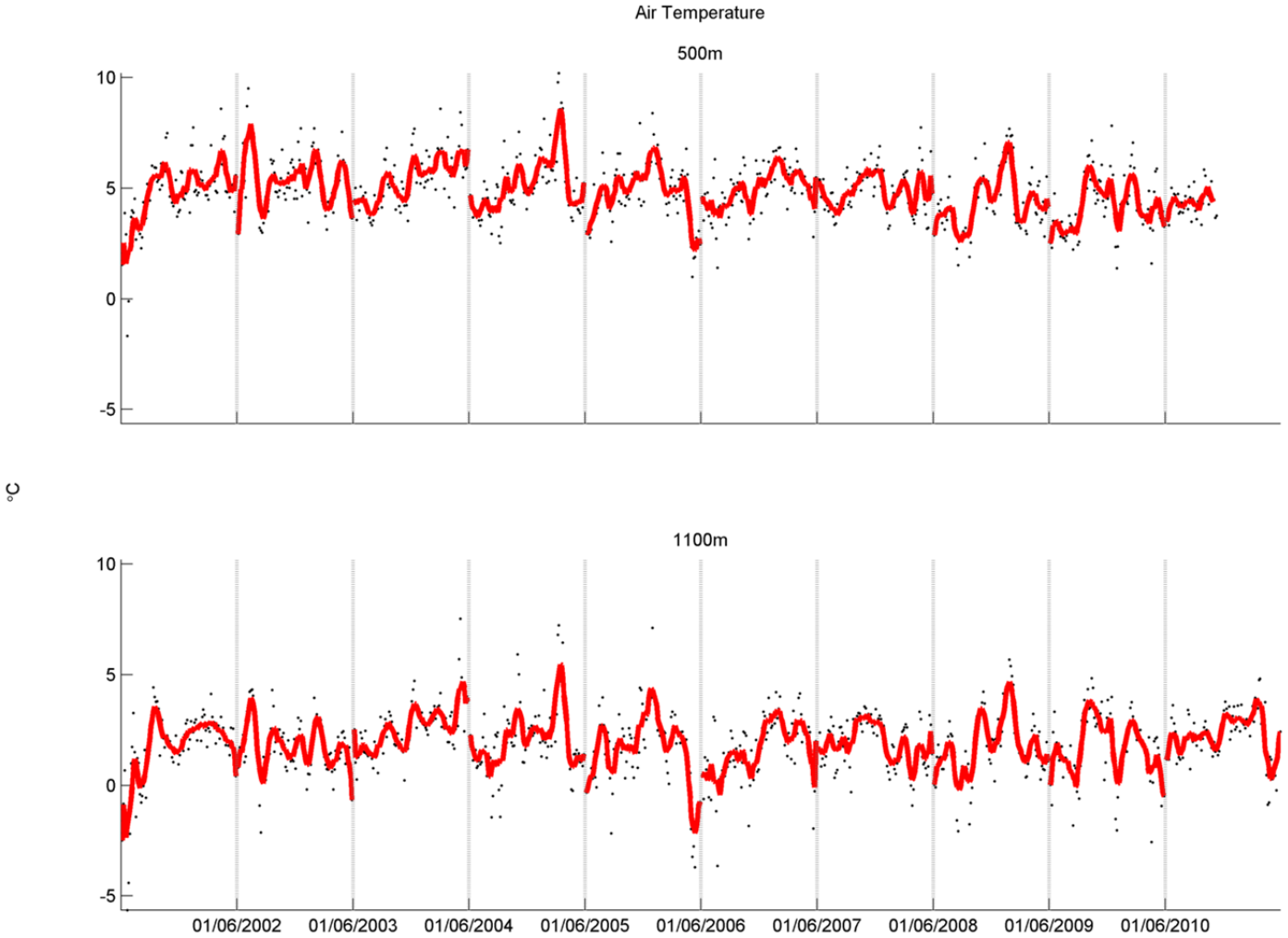

Figure 2.3. JJA daily air temperatures (dots) smoothed with 3 day centred moving average (red line). Grey lines indicate transition between August 31st and Jun 1stfor successive years. This format is used for Figure 2.4 and figures 2.6-2.8.

This cooling of the overlying air by the glacier during melt conditions may also explain the low standard deviations observed during JJA (Table 2.5), as sensible heat exchange between the cold glacier and the overlying air acts to lower the temperature sensitivity of the glacier boundary layer to thermal changes in the free-atmosphere (Gardner et al., 2009; Hodgkins et al., 2012b). Processes determining lapse rates and their relationship with the prevailing weather are evaluated in detail in Chapter 5.

Relative humidity is generally high at the AWSs (Figure 2.4), which is usual for Iceland, due to the proximity of the ocean and the maritime climate that prevails. Monthly variability indicates a gradual, seasonal increase in humidity, with minimum values observed in May and maximums found in September (500 m) and October (1100 m) (Table 2.5). The observed minimum during spring/early summer is consistent with the regime outlined by Einarsson (1984), who reports that the lowest relative humidities are usually observed during the period January-June, with May being most frequent for recording minimum values. Comparing locations, it is apparent that relative humidity increases up glacier (JJA means of 93.4% and 83.7%, and means for all months in Table 2.5 of 92.7% and 82.7% at 1100 m and 500 m, respectively).

Mixing ratios should also be compared between sites because, as a conservative variable, this metric is not affected by adiabatic processes:

$$r = \frac{\varepsilon\, e}{P - e}\ , \qquad 2.17$$

where ε is the ratio of gas constants (water vapour:dry air = 0.622), e is the saturation vapour pressure, and P is the atmospheric pressure measured at the AWS. Comparisons of mixing ratios indicate higher values at 500 m than at 1100 m during JJA (means of 4.81 g $kg^{-1}$and 4.59 g kg^{-1}). The difference is slightly reduced if data from all months are analysed (respective means of 4.37 g $kg^{-1}$and 4.20 g kg^{-1}). Compared to alpine glaciers, these humidities are low: Greuell et al. (1997) and Brock et al. (2010) report mean mixing ratios ranging between 5.3 g kg^{-1} and 6.5 g kg^{-1} at altitudes between 2030 m and 3225 m from observations in the Austrian and Italian Alps, respectively.

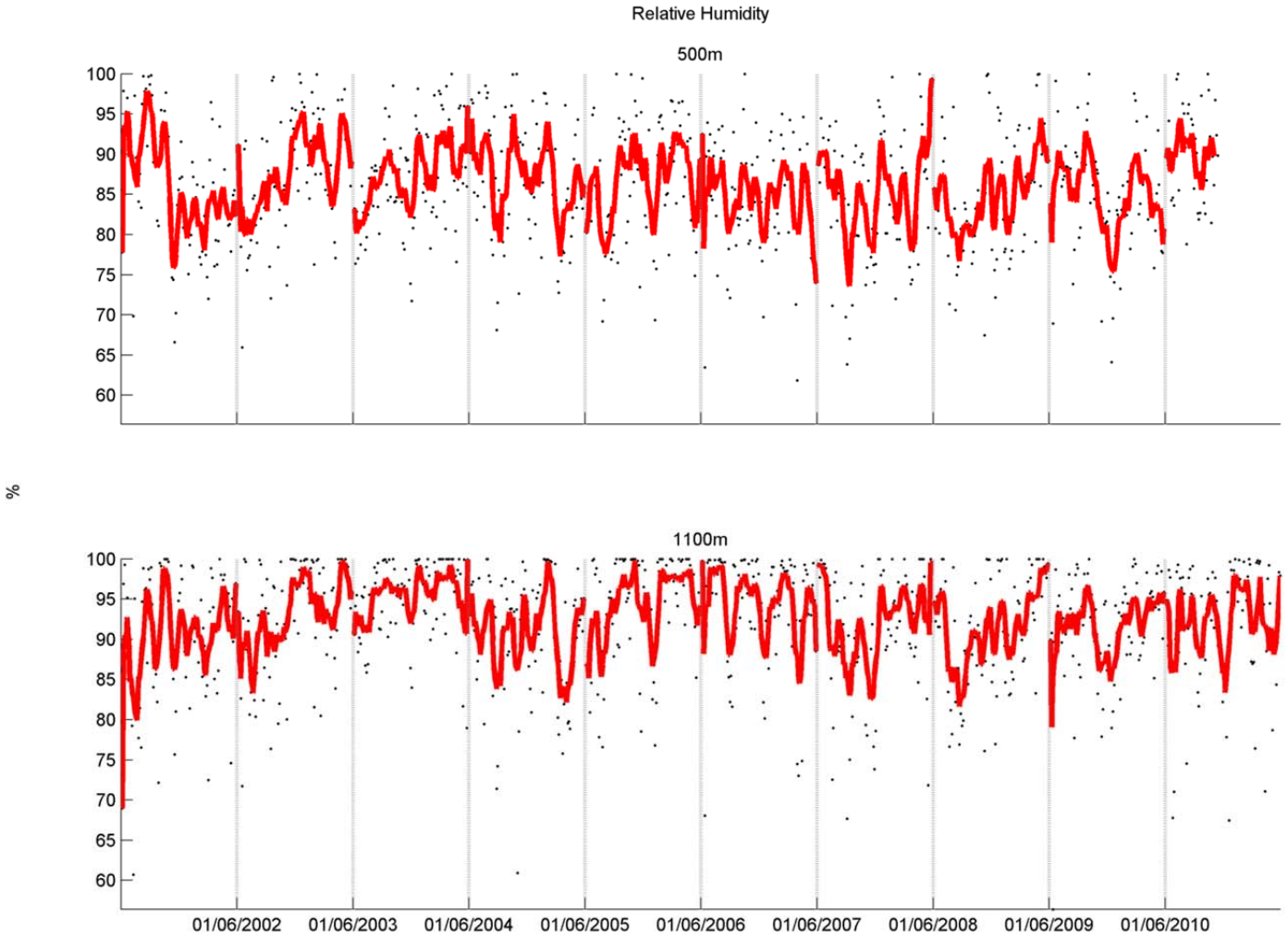

Figure 2.4. Daily mean relative humidity at each of the AWSs.

It is also interesting to note that the mixing ratio increases with decreasing elevation at Vestari Hagafellsjökull. This is pertinent because, as is shown later (Section 2.5.2), the latent heat term is positive at the lower elevation station, which means that moisture is removed from air draining downslope. Thus, the fact that the mixing ratio *increases* down-glacier requires that this extraction is more than compensated by moisture entrainment from the overlying atmosphere; this process has been documented similarly in the Alps by Van den Broeke (1997a) and Greuell et al. (1997).

Wind speeds are high at both elevations: the lowest monthly wind speed at either location is 5.35 m s^{-1}, observed at 1100 m during July. Einarsson (1984) reports similarly high monthly mean wind speeds at almost all locations across Iceland, and Björnsson et al. (2005) give comparable values from AWS investigations on the Vatnajökull ice cap in south-west Iceland. Between elevations, wind speeds are identical for the JJA period, averaging 5.46 m s^{-1} at both sites; for the extended period (May-October), slightly faster winds are observed at 1100 m than 500 m (6.1 m s^{-1} and 5.7 m s^{-1}, respectively). Wind directions are also strongly uni-modal at both locations (Figure 2.5). This tendency for the wind to blow from one direction may be quantified by the directional consistency (DC, e.g. Van den Broeke, 1997a; Björnsson et al., 2005):

$$DC = \frac{\sqrt{\overline{u^2} + \overline{v^2}}}{\frac{1}{N}\sum_{i=1}^{i=N}\overrightarrow{V_i}}, \qquad 2.18$$

in which u and v have their usual meteorological convention, the over-bars denote means, and $\overrightarrow{V_i}$ is the hourly wind speed. A DC value of one indicates that the wind always blows in the same direction, whilst a value of zero implies the wind direction follows a uniform distribution. Applying Equation 2.18 to the AWS yields relatively high DC values of 0.55 and 0.38 for the period May-October at 500 m and 1100 m, respectively, rising to 0.63 and 0.43 during JJA. High directional constancy is typical of winds over melting glaciers, because the cooling effect of the glacier causes negative buoyancy, and the magnitude of this force is typically far greater than results from the synoptic pressure gradient (e.g. Stenning et al., 1981; Van den Broeke, 1997a).

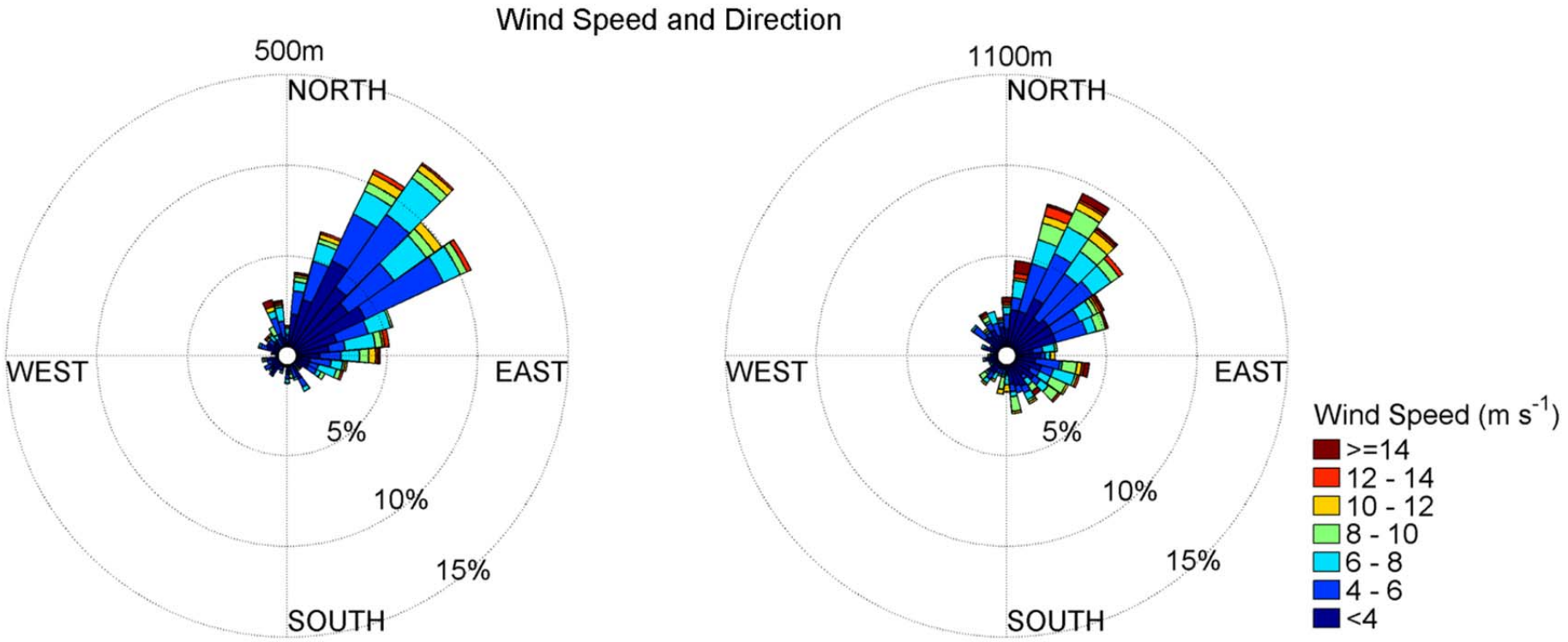

Figure 2.5. Daily mean wind speed and direction at each of the AWSs. Frequencies of wind directions (in 10° increments) for the wind-speed intervals shown in the legend above (bottom right of figure) are indicated by the radial length of each bar: the concentric rings illustrate the relative frequency of winds from each direction.

The decrease in DC with elevation is also consistent with previous observations, as typically, the surface slope is gentler and the temperature contrast between the glacier and the overlying air less pronounced at higher elevations; thus, katabatic drainage is less developed and more easily disrupted by synoptic flow (Oerlemans and Grisogono, 2002).

DCs are observed to be lower at 500 m and 1100 m if May, September and October are addressed separately from the JJA period (means of 0.47 and 0.34 at 500 m and 1100 m, respectively). The lowest DCs are found in September at 500 m and in October at 1100 m (0.34 and 0.32, respectively). This may be explained partly by the cooler air temperatures, and therefore weaker katabatic forcing that prevails during this period; but also, by the rise in the synoptic force resulting from lower atmospheric pressure that occurs in these months (Table 2.5; Figure 2.6). The reduction in air pressure from a maximum during early summer to lower values in later summer/autumn is consistent with previous summaries of Icelandic climate: Einarsson (1984) and Hanna et al. (2004) report highest atmospheric pressures in Iceland being recorded in May, whilst lower pressures during September/October on Langjökull have been associated with an increase in the frequency of low-pressure systems during this month (Guðmundsson et al., 2009). The concomitant increase in synoptic wind speeds that results from these conditions is therefore likely to contribute to the lower DCs that occur by overriding and eroding the katabatic wind.

For the radiative fluxes, mean incident shortwave radiation falls from a maximum during May (500 m) and June (1100 m), to a minimum in October, which mainly reflects the seasonal decline in potential (top of atmosphere) shortwave radiation (Figure 2.7). Between AWSs, there is an increase in incident shortwave radiation with elevation: for all months in Table 2.5, mean fluxes are 149 W m^{-2} and 178 W m^{-2} at 500 m and 1100 m, respectively; for JJA, the difference is slightly larger, with means of 177 W m^{-2} (500 m) and 221 W m^{-2} (1100 m). The cause for this increase up glacier may partly be attributed to the lower optical mass of the atmosphere at the higher elevation (Meyers and Dale, 1983). Also, the higher surface albedo at this elevation (Guðmundsson et al., 2009) could contribute to the downward shortwave flux through multiple scattering between the glacier surface and the overlying air (Konzelmann et al., 1994).

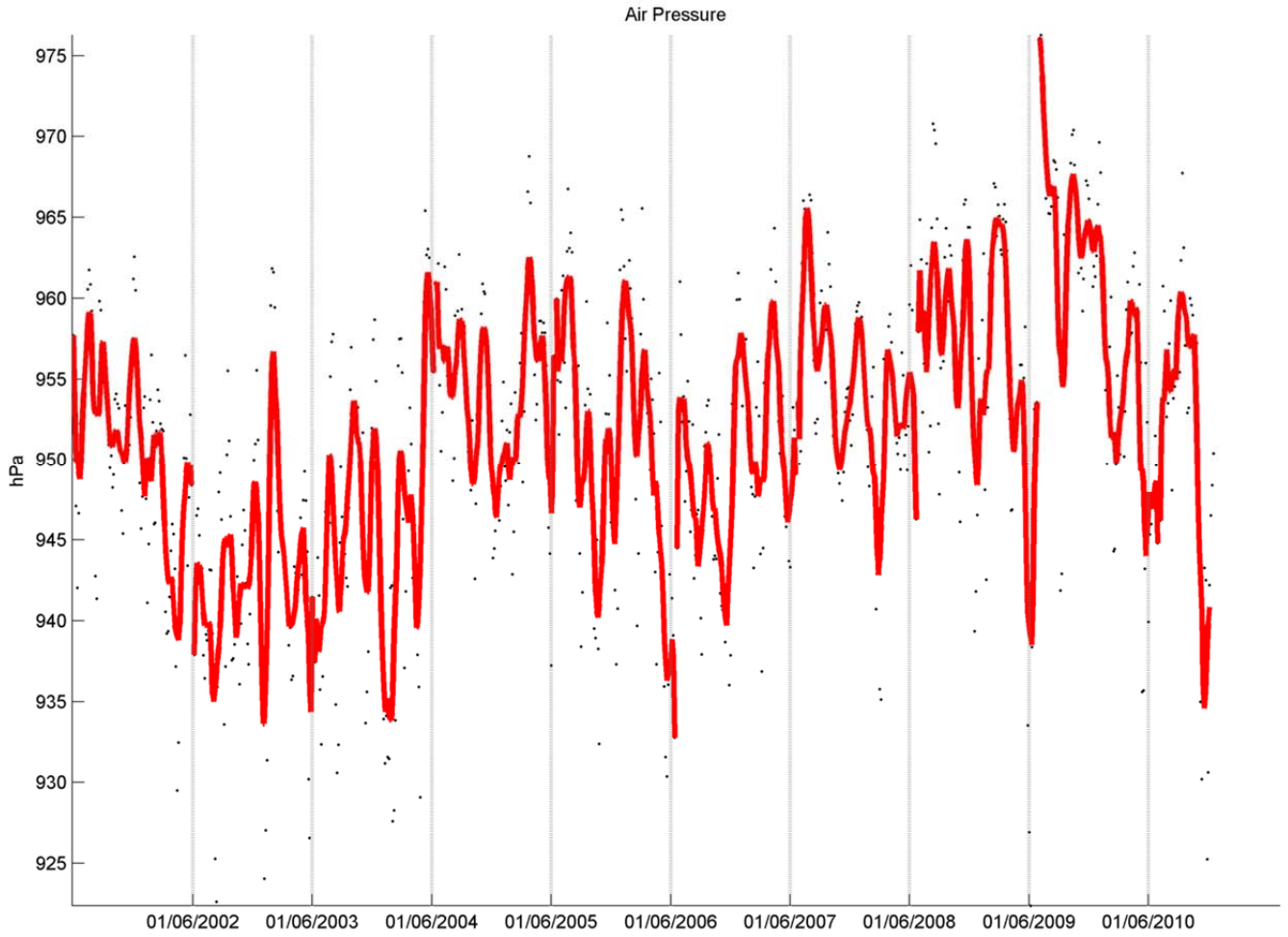

Figure 2.6. Daily air pressure. Note that only data from 500 m is displayed, because air pressure is not actually measured, but calculated from an off-glacier AWS (see text). Hence, variation between stations will only reflect the difference in elevation.

The vertical gradients in shortwave radiation obtained in this study (7.33 W m^{-2} 4.83 W m^{-2} for JJA and all months, respectively) are in close agreement with Oerlemans et al. (1999), who noted an increase in global radiation with elevation on the Vatnajökull ice cap of ~4.8 W m^{-2} (approximated from Figure 7 in Oerlemans et al. 1999) during May-August. The authors stressed that this gradient was steep relative to observations on the Greenland Ice Sheet (Oerlemans and Vugts, 1993) and at the Pasterze glacier in the Austrian Alps (Greuell et al., 1997). Oerlemans et al. (1999) attributed this to the frequent occurrence of low-level clouds at Vatnajökull. However, steep gradients have also been noted in the Alps. For example, at Haut Glacier d' Arolla, Strasser et al. (2004) noted an increase in incident solar radiation of ~11.46 W m^{-2} averaged over periods of observations made during May-September.

Longwave radiation displays less obvious seasonality. At 500 m, the monthly incident flux is related closely to temperature, and a significant correlation is observed ($r = 0.96$, $p < 0.01$). However, at 1100 m this relationship is much diminished ($r = 0.65$) and is no longer significant ($p > 0.1$). Physically, the longwave flux is proportional to the fourth power of temperature, and so the association between these variables is unsurprising at 500 m. Higher on the ice cap, the decreasing correspondence between temperature and incident longwave flux may reflect the greater importance of atmospheric emissivity at this elevation in modulating the incident flux. If atmospheric emissivity is calculated for both elevations (from $L\downarrow/\sigma T^4$, where σ is the Stefan Boltzmann constant (5.67×10^{-8}), and T is the AWS air temperature in Kelvin (cf. Sicart et al., 2010)), then very similar, relatively high values are found at each location (~0.9) for all months, and for the JJA period. These high values are also evident in Figure 2.8 from the proximity of the blue and red lines. For some days, emissivities greater than unity are even observed (dots above the blue line). This can probably be explained by the use of 2 m temperature to infer emissivity: the glacier boundary layer is characterised by a temperature inversion and, if this cooled layer is sufficiently thin, longwave radiation will also be received from the warmer 'free' air above (de Ruyter de Wildt et al., 2003; Björnsson et al., 2005).

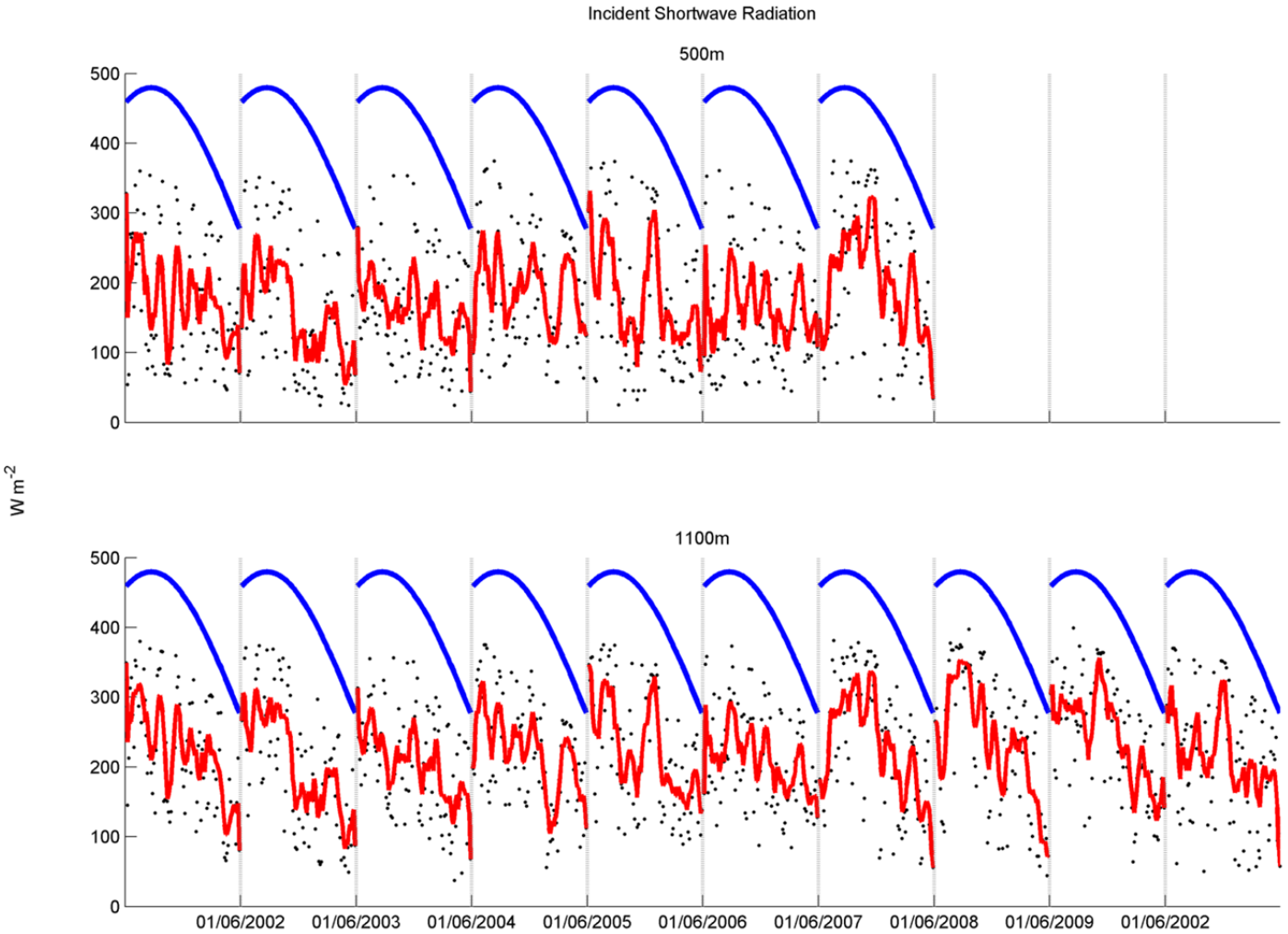

Figure 2.7. Daily incident shortwave flux at each of the AWSs. The blue lines show the potential (top of atmosphere) flux, calculated following Iqbal (1983).

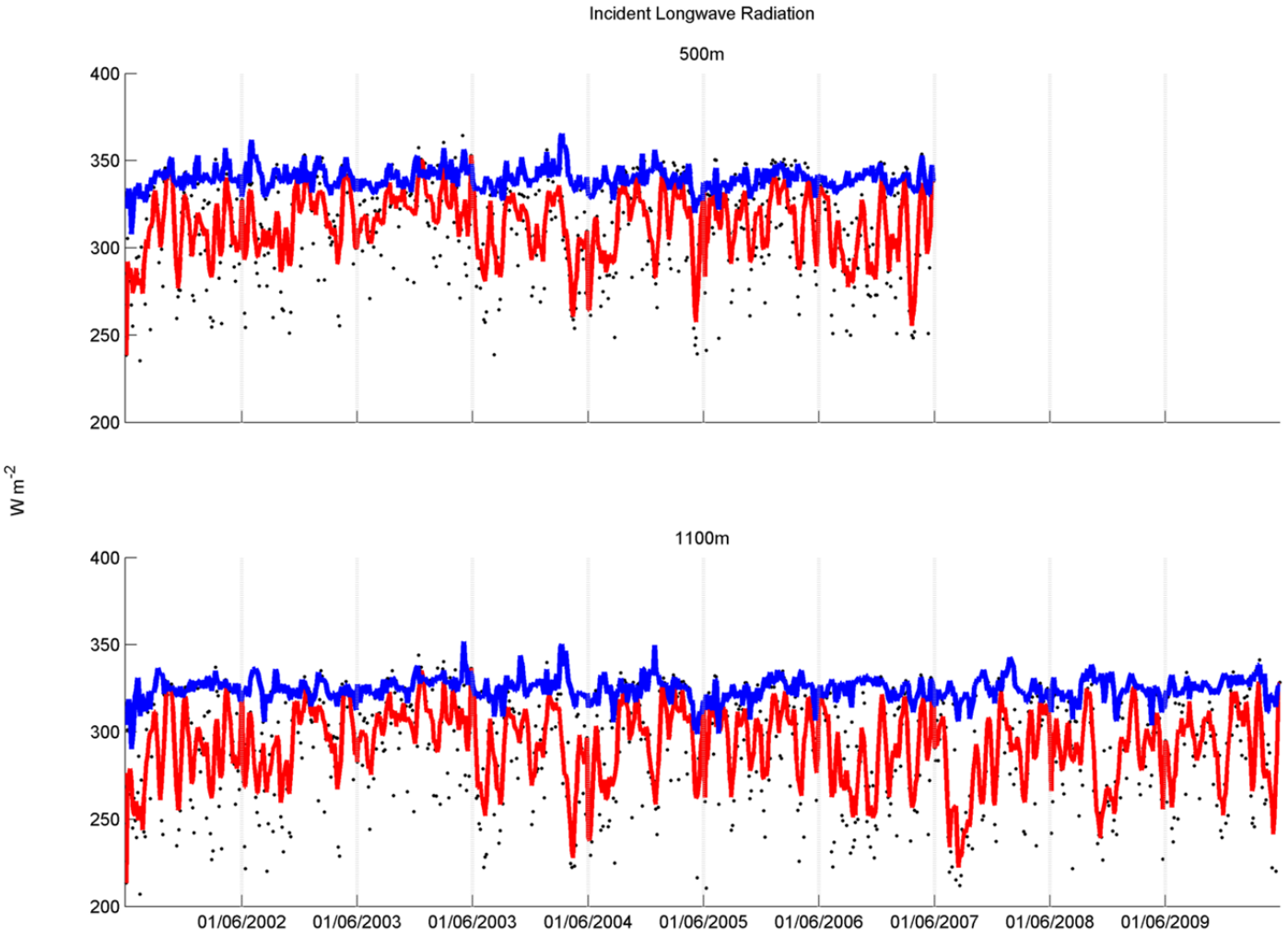

Figure 2.8. Daily incident longwave flux. The blue line gives the emittance of a blackbody at the 2-metre air temperature.

Table 2.5 Mean meteorological parameters at the AWSs by month. Note that statistics are calculated using hourly mean values. Values in brackets provide ± 1 standard deviation of the hourly values. The high standard deviation for shortwave radiation is due to the frequent occurrence of zero values.

	Temp. (°C)	**Rel. Humidty** (%)	**Wspd.** (m s^{-1})	**Short. Radiation** (W m^{-2})	**Long. Rad** (W m^{-2})	**Air Pressure** (hPa)
			500 m			
May	1.69 (2.74)	80.0 (11.9)	5.63 (3.76)	234 (254)	284 (42.3)	954 (10.4)
Jun	4.23 (1.60)	82.1 (8.83)	5.39 (2.68)	203 (233)	308 (32.6)	954 (9.32)
Jul	5.29 (1.47)	83.1 (8.78)	5.54 (2.51)	180 (221)	317 (30.4)	951 (9.13)
Aug	5.09 (1.66)	83.6 (8.27)	5.47 (2.63)	147 (196)	315 (33.2)	950 (8.82)
Sept	3.57 (2.68)	84.7 (9.29)	5.73 (3.62)	83.3 (134)	309 (37.9)	948 (10.7)
Oct	0.12 (4.01)	82.7 (11.4)	6.60 (4.39)	47.0 (87.1)	284 (45.6)	946 (13.2)
			1100 m			
May	-2.10 (3.66)	89.7 (11.4)	6.72 (4.48)	261 (264)	265 (45.0)	884 (10.4)
Jun	1.19 (1.85)	90.6 (10.0)	5.48 (3.62)	264 (258)	285 (40.8)	885 (9.24)
Jul	2.16 (1.44)	92.3 (8.49)	5.35 (3.04)	230 (245)	294 (37.2)	883 (8.96)
Aug	1.82 (1.77)	93.3 (8.15)	5.53 (3.49)	170 (209)	295 (37.4)	882 (8.13)
Sep	-0.15 (2.98)	94.9 (8.38)	7.03 (4.60)	90.1 (135)	295 (37.0)	880 (10.6)
Oct	-3.34 (4.48)	95.3 (7.63)	6.77 (5.09)	50.7 (88.8)	283 (39.0)	874 (11.9)

2.5.2. Surface energy balance modelling

The SEB was modelled for the JJA period for the years 2001-2007 and 2001-2010 at 500 m and 1100 m respectively. When measurements of ablation were available, simulated ablation was validated with the use of the density-corrected ablation measured by the UDGs. The temporal correspondence between simulated and observed ablation resulting from this modelling procedure is illustrated in Figure 2.9. This shows that, in general, the observed pattern of ablation is reproduced well at both elevations, with relatively high correlation coefficients, low RMSEs and points scattered closely around the 1:1 line.

In evaluating the SEB model's ability to simulate cumulative ablation, an attempt was made to quantify the estimated uncertainty of the simulation through perturbing the meteorological input data according to the reported sensor accuracies (e.g. Greuell and Smeets, 2001; Cullen et al., 2007; Gillett and Cullen 2011). This method involves raising or lowering each of the meteorological input variables by an amount determined by the sensor accuracy (Table 2.2), before re-running the energy balance model and comparing the results with the original, 'standard' model run.

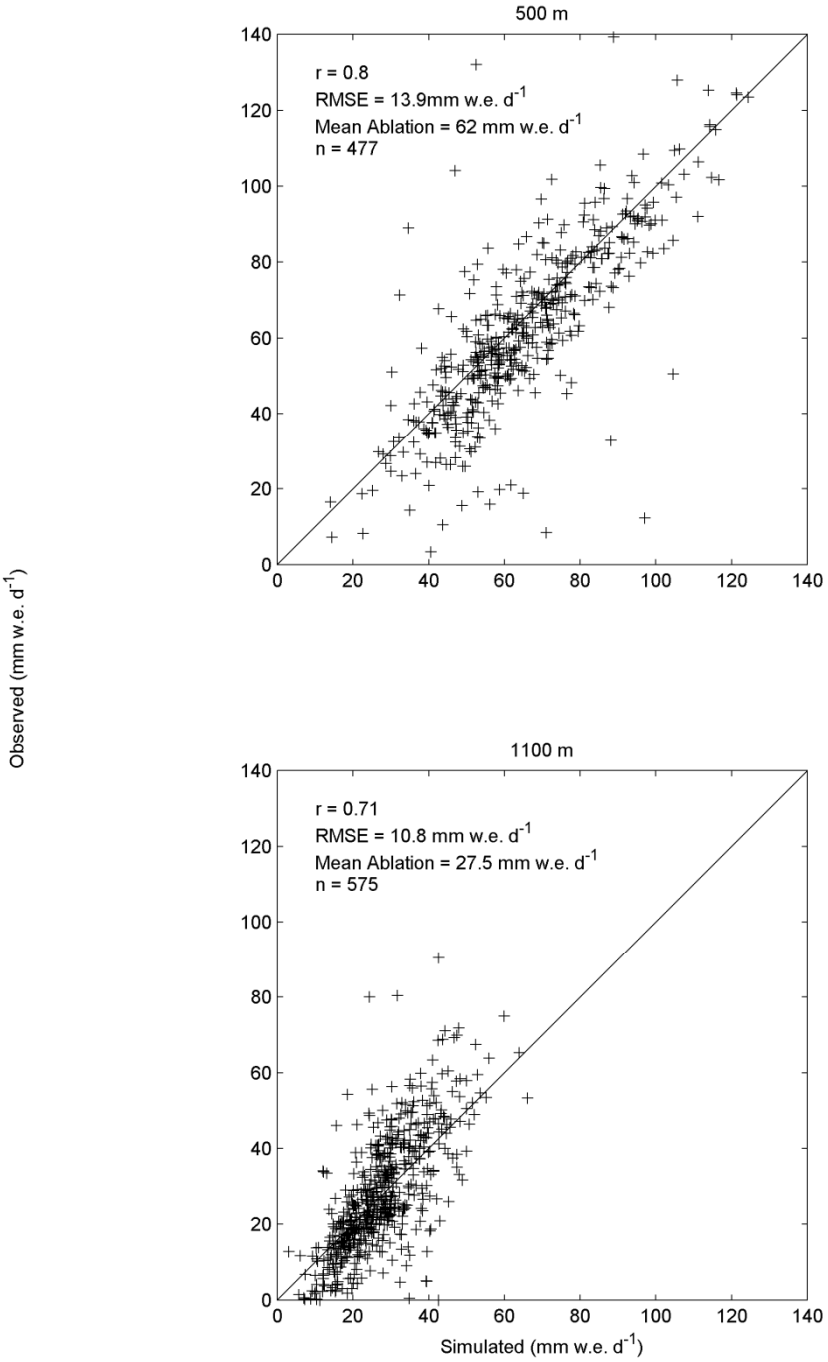

Figure 2.9. Simulated and observed ablation. The solid black line gives the 1:1 relationship.

Averaging the absolute difference between the perturbed and standard runs for the positive and negative perturbations for each sensor then results in a sensor-specific ablation uncertainty. Taking the square root of the sum of all the squared sensor-specific uncertainties then provides a probabilistic estimate of total uncertainty due to the sensor accuracies (Table 2.6). The results of integrating these estimates of uncertainty for comparison of the observed and simulated series are shown in Figure 2.10, and it is evident from these comparisons, that observed cumulative mass loss is within the uncertainty bounds of the simulated ablation for both elevations.

An attempt was also made to establish the sensitivity of the model results to the parameterization of the turbulent heat fluxes, which are not measured directly, but are calculated through the bulk aerodynamic approach. This method applies similarity theory to evaluate the sensible and latent heat fluxes, and the scheme adopted in this chapter included the calculation of stability corrections to account for variable turbulence in the glacier boundary layer (Section 2.4). Considerable sources of uncertainty in this approach are: i) the surface roughness lengths (Brock et al., 2006); and ii) the applicability of the stability functions in the conditions often encountered on glaciers (Hock and Holmgren, 1996). The effects of these sources of uncertainty on simulated ablation were therefore investigated by varying the surface roughness length of momentum (z_{0w}) (and hence z_{0T} and z_{0e} which are a function of z_{0w}—Table 2.3), and by re-running the model without applying the stability corrections.

Table 2.6. Contribution from sensor accuracies to uncertainty in simulated ablation.

Variable	**Perturbation (±)**	**500 m**		**1100 m**	
		mm w.e.	%	mm w.e.	%
Air temperature	0.2°C	744.0	1.8	650	3.0
Relative humidity	2%	495.3	1.2	395	1.8
Shortwave ↓	3%	882.0	2.1	1356	6.3
Shortwave ↑	3%	88.4	0.2	811	3.8
Longwave ↓	3%	1514.7	3.6	1559	7.3
Longwave ↑	3%	1513.2	3.6	1624	7.6
Wind Speed	0.3 m s^{-1}	867.7	2.1	335	1.6
Total uncertainty		**2630.9**	**6.3**	**2873**	**13.4**

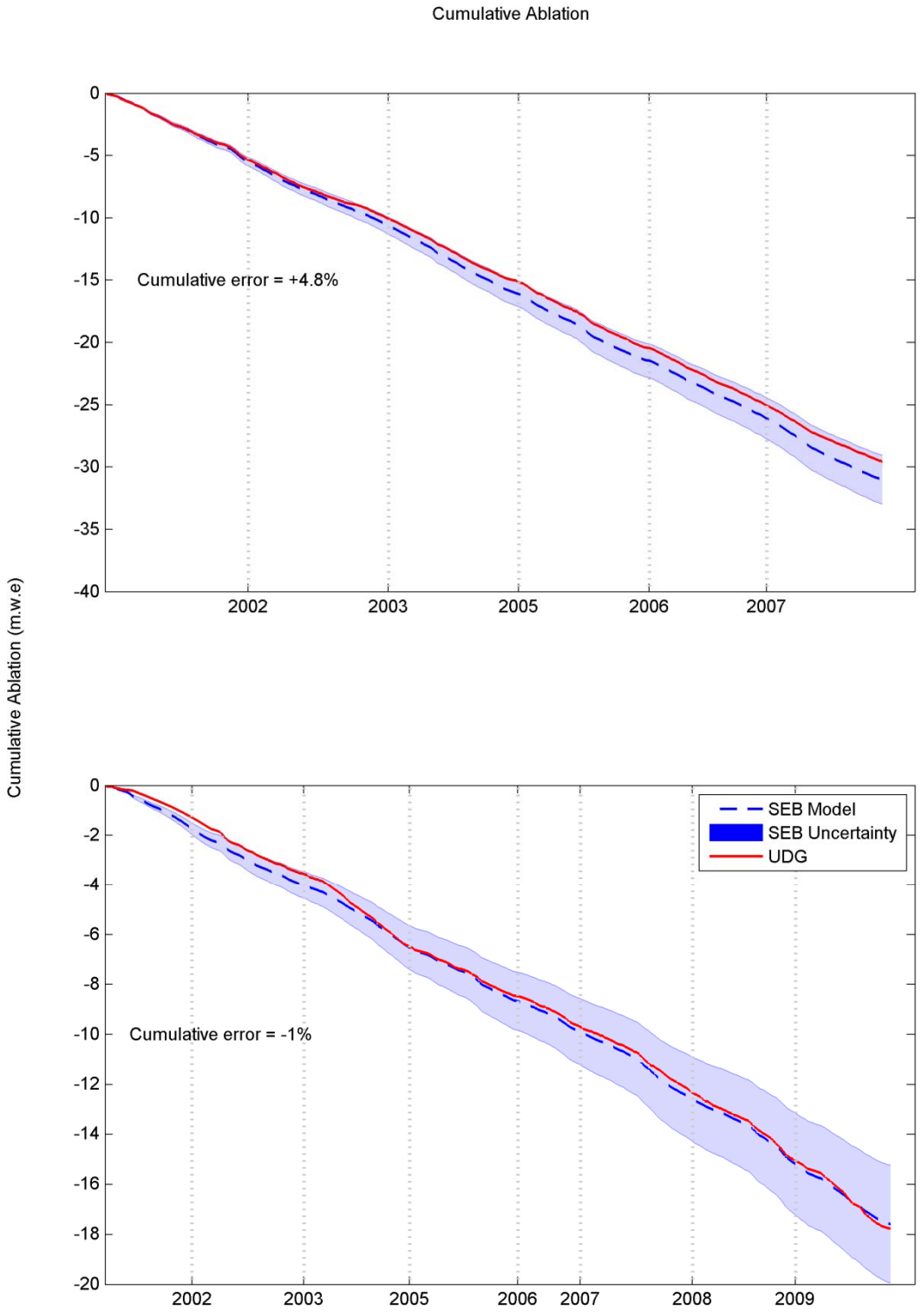

Figure 2.10. Simulated and observed cumulative ablation. The shaded areas indicate uncertainty bounds (see text).

When perturbing the roughness lengths, variations of the order ± a factor of ten were applied, such that only z_{0w} was directly scaled, and the roughness lengths for snow and firn were adjusted automatically within the model to preserve the ratios reported in Table 2.4. The results from this procedure suggested that total simulated ablation is relatively insensitive to z_{0w} variations of this magnitude: the difference in ablation between simulations with the highest and lowest roughness lengths (z_{0w} = 100 mm and 1 mm, respectively) is ~14%, and 8% at 500 m and 1100 m, respectively. The effect of turning the stability functions off also had a small effect on total ablation when re-running the model, as total ablation showed only negligible increases of ~2% at both elevations.

The reason for the relatively low sensitivities of ablation to the treatment of the turbulent heat fluxes can be explained by the energy partitioning within the SEB observed at both elevations (Table 2.7), as the majority of melt energy is provided by net radiation (~62% and ~79% at 500 m and 1100 m). Thus, only small changes in total ablation are effected when changing the treatment of the turbulent heat fluxes, which are of secondary importance within the SEB. This dominance of the radiative heat fluxes in supplying melt energy found in the present analysis is in agreement with previous modelling studies on Vestari Hagafellsjökull (Guðmundsson et al., 2009) and on other Icelandic glaciers (Oerlemans et al., 1999; Guðmundsson et al., 2005).

Table 2.7. Energy partitioning at the different AWSs, and the associated energy gradients.

	500 m		**1100 m**		**Gradient**
	W m^{-2}	**%**	W m^{-2}	**%**	W m^{-2} 100 m^{-1}
Total Melt Energy	249	-	91	-	-25
Sensible Heat Flux	67	27	17	17	-8
Latent Heat Flux	24	10	4	4	-3
Net Shortwave Flux	159	64	94	98	-11
Net Longwave Flux	-2	-1	-19	-19	-3

2.5.2.1. Spatial and temporal variability of the surface energy fluxes

The results in Table 2.7 show that all energy fluxes increase down glacier, which is consistent with energy balance investigations at the same location by Guðmundsson et al. (2009) during the period 2001-2005. The steepest gradient is found for the net shortwave flux, and the shallowest for the longwave flux; combined, the gradient for net radiation remains steeper than observed for the turbulent heat fluxes (-14 W m^{-2} 100 m^{-1}, and -11 W m^{-2} 100 m^{-1}, respectively). Whilst the decrease in net longwave radiation with elevation is consistent with the lower incident flux at 1100 m, it is interesting to observe that the sign of the net shortwave radiation gradient is counter to the trend in the incident flux (which is higher at the upper AWS: Section 2.5.1). This can, however, be explained by the role of albedo: at 500 m, the mean albedo observed during the measurement period was ~0.10, compared to an average of 0.57 at the higher elevation station. The effect of this greater reflectivity is to reduce the amount of absorbed shortwave radiation, to the extent that the net flux at 1100 m is only 59% of that at the lower AWS. To achieve a net shortwave gradient of zero (i.e. for the net shortwave flux to be equal between elevations), albedo at the higher elevation station would have to be reduced by ~50% (mean albedo of 0.28). This figure is particularly interesting when the effects of the tephra layer during 2010 are considered: whilst energy balance computations are unavailable from 500 m post 2007 (thus preventing a direct evaluation), the record from 1100 m suggests that there may have been a significant reduction in the energy gradient between the AWSs, because mean albedo at 1100 m was indeed ~50% lower during this year.

With regards to the turbulent heat fluxes, the decrease down glacier largely reflects the warmer climate that prevails at this elevation, as higher air temperatures contribute directly to the sensible heat flux, and indirectly to the latent heat flux by increasing the potential vapour pressure (Equations 2.4 and 2.5, respectively). However, variability of the wind speed could also affect the relative magnitude of these fluxes: although the mean wind speed is equal between elevations during JJA (Section 2.5.1), it is the instantaneous product of wind speed and the temperature/vapour gradient which determines the turbulent heat fluxes, and this may be very different between elevations. Furthermore, an additional contribution to the negative turbulent heat flux gradient in Table 2.7 may be provided by the difference in the magnitude of the

roughness lengths between elevations, as the mean values applied by the model for momentum (z_{0w}), were, on average, a factor of six times larger at 500 m.

Acknowledging these potential contributions to the sensible and latent heat flux gradients observed in Table 2.7, an effort was made to quantify their relative importance. This was pursued by re-running the SEB model at the higher AWS with air temperatures, vapour pressures, wind speeds and roughness lengths measured at 500 m. By substituting each of these variables in turn, and comparing the sensible and latent heat gradients to those obtained when the original 1100 m data were used, it is possible to identify the relative contribution of each of these sources of variability (Table 2.8). The results from this procedure show that the largest decrease in energy gradient for the sensible heat flux is found when the effect of air temperature is controlled for. Substituting 500 m air temperature and re-running the SEB model at 1100 m reduced the energy gradient by ~74%; a similar magnitude (72%) was observed for the latent heat flux when the SEB at 1100 m was calculated with vapour pressure taken from 500 m. Both the sensible and latent heat gradients were least sensitive to the effect of the roughness lengths, whilst the wind speed was responsible for reducing the sensible and latent heat flux gradients by ~7% and ~8%, respectively.

Table 2.8. Sensitivity of energy gradients to different parameters.

	Reduction in Energy Gradient (%)	
Variable Controlled For	Sensible Heat Flux	Latent Heat Flux
Roughness Lengths	3.9	2.2
Temperature	74	-
Vapour Pressure	-	72
Wind Speed	7	7.9

Examining seasonality of melt energy (Table 2.9) indicates maximum energy is received in July, which is the warmest month on the glacier (Section 2.5.1; Table 2.5). The month with minimum melt energy varies between elevations, with August and July minima at 500 m and 1100 m, respectively. The discrepancy between the timing of minimum melt energy can mainly be explained by the net shortwave flux, which only decreases slightly in August, and is actually at a maximum in July, a month after the peak in the incident flux (Section 2.5.1; Table 2.5). The cause for this lag may again be attributed to the role of albedo: reflectivity shows a gradual decline

throughout JJA at 1100 m (means of 0.65, 0.55 and 0.48, respectively), and this partially offsets the seasonal decline of the incident flux. The same behaviour is not evident at 500 m because albedo exhibits little monthly variability (JJA means of 0.14, 0.07 and 0.08, respectively), due to the rarity of snow cover at this elevation.

During all months, and at both locations, the radiative heat fluxes maintain their dominance in the SEB (Table 2.9). The most extreme example of this is observed at 1100 m in June, when the turbulent heat fluxes reach only ~10% of the energy supplied by the longwave and shortwave fluxes. Within this month, the latent heat flux at this elevation is actually a net energy sink, reflecting the cool temperatures and low vapour pressures that prevail (Section 2.5.1; Table 2.5). The highest fraction of energy supplied by the turbulent heat fluxes is observed for the 500 m AWS during August, although this is actually the result of the seasonal decline in net shortwave radiation at this location, rather than an absolute increase in the turbulent heat fluxes.

Table 2.9. Mean energy fluxes by month. The units of the energy fluxes are W m^{-2}; the ratios (final column) are dimensionless,

				500 m		
	Energy	SHF	LHF	Net SW	Net LW	(SHF+LHF)/(Net SW+Net LW)
June	244	61	16	174	-7	0.46
July	269	70	28	167	3	0.57
August	233	70	28	137	-2	0.72
				1100 m		
June	74	9	-2	91	-23	0.10
July	117	23	7	103	-16	0.35
August	96	18	6	89	-16	0.32

2.6. Synthesis and Conclusions

The aims of this chapter were to present details of the meteorological measurements on Vestari Hagafellsjökull, to discuss the glacier climate, and then to use these data to simulate and explore the SEB. The glacier climate was examined for the period from which observations were available from both AWSs (May-Oct), with particular attention paid to those months where positive temperatures prevailed, and in which the majority of ablation occurs (JJA). Analyses indicated clear seasonality within the 6-month period, which mirrored the general description of climatic trends across

Iceland (Einarsson, 1984). However, also apparent was the development of a distinct glacier boundary layer, which was particularly conspicuous in the temperature and wind data recorded on the glacier. Temperatures exhibited low standard deviations during JJA and shallow lapse rates, reflecting the effect of sensible heat losses to the melting glacier surface during these warmer months. The wind record also displayed evidence of being affected by these sensible heat losses: high directional constancy, and strong wind speeds indicated the presence of katabatic forcing. This glacier wind endures while negative buoyancy persists, and so long as strong synoptic winds remain absent; thus, JJA exhibits the clearest signature of katabatic drainage.

The incident radiative fluxes showed a strong dependence on timing within the measurement period. The shortwave flux was closely related to the seasonal evolution of potential radiation, and the longwave flux followed the cycle in air temperature. The dependence of incident longwave radiation on air temperature also means that this flux is affected by the cooling effect of the melting glacier. Emissivities greater than unity were observed when temperatures from 2 m were used to infer the blackbody radiation, which suggests the influence of warmer air above the glacier boundary layer also contributes to the downward flux (e.g. de Ruyter de Wildt et al., 2003; Björnsson et al., 2005). The effect of the glacier boundary layer on incident shortwave radiation is more ambiguous to define. However, an interesting result was the steep gradient observed between elevations, reaching >7 W m^{-2} 100 m^{-1} during JJA. Possible contributions to this were suggested, including: the decreasing optical air mass with elevation (Meyers and Dale, 1983); the increased scattering between the glacier surface and the overlying air, due to greater surface albedo at the higher station (Konzelmann et al., 1994); or the effects of low-level cloud cover (Oerlemans et al., 1999).

Applying a SEB model to these meteorological data led to an encouraging amount of variance in observed ablation being simulated, and cumulative totals of simulated ablation were within the uncertainty bounds of the meteorological sensors. This agreement leaves little justification for adjustment of model parameters: it is possible to tune roughness lengths to achieve an exact match between total simulated and observed ablation (e.g. Hock and Holmgren, 2005; Hulth et al., 2010), but this forces any deficiencies in the model specification to be absorbed by the turbulent heat fluxes, and has the potential to artificially alter the energy partitioning within the SEB.

Consequently, interpretation of the SEB and its relationship with synoptic forcing in later chapters would be affected. Tuning was therefore omitted in this study, and roughness lengths based on measurements in a similar environment (Section 2.4; Table 2.4), that have successfully simulated the SEB in previous investigations on Vestari Hagafellsjökull (Guðmundsson et al., 2009), were preferred. Although some uncertainty must surround the enduring applicability of these values, it is interesting to note that the model was actually somewhat insensitive to relatively large changes in their value; similarly, neglecting the stability corrections only effected small increases in total ablation. This behaviour reflects an overall low sensitivity of the model to the turbulent heat fluxes, which stems from the limited importance of this flux within the SEB, as the majority of melt energy is provided by the net radiative heat flux. At 1100 m, this is particularly evident: 79% of available melt energy during JJA is provided by net radiation.

The secondary position of the turbulent heat fluxes within the SEB was further evident when temporal and spatial variability of simulated surface energy were explored. At the most extreme, the turbulent contribution to melt energy represented only a tenth of that provided by radiation during June at 1100 m. This month also saw the minimum percentage of melt energy provided by turbulent energy at 500 m (~30%). August witnesses the maximum relative contribution from the turbulent heat fluxes, and this is greatest at 500 m (~42%). The increasing contribution of the turbulent flux to melt energy through time during JJA follows the seasonal decline in incident shortwave radiation. The increase down glacier mainly results from the warmer air temperatures and higher vapour pressures at this elevation (Table 2.8). In fact, all energy fluxes were observed to increase down-glacier, and whilst this mainly reflects the elevational gradients in the meteorological variables, an exception is the higher net shortwave radiation received at 500 m, which is due to the persistently low albedo at this elevation: reflectivity is higher and more variable at 1100 m, resulting from the greater longevity of snow cover at this location. It is interesting to observe that if the mean albedo at 1100 m is applied to 500 m, then the turbulent heat flux's contribution to the SEB during JJA would in fact be almost half (48%) at this location.

These insights obtained from the modelling results not only yield a high-resolution record of ablation, but also, *explain* processes of ablation through providing a detailed quantification of the individual energy fluxes. These data will therefore be critical to the remaining analyses within this thesis, because when supported by the meteorological data, they allow a thorough comprehension of how synoptic-scale climatic variability ultimately manifests at the glacier scale to drive ablation.

3. Meteorological Measurements and the Surface Energy Balance Part II: Storglaciären, Sweden

3.1. Introduction and Aims

Although occupying a small fraction of Earth's glacierized area, mountain glaciers and ice caps have provided the main contribution to eustatic sea level rise during the past century (Lemke et al., 2007; Meier et al, 2007). Accurate quantification of the ablation and mass balance of these ice masses for future scenarios of climate is therefore of critical importance for purposes of resource planning and hazard mitigation (e.g. Pfeffer et al., 2008). To this end, a limited number of modelling studies have attempted to provide global estimates of the future mass losses from the world's glaciers and ice caps based on climate scenarios provided by GCM simulations (Van de Wal and Wild, 2001; Raper and Braithwaite, 2006; Radić and Hock, 2011; Marzeion et al., 2012). All of these have attempted to couple climate to glacier mass balance in a causative way, and are therefore physically more desirable than estimates of glacier wastage derived from simple extrapolation of observed mass balance trends (Meier et al., 2007). However, application of such modelling approaches is challenged in space and time. Specifically, direct observations of climate from remote and mountainous environments (where many of the world's >200,000 glaciers are located) are sparse. This means that coarse-scale, gridded climatologies must be used frequently to calibrate and apply models in contemporary studies and hindcasting investigations; and similarly, simulating future mass balance necessitates the use of GCM output, with typical spatial resolutions measured in the hundreds of kilometres. The result of these challenges is that relationships must be sought between large-scale climate dynamics and mass balance. For the ablation component of mass balance, air temperature has therefore been favoured to implicitly capture the SEB in all the global-scale modelling studies cited above.

This challenge of linking processes which affect glacier mass balance to large-scale climate has been referred to as the 'scale mismatch' (Machguth et al., 2009; Kotlarski et al., 2010), and Mölg and Kaser (2011) suggest that it is only addressed by developing a multiscale understanding of glacier-climate interactions. This philosophy is central to present research, and is the main aim of the thesis (Chapter 1). Considerable difficulty in adopting a multiscale approach however, is posed by the complexities of the topography in which mountain glaciers are located. That is, mountain ranges greatly influence the overlying atmosphere (Barry, 2008) due to a complex interaction between the synoptic flow and the underlying terrain (e.g. Jiang, 2003, Medina et al., 2005; Rotunno and Houze, 2007). Glaciers themselves then act as an additional source of complexity, as they too exchange heat and moisture with the mountain boundary layer. These complications challenge the linking of synoptic scales with those required to explicitly evaluate the mass and energy budgets of mountain glaciers.

It is with these difficulties in mind that the present analyses are presented. This chapter builds on Chapter 2 by evaluating the glacier meteorology and SEB at Storglaciären, Sweden, and therefore provides a contrasting perspective on the coupling between synoptic climate and process which affect glacier ablation. The contrast stems from the geometric and topographic situation of Storglaciären (see Section 3.2 for details). As a far smaller ice mass than Vestari Hagafellsjökull, modification of the local climate by Storglaciären may be anticipated to be greatly reduced; conversely, its valley location may result in significant modification of the local climate by the complex terrain. These differences will be useful in exploring the feasibility of applying synoptic-scale climatological information to aid in simulating and understanding processes which drive glacier ablation.

The main aim of the chapter, therefore, is to present details of the glacier surface meteorology and to simulate and explore the SEB at Storglaciären. These data will be related to synoptic-scale processes in chapters 6 and 7. The aims of the present chapter run parallel to those in Chapter 2; however, an important difference between analyses at Vestari Hagafellsjökull and Storglaciären should be acknowledged: AWS measurements from Storglaciären are of limited duration, spanning only two ablation seasons (Section 3.3). The brevity of this measurement period is considered somewhat unfavourable for the aims of the thesis, as interannual variability of the prevailing

weather conditions, and the energy balance may be pronounced at Storglaciären (Hock and Holmgren, 2005). For this reason, an effort is made in this chapter to extend the on-glacier AWS record from a proximate, long-running AWS situated off-glacier. Extending the data in this way provides a larger sample of glacier-climate interactions, which will be better placed to capture low-frequency, interannual variability. Substituting off-glacier meteorological data for glacier observations in this way requires these data to be adjusted to the glacier boundary layer, so that surface energy exchange may be properly evaluated, interpreted, and explored in relation to synoptic-scale processes. This requirement is challenging, however, due to the way in which the glacier modifies the overlying atmosphere (e.g. Van den Broeke, 1997a; Greuell et al., 1997); but it is also a desirable pursuit in its own right, because simulating the SEB with data recorded away from the glacier, removes the need for prolonged glacier observations which may be logistically problematic. An additional aim of this chapter is therefore to adjust off-glacier observations to the glacier boundary layer through transfer functions, to produce a more extensive meteorological time series to simulate the SEB.

3.1.1. Structure of chapter and modelling strategy

The overall logic and structure of the analyses presented in the chapter is summarised schematically in Figure 3.1. Essentially, the aim is to simulate the SEB with meteorological data recorded on-glacier, and then to use off-glacier data to hindcast the SEB for the period prior to glacier observations. A major element of this aim is to ensure homogeneity between SEB simulations driven by on- and off-glacier, which is pursued using empirical functions to adjust the meteorological data recorded away from the glacier. SEB calculations resulting from application of these adjusted data may then be compared with simulations driven by data recorded on-glacier, which have been validated against measured ablation. Close agreement between modelled and measured ablation using the glacier data indicates the SEB model is correctly specified to capture the surface energetics; agreement between simulations driven by on- and off-glacier data indicates that the latter may be used to hindcast the SEB reliably. The organisation of the text in this chapter largely follows the steps outlined in Figure 3.1. First, the study site is outlined and information on the meteorological observations are provided (sections 3.2 and 3.3); then, details of transfer functions used to adjust the off-glacier climate data are discussed and their results summarised

(Section 3.4); next, SEB simulations are performed and their results are presented (Section 3.6); the results from these investigations are then summarised and compared to those obtained at Vestari Hagafellsjökull in Chapter 2 (Section 3.7); finally, the chapter is synthesised and conclusions are drawn in Section 3.8.

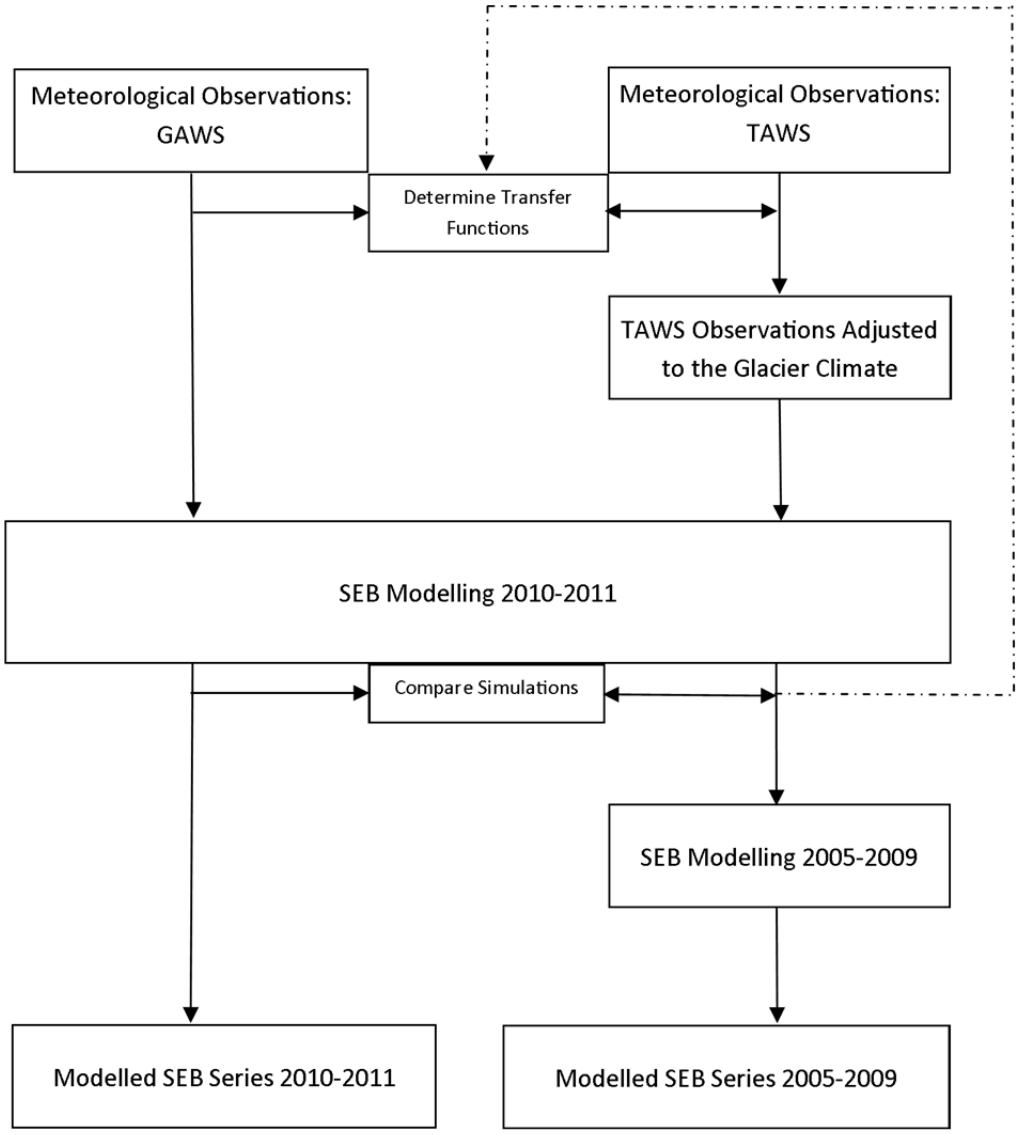

Figure 3.1. Schematic illustration of the strategy adopted in the chapter. Dotted line indicates route taken *if* transfer functions need to be refined due to limited agreement between simulated SEB series. Note that GAWS and TAWS acronyms are defined in Section 3.3.

3.2. Study Location

Storglaciären is a small valley glacier (~3 km^2) in northern Sweden. Its upper accumulation area reaches ~1700 m up the western face of Kebnekaise, and it flows eastwards towards the Tarfala Valley, terminating at ~1130 m (Koblet et al., 2010). The glacier is polythermal and the majority of the ice is temperate with a cold surface layer in the ablation area, due to the rapid runoff of meltwater (rather than refreezing) which occurs lower on the glacier. Repeated measurements indicate that the volume of this cold ice is declining (Holmlund and Eriksson, 1989; Pettersson et al., 2003; Gusmeroli et al., 2012). The mass of Storglaciären is also on a generally downward trend from a Holocene maximum around 1910 (Holmlund, 1987); although, this was interrupted by brief periods of positive balances forced by high winter accumulation during the mid-1970s, and the late 1980s to early 1990s (Holmlund and Jansson, 2005). Insights into annual mass-balance variations are available due to the esteemed and extensive history record of observation at Storglaciären, which started in 1946, is still on-going, and forms the longest continual mass-balance record in the world (Holmlund and Jansson, 1999). Besides mass-balance investigations, the glacier has also been the site of numerous investigations into glacial hydrology (e.g. Hooke and Pohjola, 1994; Jansson, 1996; Fountain et al., 2005), glacier dynamics (e.g. Hooke et al., 1989; Hanson, 1995), and melt modelling (e.g. Hock and Holmgren, 1996; Hock and Holmgren, 2005; Konya et al., 2007).

Climatologically, Sweden's location in north-west Europe means that its weather is controlled largely by air-mass advection. The greatest thermal contrast between air masses is found during winter, and the least during summer, when insolation is at a maximum. Zonal flow plays an important role in modulating the weather, with westerly winds producing negative temperature anomalies during summer (Chen and Hellström, 1999). Storglaciären itself is situated along a longitudinal gradient of continentality in the Scandinavian Caledonides. To the west, the climate is distinctly maritime; to the east, a more continental climate prevails. The declining precipitation contributes to decreasing net balance gradients moving west to east, and an increase in the elevation of glaciation (Holmlund and Jansson, 1999). The local climate of Storglaciären is described as being affected by both maritime and continental influences (Holmlund and Schneider, 1997).

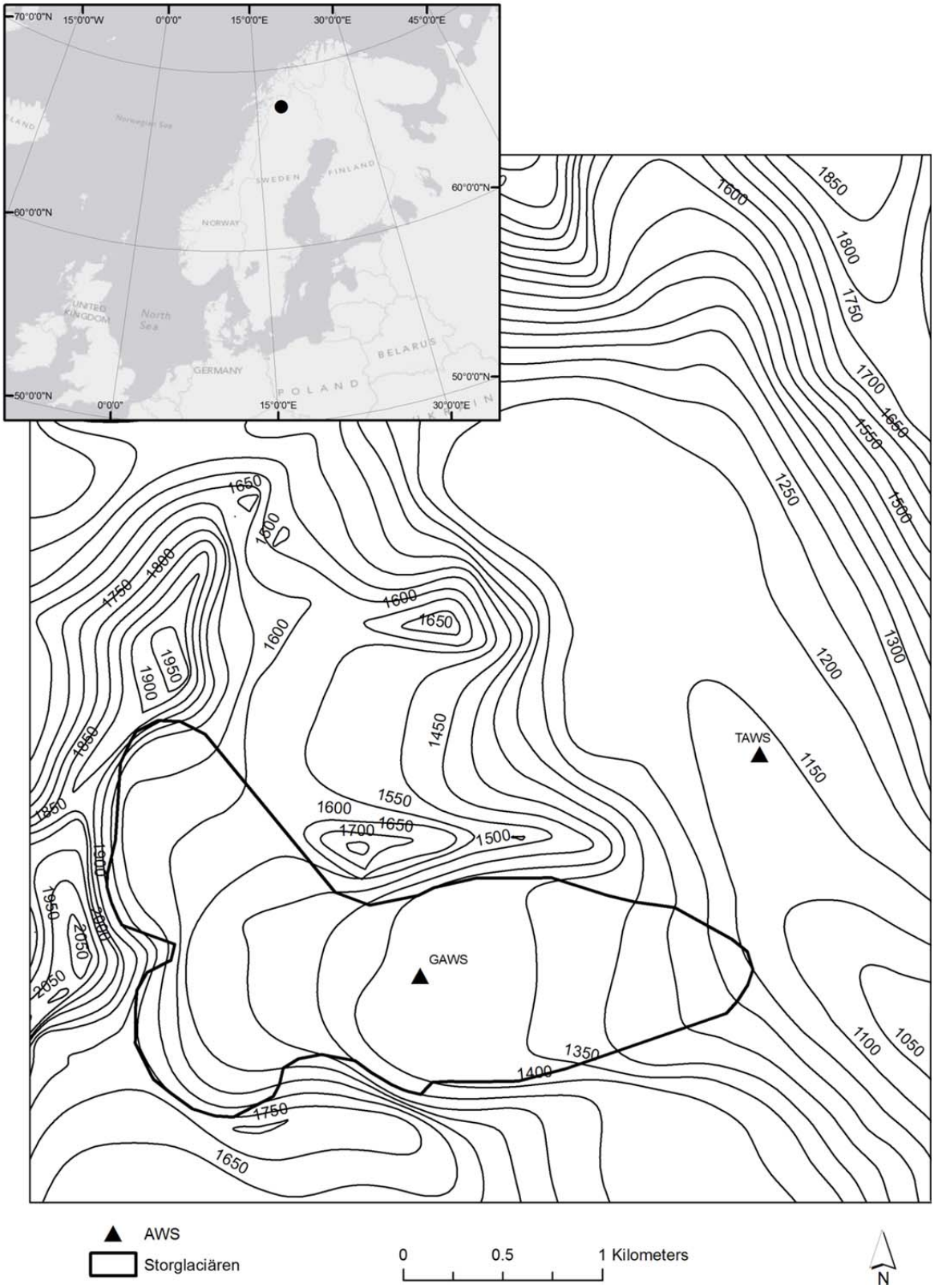

Figure 3.2. Location of AWSs used in this study (see text for explanation). Contoured map generated from DEM produced by Koblet et al. (2010).

Grudd and Schneider (1996) report mean summer (June-August) and winter (September-May) temperatures at the Tarfala Research Station (see Figure 3.2 and Section 3.3 for the location and details of meteorological measurements made at the research station) of 5.5°C and -7°C, respectively. Annual precipitation is ~1000 mm, and ~350 mm of this falls as summer rain. The precipitation totals probably serve as a minimum estimate of precipitation on Storglaciären (Koblet et al., 2010).

3.3. Meteorological Observations

Meteorological data from two AWSs are utilized in this study: from a glacier-based station (hereafter GAWS), and from the Tarfala research station (hereafter TAWS; see map in Figure 3.2 for locations). Simultaneous observations from these stations allow the construction of transfer functions, so that the glacier climate and SEB may be hindcast to extend the period of analysis.

Meteorological measurements, beginning with manual observations of temperature, have been made at Tarfala since 1946. In 1965 an automatic data acquisition system utilizing chart recorders was installed and a greater number of meteorological parameters began to be observed (soil temperature, wind speed and solar radiation). Further developments in 1985 saw the installation of a Campbell Scientific data logger and the number of observed meteorological parameters increased further (humidity, precipitation, and net radiation). Tarfala became part of the Swedish Meteorological and Hydrological Institute's (SMHI) official meteorological monitoring network in 1995, when a new AWS was installed adjacent to the existing Tarfala station. Since this time, both AWSs have logged data (Holmlund and Jansson 2002). It is the longer-running Tarfala AWS which is referred to as TAWS in this study.

Although digital records extend to 1985, the period chosen for analyses in this chapter is considerably shorter, due to the lack of homogeneity that exists in the TAWS record, caused by changing of meteorological sensors over the years (Jansson, personal communication). With these considerations in mind, the earliest date from which the TAWS data may be employed reliably is 2005: the global radiation sensor was replaced at the end of the summer in 2004 and a two-tailed Student's t-test between the pre- and post-2005 hourly global radiation data suggests rejection of the null hypothesis at the 95% confidence interval that the means between samples are

equal (t = -2.27, p = 0.02). From 2005 onwards, the record is homogeneous. However, the nature of the replaced global radiation sensor also requires comment: the instrument installed was a 'LI-COR' silicon pyranometer; these sensors are spectrally sensitive and respond to global radiation non-uniformly at wavelengths below 1100 nm and not at all to radiation above this threshold (Michalsky et al., 1991). Receipts can therefore be underestimated significantly—particularly the diffuse component of shortwave radiation during clear skies (Vignola, 1999)—and it is necessary to apply a correction to these data. In this study, a correction is performed based on data from the proximate SMHI AWS, which has recorded global radiation with a Kipp and Zonen CM21 since 2008.

The CM21 belongs to the highest ISO performance category (Kipp and Zonen, 2004) and therefore serves as a suitable reference for adjusting the TAWS record. The correction is applied by regressing TAWS global radiation recorded by the LI-COR sensor against the SMHI record for the period of synchronous observations (Figure 3.3). The resulting regression equation is then used to correct the TAWS record from 2005 onwards. Details of the instrumentation at TAWS since 2005, including sensor accuracies, are reported in Table 3.1. The multiple measurements of air temperature are averaged to produce a single variable.

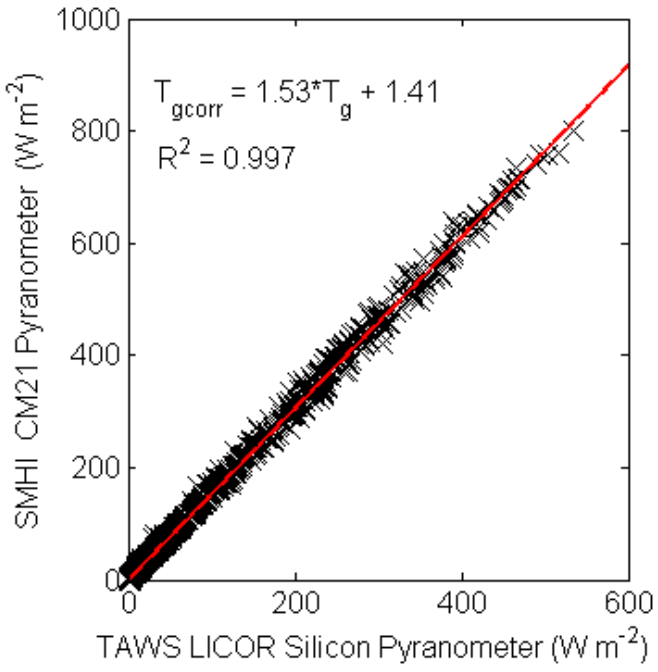

Figure 3.3. Regression used to correct TAWS pyranometer.

Table 3.1. Details of meteorological measurements at TAWS.

Parameter (height)	Sensor	Accuracy	Comment
Temperature (2 m)	2x Pt-100 thermistors	± 0.1°C at 0°C	Shielded
Temperature/relative humidity (2 m)	Rotronics Hygroclip	±0.1°C/0.8%	Ventilated
Global radiation (~2 m)	LI-COR silicon pyranometer	±5%(max), ±3%(typical)	
Wind speed/direction (3m)	Young 05103	±0.3m s^{-1},3°	

GAWS was installed on Storglaciären during early July, 2010 (Figure 3.4, left). The location chosen for the AWS was selected because this area of the glacier is flat and easily accessed due to the absence of crevasses. Moreover, being situated away from the valley sides was regarded as preferable to avoid local heat advection from rock walls; such effects would result in the sampling of meteorology which is unrepresentative of the glacier climate. The AWS itself is similar in design to that deployed on Vestari Hagafellsjökull (Chapter 2, Section 2.3), consisting of a tripod which stands freely on the glacier surface (Figure 3.4, top right). The AWS overwintered on the glacier, but (presumably) strong winds caused the station to collapse, and logger failure prevented any data being stored after the last visit of the 2010 ablation season. Measurements recommenced in early July, 2011, when the station was repaired and updated with new sensors and logger. A significant component of this update was the improvement of the radiation measurements, which facilitated explicit observation of the longwave flux.

Validation data for the SEB simulation at GAWS are provided by a UDG installed adjacent to the AWS during July 2011 (Figure 3.4, bottom right), and from a network of up to ten, two-metre, plastic ablation stakes drilled into the glacier during this year. These stakes were situated in a low-density array surrounding the AWS, and relative surface elevation change was obtained by measuring their exposed height at daily resolution. These ablation measurements were supplemented by observations at four nearby stakes that were part of the existing mass-balance measurement network on Storglaciären (Holmlund and Jansson, 1999) (Figure 3.4, left). Details of all the instrumentation installed at GAWS throughout the period of operation are provided in Table 3.2.

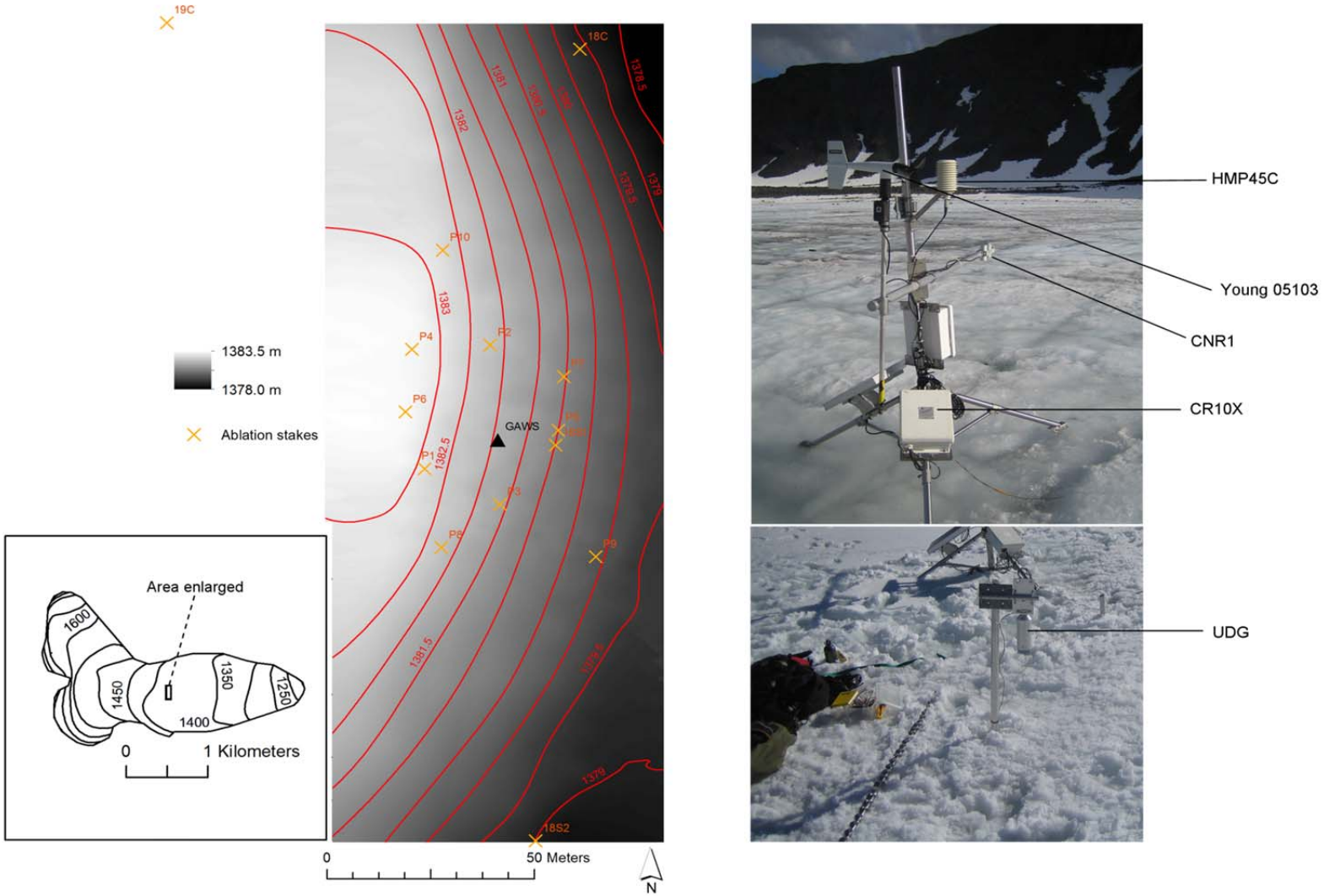

Figure 3.4. Left-hand side: location of ablation stakes. Elevation determined by kinematic differential GPS survey (note, this did not extend to the location of stake 19C). Ablation stakes prefixed with 'P' are plastic stakes installed as part of this study; the remaining stakes are part of the existing Tarfala network. Right-hand side: AWS (top) and UDG (bottom).

Table 3.2. Details of meteorological measurements at GAWS.

Parameter (height)	Sensor	Accuracy	Period (Julian day, year)
Temperature (2 m)	HMP45C	± 0.3°C at 0°C	192,2010-250,2010 & 191, 2011-245, 2011
	CS215	± 0.9°C (-40°C to + 70°C)	203, 2011-245, 2011
Relative humidity (2 m)	HMP45C	2% (0-90%), ± 3% (90-100%)	192, 2010-250, 2010 & 191, 2011-245, 2011
Wind speed/direction (2 m)	Young 05103	± 0.3m s^{-1},3°	192, 2010-250, 2010 & 191, 2011-245, 2011
Global radiation (~1.5m)	Kipp and Zonen CM7B	Not given	192, 2010-246, 2010
	Kipp and Zonen CNR1, CM3	3%	191, 2011-245, 2011
Longwave radiation (2 m)	Kipp and Zonen CNR1, CG3	3%	191, 2011-245, 2011
Net radiation (~1.5 m)	Kipp and Zonen NR lite	Not given	192, 2010-246, 2010
Accumulation/ablation (NA)	Campbell Scientific SR50	Max (0.01 m, 0.4%)	196, 2011-245, 2011

3.4. Extending the Glacier Meteorological Record: Empirical Transfer Functions

Although the distance separating GAWS and TAWS is relatively small (~2 km), an elevational difference of more than two hundred metres, and very different physical environments mean that substantial local meteorological differences may be expected between these locations. This section outlines the considerations necessary when substituting the TAWS data for those recorded on glacier. The performances of these functions are then briefly summarised (Section 3.4.7).

3.4.1. Air temperature

Determining the on-glacier air temperature at GAWS from data recorded at TAWS requires the parameterization of an effective near-surface lapse rate. This may be anticipated to be substantially steeper than the ELR of -6.5 °C km^{-1}, due to the cooling effect of the glacier surface relative to the valley floor.

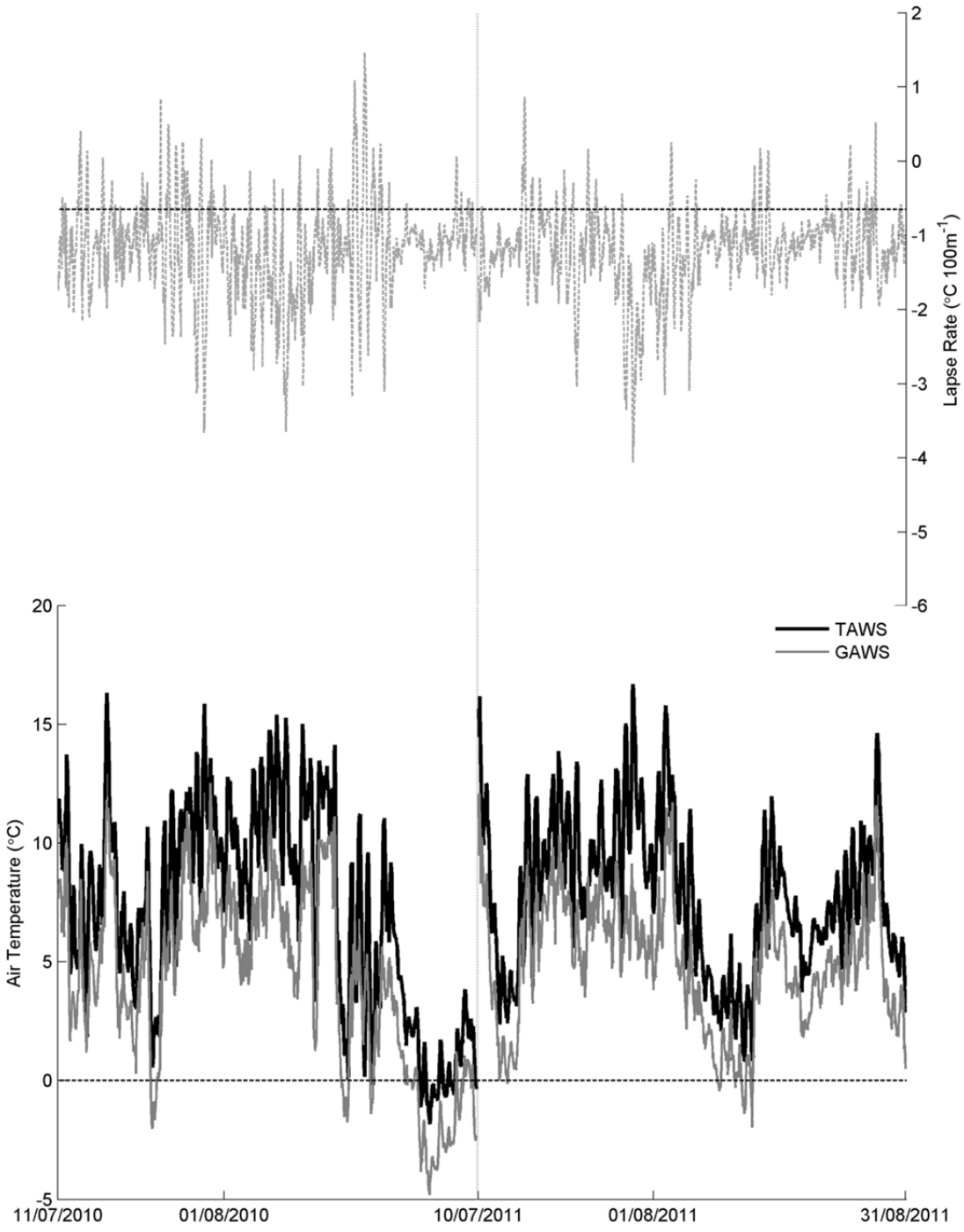

Figure 3.5. Lapse rates (top) and air temperatures (bottom) at TAWS and GAWS. Vertical grey line separates observations made in 2010 and 2011. In the top graph, the dotted, horizontal line indicates the ELR (-0.65°C $100m^{-1}$); in the bottom, it marks the freezing point.

It may also be assumed that this lapse rate is dynamic, and is influenced by more than synoptic variability alone. This is partly because near-surface lapse rates in mountain environments are heavily affected by the heat exchange with the complex topography (e.g. Pepin, 2001), but also, because the relative cooling effect of the glacier on the overlying air is temporally variable (e.g. Oerlemans and Grisogono, 2002). This behaviour is indeed evident in the air temperature recorded at the AWSs (Figure 3.5), which indicates the generally steep (mean of –1.23°C 100 m^{-1}), and variable nature of the lapse rate between stations. In an attempt to constrain this variability, the piece-wise linear regression method outlined by Shea and Moore (2010) is followed. Physically, this technique seeks to account for the decreasing sensitivity of the glacier boundary layer that occurs as the ambient air temperature increases and katabatic drainage initiates; statistically, this manifests as a breakpoint in the regression line relating the temperature data at the two AWSs. Slopes near unity can be expected before the onset of drainage, and a lower gradient anticipated after. This can be summarised:

$$G_t(t) = \begin{cases} {G_t}^* + k_1(T_t - {T_t}^*), T_t < {T_t}^* \\ {G_t}^* + k_2(T_t - {T_t}^*), T_t \geq {T_t}^* \end{cases}, \quad 3.1$$

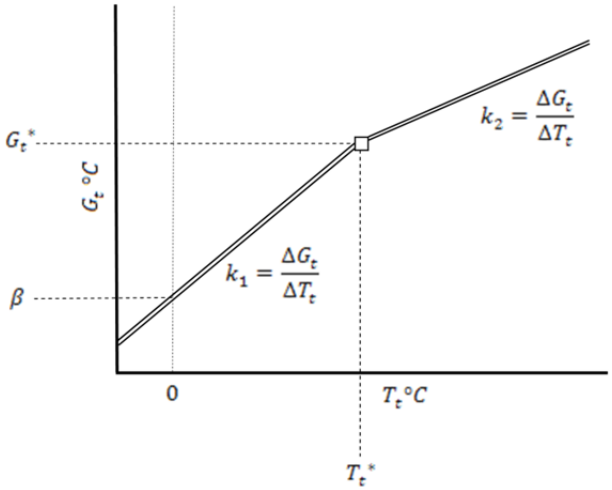

Figure 3.6. Schematic illustration of the piece-wise function used to adjust TAWS air temperature to the glacier.

where G_t and T_t are air temperature at GAWS and TAWS respectively, and the * indicates the threshold air temperature at GAWS (${G_t}^*$) and at TAWS (${T_t}^*$) that katabatic drainage initiates; k_1 and k_2 then denote the gradient of the regression line relating air temperature at these two locations, before (k_1) and after (k_2) this threshold

is reached. The coefficients for Equation 3.1 are optimized by iteratively incrementing T_t^* and then fitting k_1 and k_2 accordingly. G_t^* is found from $\beta + k_1 T_t$ (see Figure 3.6).

3.4.2. Humidity

The saturation vapour pressure of the air immediately overlying a melting glacier surface is limited to 6.11 hPa (Stull, 2000), and the direction of moisture flux over this surface is dependent on the moisture content of air advected over the glacier. Specifically, whether sublimation or condensation occurs depends on the partial pressure of water vapour in the glacier boundary layer: if this exceeds the saturation vapour pressure for ice, then a net downward flux of moisture occurs, whilst sublimation will prevail when the opposite circumstances arise. Typically, the former case is encountered during melt conditions, and the glacier exerts a drying influence on the overlying air (e.g. Van den Broeke, 1997a, b; Munro, 2004). This has been documented similarly at Storglaciären in previous energy balance studies, identifying the latent heat term to be net energy source, indicative of condensation to the surface (Hock and Holmgren, 1996, 2005; Carrivick and Hock, 1999).

The data recorded in this study also suggest a drying influence of the glacier. Figure 3.7 illustrates that similar relative humidities are observed at both locations, despite the cooler temperatures recorded on the glacier. Similarly, mixing ratios (calculated from Equation 2.17 in Chapter 2), show, in general, a very steep gradient between stations (-0.4 g kg^{-1} 100 m^{-1} and see Figure 3.7, top), which is an order of magnitude larger than that observed between AWSs on Vestari Hagafellsjökull (Section 2.5.1, Chapter 2). To account for this drying of the atmosphere between locations, piece-wise linear regression is used again, after Shea and Moore (2010):

$$G_q(t) = \begin{cases} j_1 T_q + j_2 \,, G_t > 0°C \\ j_3 T_q + j_4 \,, G_t \leq 0°C \end{cases}, \qquad 3.2$$

in which j_1 and j_3 are the slopes of the regression lines relating vapour pressure at TAWS (T_q) to that at GAWS (G_q); and j_2 and j_4 are the intercept terms. Vapour pressure, rather than relative humidity or the mixing ratio is calculated because this variable is required for evaluation of the SEB.

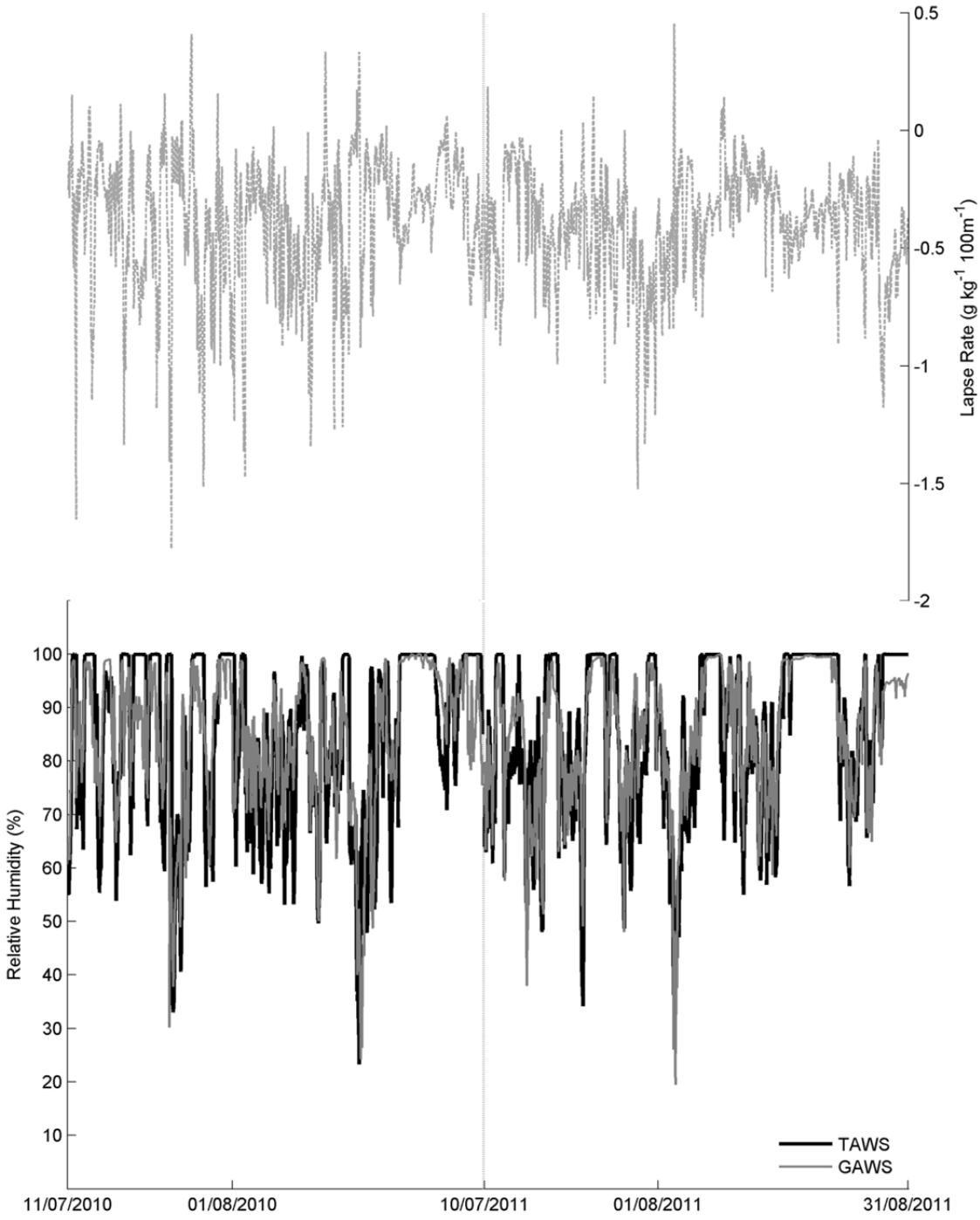

Figure 3.7. Lapse rate mixing ratio (top) and relative humidity observed at TAWS and GAWS. Vertical grey line separates observations made in 2010 and 2011.

The piece-wise treatment is analogous to the treatment of temperature and is based on physical principles. When air temperatures are above the melting point at GAWS, the saturation vapour pressure is limited to the melting point, which may exert a drying influence on the overlying air that is not evident at TAWS. In turn, a regression line relating measurements between locations with a slope less than unity may be expected; when air temperatures are freezing, however, the saturation vapour pressure is not similarly constrained, and it is less likely that the glacier dries the overlying atmosphere. It is then more probable that vapour pressures vary more closely between stations and a slope approaching unity is expected (Shea and Moore, 2010).

3.4.3. Wind speed

Wind speeds in mountainous environments are highly variable through space due to the complex interaction between the synoptic flow and the underlying topography (Whiteman and Doran, 1993; Barry, 2008). Where melting glaciers are present, this variability may increase further as local katabatic winds develop from the negative buoyancy generated by the temperature deficit of the glacier boundary layer (Stull, 2000). Extrapolating wind speed information from off- to on-glacier locations is therefore challenging (Munro, 2004). Previous authors have attempted to address this complexity with empirical approaches. For example, Björnsson et al., (2005) used linear regression of air temperatures to determine wind speed on outlet glaciers from the Vatnajökull ice cap; whilst Shea (2010) used a hybrid method, adopting the Prandtl model to simulate the katabatic contribution to the wind speed physically, and exponential functions to account for the effect of the synoptic flow.

Examination of the wind speed data from the AWSs suggests that a similar stratification between synoptic and katabatic flow may be useful in the present analyses. Periods of strong synoptic forcing may be identified by positive wind-speed anomalies recorded at TAWS (defined as deviations from the median during the entire period of TAWS observations: July-August, 2005-2011), as this station is away from the glacier's influence. During such conditions, the general agreement between stations suggests homogenization of the wind field (middle axes in Figure 3.8); indeed, a Student's t-test indicates acceptance of the null hypothesis that mean winds are equal between locations when positive anomalies are observed at TAWS (t = 0.07, p = 0.94).

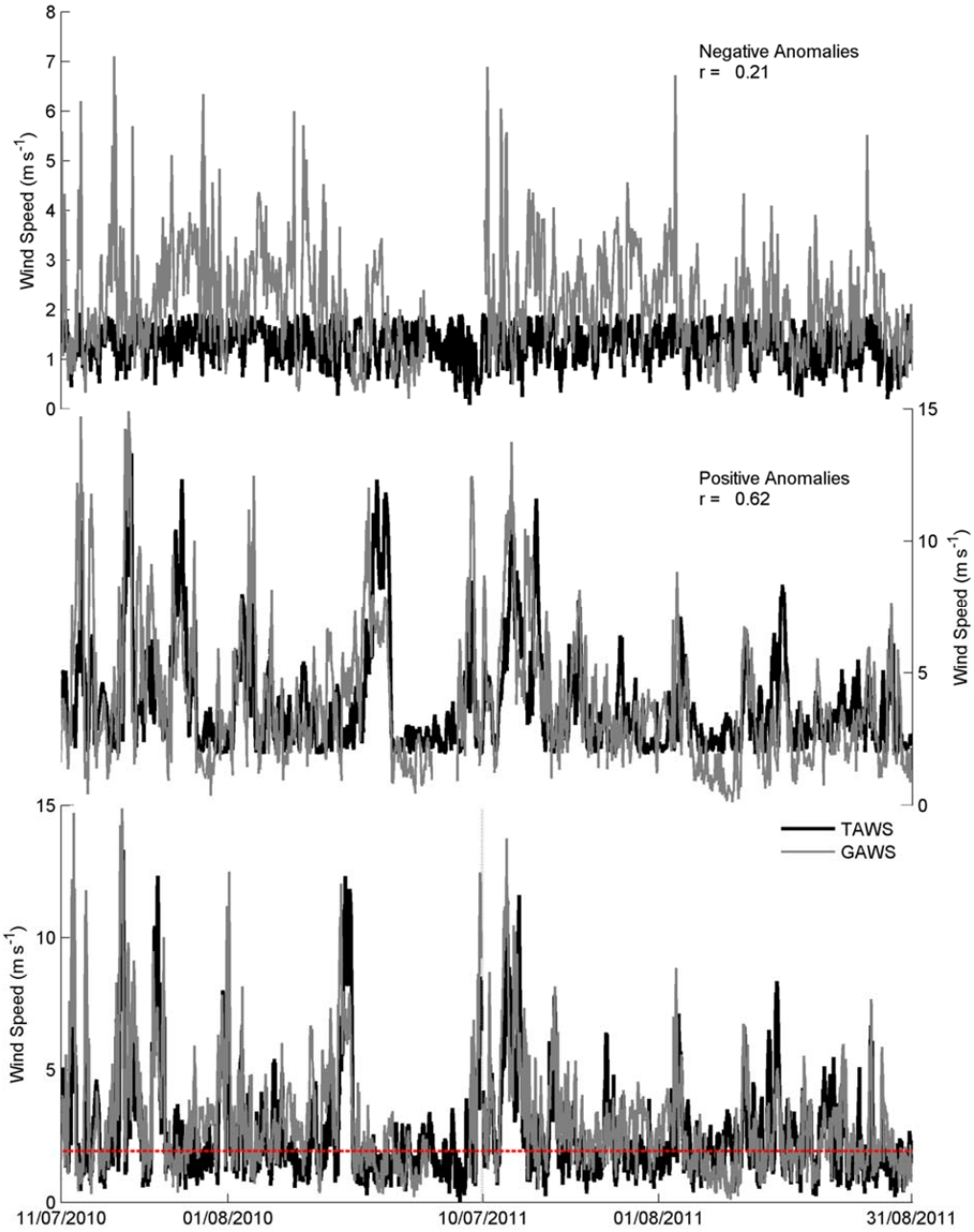

Figure 3.8. Wind speed observations and anomalies at TAWS and GAWS. Vertical grey line in the bottom graph separates observations made in 2010 and 2011. Note that anomalies are plotted as a continuous series: they do not correspond to the dates on the bottom figure's x-axis. The red, dotted line in the bottom graph indicates the median wind speed at TAWS for the period July-August, 2005-2011; this value (2.39 m s^{-1}) is used to stratify the parameterization of the wind speed at GAWS (see text for explanation).

Evidently, this condition is not observed when synoptic winds are light (i.e. negative TAWS anomalies: top axes in Figure 3.8). Although some of the occurrences of greater wind speeds at GAWS during periods of negative anomalies at TAWS may be explained by sheltering/lee effects during some wind directions, it is suggested that katabatic flow is mainly attributable. The equilibrium wind speed resulting from the negative buoyancy of the glacier boundary layer may be approximated from:

$$\overline{\overline{U}} = \left[\frac{g(\Delta\theta/\theta)\sin(\alpha)h_d}{C_D}\right]^{1/2} , \quad 3.3$$

in which g is acceleration due to gravity; $\Delta\theta$ is the potential temperature deficit of the glacier boundary layer; θ is the potential temperature in the ambient atmosphere; α is the surface slope; C_D is the drag coefficient; and h_d is the depth of the katabatic flow (Stull, 1988). An expression for h_d is given by Briggs, (1979) as:

$$h_d = 0.037[\sin(\alpha)]^{2/3}\, x \ , \quad 3.4$$

where x is downslope distance. An approximate upper limit of $\overline{\overline{U}}$ for GAWS can be obtained by setting $\Delta\theta$ to $\overline{T_t} + \Gamma dz - \overline{G_t}$, where Γ is the ELR, dz is the change in altitude, and the overbars denote the mean air temperatures at the AWSs. Then, α can then be estimated from $\mathrm{atan}(dz/dx)$ between GAWS and the back-wall of the northern accumulation basin (i.e. the maximum flow path length), which gives ~9.6° for α. If C_D is then set to 0.005 after Shea (2010), these values yield a $\overline{\overline{U}}$ of 5.8 m s^{-1}. This first-order approximation suggests the katabatic forcing is of sufficient magnitude to account for some of the high wind speeds observed in Figure 3.8 (top) during periods of light winds at TAWS.

Integrating this information, a dual scheme is proposed, whereby a direct substitution of the TAWS wind speed is adopted when positive anomalies are observed; and during negative anomalies, the katabatic wind is determined as a linear function of T_t (cf. Björnsson et al., 2005). Regression is used because of the significant correlation between these variables when wind speed anomalies at TAWS are negative and air temperatures at GAWS are positive (r = 0.51, $p < 0.01$):

$$G_w = \begin{cases} m_1 T_t + m_2 & , T_w' \leq 0 \ \ and \ G_t > 0°C \\ T_w & , T_w' > 0 \ or \ \ G_t \leq 0°C \end{cases} , \quad 3.5$$

where m_1 and m_2 are linear regression coefficients and T_w' is the TAWS wind speed anomaly.

3.4.4. Global radiation

Due to the close proximity of the on-off glacier measurement sites, it is assumed the atmospheric transmissivity is invariant over this small distance (e.g. Yang et al., 2011), which simplifies parameterization of the global radiative flux at GAWS. However, the prominent role of the shortwave radiative fluxes in the SEB on Storglaciären (Hock, 2005) demands close inspection of the topographic influences on incident global radiation, which can be of significant importance in complex terrain (Klok and Oerlemans, 2002). The approach taken to determine global radiation at GAWS closely follows that of Hock and Holmgren (2005). Global radiation is split into direct and diffuse components, and the extrapolation between on-off glacier sites treated separately. This approach is favoured as knowledge of the individual components of global radiation is required for the explicit evaluation of the role of the surrounding terrain on the incident global radiation budget.

The first stage of this procedure utilizes the ratio of received global radiation at TAWS to the potential global radiation (defined as the theoretical top of atmosphere global radiation, and calculated from standard equations of solar geometry for the latitude of TAWS and the time of day for each hourly observation (Iqbal, 1983)). This ratio may then be used to separate the direct and diffuse components of global radiation (Hock and Holmgren, 2005):

$$\frac{T_{g\_diff}}{T_g} = \begin{cases} 0.1, & ,\tau \geq 0.8 \\ 0.929 + 1.134\tau - 5.111\tau^2 + 3.106\tau^3 & ,0.15 < \tau < 0.8 \\ 1.0 & ,\tau \leq 0.15 \end{cases}, \qquad 3.6$$

in which τ is the ratio of received (T_g) to potential global radiation measured at TAWS, and T_{g_diff} is the diffuse component of the received flux at TAWS. The ratio T_{g_diff}/T_g is calculated hourly, but only when τ is defined, which is restricted to times when TAWS is not shaded and the solar elevation angle exceeds 15°; ratios at such low zenith angles are considered unreliable (Hock and Holmgren, 2005; Sedlar and Hock, 2009). Shading is calculated at 10-minute intervals from the DEM (illustrated in Figure 3.2): if the horizon angle in the direction of the sun exceeds the

solar elevation angle, TAWS is assumed to be in shade and τ is linearly interpolated between the most recent shade-free hours. The solar elevation angle is also computed from the expressions of Iqbal (1983).

The direct component of global radiation is taken as invariant between TAWS and GAWS (G_{g_dir}), although a correction is required for the slope and aspect at GAWS to evaluate the incident surface flux:

$$G_{g\_dir} = T_{g\_dir} \frac{\cos(\Theta)}{\cos(z)} \ , \tag{3.7}$$

where Θ is the angle between the normal to the slope and the solar beam at GAWS, and z is the solar zenith angle. Diffuse radiation is considered isotropic, which although not strictly true (e.g. Kondratyev, 1969), is assumed for simplicity, and is expected to cause a negligible error (Hock and Holmgren, 2005). The effect of topography on the total diffuse radiation received at GAWS (G_{g_diff}) is accounted for by the sky-view factor (F) and albedo of the surrounding terrain (α_g):

$$G_{g\_diff} = G_{diff} F + \alpha_g T_g (1 - F) \ , \tag{3.8}$$

in which G_{diff} is the diffuse radiation for an obstructed sky, and the terrain albedo at GAWS is estimated at 0.25, to account for a mixture of rock and partial snow cover on the slopes surrounding the measurement site (Hock and Holmgren, 2005). The sky-view factor is calculated from:

$$F = \frac{1}{2\pi} \int_0^{2\pi} \cos^2 \gamma d\varphi \ , \tag{3.9}$$

with γ as the elevation angle of the horizon and φ as the azimuth angle (Oke, 1987). This integral was evaluated numerically over 15° intervals following Hock and Holmgren (2005).

Isolating G_{diff} in Equation 3.8 from TAWS data requires that the contribution of terrain-reflected diffuse global radiation is subtracted from Equation 3.6. In this instance, it is also considered necessary to account for diffuse radiation originating from multiple reflections between the air and surface, as it is likely that this term

differs significantly between the persistently low albedo environs of TAWS and the more reflective surroundings of GAWS (e.g. Konzelmann et al., 1994):

$$G_{diff} = T_{g\_diff} - [\alpha_t T_g((1 - F) + \alpha_{air})] \ . \quad 3.10$$

The albedo of air (α_{air} = 0.075) is assumed to be constant, and is representative of a clean atmosphere (Iqbal, 1983). The albedo of the surrounding terrain (α_g) at TAWS is taken as invariant between the valley sides and the underlying surface and is estimated at 0.1. Sky diffuse radiation (G_{diff}) is assumed invariant between the two measurement sites.

Total incident global radiation at GAWS is evaluated depending on shading: only diffuse radiation is received for periods of shade, otherwise the sum of these components is taken as the incident flux. The multiple reflection term between the surface and air is incorporated for either case:

$$G_g = \begin{cases} (G_{g\_dir} + G_{g\_diff})[1 - \alpha_{air}\alpha_{gs}]^{-1} & , no\ shade \\ G_{g\_diff}[1 - \alpha_{air}\alpha_{gs}]^{-1} & , shade \end{cases} \ . \quad 3.11$$

It should be noted that the surface albedo term (α_{gs}), is different from that used in the calculation of slope reflected diffuse radiation (Equation 3.10), and is determined from the glacier albedo (see below). Incident global radiation is evaluated at ten minute intervals and averaged to hourly resolution.

For evaluation of the SEB, reflected shortwave radiation also needs to be parameterized, which is achieved by setting a constant, fixed albedo of 0.38, corresponding to the mean ice albedo throughout the period of observation. Prescribing the glacier albedo in this way avoids the need to define snowfall events at the measurement site explicitly. This is justified because it is the changes in potential melt energy that occur with time that is of principle interest in this study, rather than capturing the actual SEB that may be affected by the antecedent weather conditions. During 2010 and 2011, when SEB simulations forced with TAWS data are compared against results obtained from glacier observations, the measured albedo at GAWS is used to parameterize the reflected shortwave flux.

3.4.5. Incident longwave radiation

Longwave radiation is not measured at TAWS. It is thus necessary to relate this flux to other meteorological parameters which are observed. The incident longwave flux emitted by the atmosphere can be written as:

$$L\downarrow = \epsilon_{eff}\sigma {G_t}^4 \ , \qquad 3.12$$

where σ is the Stefan Boltzmann constant (5.67×10^{-8}) and ϵ_{eff} is the effective emissivity of the sky, which is a product of the clear sky emissivity (ϵ_{cs}) and a function quantifying the effect of cloud cover (C): such that $\epsilon_{eff} = \epsilon_{cs}C$, where C is always ≥ 1 (Sicart et al., 2010). Many empirical expressions have been proposed for determining clear-sky emissivity as a function of the air temperature and vapour pressure measured at screen-height (e.g. Swinbank 1963; Brutsaert, 1975). At Storglaciären, Sedlar and Hock (2009) examined many of these schemes, and suggested that ϵ_{cs} was determined best with the parameterization given by Konzelmann et al. (1994):

$$\epsilon_{cs} = 0.23 + 0.4393\left(\frac{G_q}{G_t + 273.16}\right)^{1/7.} \ . \qquad 3.13$$

Sedlar and Hock (2009) also provided a useful expression to circumvent the requirement of continuous cloud observations, usually required for quantifying C (e.g. Bolz 1949; König-Langlo and Augstein, 1994), but which are absent in this study. The proposed method quantifies the effect of cloud cover through the same transmissivity index (τ) in Equation 3.6 (the ratio of received to top-of-atmosphere global radiation):

$$C = -0.486\tau^{1.843} + 1.327 \ . \qquad 3.14$$

Having obtained values for C and ϵ_{cs}, it is then possible to quantify incident longwave radiation (Equation 3.12). Strictly, longwave radiation emitted from the surrounding topography should then be added to this (e.g. Sicart et al., 2011), but is neglected in the present analyses, due to the absence of temperature data for the emitting surfaces (i.e. the valley sides). It is considered that the effect of neglecting this additional source of longwave radiation is minimal for SEB computations: the high sky view factor at the AWS (0.92) means very little of the surrounding topography is 'seen' by the glacier surface at this location; and compared to the shortwave flux, longwave

radiation is a relatively minor contributor to the SEB at Storglaciären (Konya et al., 2007). The emitted longwave flux is calculated as a function of the glacier surface temperature, T_s:

$$L\uparrow = 0.97\sigma {T_s}^4 \ , \qquad 3.12$$

in which the value 0.97 is the thermal emissivity of an ice surface (Müller, 1985). Details of how the surface temperature is calculated are provided in Section 3.5.

3.4.6. Air pressure

Air pressure on the glacier is assumed to be invariant in time and is simply prescribed as the mean observed during the measurement period at GAWS. Although this treatment ignores variability that occurs with the prevailing weather conditions, this simplification is considered unlikely to propagate significantly to the calculation of the turbulent fluxes. This is because the standard deviation of the observed pressure time series is small (<1% of the mean), which translates to minimal changes in equations 2.4 and 2.5 (Section 2.4, Chapter 2).

3.4.7. Synthesis of empirical functions

The results of applying the empirical functions are given in figures 3.9 and 3.10, and the coefficients and performance metrics are provided in Table 3.3, which shows that the glacier meteorology is reproduced well by these functions—particularly air temperature and vapour pressure which are predicted best by the TAWS data. The regression slopes, relating observations of these variables at TAWS to observations within the glacier boundary layer, yield slopes less than unity, which is consistent with the cooling and drying effect of the melting glacier described by Shea and Moore (2010). Further agreement is observed in the shallowing of the air temperature regression slope at the upper end of the measurement range; this confirms the relationship illustrated schematically in Figure 3.6. It is interesting to observe, however, that splitting the vapour pressure regression by positive and negative air temperatures actually yields a shallower slope for cooler air temperatures, which is counter to the expectation that the drying of the glacier boundary layer would be diminished during freezing conditions (Section 3.4.2). Whilst the reason for this is unclear, no further investigations are performed, because freezing temperatures were rare during the period of observation (~10% of all observations), and any uncertainty

regarding the fitted coefficients will have a negligible effect on ablation, which is minimal (or non-existent) during such low temperatures.

Wind speed predictions are also in close agreement with those observed at GAWS, although a slight underestimation of the mean wind speed is observed (Table 3.3). The slope coefficient obtained for the katabatic component of Equation 3.5 (0.17 m s^{-1} $°C^{-1}$) is lower than that found by Björnsson et al. (2005), which can probably be attributed to glaciological differences between these two sites: flow-paths, and hence katabatic forcing, can be expected to be more developed on the far larger Vatnajökull (e.g. Ohata, 1989; Greuell et al., 1997). Longwave radiation, although not directly measured at TAWS, is similarly well simulated by the empirical treatment. There is also good correspondence for the incident global flux, for which the effects of shading and topographic reflections have been considered. Means for both incident radiative fluxes are slightly underestimated (by ~1% and ~3% for the longwave and global components, respectively); although, these errors are within the sensor accuracies reported in Table 3.2.

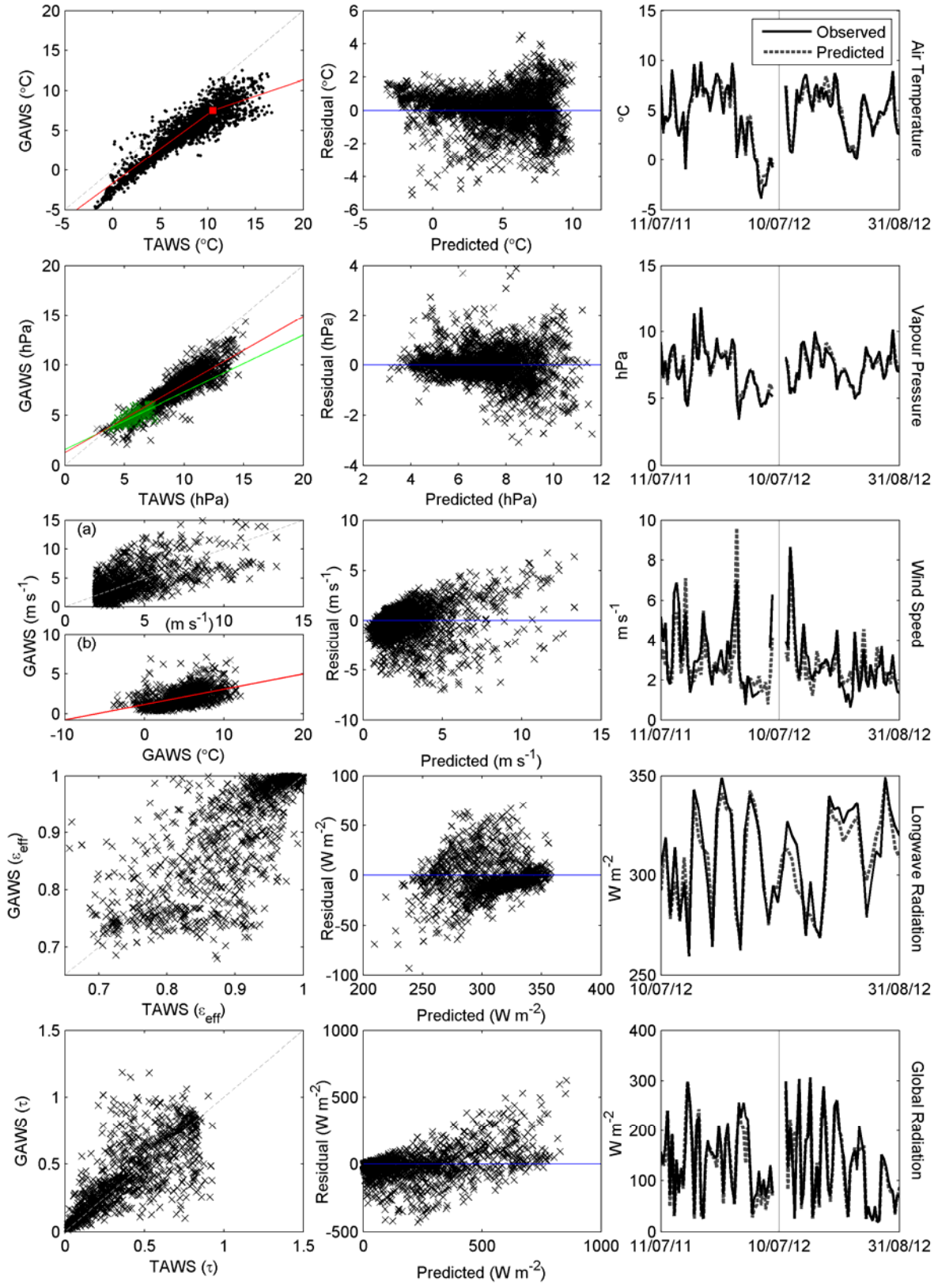

Figure 3.9. Left-hand side: relationships between TAWS and GAWS observations/parameterizations. Regression lines are in red/green, and 1:1 lines in grey. See text for explanation of the plots for longwave and global radiation. a) shows the wind speed relationship between stations during positive TAWS anomalies; b) gives the air temperature-wind speed relationship during negative TAWS anomalies. Middle: hourly residuals from applying the empirical schemes outlined in the text. Right-hand side: daily observations and predictions of meteorology at GAWS. The solid grey line separates data from 2010 and 2011.

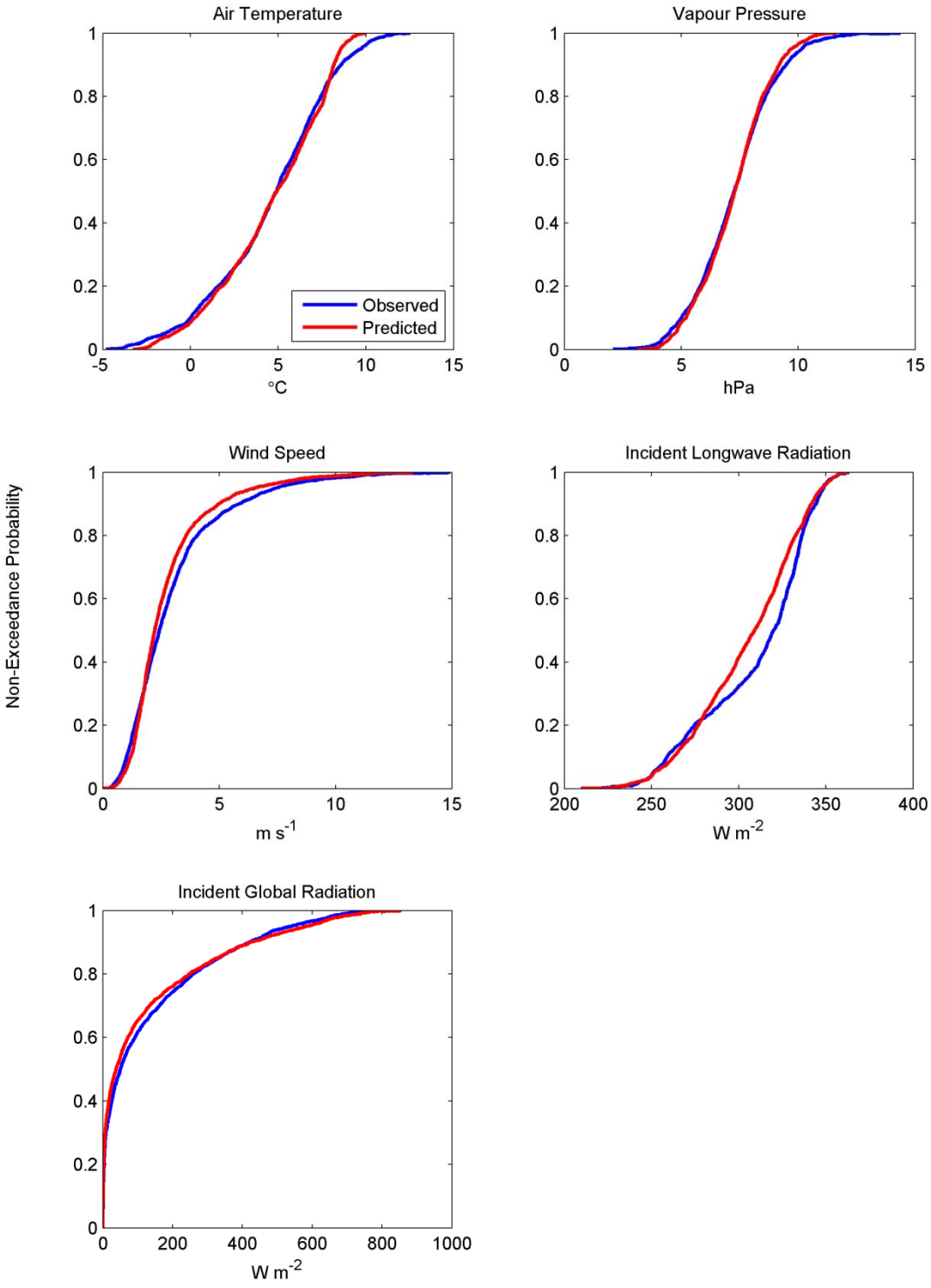

Figure 3.10. Empirical cumulative distributions for the observed and predicted meteorology at GAWS.

Table 3.3. Summary information of the empirical functions and their performance. 'Observed' refers to the meteorology measured in-situ at GAWS, and 'predicted' refers to the meteorology parameterized according to the empirical functions and the TAWS observations.

Variable	Expression	Coefficients	Mean (observed)	Mean (predicted)	r (hourly)	r (daily)
Air Temperature	$G_t(t) = \begin{cases} G_t^* + k_1(T_t - T_t^*), T_t < T_t^* \\ G_t^* + k_2(T_t - T_t^*), T_t \geq T_t^* \end{cases}$	G_t^* = 7.5°C T_t^* = 10.5°C k_1 = 0.41 k_2 = 0.88	4.6 °C	4.6 °C	0.92	0.97
Vapour Pressure	$G_q(t) = \begin{cases} j_1 T_q + j_2, G_t > 0°C \\ j_3 T_q + j_4, G_t \leq 0°C \end{cases}$	j_1 = 0.68 j_2 = 128.5 hPa j_3 = 0.57 j_4 = 159.1 hPa	7.3 hPa	7.3 hPa	0.92	0.97
Wind Speed	$G_w = \begin{cases} m_1 T_t + m_2, T_w' \leq 0 \text{ and } G_t > 0°C \\ T_w, T_w' > 0 \text{ or } G_t \leq 0°C \end{cases}$	m_1 = 0.17 m s^{-1} m_2 = 0.82 m s^{-1}	3 m s^{-1}	2.8 m s^{-1}	0.64	0.84
Incident Longwave Radiation	-	-	310 W m^{-2}	305 W m^{-2}	0.79	0.93
Incident Global Radiation	-	-	135 W m^{-2}	130 W m^{-2}	0.89	0.97

3.5. Energy Balance Modelling: Methodology

The SEB is calculated for 2010 and 2011 using both the observed GAWS data, and the adjusted TAWS record; this period is therefore used to assess the similarity of simulations driven by GAWS data and the adjusted TAWS record. During 2011, when measurements of ablation are available, SEB simulations may be validated independently. This information is used to assess the confidence in model specification. Having validated the model and evaluated the similarity of simulation results forced with GAWS and TAWS data, these latter data may be used to hindcast the SEB for the period 2005-2009 (Figure 3.1).

With regards to formulation of the SEB scheme, an important difference between simulations driven by GAWS and TAWS data is the absence of direct measurements of the emitted longwave flux; hence it must be modelled based on Ts (Section 3.4.5). This is problematic because Ts depends on the SEB, which introduces circularity. To deal with this, an iterative method is applied: for every time step, the SEB is calculated based on $Ts = 0°C$; then, if the SEB turns negative, Ts is lowered in 0.25°C increments, and the SEB re-evaluated until no flux is observed (0 W m^{-2}: Braun and Hock, 2004; Hock and Holmgren, 2005). Once the SEB turns positive, melt is assumed to resume immediately. Thus, no provision is made for eliminating the cold-content of the glacier resulting from a negative energy balance. This is justified by Hock and Holmgren (2005) due to the asymmetrical nature of this process: the effect of negative energy balances cools a near-surface volume of the glacier, whereas for melt to resume, only the surface needs to be at the melting point. Latent heat released from percolating re-freezing meltwater then effectively warms the sub-surface layers, further reducing the sub-surface cold-content. Neglecting the cold-content in this way is favoured over alternative empirical procedures which frequently retard melt until negative energy balances have been accounted for (e.g. Van de Wal and Russell, 1994)—an assumption that may systematically underestimate melt following periods of negative energy balances.

Treatment of the turbulent heat fluxes is invariant between the periods of direct observations and those driven by the adjusted TAWS record. These fluxes are evaluated according to similarity theory using the 'bulk approach', largely following the procedure adopted for Vestari Hagafellsjökull (Chapter 2, Section 2.4). However,

some important differences must be considered between these two field sites, which become pertinent in the context of the turbulent fluxes and merit further discussion. The flux-gradient similarity theory applied on Langjökull is based on the assumption of constancy of the fluxes with height and full adjustment of the flow to the underlying terrain (Brock and Arnold, 2000). Under these assumptions, and in a statically neutral boundary layer, the profiles of temperature, humidity and momentum are logarithmic. Monin Obukhov (MO) stability functions are incorporated to account for non-neutral conditions and deviation from log-profiles. Over melting glaciers, these functions serve to reduce turbulent heat transfer to account for the role of buoyant consumption of turbulent energy and the reduction in vertical mixing associated with a strong temperature inversion (Oke, 1987). Whilst these stability functions have been shown to work well at Langjökull (e.g. Guðmundsson et al., 2009; Chapter 2, Section 2.5.2), there is evidence to suggest that the profile structure found on Storglaciären is less amenable to MO similarity theory. For example, Hock and Holmgren (1996) report that air temperature profile data collected during stable stratification recorded on Storglaciären in the 1970s frequently exhibited negative deviations from the neutral logarithmic curve, as opposed to the positive deviations predicted by the MO functions. Consequently, the authors chose to neglect the effects of stability—a decision apparently vindicated by a substantial underestimation of seasonal melt (>20%) when stability corrections were applied during a sensitivity analysis of model parameters. Indeed, Holmgren (unpublished) suggests that even the neutral gradient-flux relations may underestimate vertical heat transfer on Storglaciären when the wind is particularly gusty.

Despite such findings, subsequent energy-balance models applied to Storglaciären have adopted MO stability corrections (Hock, 1998; Hock and Holmgren, 2005). Whilst these models appeared to perform favourably, this may be attributed to the way roughness lengths were tuned to match observations by the authors. Measured values of the average surface roughness length for momentum on Storglaciären, taken from profile measurements in near-neutral conditions in the 1970s, are reported by Hock and Holmgren (1996) as 2.7 mm and 0.15 mm over ice and snow surfaces, respectively. Values obtained through tuning have been substantially larger (10 mm in Hock (1998) and 7 mm in Hock and Holmgren (2005)), and no differentiation made between ice and snow surfaces. These figures must be regarded as somewhat high,

considering values reported elsewhere in the literature for glaciers in a similar geographical setting (e.g. Table 2 in Brock et al., 2006). Instead, such large values are more consistent with a balancing effect—required to counter the reduction in the turbulent heat fluxes when stability corrections are applied—than the physical properties of the glacier surface. Consequently, MO-stability corrections are not applied in this study, and the roughness lengths for ice and snow are taken as 2.7 mm and 0.15 mm, respectively. During simulations driven by GAWS data, the surface type is identified through the same density scheme outlined in Equation 2.14 (Chapter 2, Section 2.4); during 2005-2009, the glacier surface is assumed to be ice (Section 3.4.4).

3.6. Energy Balance Modelling: Results

3.6.1. Simulations forced with GAWS data

The results of modelling the SEB with GAWS data for the calibration period (2011) are shown in Figure 3.11. Uncertainty in this simulation was again estimated by perturbing the meteorological variables according to the sensor accuracies reported in Section 3.3 (Table 3.4). Inspection of these results indicates good agreement between the simulated and observed series, as both the variance in ablation and the cumulative amount are reproduced well. This gives confidence that the treatment of the energy fluxes is sufficient to capture the SEB and that the model has been correctly specified.

Table 3.4. Summary information of uncertainties resulting from sensor accuracies.

Variable	**Perturbation**	**mm w.e.**	**%**
Air temperature	0.3°C	55.5	3.3
Relative humidity	2%	31.6	1.9
Shortwave ↓	3%	55.3	3.3
Shortwave ↑	3%	21.7	1.3
Longwave ↓	3%	124.7	7.3
Longwave ↑	3%	127.1	7.5
Wind Speed	0.3 m s^{-1}	63.5	3.7
Total uncertainty		**208.1**	**12.3**

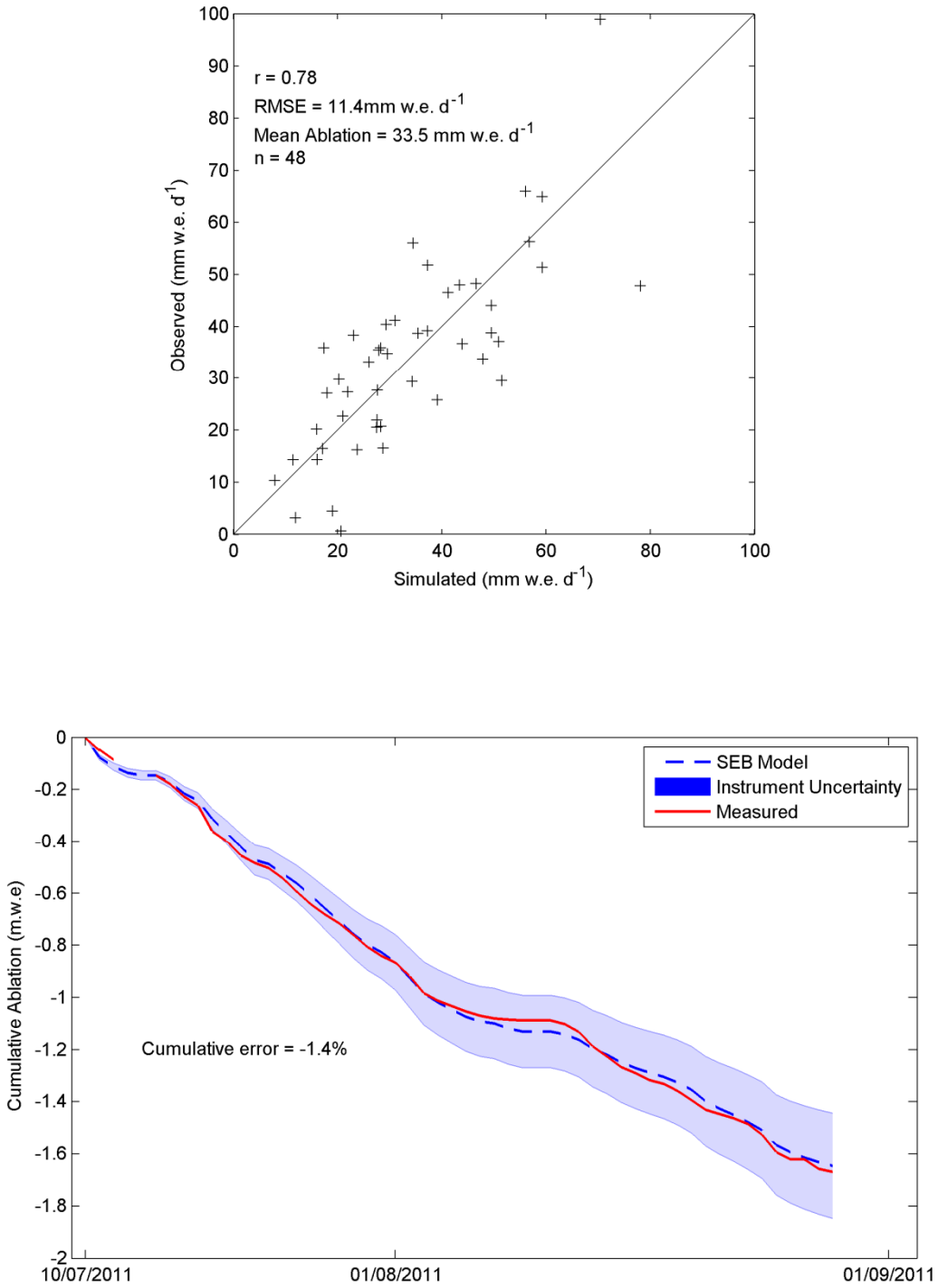

Figure 3.11. Agreement between simulated and measured ablation (top) and cumulative totals (bottom). Measured ablation was determined by first averaging all stake readings and change recorded by the UDG, and then correcting this value according to the estimated near-surface density (see text for details).

The decision to neglect the MO appears justified, as including these corrections and re-running the model led to a 12% underestimation of ablation, and a slight decrease in the correlation coefficient (0.75). Although this underestimation can of course be compensated for by scaling the roughness lengths accordingly, the magnitude of the adjustment that is needed is large: if the ratio between z_{0w} for ice and snow surface is assumed constant, and if z_{0w} for ice is iteratively incremented until simulated and observed ablation totals agree, a roughness length for ice >42 mm is required—a value which seems implausible considering previous measurements on Storglaciären (Hock and Holmgren, 1996), and the relatively smooth glacier surface in the vicinity of the measurement location (Figure 3.4). This physically unrealistic scaling, and the generally good performance of the melt model when the MO functions are neglected and the roughness lengths left un-tuned, supports the current treatment of the turbulent heat fluxes. No further alterations of the SEB routine are therefore considered necessary.

3.6.2. Comparison of simulations driven by GAWS and TAWS data

For the 2010 and 2011 ablation seasons, SEB modelling results were compared between simulations driven by the GAWS and TAWS data to ascertain the suitability of the adjusted TAWS data for determining the SEB in the absence of on-glacier observations (Figure 3.1). The results of these comparisons indicate good agreement between the model runs: ablation is very strongly correlated between series, and points lie close to the one-to-one line (Figure 3.12), indicating little unsystematic and systematic error, respectively (Willmott, 1981). This means that cumulative ablation totals are almost identical between simulations (TAWS data predicts ~1.5% more ablation). Correlation between the individual energy fluxes is also high, with values ranging between 0.86 (sensible heat flux), to 0.98 (shortwave heat flux). This agreement between the individual energy fluxes is important for interpreting the linkages between large-scale circulation and processes driving ablation during later analyses. Comparison of the relative contribution of the energy fluxes to the SEB also yields very similar results between model runs forced with the GAWS and TAWS data (Table 3.5). It should be noted that these contributions are in agreement with previous calculations made at Storglaciären, as Hock and Holmgren (1996, 2005), Carrivick and Hock, (1999), and Konya et al. (2007) all report that approximately 60% of melt energy is supplied by net radiation.

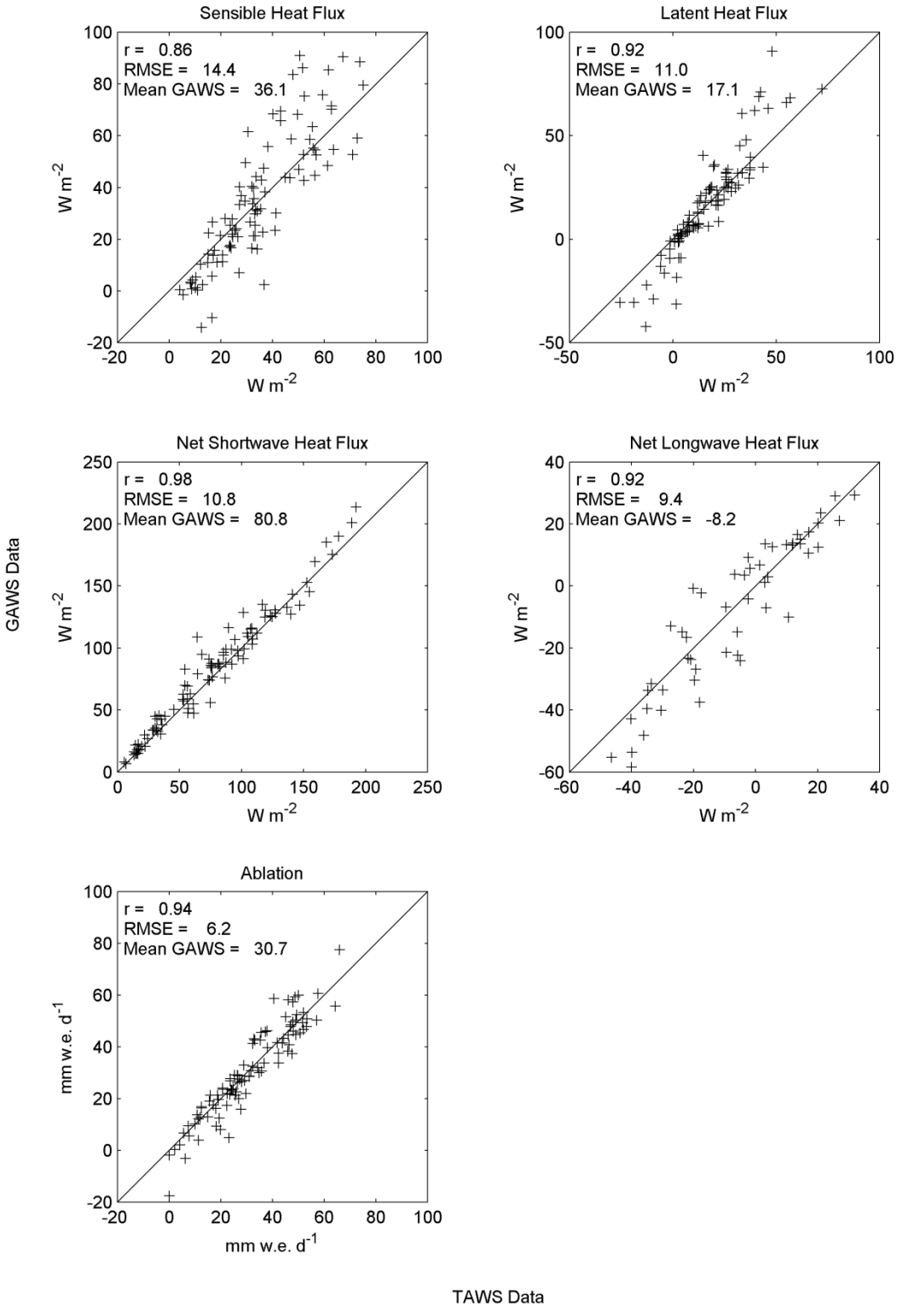

Figure 3.12. Comparison of energy fluxes and ablation from simulations forced by GAWS data and adjusted TAWS data. Note that units of the RMSE and mean fluxes/ablation indicated on figures are the same as the respective axes labels.

Table 3.5. Comparison of energy fluxes from simulations driven by GAWS data and adjusted TAWS data.

	GAWS		TAWS	
	W m^{-2}	%	W m^{-2}	%
Total Melt Energy	120.1	-	118.9	-
Sensible Heat Flux	33.9	28.2	34.7	29.2
Latent Heat Flux	15.4	12.8	15.9	13.4
Net Shortwave Flux	81.2	67.6	76.8	64.6
Net Longwave Flux	-8.2	-6.8	-6.7	-5.6
Ground Heat Flux	-2.1	-1.8	-1.8	-1.5

In investigating the utility of the TAWS data for calculating the SEB, an effort was also made to establish the sensitivity of the simulations to the empirical schemes outlined in Section 3.4. Specific attention was given to those variables required for evaluation of the turbulent heat fluxes, as this energy source is considered to be the most problematic to evaluate from climate data recorded outside the glacier boundary layer (Munro, 2004). To facilitate this investigation, different methods of adjusting the TAWS air temperature, vapour pressure and wind speed record to the glacier climate were applied, before re-running the SEB model to ascertain the effect on the turbulent heat fluxes and ablation (Table 3.6).

Table 3.6. Sensitivity of the turbulent heat fluxes and ablation to the empirical functions used to adjust TAWS data.

Variable	**Treatment**	**Δ% Turbulent Heat Flux**	**Δ% Ablation**
Air temperature	Linear regression	-0.4	-0.3
	ELR	16.7	7.7
Wind Speed	No katabatic forcing	-8.8	-3.7
Vapour pressure	Linear regression	0.7	0.4

Notable from these experiments was the sensitivity of the model to the treatment of the wind: neglecting the katabatic component of the wind speed (i.e. the thermal forcing; Section 3.4.3) resulted in almost a 9% decrease in the turbulent heat flux. This likely reflects the non-linearity of the relationship between air temperature and the sensible heat flux that results from the correlation between air temperature and wind speed. Neglecting this relationship may significantly reduce the calculated flux, because the transfer of sensible heat is dependent on the product of these two

variables (Braithwaite and Olesen, 1990; Equation 2.4, Chapter 2). Similarly, the importance of careful consideration of the glacier's cooling effect was apparent when investigating the treatment of air temperature, as applying the ELR resulted in a substantial increase of the turbulent heat fluxes and ablation. On the other hand, the use of simple linear regression, rather than the piece-wise functions suggested by Shea and Moore (2010), produces sensible and latent heat fluxes that are within 1% of the simulations driven by the TAWS data generated by the functions given in Section 3.4.

3.7. Comparisons with Vestari Hagafellsjökull

Having established the integrity of the extended SEB record, comparisons may be made with the data obtained from Vestari Hagafellsjökull in Chapter 2 (Table 3.7). These data highlight important meteorological and energetic contrasts between locations, which are desirable for investigating the utility of coupling synoptic-scale climatology to processes within the glacier boundary layer. In particular, it is evident that the climate of Vestari Hagafellsjökull is both cooler and drier than Storglaciären. The valley glacier experiences warmer air temperatures than at 1100 m on Vestari Hagafellsjökull, and similar temperatures to the 500 m station, despite being situated at a much higher elevation. Also, the mixing ratio observed at Storglaciären is higher than at either elevation on Vestari Hagafellsjökull. These differences propagate to the SEB by ensuring that the turbulent heat fluxes are greater at Storglaciären than at 1100 m on Vestari Hagafellsjökull; at 500 m, however, this is reversed as both the sensible and latent heat fluxes are higher than on the valley glacier. This may be partly attributed to the higher roughness lengths used in the calculation of these fluxes for ice surfaces on Vestari Hagafellsjökull, but also, to the much greater wind speeds which are experienced on the ice cap (Table 3.7).

The windier and cooler conditions experienced at Vestari Hagafellsjökull are partly a function of the differences in regional climate which prevail at these locations, which is independent of processes within the glacier boundary layer. The mean July-August temperature at Hveravellir (a weather station run by the Icelandic Meteorological Office in the Central Highlands, ~10km from Langjökull and 641 m elevation) is 8.3°C, and the mean wind speed is 5.8 m s^{-1} for the period 2002-2010; at TAWS (1135 m), the corresponding values are 8°C, and 2.6 m s^{-1}. When elevational differences between locations are factored in, this translates to a relatively warmer

climate in the vicinity of Storglaciären. This, and the greater wind speeds observed around Vestari Hagafellsjökull are probably attributable to the maritime nature of the climate, and the more frequent passage of cyclones that occur at this location (Einarsson, 1984).

The incident radiative parameters also exhibit differences between locations, as the ice cap experiences somewhat greater receipts for both the long and shortwave fluxes. The reduced shortwave flux received at Storglaciären is also probably the result of a locally more overcast climate, rather than processes within the glacier boundary layer: latitudinal considerations of the incident solar flux would actually suggest ~6 W m^{-2} increase in the mean flux at Storglaciären, due to the longer duration of illumination at this more northerly location in July and August. However, it should also be considered that enhanced topographic shading may contribute to the reduced flux at the valley glacier, as this alone reduces the potential incident flux by ~10%.

Table 3.7. Comparison of July-August meteorology and energy balance components between locations on Vestari Hagafellsjökull and Storglaciären.[a] Values for 500 m on Vestari Hagafellsjökull span 2001-2010, except for the incident radiative fields and the calculated energy fluxes, which extend only to 2007 (due to uncertainty of CNR1 sensor calibration: Chapter 2, Section 2.4). [b]At 1100 m on Vestari Hagafellsjökull, all values are for the period 2001-2010, and at Storglaciären, values are taken from in-situ observations when possible and from the synthesised series when not (2005-2011).

	[a]Vestari Hagafellsjökull 500 m	[b]Vestari Hagafellsjökull 1100 m	[c]Storglaciären 1387 m
Air Temperature (°C)	5.3	2.0	5.1
Wind Speed (m s^{-1})	5.3	5.4	2.9
Mixing Ratio (g kg^{-1})	5.0	4.7	5.2
Incident Shortwave Radiation (W m^{-2})	163.2	200.0	157.2
Reflected Shortwave Radiation (W m^{-2})	12.6	104.5	62.2
Incident Longwave Radiation(W m^{-2})	315.6	311.2	301.3
Emitted Longwave Radiation (W m^{-2})	314.9	311.2	313.8
Sensible Heat Flux (W m^{-2})	70.0	20.2	38.7
Latent Heat Flux (W m^{-2})	28.1	6.6	13.4
Ground Heat Flux (W m^{-2})	-	-	-2.2
Total Energy (W m^{-2})	249.4	122.4	132.4
Ablation (mm w.e. d^{-1})	65.1	29.9	34.6

With regards to longwave radiation, it is particularly interesting to observe that the amplified flux received at Vestari Hagafellsjökull occurs despite the drier and cooler conditions which prevail at this location. That is, because incident longwave radiation depends upon the temperature of the atmosphere and the effective emissivity, which itself is a function of the vapour content (Section 3.4.5), it is surprising that Storglaciären receives a smaller incident flux.

A possible explanation for this may be the cooling and drying effect of the melting glacier surface on the overlying air: Björnsson et al. (2005) outline that longwave radiation received by a glacier surface is affected by the glacier boundary layer, which is colder and drier than the air above (Van den Broeke, 1997a). A consequence of this static stability is that the incident flux is typically lower than would be expected from the temperature and vapour content of the free atmosphere, but higher than would be anticipated from the observed values of these variables in the glacier boundary layer. The greater incident longwave flux found on the ice cap may therefore be explained by additional radiation emitted by a warmer and wetter atmosphere overlying the glacier boundary layer. This effect would not similarly be apparent at Storglaciären if the glacier boundary-layer's temperature and humidity varied less substantially from the overlying atmosphere—a condition which is considered likely because the far larger ice-mass at Vestari Hagafellsjökull will probably create a more discrete glacier boundary layer, as this typically becomes more thermally distinct as a function of flow-path length (Greuell and Böhm, 1998; Shea and Moore, 2010). It is additionally possible that the greater development of a glacier boundary layer at Vestari Hagafellsjökull contributes to the relatively lower temperatures found at this location, as heat and moisture exchange with the melting glacier surface would chill and dry the atmosphere (Van den Broeke, 1997a; Oerlemans and Grisogono, 2002).

3.8. Synthesis and Conclusions

The aim of this thesis is to explore the relationship between processes of ablation and larger-scale synoptic circulation. A requirement therefore, is to obtain detailed information of the glacier boundary-layer meteorology and the surface energetics. This was addressed by presenting meteorological data observed at Storglaciären, which were subsequently used to simulate the SEB. Thus, these data complement those provided from investigations at Vestari Hagafellsjökull in Chapter 2. However,

direct meteorological observations from Storglaciären were of limited duration, and so a major objective of this chapter was to extend this record using off-glacier observations. The benefits of a temporally more extensive data set from Storglaciären are the broader range of synoptic conditions that may be witnessed, which provides greater insight into the coupling of the local and synoptic scales through time.

Extending the glacier-climate record in this chapter was achieved by adjusting meteorological observations made at TAWS to the glacier boundary layer. This necessitated careful consideration of how the melting glacier affects the overlying air, and was catered for by applying empirical transfer functions. Piece-wise regression was used to adjust air temperature and vapour pressure to the glacier, after Shea and Moore (2010), and following Björnsson et al. (2005), simple linear regression was applied to infer the effect of katabatic forcing on the wind speed. Parameterizing the shortwave and longwave incident radiative fluxes was then achieved by adopting the methods of Hock and Holmgren (2005) and Sedlar and Hock (2009), respectively. These functions saw an encouraging amount of the variance in the observed glacier meteorology being captured, particularly at daily resolution. Indeed, the effect of this good agreement was evident when simulating the SEB with the on- and off-glacier data, as the differences between the calculated energetics were negligible. This provides confidence of homogeneity when integrating the two series to provide one continuous record of the SEB. Moreover, the good agreement observed between simulated ablation and measurements during 2011 suggests that the SEB model realistically captures the surface energetics. This indicates that the continuous series (Figure 3.13) may be used reliably to elucidate the relationships between ablation processes and synoptic circulation.

These data augment those in Chapter 2 due to the contrasting climatic setting, and scale of Storglaciären, which propagate to the meteorology, and manifest as a warmer and wetter climate, with lower wind speeds and subdued radiative fluxes relative to the ice cap. Considering the aim of the thesis, the contrasts between the Icelandic and Swedish glaciers will be valuable for assessing the feasibility of usefully coupling local processes which drive ablation with atmospheric processes.

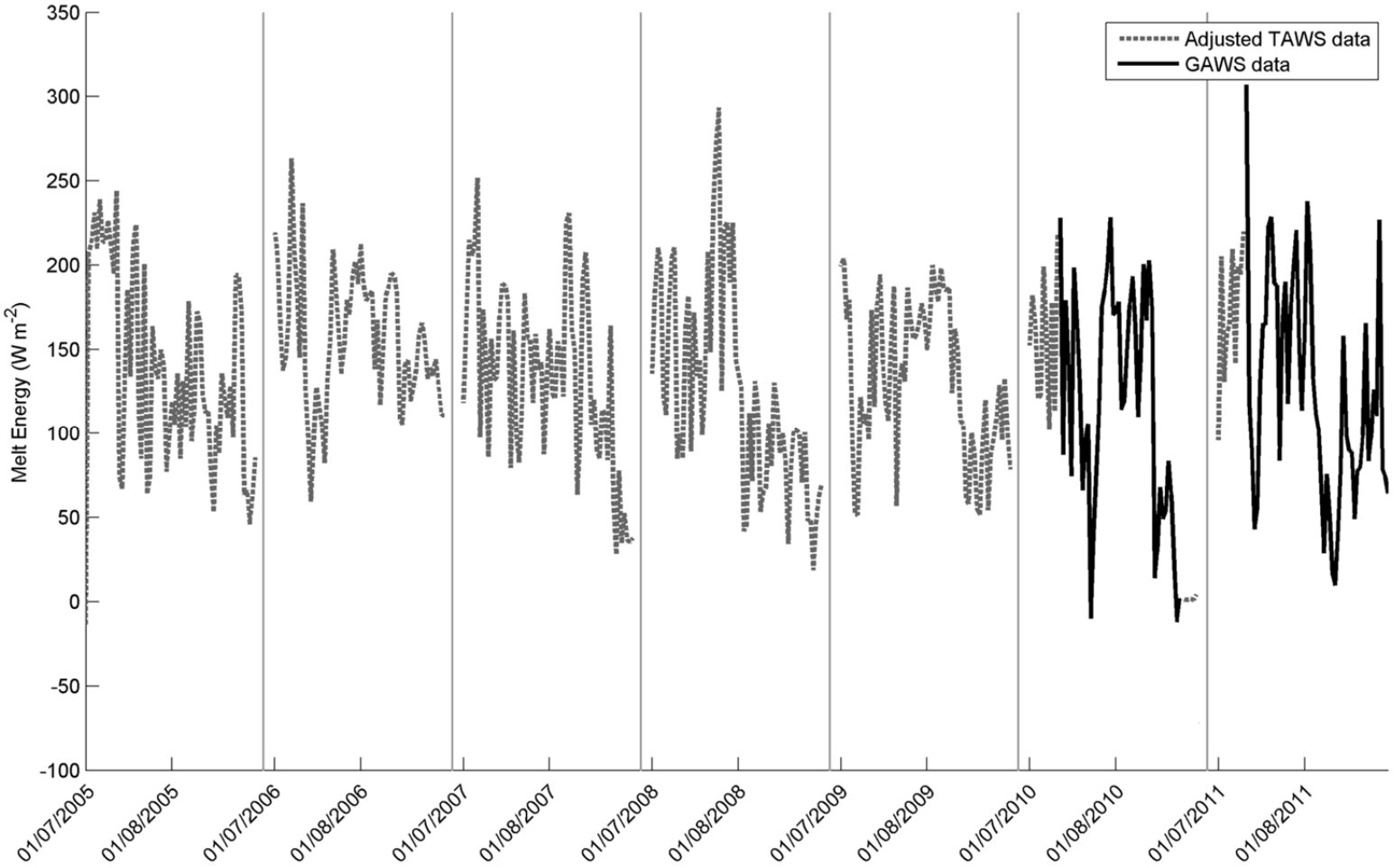

Figure 3.13. Surface energy balance 2005-2011, calculated with GAWS data and the adjusted TAWS record. The solid grey lines separate successive ablation seasons (July-August).

4. Development of a Synoptic Classification Procedure for Application to Vestari Hagafellsjökull and Storglaciären

4.1. Introduction

The overall goal of this study is to contribute to an enhanced understanding of the relationship between large-scale atmospheric dynamics and processes which drive glacier ablation. Mölg and Kaser (2011) outline that research tasked with this aim has principally been approached from three directions: i) regression based studies, which seek to identify statistical relationships between atmospheric circulation and mass balance components directly (i.e. 'lumped' applications e.g. Shea and Marshal, 2007; Matulla et al., 2009; Yarnal, 1984a); ii) studies which attempt to explain the linkages between large-scale atmospheric processes and mass- or energy-balance variability (e.g. Francou et al., 2004; Vuille et al., 2008b); and iii) downscaling studies, which adopt a process-based approach, by first linking local meteorology with large-scale atmospheric data, and then applying these downscaled data to drive energy/mass-balance models (e.g. Reichert et al., 2001; Radić and Hock, 2006; Rye et al., 2010). Studies in this field often seek to balance the benefits of simplicity given by regression-based models, against the greater information about physical processes offered by models applied to downscaled data.

In this regard, classification techniques familiar to synoptic climatology are a suitable compromise. These methods seek to group large-scale climate parameters into nominal categories for evaluating linkages with local response variables (e.g. boundary-layer meteorology, or other indices reflecting localised environmental processes). The attraction of such an approach may be credited to the increase in physical interpretability that is achieved by reducing complex data into simple

homogenous groups, for which the response of local response variables may be assessed. Elsewhere in the environmental sciences, approaches utilizing synoptic analogues have exhibited excellent predictive power (e.g. Zorita and Storch, 1999; Hidalgo et al., 2008; Abatzoglu and Brown, 2012), comparable to, or even exceeding regression-based techniques (e.g. Kalkstein and Corrigan, 1986). It must also be considered that synoptic climatological approaches hold substantial intuitive appeal for applications regarding glacier mass balance. That is, processes of accumulation and ablation signify the net result of interactions between multiple meteorological elements and adopting a framework of analyses which embraces this synergy is therefore desirable. The attraction toward synoptic techniques in glacier-climate studies is strengthened further when considering the remote location typical of glaciers and ice caps, such that modest data requirements for data collected in-situ become increasingly appealing.

Despite these benefits, synoptic classifications remain under-utilized in glacier-climate research. The thesis makes a contribution in this regard by investigating how glacier meteorology (Chapter 5) and ablation (Chapters 6 and 7) are related to synoptic-scale atmospheric variability; to achieve this, a methodology which utilizes classifications is pursued. The aim of the present chapter is to introduce the synoptic dimension of this study. Specifically, this chapter elaborates on the details and terminology of synoptic classifications (Section 4.2), before outlining previous contributions that have used synoptic approaches to approach problems relevant to glacier climate interactions (sections 4.2.1 to 4.2.5). This information is then integrated to develop an appropriate framework of synoptic analyses for the thesis, which is described in sections 4.3 and 4.4, before the results of its application are presented (Section 4.5). Finally, the chapter is synthesised and conclusions are drawn in Section 4.6

4.2. Synoptic Climatological Classifications

The aim of classifying in synoptic climatological analysis is to empirically link local weather variability with large-scale processes of atmospheric circulation by reducing a wealth of multivariate climate data (e.g. geopotential height fields, or meteorological variables) into nominal categories or groups which exhibit largely homogeneous characteristics (Philipp et al., 2010). The ease of interpretation provided by this reduction of complexity has led to wide application of synoptic climatological techniques within environmental analysis (e.g. studies of droughts, typhoons, air pollution, surface frosts, temperature and precipitation: Huth et al., 2008). Whilst a great variety of methodologies exist for determining synoptic categories, a unifying objective is the discrimination of discrete groups, exhibiting minimum-intra, and maximum-inter group-variance respectively. Additionally, the number of categories identified should remain small enough for the interpretability to be maintained.

Discussion of synoptic classification can be simplified by differentiating between techniques which adopt: i) a kinematic approach which aggregates observations based on flow parameters, such as geopotential height surfaces and sea level pressures; and ii) classifications that include additional meteorological variables and principally discriminate based on synergies of atmospheric thermal and moisture properties (Bower et al., 2007). Within the literature, these approaches are often referred to as ‘weather’ and ‘air mass’ typing procedures, respectively (e.g. Carrivick and Brown, 2001; Bower et al., 2007; Jiang, 2011). However, Huth et al. (2008) suggest that the ‘air mass’ terminology may be unsuitable if only surface observations are utilized, and recommends ‘weather classification’ as a more generically appropriate term. Consequently this is the terminology adopted for this study. To avoid ambiguity, references to categories defined by i) are renamed as ‘circulation types/categories, whilst the term ‘weather’ category/type is reserved for the results of ‘weather classifications’ (i.e. methodologies consistent with ii).

Circulation classification schemes may themselves be sub-divided: ‘automated’ and ‘manual’ divisions are frequently differentiated in the synoptic-climatological literature (Philipp et al., 2010). Huth et al. (2008) summarise that manual approaches to classifying circulation essentially depend on the subjective judgment of a skilled practitioner, based on either expert opinion, e.g. the Hess-Brezowsky

Grosswetterlagen (Baur and Nagel, 1944; Hess and Brezowsky, 1952), or geometrical considerations, which assess the similarities of circulation parameters (e.g. the Lamb classifications: Lamb, 1972). With the advent of modern computing power, automated techniques have largely replaced their time-intensive, manual counterparts. Esteban et al. (2006) highlight the adoption of correlation maps (Lund, 1963) and sum-of-squares techniques (Kirchofer, 1973) in being able to replicate manual classifications. More commonly, however, circulation categories are now determined through multivariate techniques: cluster analysis of data reduced in dimensionality by Principal Components Analysis (PCA) is the most the most frequent method recorded in a comprehensive overview by Huth et al. (2008).

Weather classifications, are somewhat different to their circulation counterparts, due to the explicit inclusion of multivariate meteorological data in the typing procedure. The notion of joining events according to their 'weather' characteristics stems from the work in 'complex climatology', pioneered by Federov (1927)—the term originating from 'weather complexes' describing the joint occurrence of several weather elements (Barry and Perry, 1973). The benefit of determining categories based directly on observed weather, rather than implicit inference from circulation patterns, is sometimes countered by limited transferability of results obtained from these approaches (Bower et al., 2007; Philipp et al., 2010).

4.2.1. Synoptic climatological classifications applied to studies of meteorological variability in mountainous and glacierized environments

Ablation is determined by the energy exchange between the glacier surface and the boundary-layer meteorology. To understand how it is related to synoptic scale atmospheric processes therefore requires elucidation of the relationships between micro-meteorological variability and wider-scale synoptic forcing. This is challenged, however, by the complex physical environments in which glaciers are located, and by the way in which glaciers may actively modify the local climate through heat and moisture exchange with the atmosphere (see chapters 2 and 3 for further discussion of this point). The physical complexity stems from the mountainous terrain in which glaciers are typically situated, as the spatial gradients of meteorological variables and meso-scale circulation are steep in these environments (Abatzoglou and Brown, 2012); this problematizes the determination of local meteorology from large-scale

atmospheric processes. These challenges have provoked numerous attempts at downscaling climate parameters in the field of glacier-climate interactions (e.g. Reichert et al., 1999; Radić and Hock, 2006; Hofer et al., 2010; Jarosch et al., 2012), and in a host of other physiographic applications in mountainous terrain (e.g. Hay and Clark, 2003; Salameh et al., 2009; Gutman et al., 2012; Abatzoglou and Brown, 2012).

Most frequently, empirical-statistical relationships have been sought to bridge the gap between local meteorology and spatially-coarse climate variability, that are computationally far more efficient than their dynamical counterparts (Mölg and Kaser, 2011), but which are compromised by possibly over-simplifying complex physical processes (Hidalgo et al., 2008). Strictly, synoptic classifications are a manifestation of statistical downscaling if the objective is prediction of local meteorological fields from the derived categories, but also, this categorization approach provides a convenient framework for exploring the nature of how local and large-scale climatic variability are related. It is in this latter exploratory context which classification schemes have been more frequently applied for climatological analysis in mountainous and glacierized environments.

In the mid, and sub-polar latitudes, where atmospheric variability is greatest (Lockwood, 1974), synoptic climatological approaches hold strong appeal as a framework for meteorological analysis. Some workers, motivated by the sensitivity of glaciers to this variability, have therefore adopted such techniques in their investigations. Particularly notable contributions have focused on the glacierized environs of the North Atlantic. For example, Käsmacher and Schneider (2011) explored circulation patterns driving temperature and precipitation anomalies in Svalbard, using a Self-Organizing Map routine to classify 500 and 700 hPa levels over a 2.5 x 2.5° grid. Application of this artificial neural network technique resulted in the authors concluding that nine types were sufficient to describe circulation variability around the Svalbard Archipelago, and that these provided a useful framework for analysing temperature and precipitable water content anomalies. The derived types yielded relationships which were physically consistent with *a priori* considerations of local flow regimes: warm, wet anomalies were associated with circulation types which produced southerly geostrophic flow, whilst cooler and drier conditions were accompanied by the advection of air from north and north-easterly

directions. A particularly interesting result from this study was the authors' attempt to relate the circulation types to the North Atlantic Oscillation (NAO). The advection of warm and humid southerly air was found to occur at times when the NAO was in a positive phase, corresponding to periods of enhanced westerlies across the mid-latitudes (Visbeck et al., 2001). Furthermore, because the identified circulation types were useful at capturing seasonal meteorological variability, Käsmacher and Schneider (2011) suggested that these synoptic categories may be useful for analysing the impact of interannual atmospheric variability on the region's glaciers and ice caps.

Fettweis et al. (2013) contributed further to the understanding of temperature variability in the high latitudes of the North Atlantic by using the classification scheme outlined by Fettweis et al. (2011) to group 500 hPa heights. Through examining circulation patterns over a grid which covered the entire Greenland Ice Sheet (GrIS) and extended east as far as the Svalbard Archipelago, this research sought to address the paradox of recent warming and increased melt over GrIS (Tedesco et al., 2008; Rignot et al., 2011; Hanna et al., 2012), which has not been similarly observed in Svalbard, despite the proximity of these locations. In agreement with Käsmacher and Schneider (2011), the authors implicated the NAO in being an instrumental factor driving this behaviour. It was observed that positive temperature anomalies over the GrIS coincided with a negative phase of the NAO, producing anticyclonic flow over this region, and favouring warm air advection over the western margin of the ice sheet. These conditions also result in northerly flow and cold air advection over the eastern side of the GrIS and the Svalbard Archipelago. It was therefore concluded that the recent negative phase of the NAO could explain the paradoxical behaviour investigated. The authors then demonstrated further the importance of considering synoptic types by using flow analogues to account for the observed warming over the GrIS during the period 1993-2012. By following a simple scheme, in which daily 700 hPa temperatures (1993-2012) were estimated from past observations (1961-1990) on days that were synoptically similar, they could attribute ~70% of the warming (1993-2012) to changes in atmospheric circulation. By comparison, only ~27% was considered to be the result of the linear trend describing the rise in global mean air temperature during the same period (note that the authors attribute the 3% shortfall in reconstructing the observed temperature increase to the fact that the flow-analogue method is insufficient to reproduce exceptional climate

anomalies). Fettweis et al. (2013) therefore provided a convincing and timely reminder of the need to integrate synoptic variability into glacier-climate studies.

Investigating how air temperature and synoptic-scale processes are related has been similarly prominent in studies that have focused on mountainous environments. In particular, research into near-surface lapse rates (hereafter lapse rates) has sought to incorporate synoptic climatological information (e.g. Pepin, 2001; Stahl et al., 2005, Blandford et al., 2008). This may be attributed to the complexities of atmospheric processes which determine this parameter. Lapse rates are mainly determined by the moisture content of the prevailing air mass, but in mountainous terrain, additional modification occurs because near-surface air temperatures are heavily affected by energy exchange with the Earth's surface (Blandford et al., 2008). Synoptic classifications are well placed to address such complexity: nominal grouping provides a convenient and practical framework to investigate intricate and interconnected processes; in turn, this facilitates physical controls on the lapse to be evaluated.

Synoptic controls on lapse rates over glaciers have also received attention. Here, the fact that the surface is limited to an upper maximum of 0°C results in a persistent cooling effect when melt conditions arise, which in turn may produce lapse rates which are very different from free-air values (Greuell and Böhm, 1998; Hodgkins et al., 2012b). In this regard, Marshall et al. (2007) offered a synoptic interpretation of lapse-rate variability over the Prince of Wales Icefield on Ellesmere Island, Canada. In this study, indices were constructed to describe different attributes of synoptic flow at the height of the 500 hPa surface. Through calculating the easterly and westerly components of airflow, in addition to its speed and vorticity, the authors were able to demonstrate significant coherence between synoptic circulation and daily lapse-rate variability. Specifically, it was noted that cyclonic types led to air temperature decreasing more rapidly with elevation (a steeper lapse rate), whilst temperature inversions (a shallower lapse rate) were found to occur with positive 500 hPa height anomalies and anticyclonic curvature. Interesting, however, was the seasonal non-stationarity of this relationship, as these correlations only persisted during summer and autumn (June-November); outside these months, no significant correlations with the synoptic flow parameters were observed. Instead, it was noted that the best indicator of lapse-rate variability during winter and spring was given by observations of air temperatures themselves, as cool conditions resulted in shallower lapse rates

occurring. Air temperatures, and indeed, lapse rates, are important for studies of glacier ablation because this variable is frequently used to account for melt energy implicitly in spatially distributed glacier models (Hock, 2003). Following Marshall et al. (2007) additional authors have sought to explain glacier lapse-rate variability with proxies of synoptic conditions (e.g. Gardner et al., 2009; Hodgkins et al., 2012a, b). However, none of these studies has applied synoptic classifications; this is addressed in detail in Chapter 5 of the thesis.

In addition to air temperatures, a limited number of researchers have more generally investigated how the glacier boundary-layer's meteorology varies as a function of synoptic forcing. For example, Konya and Matsumoto (2010) manually categorized days into weather types, deduced from observations at Glaciar Exploradores in Chilean Patagonia, and found that pronounced differences in the spatial distribution of temperature and radiation occurred over the glacier during these types. Most notable was the variable extent of glacier boundary-layer development, which was observed to be most evident during clear, sunny days, and less so when rainy conditions persisted. Hannah et al. (2000) also used a weather-category approach to determine spatial microclimatic variability at Glacier du Taillon in the French Pyrénées, and found that categories associated with minimal cloud cover accentuated spatial variability in both solar radiation and air temperature. These studies have been important in illustrating the potential of synoptic typing schemes in constraining microclimatic variability across glaciers, which is required for the successful implementation of physically-based SEB models that are heavily reliant on this information.

4.2.2. Synoptic climatological classifications applied to studies of glacier-climate mass and energy exchange

Although limited, notable studies have directly examined the linkages between synoptic conditions and the mass/energy balance of glaciers. Contributions have been made at the 'lumped' scale, that is, investigations which have sought to relate mass balance variability to synoptic variability in a gross way, without explicitly determining how these spatial scales are related; but also, by researchers who have attempted to develop a process-based understanding of how meteorology at the synoptic-scale propagates to the glacier boundary layer. This latter body of work has

tended to focus on ablation and the energy balance at the glacier surface, and is therefore especially pertinent to the aims of the thesis.

4.2.2.1. Synoptic climatological classifications and elements of glacier mass balance

In an example of a 'lumped' synoptic glacier-climate investigation, pioneering work conducted by Hoinkes (1968) saw the adoption of the manual, Hess-Brezowsky Grosswetterlagen to explain the variation in the front positions and of glaciers in the Alps. By grouping Grosswetterlagen into five seasonally-differentiated, broad categories, representing 'favourable' and 'unfavourable' conditions for glacier advance, the author was able to attribute appreciable variation in front positions to the combined effects of the relative frequency of these groups. Moreover, when refining the study to include recent mass-balance data of selected glaciers, a good general agreement between groups' frequency and annual mass-balance variability was observed. Specifically, a useful indicator of annual mass balance could be obtained from the ratio of cyclonic to anticyclonic groups prevailing throughout the summer. The explanation offered for this was that higher net radiation and warm air temperatures accompanying anticyclonic circulation, coupled to a decrease in occurrence of summer snowfall, resulted in increased ablation when these conditions persisted. So encouraging were these results, the author concluded that despite the 'rudimentary' treatment of the Grosswetterlagen, this circulation-based approach to glacier studies held more promise than the use of 'classical' proxies of mass balance, such as air temperature and precipitation.

Synoptic forcing of annual mass balance variability was also explored by Yarnal (1984a). Using the circulation-based Kirchofer (1973) sum-of-squares technique, this study sought to explain the mass balances of Peyto and Sentinel glaciers, western Canada, by classifying the height of the 500 hPa surface. In a grouping procedure similar to that employed by Hoinkes (1968), circulation categories were aggregated into a small number of types based on interpretations of the categories' meteorological attributes (e.g. wet/dry, cool/warm). Subsequent multiple regression analysis using the frequency of these types as predictors resulted in an encouraging amount of variance of the mass balance being explained. An interesting element to this research was the importance of synoptic scale in determining mass balance. Peyto

Glacier responded more clearly to large-scale circulation patterns, whilst Sentinel Glacier was especially sensitive to high wave-number (smaller scale) synoptic patterns. More generally, this study agreed with that of Hoinkes (1968): warm, dry types manifested in high melt rates, whilst cyclonic conditions were important contributors to positive glacier mass balances.

Further insights into the relationship between synoptic scale processes and mass balance were provided by Fealy and Sweeney (2007), who used PCA and cluster analysis to objectively group days in weather classification at sites within Norway. Through correlating the annual frequency of these types with mass-balance components of glaciers in both Norway and Sweden, the authors were able to attribute the anomalous advance of Scandinavian glaciers at the end of the last century to an increase in the frequency of warm, maritime weather categories, which acted to enhance accumulation; drier continental types were found to amplify summer ablation and suppress winter accumulation. The benefits of this weather-classification procedure for predictive mass-balance modelling were demonstrated by simulating the summer and winter balances of Rembesdalskåka, Norway: regressing the annual frequency of specific categories' annual occurrence led to approximately 60% of the variance in both mass balances components being explained. Such explanatory power was shown to be a considerable improvement over using temperature and precipitation as regression predictors, and highlighted the suitability of a weather classification to studying mass balance variability.

Mote (1998a) demonstrated the use of synoptic climatological approaches in glacier-climate interactions at the ice-sheet scale. Through applying an S-mode PCA of 700 hPa heights, the author investigated the effect of mid-troposphere teleconnection patterns in controlling the spatial extent of melting for eight discrete regions of the ice sheet. By treating the teleconnection patterns (i.e. component scores) as predictors of melt extent in a stepwise multiple regression analysis, this study established that approximately half of its daily variation could be explained. Temporal and spatial variability of the regression model's skill was attributed chiefly to heterogeneity of the ice sheet's albedo with time, and the role of topographic barriers acting to modulate local energy exchange. Most notably, however, was the conclusion that changes in the teleconnections explained over half of the interannual trend in melt extent on the GrIS during 1979-1989.

Although not strictly a classification-based study, the work of Mote (1998a) was a precursor to a synoptic circulation classification by Mote (1998b) which sought to address processes contributing to particularly low and high melt events on the GrIS more explicitly. Through cluster analysis of days exhibiting proximate component scores from the S-mode PCA (i.e. similar time-realisations of the teleconnection patterns), categories were identified which displayed significant differences in melt extent; the role of onshore winds in delivering sensible heat through warm air advection was identified as an important control on melt. The author continued to highlight the need for spatial discretization, however, as the ice sheet exhibited regional variability in melt response to specific synoptic categories prevailing. A general conclusion from the work of Mote (1998a, b) was recognizing the importance of the role of mid-tropospheric circulation in distributing any climate warming signal, which should be acknowledged in future mass balance studies.

Recently, Fettweis et al. (2011) emphasised this point further by examining synoptic circulation in the context of the dramatic increase in melting on the GrIS that has occurred during the last few years. By classifying 500 hPa anomalies into eight types, the authors reported that an unprecedented persistence of types which favour warm air advection can account for the recent increase in melt events. Specifically, it was noted that a shift in the relative frequencies of circulation types occurred around the year 2000, with warm types becoming increasingly common since this time. By integrating results from MAR, the regional climate model (which simulated the surface energy balance), this study also provided an insight into how the rate of melting responds to synoptic variability at daily resolution. Interestingly, it was shown that, whilst the melt rate was highly correlated with 500 hPa circulation variability, the thermal inertia of the GrIS can introduce phase shifts in the surface response, as the cold content of the near-surface must be eliminated and the surface brought to the freezing point before melting can commence. It must be emphasised that this highlights the importance of integrating information about the surface energetics into synoptic analyses of glacier-climate interactions. That is, if mass, rather than energy balances are studied, it is possible that the relationship between synoptic circulation and surface ablation may be somewhat erroneously extracted, due to the effect of antecedent conditions affecting the glacier surface (the cold content, in this example). Adoption of a process-based approach in which specific energy balance components are related

to synoptic variability mitigates against this potential limitation and provides a more robust, physically-based framework for analysis.

4.2.2.2. Synoptic climatological classifications and the surface energy balance

Pioneering insights into the relationship between the surface energy balance and synoptic-scale processes were provided by Alt (1978), who built upon the work of Holmgren (1971) on the Devon Island Ice Cap in the Canadian Arctic Archipelago. By manually identifying three broad groups of circulation from 500 hPa and 850 hPa height fields, this study specifically investigated the effect of the timing of circulation types within the mass balance year. The transition toward a process-based study was facilitated by the acquisition of meteorological and heat-flux data from both the ice cap, and from one of its outlet glaciers (separated vertically by more than 1 km). This also gave the opportunity to assess the spatial variability of glacier response to synoptic-scale forcing. The study's results again highlighted the role of cyclonic activity in contributing to positive mass balances: the persistence of a quasi-stationary cyclone in all seasons was associated with years of strongly positive accumulation. Conversely, pronounced negative mass balances were found to be the result of well-developed anticyclonic conditions. Addressing the spatial variability in mass balance response to circulation patterns identified, Alt (1978) concluded that melt at the outlet glacier was associated with both clear skies and warm air advection; melting at the higher altitude (the ice cap) required warm air advection, and was particularly sensitive to the length of the ablation season. Further insights elucidated the effect of the timing of certain circulation types within the melt season. Specifically, it was reported that melt during anticyclones was subdued early in the ablation season on the ice cap, due to the generally higher albedo at this time of year, which largely offset the high shortwave radiative associated with these types. On the other hand, persistent early-summer anticyclones at the lower glacier site were still found to be important agents of ablation. By complementing synoptic circulation data with on-glacier, boundary-layer meteorological data, the studies of Holmgren (1971) and Alt (1978) were important in being the first to address the heat fluxes resulting from synoptic scale circulation explicitly.

Continuing this focus, Hay and Fitzharris (1988) conducted a thorough investigation into melt energy partitioning and its dependence on synoptic-scale atmospheric circulation at Ivory Glacier, New Zealand. Energy fluxes were analysed and three periods, marked by distinct SEB regimes, were selected for comparison to synoptic weather charts (sea level pressure, the locations of fronts, and the location of rain). High contributions of net radiation to the SEB were characterised by anticyclonic circulation, at which time the turbulent heat fluxes remained relatively muted, due to the advection of cold, dry air over the glacier. The highest melt events were associated with a blocking anticyclone to the east and northeast of New Zealand. In these instances, the turbulent heat fluxes became significant contributors to the SEB, due to the intrusion of warm and humid air over the study site. Finally, a disturbed zonal circulation was observed to be responsible for lowering the turbulent heat fluxes, and producing variable contributions of radiative heat energy owing to the passage of frontal systems and intermittent cloud cover. Acting on this information, the authors manually assigned all days to five synoptic categories, based on the direction of airflow across the island. This classification saw distinct differences in the resulting energy partitioning and total melt. In particular, two key categories associated with the advection of sub-tropical (northerly) air over the island and enhanced turbulent fluxes led to significantly higher melt rates.

Similar tendencies for high melt resulting from northerly airflow were found in another southern-hemisphere subjective classification at King George ice cap administered by Braun et al. (2001). This research found that the advection of southerly air from the Antarctic interior inhibited melt, due to low temperatures suppressing the turbulent heat fluxes. Air of north-westerly origin, relatively warm and humid from having crossed the ice-free Southern Ocean produced the highest melt rates, despite dense cloud coverage. These results were important in underlining the importance of a synoptic control on ablation. In particular, this study echoed that of Hay and Fitzharris (1988) in emphasising the role of airflow direction in being a major control on melt: conditions promoting the turbulent heat fluxes resulted in the greatest melt events, despite the fact that on a seasonal basis, net radiative energy remained the major contributor to the SEB in both cases. Furthermore, Braun et al. (2001) astutely highlighted the need to adopt a synoptic approach to melt studies in high latitudes with relatively cold ablation seasons, as synoptic conditions

characterised by a negative SEB (i.e. cold air advection) would not manifest in increased melting for a small warming in climate. A growing need for interannual studies to determine the feasibility of a synoptic approach in assessing the ice cap's sensitivity to warming was therefore identified as a priority for future research.

Weather classifications have also been applied to explore the relationship between processes of energy exchange and synoptic climatic variability. The utility of these approaches lies in the explicit treatment of weather variables within the classification procedure. Indeed, relying on implicit relations between circulation (airflow) and local meteorology may be vulnerable to oversimplification of complex, time-evolving processes. An example of the potential limits of circulation-based classification schemes is given by Yarnal (1984b), who noted that circulation types classified through an objective procedure (Kirchofer, 1973) varied in position when ranked by temperature on a seasonal basis at Sentinel Glacier. This variability likely reflects the changing surface conditions over which air is advected. Such changes propagate to the overlying air by influencing rates of atmosphere-surface energy fluxes. Air advection over a terrestrial snow cover, for example, often results in a cooling effect and an increase in the air mass's static stability (Barry and Chorley, 2009). Moreover, Philipp (2009) highlights an additional consideration, commenting on the importance of context within circulation classifications: the evolution of circulation (i.e. multi-day sequence) is a control on local processes because antecedent conditions will affect local manifestations of weather. Thus, information from single-day classification procedures may be compromised to some extent if this information is omitted.

Weather classifications are therefore advantageous for studies of surface energy exchange, due to the direct inclusion of observed weather conditions in defining synoptic categories. Brazel et al. (1992) demonstrated this benefit by analysing the SEB at West Gulkana Glacier, Alaska. Through the use of surface meteorological observations from a first-order weather station in nearby Fairbanks, days were classified into eleven types in an automated procedure, based on the diurnal evolution of seven parameters describing the prevailing weather. These data, supported by micrometeorological and ablation recorded on-glacier, aided in elucidating linkages with the SEB. The turbulent heat fluxes were again observed to be highly variable between weather categories. In particular, it was noted that katabatic forcing could produce elevated winds to enhance these fluxes, even though synoptic winds were

slack at Fairbanks. This emphasised the synergistic relationship between the glacier and the synoptic conditions in determining the local microclimate and SEB. Perhaps most importantly, however, the authors acknowledged the role of surface albedo as a control on the resulting energy fluxes: due to seasonal deterioration of the surface, the timing of categories' arrival would affect the energy partitioning and the net melt energy, as more shortwave radiation is absorbed by the surface. Despite this potentially limiting factor to a weather-category based approach to melt modelling, the study concluded that continued retreat of the West Gulkana Glacier since 1957 was in close agreement with what could be expected from the timing and duration of weather categories' occurrence throughout that same period.

Since the work of Brazel et al. (1992), the use of weather categories in SEB investigations has been adopted elsewhere. Hannah and McGregor (1997) applied the same automated classification procedure to meteorological data collected within the glacier boundary layer at Glacier du Taillon. Identifying a similar number of categories as Brazel et al. (1992), this study declared that ten types could adequately describe the range of surface meteorology recorded. Aggregating these into three groups characterised by similar melt (low, medium and high), the authors noted that very different synoptic situations could result in similar melt rates, but very different SEB partitioning. Moreover, the issue of intra-category variability of melt rates was addressed explicitly: continental types were observed to exhibit inherently less variable melt rates than those categories characterised by air mass transitions. In agreement with Brazel et al. (1992), the albedo of the glacier surface was also identified as a source of intra-category melt-rate variability: the authors noted that melt energy in categories characterised by high net shortwave radiation would be enhanced preferentially as the season progressed. A further application of this weather-category approach was the work of Hannah et al. (1999), also at Glacier du Taillon, which reached a general conclusion that echoed the work of some of the prior circulated-based classification schemes, in stating that low and high-ablation conditions resulted from cyclonic and anticyclonic circulation respectively. This information was used to speculate the possibility higher melt rates due to an extension of the North-African subtropical ridge, which may result from climate change.

4.2.3. Summary of synoptic climatological classifications

Studies in both glacierized and mountainous environments have demonstrated the utility of adopting a synoptic framework for analysing meteorological variability. Building on these principles, researchers have also exploited the holistic properties of classification schemes for describing the variability of glaciers' mass balance. The reductionism offered by these approaches enhances physical interpretability of glacier-climate interactions and classification techniques have been used successfully to contribute to predictive glacier mass balance models. Refinements of these studies are those which have explicitly addressed process. In particular, some workers have focused on exploring how synoptic variability propagates to the SEB to drive ablation. Here, the utility of synoptic classifications lay in the way that the complex evolution of the glacier boundary layer and its microclimate is captured and related to synoptic forcing. It is these benefits which are explored in the thesis.

The synoptic contribution to glacier-climate interactions offered by the present research is the temporal and spatial ambition of the study. That is, whilst glacier boundary-layer meteorological, and SEB data have been recorded and related to synoptic processes before (see references above), these studies have been of limited duration. The ten- and seven-year record from Vestari Hagafellsjökull and Storglaciären, respectively, provides an excellent opportunity to evaluate the synoptic climatological controls on microclimate (Chapter 5) and surface energetics (chapters 6 and 7), to an extent that has not been pursued previously. Similarly, the contrasting topographic settings of the study locations offer analogous insights into the spatial transferability of results. The next part of this chapter provides details of a synoptic classification scheme to be employed in this study (sections 4.3 and 4.4), before presenting results of the classified types (Section 4.6).

4.3. A Synoptic Classification Scheme for Vestari Hagafellsjökull and Storglaciären

To investigate the links between synoptic-scale climate, microclimate and the SEB at the two study locations, an automated classification procedure is favoured. This decision is taken because a manual scheme would be demanding in light of the extended nature of the data series: analysis at daily resolution would require the classification of over 920 and 427 days for Vestari Hagafellsjökull and Storglaciären, respectively.

It is also decided that a weather-typing procedure, rather than a circulation-based classification technique is preferred. This decision partly reflects the fact that the most detailed synoptically-focused SEB studies to date have adopted weather-typing techniques (Brazel et al., 1992; Hannah and McGregor, 1997; Hannah et al., 1999); but also, because weather typing is intrinsically appealing for studying the glacier micro-climate and its SEB. The attraction is due to the way multiple meteorological elements are included directly in the typing procedure, rather than being implicitly inferred from the atmosphere's dynamic properties. This is considered as desirable, because the energy fluxes resulting at the glacier surface are a function of the totality of meteorological elements' interaction, rather than the atmosphere's kinematic characteristics, which are the explicit focus of circulation-based classifications. The specific weather-typing procedure described herein closely follows the 'Temporal Synoptic Indexing' (TSI) routine pioneered by Kalkstein and Corrigan (1986) and employed subsequently by (Brazel et al., 1992; Hannah and McGregor, 1997; Hannah et al., 1999).

4.4. Temporal Synoptic Indexing: Data and Methods

The TSI technique adopted in this study utilizes gridded ERA-interim data, which is the latest reanalysis product offered by the European Centre for Medium Range Weather Forecasting (ECMWF) and was introduced briefly in Chapter 2, Section 2.4. The reanalyses data provide a multivariate, spatially complete and physically coherent data set describing atmospheric circulation and consist of global observations assimilated by a numerical forecast model (Dee et al., 2011). The global coverage of these data make reanalysis products ideally suited to studies in remote or inaccessible terrain, where prolonged in-situ measurements are challenging. These attributes have seen the use of reanalysis data in glaciological studies increase. Examples include: energy balance modelling (Hock et al., 2007; Rye et al., 2010); temperature-index modelling (Hanna et al., 2005; Radić and Hock, 2006; Hock et al., 2007); parameterization of near-surface, on-glacier lapse rates (Gardner et al, 2009; Hodgkins et al., 2012a, b); and the identification of atmospheric indices' relationship to glacier mass balance (Shea and Marshall, 2007).

The choice of which climatic elements to retain for classification was determined by this study's aim of investigating the effect of synoptic scale meteorological variability on processes of ablation; the variables chosen for inclusion are therefore guided by *a priori* consideration of meteorological elements that are likely to affect components of the SEB. Additionally, the TSI procedure was developed for the identification of 'air masses' (Kalkstein and Corrigan, 1986), which associates source areas with categories (Barry and Chorley, 2009). This is a useful concept to retain for the purposes of this study, as it allows discussion of the categories identified to be contextualised in the synoptic climatological literature. Consequently, the variables chosen for inclusion in this study were as follows:

- dewpoint temperature (2 m);
- air temperature (2 m);
- west-east wind scalar (the 'U' component of wind speed; 10m);
- south-north wind scalar (the 'V' component of wind speed; 10m);
- surface air pressure;
- total cloud cover.

Temperature and humidity are retained for the effect that these variables have on the sensible and latent heat fluxes respectively; these variables are also considered to be key air mass indicators (Barry and Perry, 1973). The U and V wind components provide information about wind speed and direction: wind speed is important for its effect on the turbulent heat fluxes, whilst the wind direction is evidently important for determining the origin of advected air (and hence air-mass source). The wind direction is regarded as additionally important as it implicitly considers the effect of local topographic barriers in modulating local micro-meteorology. Cloud cover is included because this parameter is relevant for both the longwave and shortwave radiative energy components (e.g. Sedlar and Hock, 2009; Klok and Oerlemans, 2002). Processes of mass convergence and uplift are quantified by air pressure which, along with cloud cover, has been used extensively in other weather classifications (e.g. Kalkstein and Corrigan, 1986; Kalkstein et al., 1990; Brazel et al., 1992; Kalkstein et al., 1996; Cheng and Lam, 2000; Bejarán and Camilloni, 2003; Fealy and Sweeney; 2007; Bower et al., 2007). These variables were obtained at 6-hourly intervals (00, 06, 12 and 18 UTC) for the 1.5° × 1.5° grid boxes in closest proximity to the study locations (Figure 4.1) for input into the TSI procedure. At Storglaciären, the TSI procedure is performed on the reanalysis data for July-August, 2005-2011, and at Vestari Hagafellsjökull for the period June-August, 2001-2010.

Ultimately, the methodology employed by TSI classifies individual days into categories through application of a clustering algorithm; however, prior to this stage, PCA is performed on the data. This is required to remove co-linearity within the meteorological variables, which maximises the 'disconnecting power' of the subsequent clustering procedure (Huth et al., 1993). The goal of PCA is to reduce a large number of variables exhibiting varying degrees of co-linearity to a smaller number of orthogonal components, whilst preserving as much variability in the original data as possible (Wilks, 1995). The input to the PCA is a similarity matrix. When the variables contain different units (e.g. air pressure and cloud cover), this should be in the form of a correlation, rather than a covariance matrix (Kalkstein et al., 1990). For the data in this study, the correlation matrix is a $k \times k$ symmetric matrix, where $k = 24$ (6 parameters measured 4 times daily). PCA is therefore a way of reducing the number of variables required to describe each day's meteorology.

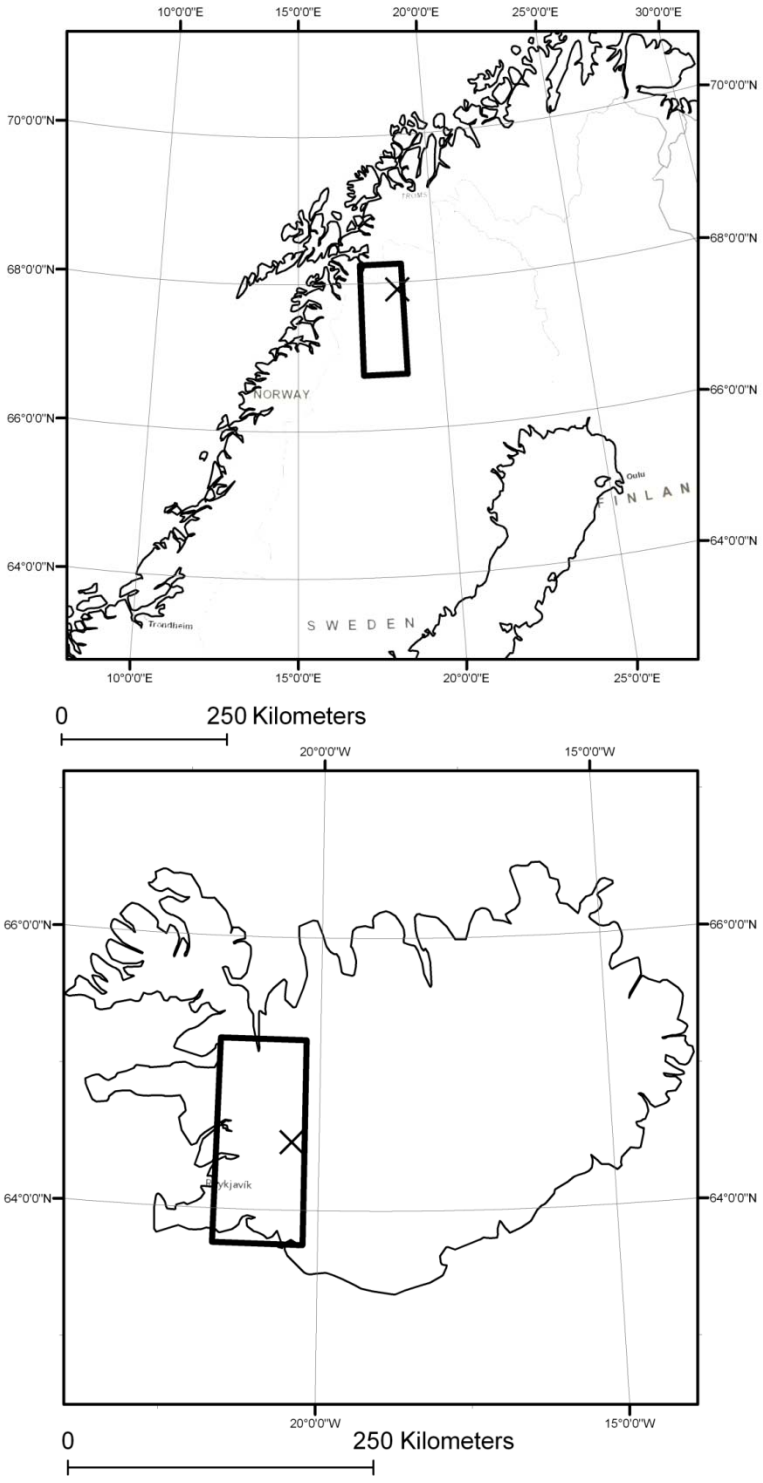

Figure 4.1. Location of grid cells from which reanalysis data are extracted.

The principal components (PCs) are calculated as a linear function of the original, standardised, *k* variables, and are a projection of these data onto the *m* eigenvectors:

$$u_m = \sum_{k=1}^{K} e_{km}\, x'_k \ , \qquad 4.1$$

where u_m is the m^{th} PC, e_{km} are coefficients and x'_k are the *k* variables, standardised according to:

$$x'_k = \frac{x_k - \overline{x_k}}{\sigma x_k} \ , \qquad 4.2$$

in which the overbar denotes the mean and σ indicates the standard deviation. Each PC can therefore be considered as analogous to a weighted average; the weights (the e_{km} coefficients) are dependent on the correlation between the original variables and eigenvectors (Johnson, 1991), subject to the constraint that:

$$\sum_{k=1}^{K} {e_{km}}^2 = 1 \ . \qquad 4.3$$

For *k* variables there are *k* possible PCs, although it is hoped that much of the variance in the original data can be represented by many fewer components (Wilks, 1995). The choice as to how many PCs to retain, however, is a matter of judgement. In this study, a scree plot is used to assist in the decision making, which involves a line plot of each component's eigenvalue: a steep break in slope is an indicator of a large relative change in the amount of variance explained by the PC, and suggests a suitable cut-off point (Wilks, 1995).

Whilst the rotation of the PCs is an important consideration for some applications within the atmospheric sciences, this is primarily to aid in their physical interpretation (e.g. Mote, 1998a). For the TSI methodology, PCA is only required to reduce the dimensionality of the data into orthogonal components, so that the efficacy of the clustering procedure is maximised; no rotation is therefore required (Huth et al., 1993; Kalkstein et al., 1990). The clustering algorithm is therefore performed on daily PC scores as calculated through Equation 4.1.

Days characterised by similar meteorological conditions will manifest in proximate component scores. The aim of the clustering procedure is to aggregate these scores into homogenous groups. For this purpose, an agglomerative, hierarchical clustering algorithm is applied. This method starts with each of the days in a separate cluster, then, at each stage, the two most similar (closest) clusters are joined until all days reside in a single group. The distance between any two clusters ($L_{1,2}$) is evaluated according to the average linkage method:

$$L_{1,2} = \frac{1}{n_1 n_2} \sum_{p=1}^{N_1} \sum_{q=1}^{N_2} D_{pq}^2 \ , \qquad 4.4$$

where $n_1$and n_2 are the numbers of members (days) in each of the clusters being evaluated; p and q are the order of observation within each cluster (1... n_1 and 1... n_2, respectively); and D^2 is the squared Euclidean distance (Kalkstein et al., 1987), calculated from:

$$D^2 = \sum_{m=1}^{M} (u_{mp} - u_{mq})^2 \ . \qquad 4.5$$

Thus, the squared difference is taken across each of the retained PCs. This average linkage method is preferred over other, frequently-used agglomerative algorithms, following Kalkstein et al. (1987), who found this technique to be superior to the Ward's and centroid methods for the TSI procedure: the former failed to partition 'extreme' events into distinct clusters, and the latter was prone to 'snowballing', whereby larger clusters grew at the expense of smaller ones. Because the agglomerative, hierarchical algorithm joins all days into a single group, the stage at which the algorithm is terminated determines the number of clusters that are retained. Deciding when this termination should occur is therefore of significant importance, and represents the second critical decision in the TSI procedure, after choosing how many PCs to retain.

Although some sophisticated methods have been proposed to assist with deciding on how many clusters are appropriate (Joliffe and Philipp, 2010), the lack of consensus about which rule to apply (Everitt et al., 2001) means that judgement-based methods remain the most popular (Baxter, 1994). Among such approaches is the use of the

distance measure (Equation 4.4). This involves examining a line plot of the value of L at each point in the agglomeration schedule: a large increase in value (break in slope) indicates that two dissimilar clusters have been fused and suggests a suitable point to truncate the algorithm. This method has been used in synoptic climatological studies before (e.g. Kalkstein and Corrigan, 1986; Fernau and Samson, 1990; Mote, 1998b; Fealy, 2004), and is used in this study. To aid in the visual inspection of the distance measures, the values at each step were standardised according to:

$$L'_{i+1} = \frac{L_{i+1} - \bar{L}}{\sigma_L} \,, \tag{4.6}$$

in which L is the distance measure as given by Equation 4.4, i is the stage of the agglomeration (1...n – 1), and the overbar and σ are the mean and standard deviation of the previous i distance measures, respectively (Everitt et al., 2001). Inspection of the agglomeration schedule in this way may be challenged in the presence of multiple breaks of slope (Aldenderfer and Blashfield, 1984). To aid decisions in such instances, the following were used as a guide: i) too many clusters are preferred over too few; and ii) the partitioning of days within clusters should be physically plausible, such that the occurrence of one or two very large clusters and many small clusters would be undesirable (e.g. Huth et al., 1993). The first condition is imposed because the retention of a larger number of clusters not only leads to greater homogeneity within those clusters identified, but also allows the possibility of aggregating clusters at a later stage based on subsequent analysis of their meteorological characteristics and effect on the SEB. The second criterion mainly relates to prior considerations of weather types at the study locations. Iceland's climatological setting, being regularly affected by contrasting air masses and disturbances in the polar front (Einarsson, 1984), means that a limited number of large weather types would be unlikely to capture this variability. The same considerations apply to Storglaciären's location in northern Sweden, which is similarly influenced by frequent extratropical cyclones and both maritime and continental air masses.

4.5. Temporal Synoptic Indexing: Results

Inspection of break points in the line plots of each component's eigenvalue (Figure 4.2) suggested five PCs were suitable to retain for Vestari Hagafellsjökull and Storglaciären. This decision is supported further by the sixth component's eigenvalue being less than one for both sites, which indicates that this component accounts for less variance than any one of the original variables, and is an additional criterion often employed for determining the number of PCs (e.g. Hodgkins et al., 2005).

The component loading matrices (tables 4.1 and 4.2) illustrate that the first PC accounts for much of the variance of the thermal and moisture variables. The south-north wind scalar similarly loads positively on the first PC for both locations, which indicates an unsurprising association between warmer air temperatures and southerly airflow. For Storglaciären, the west-east wind scalar also loads on PC1, suggesting colder (warmer) temperatures accompany westerly (easterly) airflow. This differs from Vestari Hagafellsjökull, but is consistent with the findings of Chen and Hellström (1999) who report that during the summer time, the advection of maritime air from the west produces negative temperature anomalies for this area of north-western Sweden. The explanation for this behaviour is that during the summer months, maritime air masses are relatively cool compared with air of easterly origin that has been warmed by the continent during this period of maximum insolation. At Vestari Hagafellsjökull, a similar relationship is not observed because easterlies must cross the ocean before reaching Iceland. Indeed, irrespective of air flow direction, all air masses that arrive on Iceland are modified by their passage over open ocean (Einarsson, 1984).

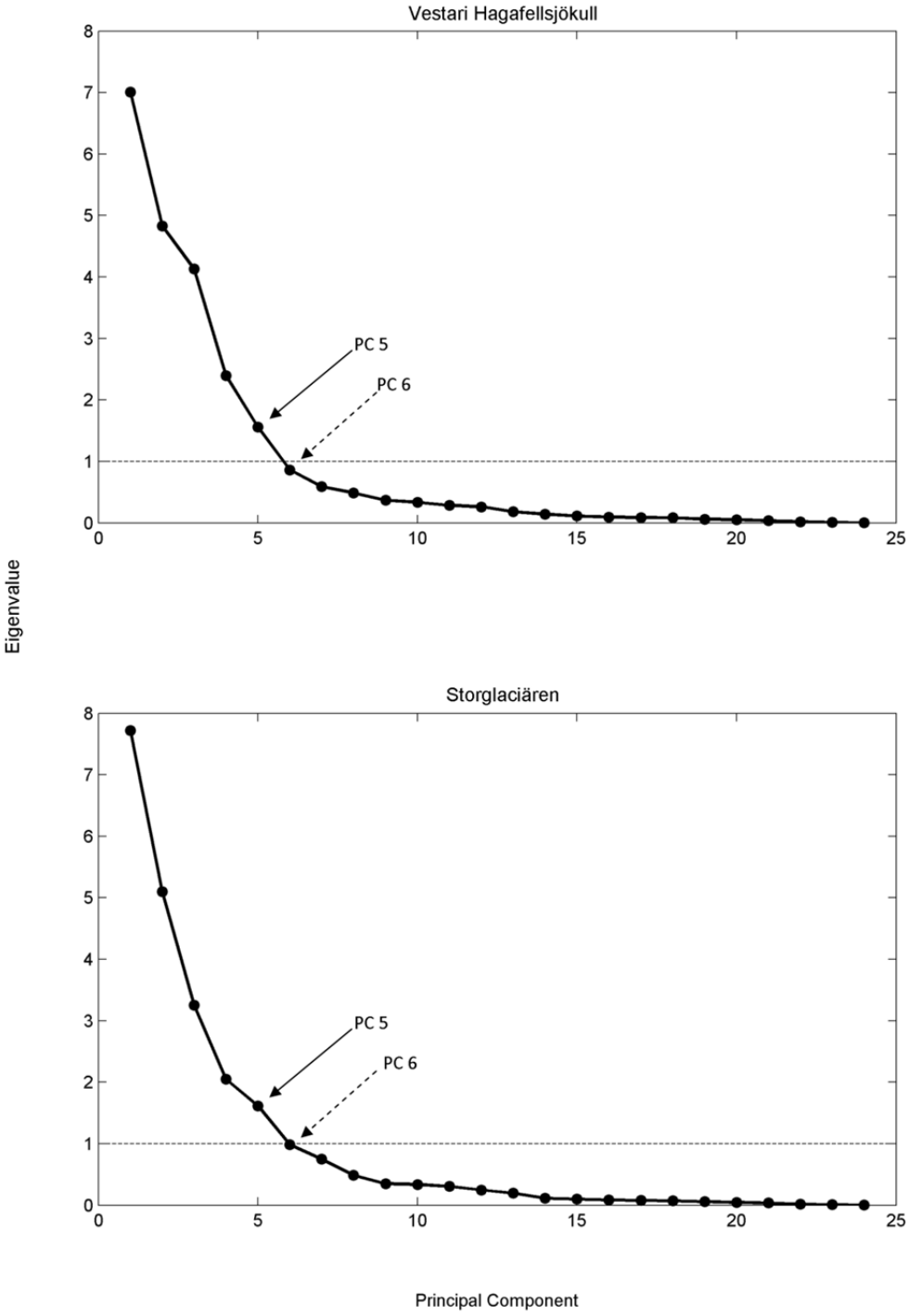

Figure 4.2. Scree plots of PC's eigenvalues. The arrows indicate the points between which a break in slope occurs; the solid line points to the PC before which a large drop occurs in the relative amount of variance explained, and is taken as the point to truncate PC extraction.

Table 4.1. Principal Component loading matrix for Vestari Hagafellsjökull. Note that loadings <0.1 are not shown. This convention is also applied in Table 4.2.

Meteorological variable	**Time**	**Component**				
	(UTC hour)	1	2	3	4	5
Dewpoint temperature						
	0	0.89		0.21	0.22	
	6	0.94		0.12	0.16	
	12	0.92		0.16	0.13	
	18	0.86		0.17		
Air temperature						
	0	0.83		0.41	0.12	
	6	0.91		0.26		
	12	0.59	0.36	0.59		-0.16
	18	0.49	0.44	0.61		-0.11
West-East wind scalar						
	0		0.48	-0.50	0.47	
	6		0.44	-0.56	0.62	
	12	0.11	0.45	-0.60	0.56	-0.14
	18		0.43	-0.48	0.53	-0.16
South-North wind scalar						
	0	0.58	-0.22	-0.53	-0.16	-0.25
	6	0.61	-0.18	-0.56	-0.26	-0.35
	12	0.56	-0.20	-0.51	-0.41	-0.40
	18	0.50	-0.14	-0.46	-0.41	-0.39
Air pressure						
	0	0.11	0.79	-0.17	-0.47	0.21
	6		0.85	-0.17	-0.43	0.20
	12		0.88	-0.19	-0.36	0.19
	18		0.87	-0.18	-0.29	0.19
Total cloud cover						
	0	0.31	-0.43	-0.30		0.49
	6	0.38	-0.31	-0.41		0.58
	12	0.27	-0.47	-0.52		0.40
	18	0.19	-0.41	-0.42	-0.21	0.22
Variance Explained (%)		29.2	20.1	17.2	10.0	6.5
Cumulative Variance Explained (%)		29.2	49.3	66.5	76.5	**83.0**

Table 4.2. Same as Table 4.1, but for Storglaciären.

Meteorological variable	**Time**	**Component**				
	(UTC hour)	1	2	3	4	5
Dewpoint temperature						
	0	0.71	-0.16	0.56		-0.14
	6	0.86		0.44		
	12	0.84	-0.11	0.40		
	18	0.84		0.25		
Air temperature						
	0	0.76		0.51		-0.13
	6	0.86	0.19	0.34	-0.16	
	12	0.82	0.39		-0.25	0.10
	18	0.79	0.40		-0.23	
West-East wind scalar						
	0	-0.58	0.42	0.44		0.19
	6	-0.55	0.44	0.52		0.31
	12	-0.43	0.34	0.58		0.53
	18	-0.38	0.19	0.62	0.12	0.48
South-North wind scalar						
	0	0.54	-0.32	-0.11	0.27	0.47
	6	0.59	-0.40	-0.29	0.32	0.45
	12	0.54	-0.39	-0.36	0.36	0.37
	18	0.39	-0.36	-0.41	0.39	0.24
Air pressure						
	0	0.31	0.78	-0.18	0.42	-0.14
	6	0.25	0.84	-0.17	0.41	-0.15
	12	0.19	0.86		0.42	-0.13
	18	0.15	0.86		0.40	-0.12
Total cloud cover						
	0	-0.32	-0.36	0.42	0.35	-0.21
	6	-0.28	-0.44	0.33	0.47	-0.28
	12		-0.56	0.32	0.45	-0.19
	18	-0.15	-0.45	0.32	0.40	-0.24
Variance Explained (%)		32.2	21.2	13.6	8.5	6.7
Cumulative Variance Explained (%)		32.2	53.4	67.0	75.5	**82.2**

Air pressure dominates the second PC in both instances, which is also associated with negative loadings of cloud cover and the south-north wind scalar, whilst the west-east wind scalars load positively. Beyond Component two, similarities of PC loadings between locations are less evident, reflecting the somewhat different climate that prevails at these locations. Physical interpretation of the loading matrices is also more challenging for PCs three to five, although, this mainly reflects the inherent difficulties in attaching physical meaning to PC loadings when no rotation is applied (Preisendorfer and Mobley, 1988; Easterling, 1990; Huth et al., 1993). Difficulty in physical interpretability is unimportant for the TSI, however, as the PCA is only required for data reduction and the removal of co-linearity among the variables. The five component solution is seen as sufficient in this regard, as it represents a significant reduction in data dimensionality, whilst retaining ~82% and 83% of the variance in the original variables for Storglaciären and Langjökull, respectively.

Having decided on the number of components to retain, the PC scores calculated from Equation 4.1 were subject to the agglomerative, hierarchical clustering algorithm. For Vestari Hagafellsjökull, this procedure initially suggested that a seven cluster solution may be appropriate (Figure 4.3a); however, this resulted in an undesirable partitioning of days, with over 80% of days assigned to a single group (Figure 4.3b). To mitigate against this insufficient differentiation, the largest group was subject to a second clustering procedure (using the original component scores: Kalkstein et al., 1990; Fealy and Sweeney, 2007). This re-clustering suggested a 24 cluster solution (Figure 4.3c), for which the distribution of days among categories seemed more physically plausible (Figure 4.3d). Combining these 24 clusters with the 6 formerly identified in the first stage of this two-step process, resulted in 30 clusters being retained for Vestari Hagafellsjökull. The line plot of the cluster agglomeration schedule for Storglaciären (Figure 4.3e) indicated 21 clusters were suitable for retention. Subsequent examination of the partitioning of days among these clusters gave no suggestion of a physically unrealistic aggregation (Figure 4.3f) and the 21 cluster solution was accepted.

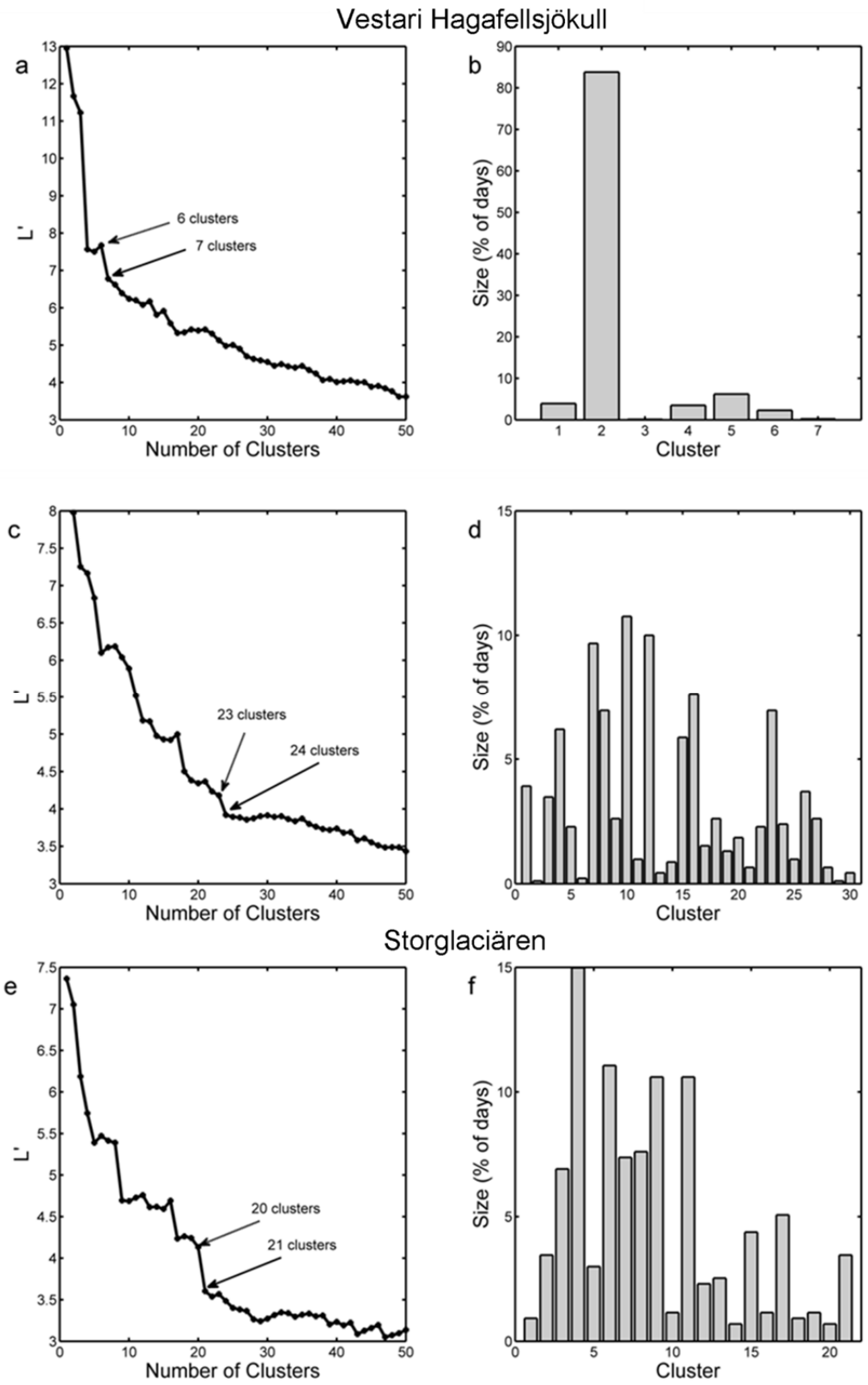

Figure 4.3. Left-hand side: scree plots of the standardised distance (Equation 4.6) at which clusters were merged during the agglomeration schedule. Right-hand side: the partitioning of days within the identified clusters.

If the clustering solutions are compared between locations, it is evident that the standardized distances (Equation 4.6) between merged clusters exhibit greater variability in the agglomeration schedule for Vestari Hagafellsjökull than Storglaciären (Figure 4.3a and 4.3e). This shows that the weather categories (clusters) joined at each step are more distinct at Vestari Hagafellsjökull, which is intuitive based on the contrasting character of Iceland's climate. Figure 4.4 aids illustration of this contrast by showing long-term (1981-2010) Jun-August sea surface temperature anomalies with respect to the zonal mean. These steep temperature gradients surrounding Iceland propagate to contrast in the weather types through heat and moisture exchange between the atmosphere and ocean—over which all air masses must pass on their way to Vestari Hagafellsjökull. Moreover, it should be considered that the cooler sea surface temperatures are due to the proximity of the GrIS. The contrast between air masses originating from the ice sheet and from the sub-tropical North Atlantic will contribute to the pronounced differences observed between weather types at Vestari Hagafellsjökull.

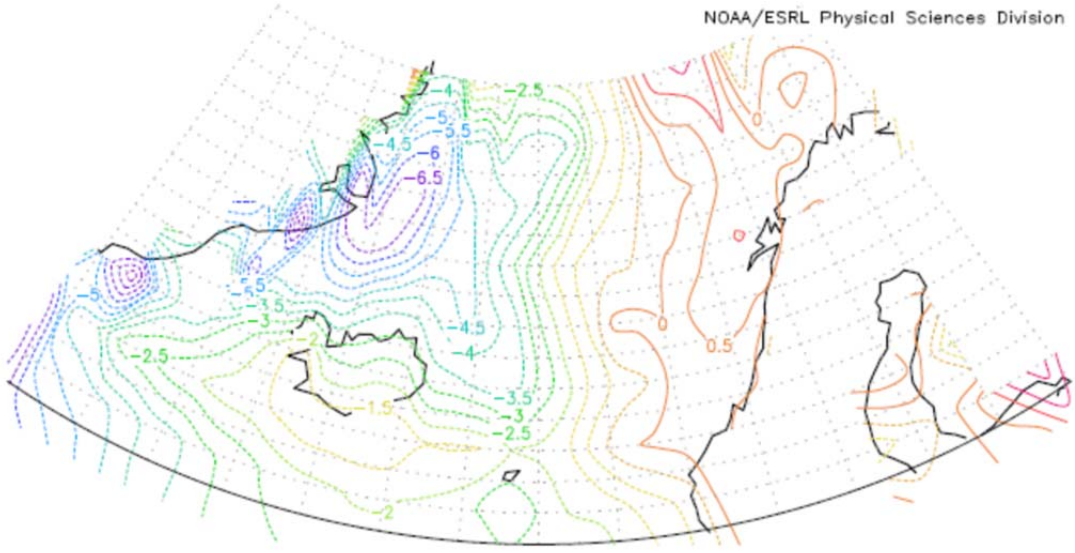

Figure 4.4. Long-term (1981-2010) zonal mean-subtracted sea-surface temperatures (°C). Data obtained from the Physical Sciences Division, Earth System Research Laboratory, NOAA, Boulder, Colorado, http://www.esrl.noaa.gov/psd/.

At Storglaciären, the situation is very different: the sea surface temperatures are relatively warm for this latitude (Figure 4.4) and thermal gradients along the coast are muted. Chen and Hellström (1999) also report that thermal contrasts between easterly-continental and maritime-westerly airflow are at their minimum during the summer months. The greater number of types recognized at Vestari Hagafellsjökull is also plausible, considering that the period of analysis spans a greater time interval (June-August, rather than July-August at Storglaciären). Thus, seasonal effects, such as the warming of the ocean surrounding Iceland from June to August are more likely to contribute to variability in the weather experienced at Vestari Hagafellsjökull; the seasonal cycle can be expected to be minimal during the two month period of observations for Storglaciären. Furthermore, Iceland is situated in an area associated with frequent cyclogenesis (Wang and Rogers, 2001; Hanna et al., 2004), and the weather experienced in Iceland is sensitive to changes in their resulting paths (Einarsson, 1984); subtle changes in storm tracks and intensity will therefore propagate to variability in the prevailing weather, and may be a contributing factor to the greater number of types identified at Vestari Hagafellsjökull.

If consideration is only given to those clusters consisting of five or more days (e.g. Huth et al., 1993), then there are 17 and 25 types for Storglaciären and Vestari Hagafellsjökull, respectively. Although the location-specific nature of the classified meteorological data precludes a rigorous comparison of the number of categories identified within the literature, the results obtained here are in general agreement with other multi-year studies, falling squarely within the range of the number of circulation types found by other authors within Europe (4-40: Huth et al., 2008). More specifically, although no ready comparison is available for Langjökull, the number of categories found for Storglaciären is in close agreement with the findings of a TSI procedure employed by Fealy (2004): during the summer months, he identified a total of 21 types at a site in northern Norway which is in close proximity to Storglaciären (~2°N further north and ~2° further east).

4.5.1. Weather categories

A discussion of all the types identified is beyond the scope of this chapter, but it is considered useful to address some of their features briefly—particularly the characteristics of categories which fall either end of the spectrum, in being especially rare or persistent. To this end, tables 4.3 and 4.4 provide the means of the reanalysis meteorology and the partitioning of days among categories; figures 4.5 and 4.6 illustrate parameters describing the statistical distribution of their meteorological variables. These data show that at Vestari Hagafellsjökull, the largest five categories represent ~50% days and the largest ten hold ~70% of days; more than 90% of days are held by the largest 17 weather types. Examination of the smallest weather categories indicates, unsurprisingly, that these are characterised by extremes. For example, of the six smallest categories (smallest fifth: types 2, 6, 13, 30, 28 and 29), three are associated with the highest wind speeds (categories 2, 29 and 30). These categories probably reflect the passage of cyclones associated with the Icelandic low, as airflow has a positive easterly component (-ve U) in each of these types. Category 2, however, is appreciably cooler than types 29 and 30, which is consistent with its northerly component of airflow (-ve V). Table 4.3 also suggests that this weather type is probably a more extreme manifestation of Weather Category 3. Of the remaining categories, which represent the smallest 20% by group size, Category 6 is typified by very low air pressure, and types 13 and 28 are rather warm, although their mean air temperatures are not exceptional (Table 4.3; Figure 4.5).

The most frequently occurring weather types at Vestari Hagafellsjökull are categories 10 and 12, which account for more than 20% of days between them (~10 and ~11%, respectively). Category 10 is characterised by airflow from the southwest, and this produces conditions that are relatively humid, signalled by the fact that dewpoints are significantly above the overall mean, despite the slightly cooler than average air temperatures which are observed (Figure 4.5). Cloud cover is also high during this weather type. In general, these conditions are consistent with the ‘south-western’ type described by Einarsson (1984), in which an air mass originating in sub-polar North America is advected over the North Atlantic, and becomes somewhat unstable having crossed the open ocean.

Table 4.3. Summary of weather categories' meteorology at Vestari Hagafellsjökull.

Weather Category	Dewpoint Air Temp (°C)	Air Temp (°C)	U ($m\ s^{-1}$)	V ($m\ s^{-1}$)	Wind Speed ($m\ s^{-1}$)	Air Pressure (hPa)	Total Cloud (fraction)	n
1	7.2	9.0	2.5	4.4	5.6	966	0.90	36
2	3.2	8.1	-3.5	-9.0	9.7	954	0.73	1
3	1.5	6.0	-0.9	-4.7	5.4	970	0.60	32
4	3.9	8.9	0.4	-1.4	2.9	982	0.41	57
5	12.1	15.5	-0.4	-0.7	2.1	983	0.48	21
6	5.3	7.9	-0.8	0.5	4.1	939	0.70	2
7	8.8	11.1	-1.7	1.1	2.8	971	0.91	89
8	8.7	10.5	0.8	3.0	3.7	972	0.93	64
9	5.3	9.1	0.8	1.5	2.6	980	0.56	24
10	6.6	9.7	0.4	0.7	2.4	981	0.85	99
11	9.8	12.8	1.1	-1.2	2.1	974	0.59	9
12	7.3	11.4	-0.5	-0.7	2.1	975	0.48	92
13	7.9	12.7	-2.5	-1.7	3.3	957	0.55	4
14	6.3	10.7	-3.0	-4.8	6.0	958	0.68	8
15	4.5	9.0	-1.3	-2.1	3.1	974	0.56	54
16	6.3	9.8	-1.1	-0.9	2.7	967	0.76	70
17	9.1	12.9	-0.6	0.9	2.0	982	0.36	14
18	4.7	7.9	1.5	-0.2	2.3	973	0.79	24
19	3.3	7.7	-3.5	-2.4	4.6	969	0.82	12
20	5.7	8.2	-3.1	-1.2	4.3	961	0.93	17
21	8.4	12.1	-5.4	1.6	6.0	959	0.74	6
22	6.8	10.5	-5.0	0.2	5.3	969	0.80	21
23	9.9	12.2	0.5	0.6	2.2	980	0.86	64
24	9.0	10.8	-1.1	-0.1	2.5	960	0.88	22
25	7.1	9.2	1.2	-2.9	3.8	960	0.89	9
26	5.3	8.3	-2.0	2.3	3.7	975	0.89	34
27	8.3	10.4	-3.5	4.7	6.2	968	0.92	24
28	9.3	13.9	-3.8	0.3	4.4	973	0.52	6
29	7.9	9.7	-7.9	3.3	9.5	953	0.98	1
30	6.5	9.1	-4.8	5.1	7.3	984	0.98	4

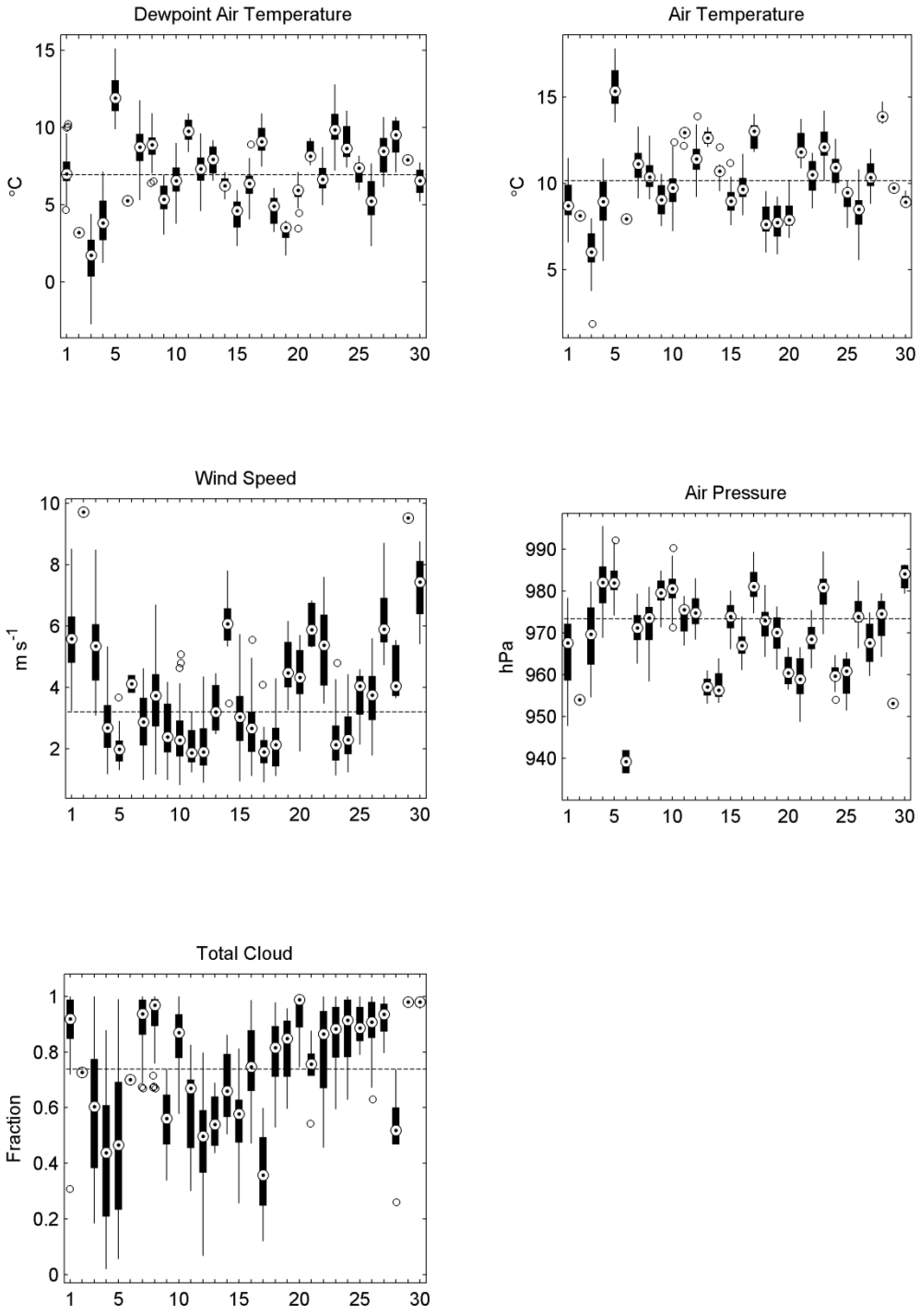

Figure 4.5. Box and whisker plot of categories' reanalysis meteorology at Vestari Hagafellsjökull. Boxes denote the upper and lower quartiles, circles with dark centres show the median, and hollow circles give the outliers. The whiskers extend to the most extreme value which is not considered an outlier, and the dotted, horizontal line gives the overall mean. Note that outliers are identified as such if they are more than 1.5 times the interquartile range above (below) the 75th (25th) percentile of the meteorological variable being plotted. The choice of 1.5 means that, if the data are normally distributed, the whiskers will bound ~99.3% of the data. Figure 4.6 adopts the same conventions.

By contrast, Category 12 results in more favourable conditions prevailing. The air temperature during this type is appreciably above average, and cloud cover is suppressed. These conditions result from north-easterly flow and, according to Einarsson (1984), often occur when the Greenland High is particularly well developed.

At Storglaciären, the partitioning of days is similar, with the largest five categories accounting for ~54%, and the largest 10 types holding ~80% of all days. There are no categories consisting of a solitary day at this location, but 7 have a group size less than ten days (Table 4.4). Of these, four are typified by cold anomalies (categories 1, 10, 18 and 20), which generally result from north-westerly flow—the exception being Category 20 in which the wind blows from the south east.

Table 4.4. Summary of weather categories' meteorology at Storglaciären.

Weather Category	Dewpoint Air Temp (°C)	Air Temp (°C)	U ($m\ s^{-1}$)	V ($m\ s^{-1}$)	Wind Speed ($m\ s^{-1}$)	Air Pressure (hPa)	Total Cloud (fraction)	n
1	1.5	5.8	2.1	-1.5	2.8	933	0.55	4
2	3.4	9.6	-0.3	-0.7	2.0	929	0.39	15
3	8.3	13.8	-0.2	1.0	1.8	925	0.38	30
4	10.2	13.3	0.3	0.8	2.0	926	0.74	65
5	8.1	10.8	2.0	-1.9	3.1	921	0.91	13
6	5.8	10.0	2.2	-0.8	2.9	928	0.72	48
7	7.6	11.1	-1.7	2.1	3.1	929	0.79	32
8	10.3	12.7	-1.2	3.0	3.6	921	0.85	33
9	7.8	10.3	-1.8	0.8	2.5	918	0.86	46
10	0.9	3.4	1.1	-1.1	1.8	916	0.93	5
11	5.0	8.0	1.5	-0.7	2.4	918	0.85	46
12	11.2	14.3	-3.4	0.6	3.7	921	0.79	10
13	6.2	8.9	3.7	1.5	4.5	923	0.93	11
14	13.5	17.6	-1.1	2.0	2.5	924	0.44	3
15	9.6	16.6	-0.5	0.3	1.6	934	0.29	19
16	5.0	11.6	0.7	-1.4	1.9	918	0.26	5
17	3.0	7.1	-1.4	1.6	2.5	923	0.62	22
18	3.0	6.3	5.1	-2.4	5.8	927	0.95	4
19	9.4	10.6	1.6	-0.4	2.5	909	0.95	5
20	6.1	9.0	-0.2	3.6	4.2	910	0.81	3
21	8.9	13.6	2.1	-0.7	2.6	935	0.78	15

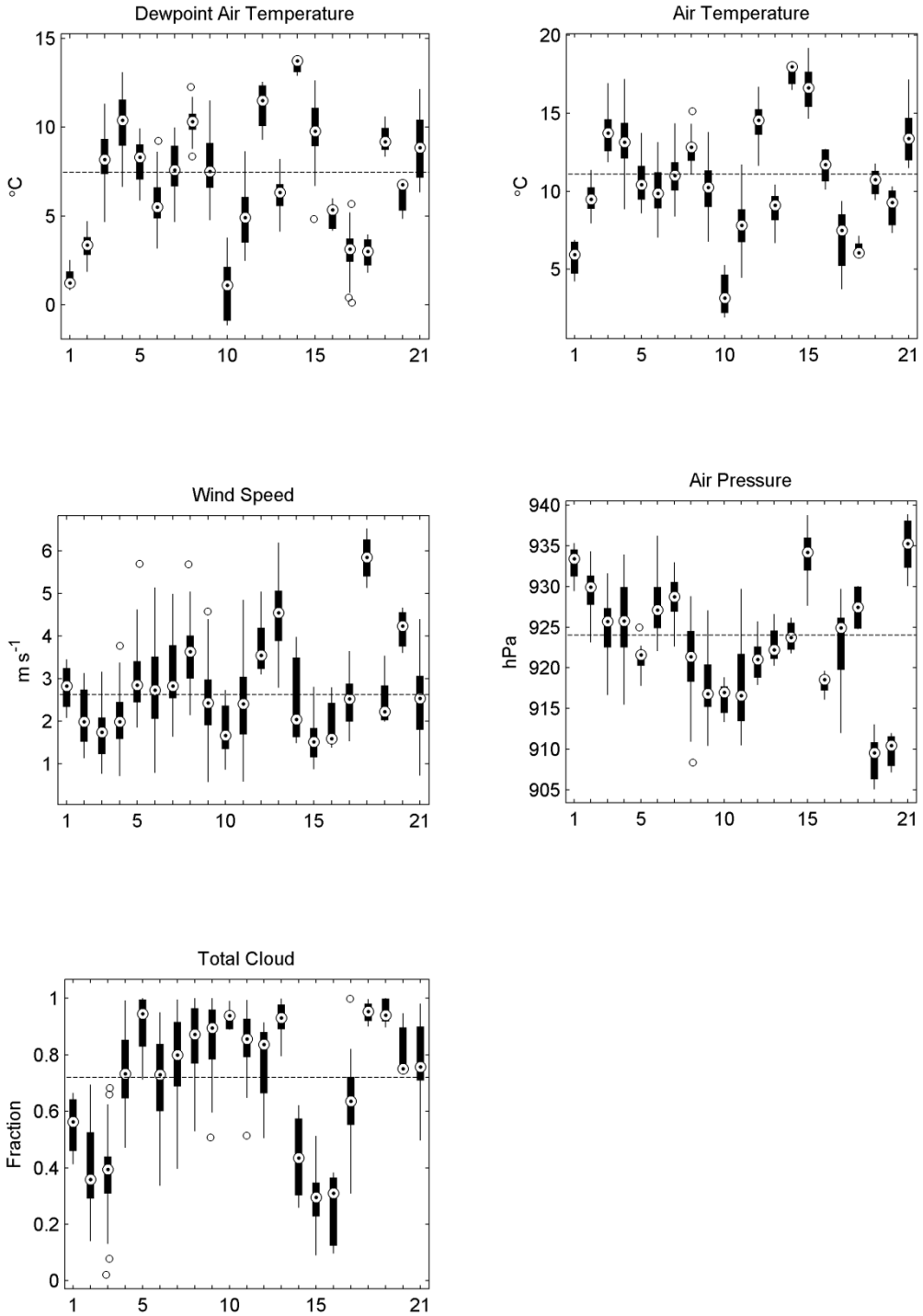

Figure 4.6. Same as Figure 4.5, but for Storglaciären.

Of the remaining small groups (holding <10 days), Category 14 is especially warm and is associated with south easterly winds prevailing. Categories 16 and 19 have negative air-pressure anomalies; Category 16 is also somewhat distinct in the very low cloud amounts observed (Table 4.4; Figure 4.6). The most frequent weather types at Storglaciären are categories 4 and 6, which account for ~26% of all days (~15 and ~11%, respectively). The contrast between these types comes mainly from the difference in air temperature (>3°C higher in Category 4). The warmer conditions of this type are consistent with the southerly component of airflow observed; during Category 6, the wind blows from the north-west. In other aspects, these types are fairly similar, recording positive anomalies of air pressure and both wind speeds and cloud cover that are approximately equal to the overall mean.

4.6. Synthesis and Conclusions

The aim of the present chapter was to introduce the synoptic dimension of the thesis. This was achieved by outlining the contributions made by previous workers in fields relevant to the objectives of this research. Furthermore, this information was integrated to construct a suitable framework for subsequent analyses. In particular, a synoptic climatological classification was considered to be appropriate, due to the holistic benefits of these techniques, which, it was argued, are desirable for examining the complexities of meteorological processes within the glacier boundary layer. More specifically, a weather- rather than a circulation-based classification scheme was favoured for use in this study, due to the way in which these methods explicitly address the daily evolution and synergy of multiple meteorological elements. Such attributes are considered as especially important for determining the effect of synoptic-scale processes on glacier micrometeorological variability (Chapter 5) and ablation (Chapters 6 and 7).

To implement the weather classification, the TSI procedure of Kalkstein and Corrigan (1986) was followed, which led to 30 and 21 weather categories being identified for Vestari Hagafellsjökull and Storglaciären, respectively. Whilst the subjectivity of this approach is acknowledged, the number of groups identified is physically realistic, and consistent with the most readily comparable studies. A comparison of weather types between locations showed that categories are generally more distinct at Vestari Hagafellsjökull. It was suggested that this is probably due to the steep thermal

gradients in sea surface temperatures surrounding Iceland which modifies approaching air. The contrast between cold air masses originating from Greenland with those advected from the south is also likely to contribute to the more pronounced differences between weather types. As an additional reason, it was suggested that the frequent cyclogenesis found in the proximity of Iceland may contribute to enhanced heterogeneity between categories at Vestari Hagafellsjökull. This was supported by the fact that some of the smaller (extreme) types at this location were classified as distinct due to their elevated wind speeds—probably reflecting enhanced cyclonic activity. Further examination of individual weather categories' meteorology yielded results which were physically consistent. The most frequent types at Vestari Hagafellsjökull differed mainly in terms of their air temperatures and cloud cover, with north-easterly flow responsible for particularly favourable conditions. At Storglaciären, differences between the most frequent types were principally restricted to air temperatures, with warmer weather being associated with air of southerly origin. These weather categories will be used in conjunction with the boundary layer meteorological and heat balance data of Chapters 2 and 3 of this thesis to evaluate synoptic aspects of glacier-climate interactions further.

5. A Synoptic Investigation into Lapse-Rate Variability at Vestari Hagafellsjökull

5.1. Introduction

Air temperature is required as a driving variable in nearly all snow and glacier melt models, yet must be frequently: i) extrapolated/interpolated from point observations; or ii) downscaled from gridded climate data, before melt may be simulated at the location(s) of interest (Hodgkins et al., 2012b; Gardner and Sharp, 2009). A strong attraction of empirical, temperature-based methods of simulating melt is the relative ease with which this can be achieved (Hock, 2003), due to the fact that horizontal changes in air temperature are usually gradual (Marshall et al., 2007; Barry and Chorley, 2009). Vertical change in temperature (the lapse rate) is comparatively steep, however, and recent research has emphasised the need to constrain variability of vertical temperature gradients over melting snow and ice surfaces to improve melt simulations (e.g. Konya et al., 2007).

In this study, the lapse rate (Γ) is defined:

$$\Gamma = \frac{dT}{dZ} = \frac{(T_1 - T_2)}{(Z_1 - Z_2)}\ , \qquad 5.1$$

where T is air temperature and Z is elevation; the subscripted integers refer to ranked elevations (higher subscript indicating higher elevation). A positive lapse rate therefore indicates an increase in air temperature with increasing elevation. This terminology is consistent with that generally used in the glaciological literature (e.g. Braun and Hock, 2004; Hanna et al., 2005; Marshall et al., 2007; Petersen and Pellicciotti, 2011). The terms ‘steep’ and ‘shallow’ are then applied after Pepin and Losleben (2002) and Petersen and Pellicciotti (2011), to describe large and small

decreases of air temperature with height, respectively. This terminology is the same as was introduced briefly in Chapter 4 (Section 4.2.1).

Constant lapse rates are commonly employed in glaciological melt studies, and often, lapse rates in close proximity to the ELR (~-6 to -7°C km^{-1}) are applied (e.g. Oerlemans and Hoogendoorn, 1989; Flowers and Clarke, 2002; Arnold et al., 2006; Machguth et al., 2006; Raper and Braithwaite, 2006; de Woul et al., 2006; Paul et al., 2009; Paul and Kotlarski, 2010). However, research has suggested that the use of the ELR over glaciers during the ablation season is inappropriate, as lapse rates have frequently been observed to be somewhat shallower than this (Greuell et al., 1997; Hock and Noetzli, 1997; Steffen and Box, 2001; Marshall et al., 2007; Gardner et al., 2009; Hodgkins et al., 2012b).

Greuell and Böhm (1998) addressed the physical processes controlling lapse rates and emphasised the role of sensible heat exchange with the glacier: air flowing down-slope is cooled diabatically through contact with the surface, which remains limited to a maximum temperature of 0°C. The resulting lapse rate is then a balance between adiabatic warming of descending air, and the cooling resulting from sensible heat transfer with the underlying ice or snow surface. This led the authors to suggest that glacier slope angle was critical in determining the spatial distribution of lapse rates; temporal variability was attributed to the rate of sensible heat exchange, which would be enhanced as air temperatures increased. That is, because the glacier surface cannot warm above the melting point, higher air temperatures simply amplify the heat flux from the atmosphere to the glacier, resulting in an enhanced cooling effect on the overlying air.

With these processes in mind, recent research has focused on developing practical, empirical adaptations to parameterize temperature over melting glaciers. Arguably the most attractive of these to date, is the method proposed by Gardner et al. (2009) and subsequently applied by Hodgkins et al. (2012a, b). This technique uses simple linear regression of free-atmosphere (reanalysis) air temperatures to account for the shallowing of lapse rates that occurs when the temperature deficit of the glacier boundary layer is enhanced (Shea and Moore, 2010). Despite the fact that the reanalysis data do not resolve the glacier boundary layer explicitly, both Gardner et al. (2009) and Hodgkins et al. (2012a) demonstrated the skill of the regression model

relative to application of the ELR: errors in temperatures extrapolated from a solitary AWS were reduced considerably using the regression approach.

Whilst the approach outlined by Gardner et al. (2009) holds considerable promise, due to its simplicity and minimal requirements for data recorded in situ, there is reason to believe that further treatment of lapse rates may be warranted. This understanding is motivated by the fact that near-surface lapse rates are not just affected by sensible heat exchange with the glacier; yet it is only this mechanism which is directly considered when free-air temperature is taken as a solitary predictor in regression approaches. That is, free-atmosphere lapse-rate variability is controlled by diabatic processes of phase transition (Stull, 2000), and locally, particularly in mountainous terrain, by additional processes of turbulent and radiative energy exchange with the Earth's surface (Barry, 2008). These factors are not associated with air temperature in a simple way. Thus, if their effects propagate to the glacier boundary layer, regression using only this parameter will be unlikely to describe lapse-rate variability sufficiently. As an illustration of this, Hodgkins et al. (2012b) found that, although air temperature provided a good indicator of low frequency lapse-rate variability at Vestari Hagafellsjökull, its correlation with daily variability was limited.

The need to address high-frequency lapse-rate variability further has been highlighted by numerous researchers, who have demonstrated that neglecting short-term change can lead to substantial errors in both empirical and physically-based energy balance models. For example, Braun and Hock (2004) warned against the application of time-averaged values on King George ice cap, Antarctica, as shallow lapse rates were associated with warm air advection. Substantial and systematic underestimation of melt at higher elevations would therefore result if the lapse rate were not adjusted accordingly. Similarly, Petersen and Pellicciotti (2011) showed that considering sub-daily lapse-rate variability reduced calculated melt at Juncal Norte Glacier, Chile, due to steeper lapse rates persisting during the afternoon, when temperatures were higher. The causative factor to which this association was attributed, was the valley wind: its peak velocity coincided with the diurnal thermal maxima; this thermally driven circulation then eroded the katabatic wind, which in turn, reduced the downslope cooling described by Greuell and Böhm (1998).

5.2. Aims

It is therefore apparent that further examination into lapse-rate variability is justified, and this is pursued in the present chapter. Specifically, it is suggested that a synoptic approach is particularly suited to examining glacier lapse rates. This reasoning is motivated by the fact that synoptic investigations have previously proven their worth for examining lapse-rate variability in mountainous terrain (Pepin, 2001; Pepin and Kidd, 2006; Blandford et al., 2008; Choi et al., 2011), and initial investigations suggest that similar approaches may also be useful in glacierized regions (Marshall et al., 2007).

The chapter's aim, therefore, is to make a contribution in this regard by exploring synoptic controls on glacier lapse-rate variability. This is approached from two directions. Firstly, indicators of synoptic-scale atmospheric variability are used to probe linear relationships between meteorological variables and the lapse rate. Such an approach facilitates causal mechanisms affecting the lapse rate to be investigated, and has been used previously to explore lapse-rate variability (Pepin et al., 1999; Pepin, 2001). The second technique pursued in this chapter adopts the synoptic weather types from Chapter 4 to examine lapse rates. This brings a holistic dimension to the analyses, which is considered to be highly suitable for this application. Glacier lapse rates are a complex function of the large scale flow and its interaction with the underlying terrain; the reductionism offered by classifications, and the increased physical interpretability which this promotes, is therefore particularly appealing.

In addition to a general exploration of lapse-rate variability, an effort is made in this chapter to quantitatively constrain lapse rates. This is pursued in the form of: i) a linear model which utilizes synoptic meteorological variability; and ii) an analogue model that uses the synoptic weather categories to forecast lapse-rate variability. The data and methods used to pursue these approaches are detailed in Section 5.3; results of analyses are presented in Section 5.4 and discussed in Section 5.5, before conclusions are drawn in Section 5.6.

5.3. Data and Methods

5.3.1. Data sources

The first source of data used in this study is the temperature data recorded at the two long-running AWSs (A500 and A1100) on Vestari Hagafellsjökull (details of which were provided in Chapter 2). Data are used from JJA each year. This period is chosen because it represents the bulk of the ablation season, and during a previous study at this location by Hodgkins et al. (2012b), these months were characterised by the shallowest lapse rates (most different from the ELR). Hence, this interval provides a good test for further investigation into ablation season controls on the lapse rate. In addition, limiting the analysis to these months is a choice motivated by consistency, as complete temperature records from September are absent in 4 of the 10 years studied.

It should be noted that the lapse rates defined in this study (which are calculated from the two AWSs according to Equation 5.1) are not necessarily considered to be representative of those over Vestari Hagafellsjökull as a whole. Indeed, it is not even presumed that the temperature is a linear function of elevation. It is only the temporal variability of the lapse rate which is of interest in this study and differencing the air temperatures observed at the two AWS, separated vertically by 600 m, is a suitable means to assess this (cf. Hodgkins et al., 2012b).

To determine lapse rates, temperature data are aggregated to daily means. This resolution is chosen as a compromise that mitigates against short-term sensor errors due to processes such as solar heating (e.g. Georges and Kaser, 2002), whilst retaining the high-frequency variability that is anticipated to be the result of changes in the prevailing meteorology. The error (δ) of the calculated lapse rates is estimated following Hulth et al. (2010):

$$\delta\Gamma = \frac{1}{dz}\sqrt{{\delta T_{500}}^2 + {\delta T_{1100}}^2}\ , \qquad 5.2$$

in which dz is the change in elevation between the AWSs and δT_{500} and δT_{1100} are the respective sensor accuracies (± 0.3°C at 0°C). This yields an estimated lapse-rate accuracy of 0.07°C 100 m^{-1}.

The second source of data utilized in this chapter is the ERA-Interim reanalysis data described in Chapter 4: 2 m air temperature, 2 m dewpoint temperature, 10 m easterly component of wind speed (U), 10 m northerly component of wind speed (V), total cloud cover, and surface air pressure. These data, in addition to forming the basis of weather-category memberships (Chapter 4), are considered as suitable to extend to the correlation and regression analyses in this chapter because they represent a summary of the thermodynamic state of the atmosphere, and thus may be anticipated to provide information on lapse-rate variability. Furthermore, this suite of variables includes most of those which have previously been found to correlate with lapse rates (e.g. Pepin et al., 1999; Pepin, 2001; Gardner et al., 2009). The AWS data are only used to determine lapse rates themselves in this study; all meteorological information used to explore their variability is derived from the regional, reanalysis data.

5.3.2. Correlation and regression analyses

To elucidate the role of specific components of the regional climate data, the strength and direction of the linear association between daily lapse rates and each of the reanalysis variables is assessed. This is achieved though the calculation of zero- and higher-order (i.e. partial) Pearson's product-moment correlation coefficients: the zero-order correlations are retained for comparison with previous research conducted at Vestari Hagafellsjökull (Hodgkins et al., 2012a, b), and elsewhere (Pepin et al., 1999; Pepin, 2001; Gardner et al., 2009), whilst the higher-order coefficients enable spurious correlations to be detected and help to probe the causal links between the regional climatology and the lapse rate (Healey, 1993).

To assess the possibility of forecasting lapse rates through regression objectively, a bi-directional, step-wise approach is followed. This involves the successive addition of reanalysis variables to a regression model, based on each variable's p value: those with the smallest p values are added at each iteration; variables already in the model are removed if the probability of a non-zero regression coefficient falls below a pre-determined threshold. In this study, a p value of 0.05 is required to enter the model, and terms are removed if the probability of a non-zero coefficient (i.e. $1 - p$) falls below 90% (0.9). This stepwise procedure is completed multiple times in a cross-validation routine (described below), which helps mitigate against over-fitting and provides a realistic estimate of forecast skill.

Prior to regression modelling, all of the reanalysis variables (X_i) are transformed to z scores, according to:

$$\boldsymbol{Z_i = \frac{X_i - \overline{X_i}}{\sigma_i}}\ , \qquad 5.3$$

where the overbar denotes the mean and σ is the standard deviation—both of which are calculated for the period of study (JJA, 2001-2010). Standardizing the scores in this way enables the relative sensitivity of the lapse rate to the different reanalysis variables to be readily determined from the regression analysis.

5.3.3. Synoptic types and lapse rates

The effects of different synoptic types on the lapse rate are explored by utilizing the weather categories presented in Chapter 4. As a first step to ascertain whether synoptic type affects the glacier lapse rate, one-way analysis of variance (ANOVA) is applied to the daily lapse rate data, stratified by weather category. This tests the null hypothesis that the mean lapse rate is equal in all weather categories by comparing the ratio of within-group, to between-group variation. Rejection of the null hypothesis is evidence that the difference in lapse rates between groups is greater than would occur due to sampling error alone and indicates that synoptic type affects the lapse rate (McKillup, 2005). As a second step, a one-sample Student's t-test is performed on each of the weather categories to determine the statistical significance of divergence from the ELR. This test is useful for establishing during which synoptic conditions the assumption of the ELR breaks down, and should therefore not be applied. To facilitate these statistical analyses, very small weather categories are omitted from the procedure. Following Huth et al. (1993), these are defined as groups consisting of less than 5 days. Based on this rule, 25 of the 30 categories are entered into the ANOVA and t-tests, representing >98% of all days classified.

To investigate the effect of synoptic type on the lapse rate further, all 30 weather categories are ranked by the observed lapse rate and divided into quintiles. The top and bottom quintiles (i.e. the weather categories with the shallowest and steepest lapse rates) are then retained for further analyses. For these weather categories, the wider-scale synoptic circulation is examined. This is performed to contextualise the weather categories' meteorology, and it also facilitates comparison with previous

investigations that have examined the association between synoptic circulation and lapse rates (e.g. Braun and Hock, 2004; Marshall et al., 2007). Specifically, the quintiles are chosen for analyses because these represent conditions which exhibit the greatest departures from the mean. Hence, by investigating these weather types in detail, more information may be extracted regarding the processes driving lapse-rate variability.

To explore the merits of using synoptic type to predict the lapse rate quantitatively, an analogue model is developed. This simply prescribes the lapse rate on day i as a function of weather category (WC) occurrence, and the mean lapse rate within that category:

$$\Gamma_i = \bar{\Gamma}(WC_j) \ , \qquad 5.4$$

where j (1...30) indicates weather-category membership of day i. The main benefit of this approach is that the net effect of the prevailing meteorology on the lapse rate is considered implicitly. This method makes no assumptions regarding the linearity of the lapse rate response to synoptic forcing. The caveat, however, is that lapse rates are not modelled as a continuous function, and considerable intra-group lapse-rate variability can be expected to remain (e.g. Kalkstein and Corrigan, 1986).

5.3.4. Cross-validation procedure

To establish the relative benefits of parameterizing lapse rates though regression or by synoptic type, a cross-validation procedure is applied. This is a widely-used technique in the atmospheric sciences (e.g. Elsner and Schertmann, 1994; Michaelson, 1987; Hofer et al., 2010; Blandford et al., 2008; Marzeion et al., 2012; Marzeion and Nesje, 2012). The general procedure in cross validation is to estimate model parameters using a sub-section of the data, and then to use these estimates for hindcasting the remainder of the series being simulated. By repeatedly calibrating the model on different subsections of data, an insight into the stability of the fitted parameters is obtained. In addition, because the hindcasted series is modelled using coefficients which are derived from independent sub-sections of data, a realistic estimate of model skill is provided (Elsner and Schertmann, 1994).

In the present study, cross validation is implemented by successively leaving out each of the 10 years of lapse-rate data, and calibrating model parameters (regression coefficients and mean lapse rates for each weather category) from the remaining 9 years' data. These parameters are used to hindcast daily lapse rates in the year that was left out of the parameter calibration stage. Calibration is therefore performed 10 times, resulting in an ensemble of model parameters and a 10-year, hindcasted record of daily lapse rates; validation is completed by comparing the simulated and observed lapse rate series for the 10-year period.

To simulate a more realistic forecasting application, special consideration is given to weather categories: it is assumed that for every year, each day's weather-category membership is unknown in advance. This is considered to be consistent with a forecasting scenario, in which weather categories have been identified during a calibration period, and new observations must be joined to these existing groups. To assign days, the PC scores from Chapter 4 (Section 4.5) are utilized; membership is allocated to the weather category which minimizes the vector product:

$$\left[\mathbf{X}_i - \mathbf{X}_j\right]' \left[\mathbf{X}_i - \mathbf{X}_j\right] \ , \qquad 5.5$$

where the vector $\mathbf{X}_i$ contains the PC scores for day i and $\mathbf{X}_j$ is the vector containing the centroids (means of each PC) for each weather category (e.g. Huberty 1994). Allocating days to weather categories in this way, rather than repeating the cluster analysis described in Chapter 4 (Section 4.4), prevents category membership of those days in the calibration period from being changed. This ensures that days in the year being simulated are assigned to a group that has already been identified, and therefore guarantees the availability of calibration data for every day being modelled. It should also be noted that although the frequency of specific weather types may change somewhat from this procedure, their meteorological attributes should remain largely unchanged.

Model performances are evaluated through the Root Mean Square Error (RMSE), given by:

$$\mathrm{RMSE} = \left[\frac{1}{df}\sum\left(\Gamma - \Gamma'\right)^2\right]^{1/2} \ , \qquad 5.6$$

in which Γ' is the modelled lapse rate, and df is the degrees of freedom, given by: n – P – 1, with P is the number of predictors. Pearson's product-moment correlation coefficients are also calculated to determine the agreement between simulated and observed lapse rates.

5.4. Results

5.4.1. Air temperature and lapse rates

Mean temperatures and lapse rates stratified by year are presented in Table 5.1. The mean temperatures for the duration of the study period were 1.7°C and 4.9°C at 1100 m and 500 m, respectively. Average daily temperatures below freezing were rare at 1100 m (~10% of days), but were even more infrequent at 500 m, where less than 1% of days averaged below 0°C. The mean lapse rate for the entire period was -0.53°C 100 m^{-1} (for more details on air temperature variability see Chapter 2, Section 2.5.1). This figure is in agreement with that observed by Hodgkins et al., (2012b) for JJA, 2003-2007, and with the value obtained by Jóhannesson et al. (1995) from tuning a degree-day melt model at Sátujökull, an outlet glacier of nearby Hofsjökull.

Table 5.1. JJA mean air temperatures and lapse rates. Values in brackets are ± one standard deviation. [a]Temperature record at 500 m only extends to the 11th of July in 2010. Note that both air temperatures and lapse rates are calculated using daily mean air temperatures observed at the AWSs.

Year	Mean temperature: 500 m (°C)	Mean temperature: 1100 m (°C)	Γ (°C 100 m^{-1})
2001	4.82 (1.52)	1.52 (1.66)	-0.55 (0.17)
2002	5.40 (1.33)	1.5 (1.18)	-0.64 (0.15)
2003	5.38 (1.15)	2.38 (1.14)	-0.50 (0.12)
2004	5.18 (1.48)	1.91 (1.55)	-0.55 (0.13)
2005	4.80 (1.36)	1.45 (1.78)	-0.56 (0.17)
2006	4.95 (1.05)	1.40 (1.44)	-0.59 (0.13)
2007	4.86 (0.94)	1.70 (1.04)	-0.53 (0.13)
2008	4.37 (1.33)	1.58 (1.45)	-0.46 (0.12)
2009	4.19 (1.28)	1.52 (1.51)	-0.44 (0.13)
[a] 2010	4.36 (0.59)	2.29 (1.08)	-0.39 (0.11)

The persistence of lapse rates shallower than the ELR (~80% of days), is a further suggestion that its use over melting glaciers is inappropriate; the need to temporally constrain its variability is highlighted by the standard deviation, which is beyond that which may be expected from sensor error alone (0.07°C 100 m^{-1}, Equation 5.2).

Averaged across all years, lapse rates remain reasonably stable from month-to-month (JJA averages of 0.51, 0.52 and 0.54 °C 100 m^{-1}, respectively). Interannual lapse-rate variability is considerable, however, and it is interesting to observe that the last three years have seen the shallowest lapse rates on record (Table 5.1); although, this should be interpreted with caution, as much of the temperature data from 500 m are missing during 2010 (see Table 5.1 caption).

5.4.2. Correlation and regression analyses

The results of the zero- and higher-order correlations are provided in Table 5.2. Examination of the zero-order correlations indicates that the strongest association with the lapse rate is found for wind speed, for which a modest, negative correlation is observed, indicating a steepening of the lapse rate (becoming more negative) as wind speed increases. The remaining correlations are somewhat lower, although, most are still highly significant (p <0.01). Of particular note from the other zero-order correlations is the low value of the coefficient obtained for temperature. This is surprising because temperature has previously been acknowledged as a strong control on glacier lapse rates (Greuell and Böhm, 1998; Gardner et al., 2009; Hodgkins et al., 2012a, b). Moreover, Hodgkins et al. (2012a) observed a higher daily correlation with temperature on Vestari Hagafellsjökull (0.56) during the spring period (late April to May). It is emphasised that this discrepancy is not due to the reanalysis data used: Hodgkins et al. (2012a, b) used data from the 750 hPa surface, and in this study, data from the surface (2 m) are employed; for the data in this chapter, correlations with the lapse rate are even lower for temperature from the 750 hPa surface (r = 0.16, p < 0.01, n = 869). Possible reasons for the difference between the results presented here and those given by Hodgkins et al. (2012a) are suggested in Section 5.5.1.

Examination of the partial correlation coefficients further underlines the prominent association between the wind speed and the lapse rate, as the value of the correlation coefficient is largely unchanged. This gives confidence that there is a direct relationship between wind speed and the lapse rate. The largest change between the correlation coefficients and the partial coefficients is observed for temperature and dewpoint temperature, resulting from the strong co-linearity between these variables (r = 0.81).

Results from applying the bi-directional step-wise regression model to the entire data set (i.e. all years, with no cross-validation procedure) suggested a six-term regression model. All terms in this model were highly significant (p <0.01; Table 5.2). The regression weights (α) for these variables are also presented in Table 5.2, which indicate that the lapse rate is most sensitive to the wind speed. Applying this regression model accounts for 38% of lapse rate's variability; however, it is evident that some conditional bias is present, indicated by the over (under) estimation of lapse rates at the lower (upper) end of the observed range (Figure 5.1).

5.4.3. Synoptic types and lapse rates

Lapse rates for each of the weather categories are shown in Figure 5.2. The results of the one-way ANOVA for the 25 main weather categories (F = 14.8, N = 851, df = 23 and 827; critical F value = 1.54 at p = 0.05) indicate that the null hypothesis (that mean lapse rates are equal between weather categories) should be rejected, and therefore suggests that on-glacier lapse rates are affected by synoptic weather type. Examination of the Student's t-test results then showed that only four of the 25 weather categories had mean lapse rates that were not significantly different from the ELR (at p = 0.05); of the twenty-one categories that were different, nineteen had mean lapse rates that were shallower than the ELR.

The wider-scale circulation of the weather types in the shallowest and steepest quintiles (as stratified by lapse rate) was explored by plotting the sea level pressure and height of the 500 hPa surface for the respective categories' centroid days (Figure 5.3). These data show that shallow lapse rates are typically associated with higher air pressure over Iceland. According to Einarsson (1984), such conditions are usually the result of an extension of the Greenland high and produce fair weather over Iceland. This view is supported by the reanalysis meteorological data, as this quintile contains both the warmest (WC 5) and least-cloudy (WC 17) weather types. Indeed, only two categories in this shallow lapse rate quintile would not also be included in the top quintile of air temperatures (WCs 12 and 10), or in the bottom quintile of cloud cover (WCs 23 and 10). It should be noted, however, that whilst Category 13 is both warm and has little cloud cover (5^{th} warmest and 6^{th} lowest cloud cover), its wider-scale circulation is somewhat different, as relatively low air pressure and a closed pattern in the isolines is observed. This circulation is similar to Einarsson's (1984) description

of the 'Eastern' weather type, in which a low sits to the south of Iceland. The favourable conditions outlined by the author for western Iceland during this type are in agreement with those observed in the reanalysis data in the present study.

Table 5.2. Correlation coefficients (r_{xy}), partial correlation coefficients ($r_{xy.z}$), and respective *p*-values quantifying the strength of the linear relationship between each of the reanalysis variables and the lapse rate. Standardised regression coefficients are provided in column labelled 'α'. The absolute value of the *t*-statistic and associated *p* values for the coefficient estimates are given in the last two columns. Dewpoint temperature was omitted from the final model.

	r_{xy}	p_{xy}	$r_{xy.z}$	$p_{xy.z}$	α	|*t*|	*p*(α)
Air Temperature	0.27	0.00	-0.02	0.59	0.023	5.14	0.00
Dewpoint Temperature	0.21	0.00	0.03	0.45	-	-	-
U	0.08	0.02	-0.11	0.00	-0.014	3.19	0.00
V	-0.14	0.00	-0.13	0.00	-0.018	3.83	0.00
Wind Speed	-0.58	0.00	-0.50	0.00	-0.081	17.30	0.00
Air Pressure	0.26	0.00	0.13	0.00	0.018	4.01	0.00
Total Cloud	-0.06	0.08	0.10	0.00	0.018	3.85	0.00

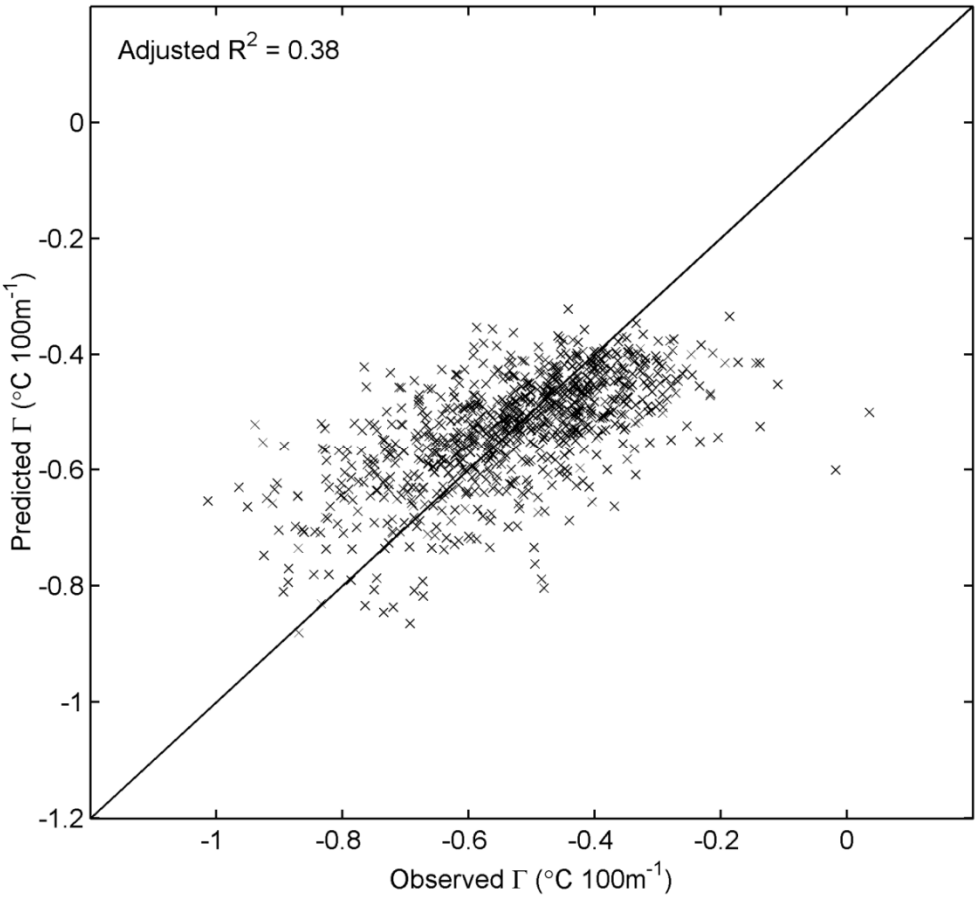

Figure 5.1. Observed lapse rates against those predicted by the stepwise regression model.

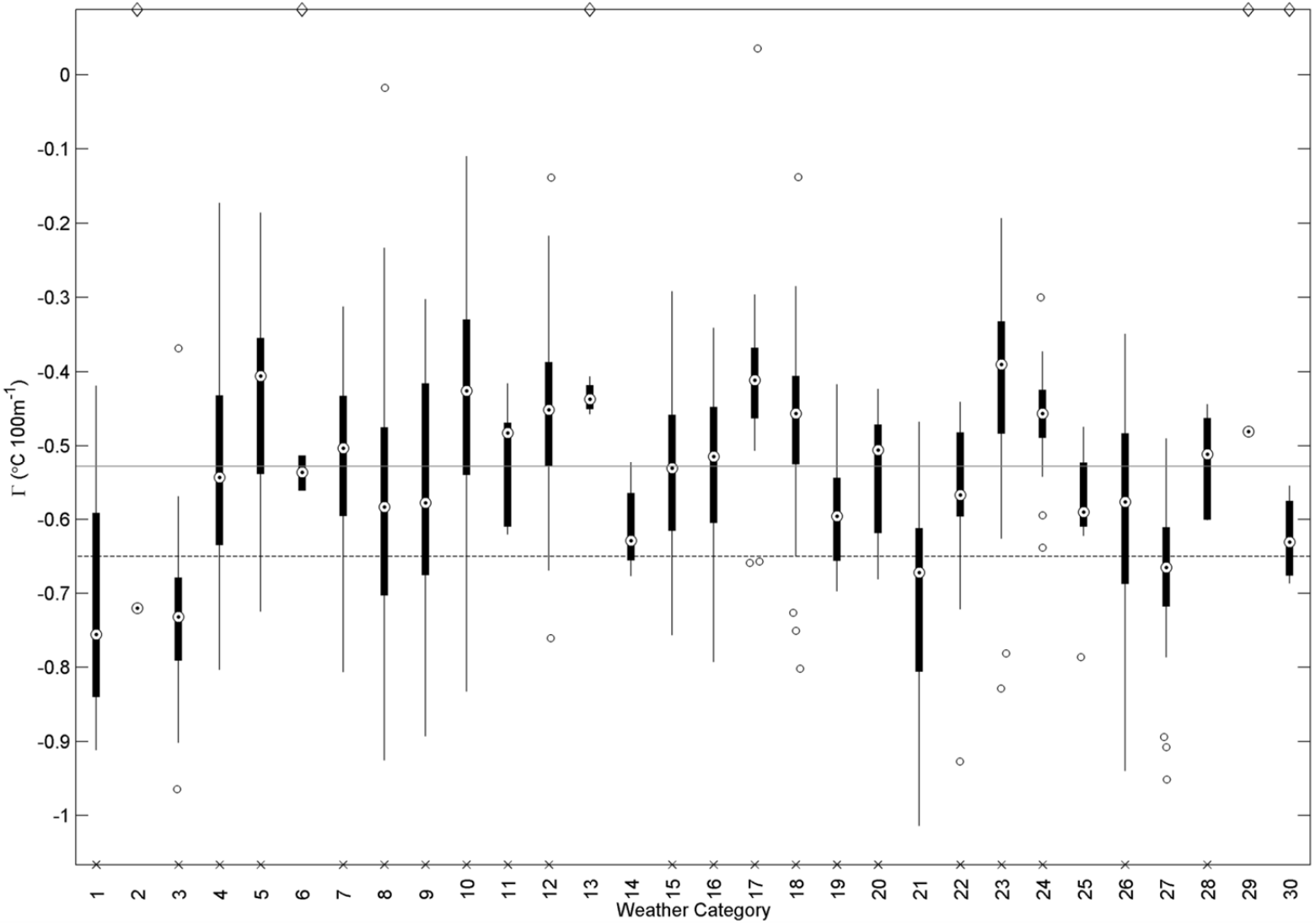

Figure 5.2. Box plots of lapse rates between weather categories. For reference, the solid grey line gives the overall mean lapse rate, and the dotted line shows the ELR. The format of the box and whisker plot is that such that dark boxes mark the middle 50% of the data and the whiskers (lines) reach the limits of the data which are not considered as outliers. The crosses on the x axis indicate those categories which have lapse rates that are statistically different from the ELR; diamonds at the top of the plot show weather categories excluded from the t-tests due to small sample size (n <5). Note that the outliers (hollow circles) are defined in the caption of Figure 4.5 (Chapter 4, Section 4.5.1).

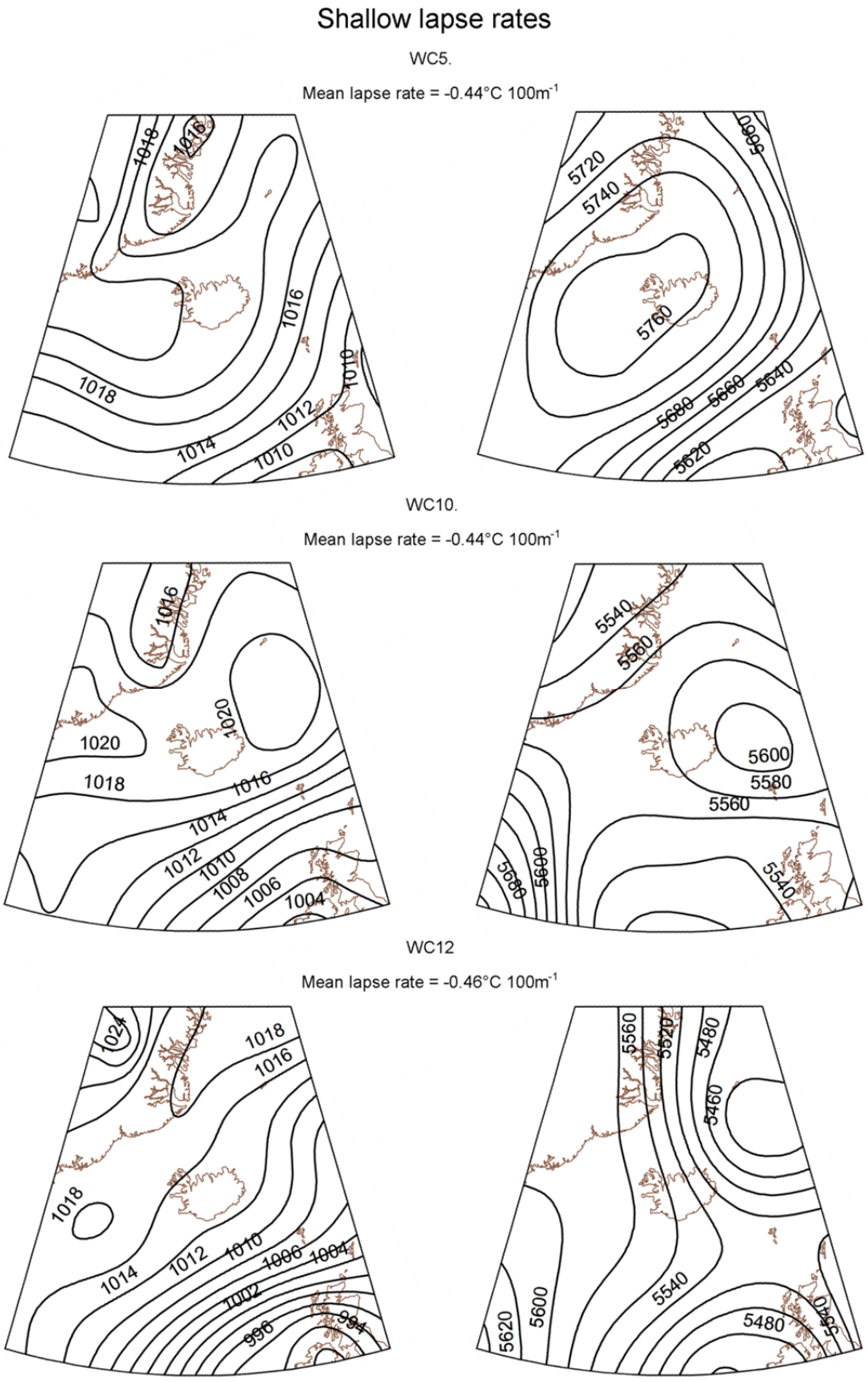

Figure 5.3. Wider-scale synoptic circulation for the centroid days of weather categories comprising the shallowest and steepest lapse rate quintiles. Left-hand side gives the mean sea level pressure, and right-hand side gives the height of the 500 hPa surface in metres. Data were extracted from the ERA Interim data archive (see Chapter 4) at 4 times daily (00:00 06:00, 12:00, 18:00 UTC). Centroid days for each weather category are identified as those days which have PC scores that are closest (minimum Euclidean distance) to the group mean; for these days, the 4 times daily observations are averaged to produce a daily mean before being plotted.

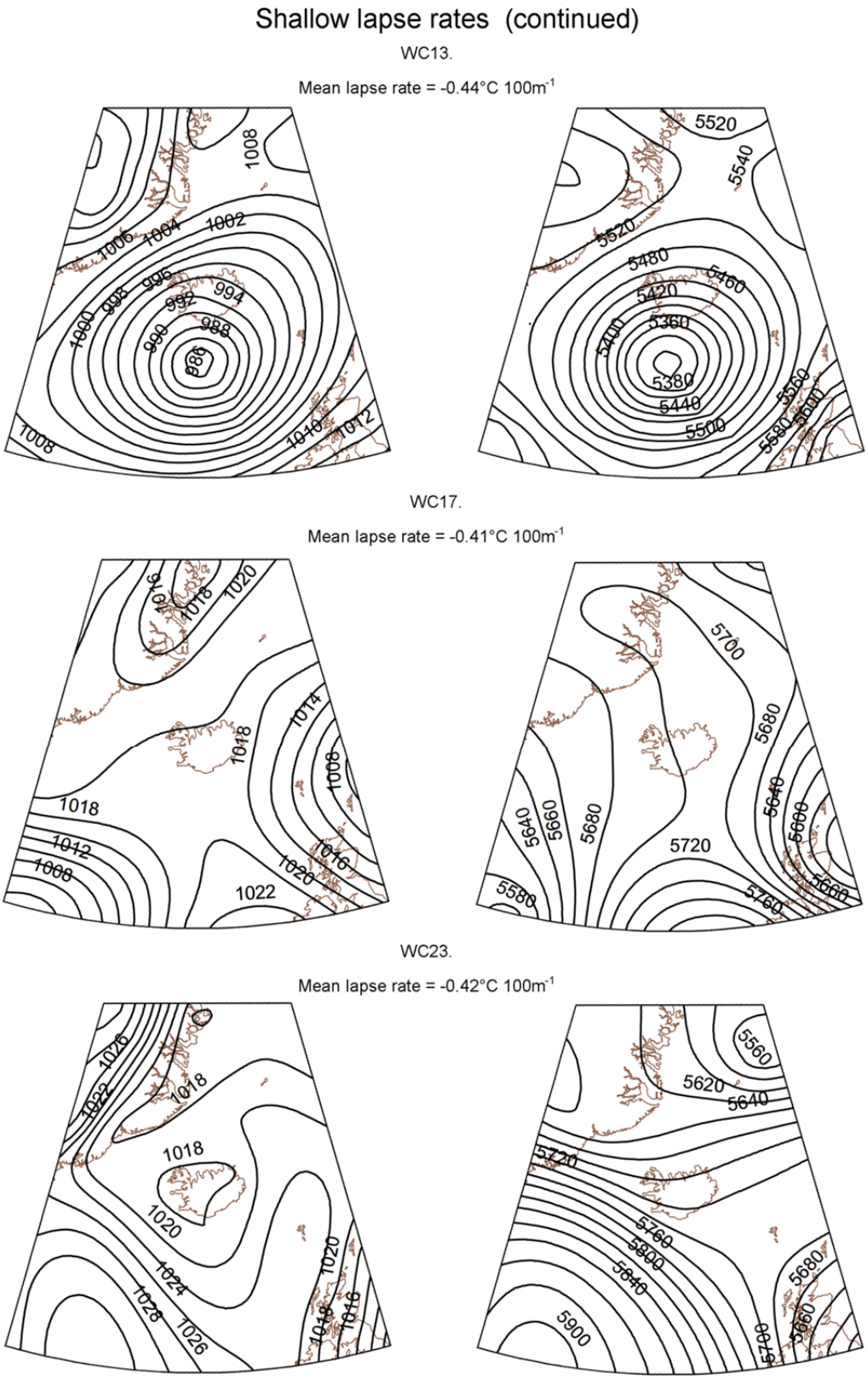

Figure 5.3. (Continued).

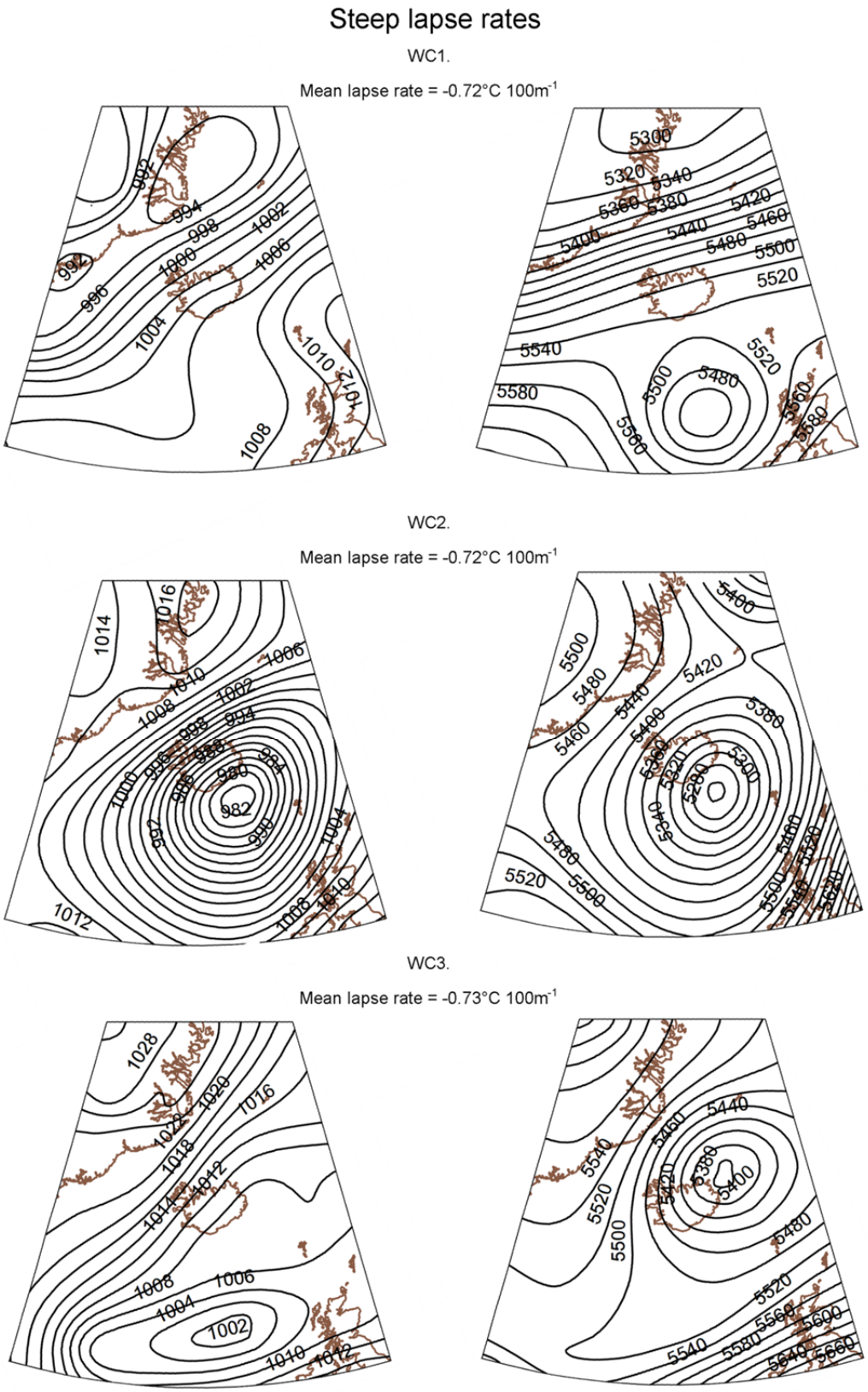

Figure 5.3. (Continued).

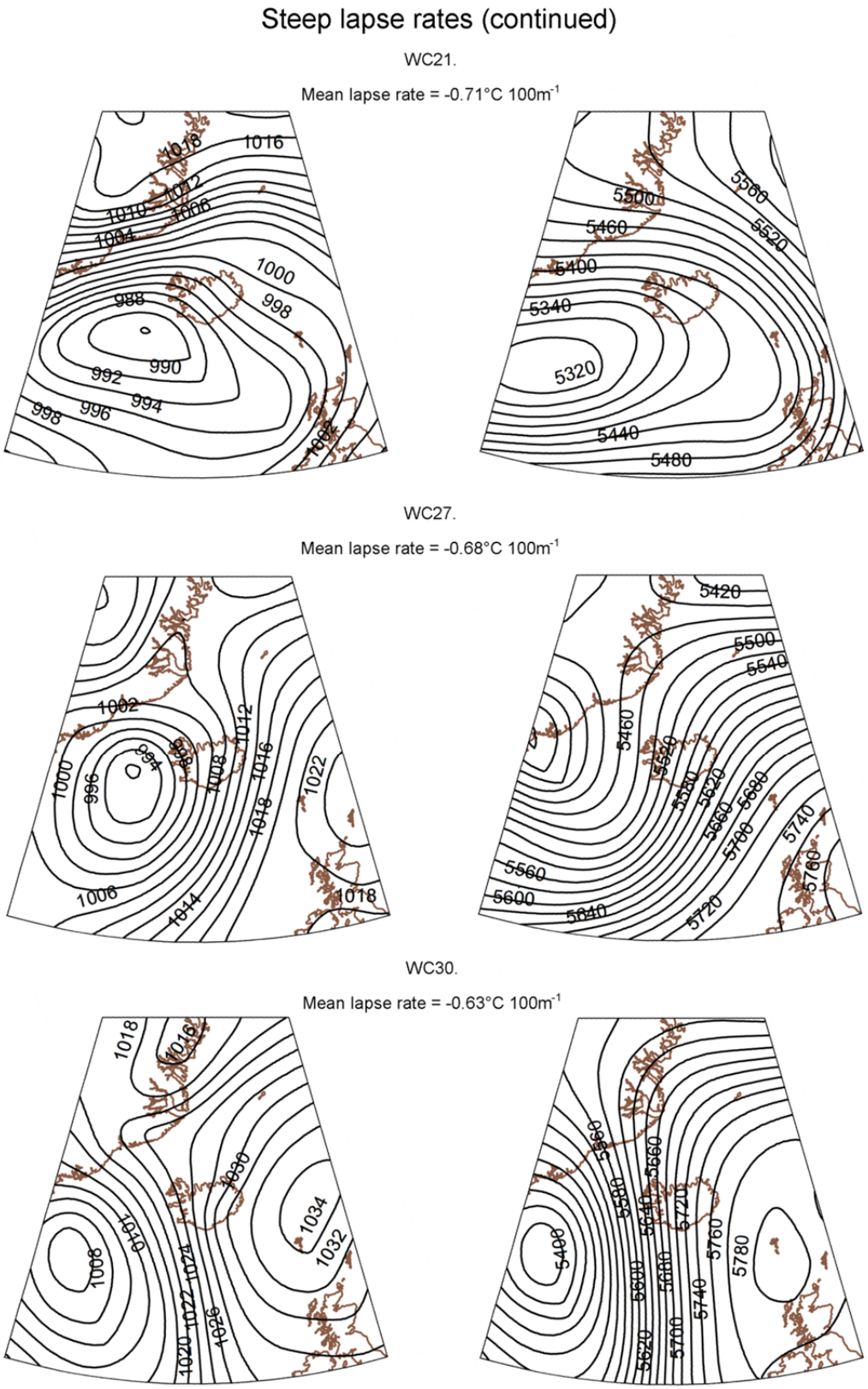

Figure 5.3. (Continued).

Figure 5.3 indicates that steep lapse rates are more commonly associated with low-pressure anomalies and cyclonic curvature. Closer spacing of the isolines is also observed more frequently for the weather categories in this quintile, which will result in faster gradient winds during these types. This is also highlighted in the reanalysis meteorological data, as four of the six windiest weather categories are found in this quintile. These results, in emphasising the role of the wind speed, are in agreement with the correlations presented above (Section 5.4.2). With regards to previous studies, the general tendency for cyclonic and anticyclonic curvature in the steep and shallow quintiles, respectively, is in qualitative agreement with Marshall et al. (2007) who noted similar associations from analysis of lapse-rate variability on the Prince of Wales icefield, Canada. However, these findings contradict those of Braun and Hock (2004), who found that passing low-pressure systems produced shallow lapse rates on King George Island, Antarctica.

5.4.4. Cross validation

The initial choice of parameters chosen in the stepwise regression model (Section 5.4.2) proved to be robust during the cross-validation procedure, as the same six terms reported in Table 5.2 were included in each of the final models. The coefficients for these retained variables were significant for each year (p <0.01) and their values exhibited little variability (Table 5.3), which gives confidence that the initial model had not been over fitted.

Table 5.3. Values for the regression coefficients obtained through the cross-validation procedure. Column 'σ' provides the standard deviation of the coefficient's value. $|\bar{t}|$ is the mean absolute value of the t-statistic, and $\bar{p}$ is the corresponding mean p value. The intercept obtained from the cross validation which completes the regression equation is equivalent to the mean lapse rate (-0.53°C 100 m^{-1}).

Parameter	**Mean**	**σ**	$\|\bar{t}\|$	$\bar{p}$
Temperature	0.023	0.003	4.88	0.00
Dewpoint Temperature	-	-	-	-
U	-0.014	0.003	3.02	0.01
V	-0.018	0.004	3.64	0.01
Wind Speed	-0.081	0.003	16.45	0.00
Air Pressure	0.018	0.003	3.80	0.00
Total Cloud	0.018	0.003	3.65	0.00

When comparing the performance of the synoptic and regression models applied during the cross-validation, it is evident that there is relatively little difference in their ability to simulate the lapse rate, as the average RMSEs are in reasonably close agreement (Table 5.4). The range of each model's ability to capture lapse-rate variability is illustrated further in Figure 5.4, which gives the correlation coefficient between the observed and modelled series on an annual basis. These results are consistent with the RMSEs, in showing that the regression model tracks lapse-rate variability slightly more closely: only in 2003 and 2008 does the weather-category model achieve a lower RMSE, and only in 2008 is the observed correlation higher than for the regression model. For context, it should be noted that both models offer significant improvements over the approach of forecasting lapse rates using temperature as the solitary predictor in a regression equation (cf. Gardner et al., 2009; Hodgkins et al., 2012a, 2012b): simulating lapse rates in the cross-validation procedure with this technique resulted in a mean correlation coefficient of only 0.18; this compares to coefficients of 0.51 and 0.62 achieved by the weather-category and lapse-rate models respectively (i.e. the dotted lines in Figure 5.4). Thus, the results presented here offer a significant improvement in capturing daily lapse-rate variability at this location.

Table 5.4. Annual error metrics for the regression and weather-category lapse-rate models. Note that all units are °C 100 m^{-1}.

	RMSE		**MSE**	
Year	Weather Category	Regression	Weather Category	Regression
2001	0.147	0.143	-0.016	-0.026
2002	0.160	0.157	-0.102	-0.105
2003	0.108	0.101	0.003	-0.015
2004	0.131	0.145	-0.020	-0.021
2005	0.144	0.133	-0.011	0.003
2006	0.114	0.099	-0.055	-0.050
2007	0.118	0.098	-0.013	-0.010
2008	0.143	0.151	0.093	0.088
2009	0.126	0.119	0.080	0.077
2010	0.144	0.146	0.110	0.137
Mean	0.133	0.129	0.007	0.008

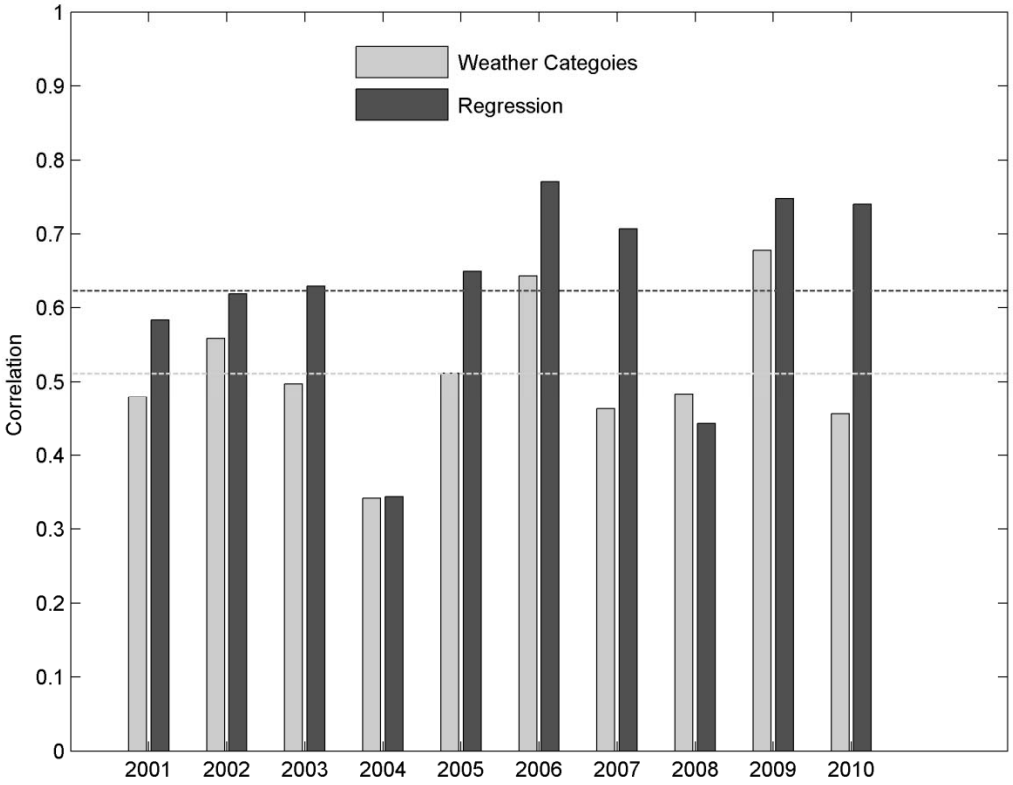

Figure 5.4. Correlation coefficients between annual modelled and observed lapse rates.

Whilst the weather-category lapse-rate model explained an encouraging amount of variance, it was considered likely that its performance could be improved further by optimizing the analogue approach. The motivation behind this is that synoptic weather types are not completely homogeneous with regards to their meteorology, and within-type lapse-rate variability can therefore be expected to remain. This may be a limiting factor affecting the performance of the weather-category analogue model. Consequently, within the cross-validation scheme, the effect of using analogues that were more synoptically similar to the day being simulated was investigated. More specifically, this technique involved parameterizing the lapse rate as a function of the *most* synoptically similar day(s), rather than as the mean of the synoptic type.

That is, for each day (i) the lapse rate is simulated, a day (k) in the calibration years (i.e. not in the year being simulated) is sought which minimizes:

$$[\mathbf{X}_i - \mathbf{X}_k]'[\mathbf{X}_i - \mathbf{X}_k] \ . \qquad 5.7$$

This is similar to Equation 5.5, such that the $\mathbf{X}$ still denotes the PC scores for the respective days; however, rather than minimizing the distance to the nearest synoptic weather type ($\mathbf{X}_j$ in Equation 5.5), the nearest day(s) is(are) sought. This technique addresses the effect of synoptic dissimilarity within groups by *only* using the *most* similar synoptic conditions as an analogue. In addition, through relaxing the condition set by Equation 5.7 to include the n most similar days, and thence prescribing the lapse rate as the mean of these days, an estimate of the sensitivity of the synoptic model to group size may be obtained.

The results from application of this procedure, plotted in Figure 5.5, suggest that using the most synoptically similar day as a solitary analogue actually leads to a considerably poorer model performance in the lapse rate simulation. However, as the number of synoptically similar days is increased slightly, both the RMSE and the correlation metrics rapidly improve; performance then monotonically declines as the number of similar days is increased further.

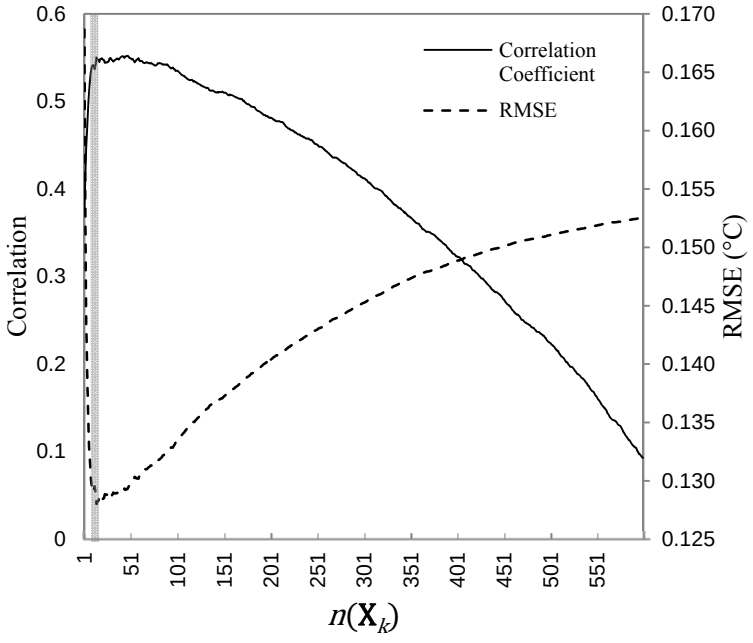

Figure 5.5. Performance of the optimized analogue approach as a function of the number of analogue days used to simulate the lapse rate (x-axis). The grey line indicates the best solution according to Equation 5.8.

The optimum number of analogue days to average the lapse rate over is found by defining a skill score (SS) according to:

$$SS_n = \frac{RMSE_n}{RMSE_{max}} + r_n \ , \qquad 5.8$$

where $RMSE_{max}$ is the highest RMSE observed, r is the correlation coefficient, and the subscript n denotes the number of most synoptically similar days over which the lapse rate was averaged during the cross-validation procedure (for example, when n = 3, each day's lapse rate was calculated as the mean of the 3 most synoptically similar days). Application of Equation 5.8 indicates that the optimum performance (highest SS) is found when the lapse rate is forecast as the average of the 15 most similar synoptic analogues: this yields mean annual correlation coefficients and RMSEs of 0.58 and 0.127°C 100 m^{-1}, respectively. The optimised analogue technique therefore results in a mean correlation coefficient which is higher than that achieved by the original weather-category model, but still slightly lower than obtained with the regression model. However, the RMSE for this optimized model is slightly lower than either of those recorded in Table 5.4, and is therefore the best performing model in this regard. The performance of this optimized model during the cross validation is visually compared to that of the stepwise regression and the original weather-category model in Figure 5.6.

An interesting aspect of the models' performance is that their ability to simulate interannual variability is limited (Figure 5.7). In particular, it is apparent that changes of the modelled lapse rates are relatively muted from year to year compared with observations. Furthermore, the models fail to reproduce the progressive shallowing of lapse rates that has occurred during the measurement period satisfactorily. This is quantitatively demonstrated with the aid of regression: when regressed upon year, the observed trend in the lapse rate between 2001-2010 is 0.018°C 100 m^{-1} a^{-1}, which is significant at p = 0.05. None of the models produce a similarly significant trend. Possible reasons for this shortcoming of the models are suggested in sections 5.5.2 and 5.5.3.

Despite these limitations, the advantages of parameterizing lapse rates with the regression and analogue models are evident when considering the potential effect on ablation. Table 5.5 provides the sum of positive temperatures calculated by extrapolating the temperature up/down glacier based on the simulated lapse rates. Positive temperatures (frequently called positive degree days or 'PDDs') are given because this is a parameter often used in empirical melt models (Hock 2003, 2005), and Hodgkins et al. (2012a) previously demonstrated an improvement in forecasting PDDs at this location when the lapse rate was parameterized through regression, with temperature as a solitary predictor. The errors presented in Table 5.5 for the models developed in this chapter therefore represent an improvement in this regard.

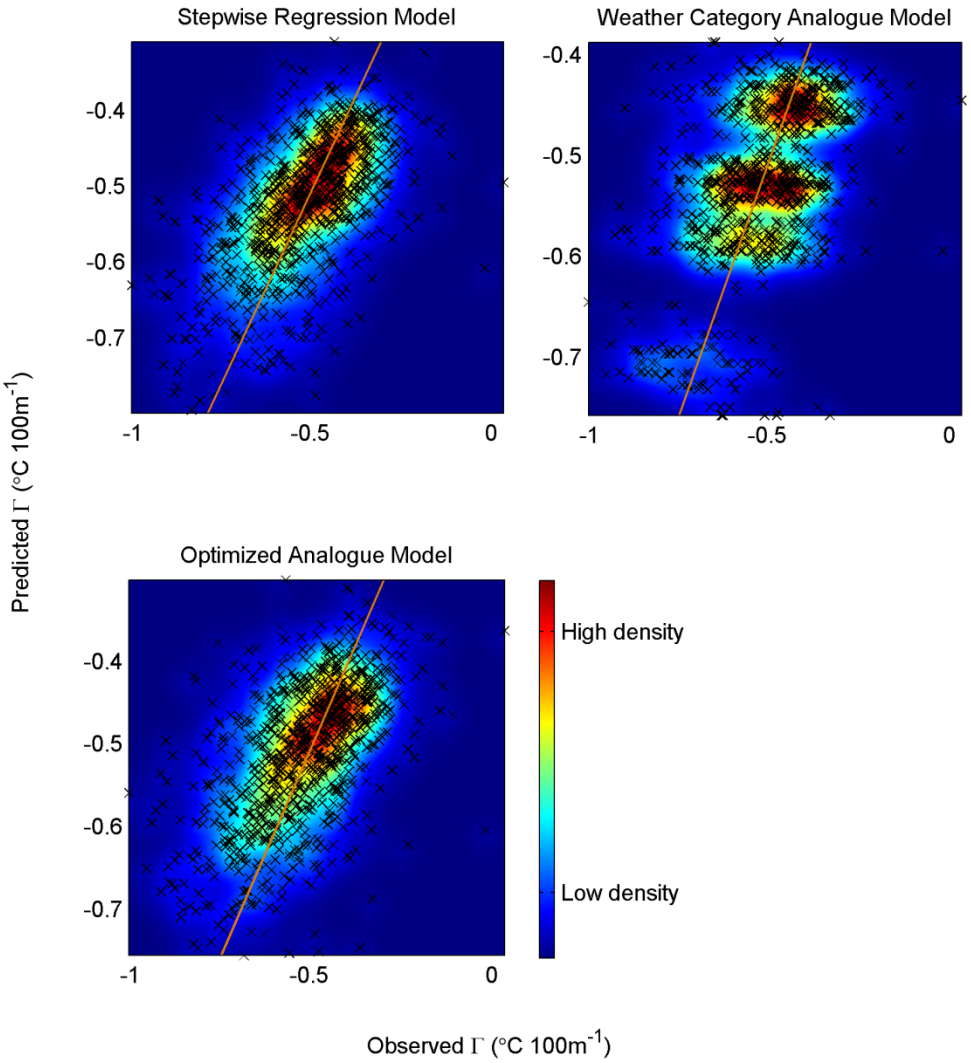

Figure 5.6. Observed versus lapse rates predicted by the models discussed in the text. Colour ramp indicates relative bivariate density; orange line illustrates the 1:1 relationship.

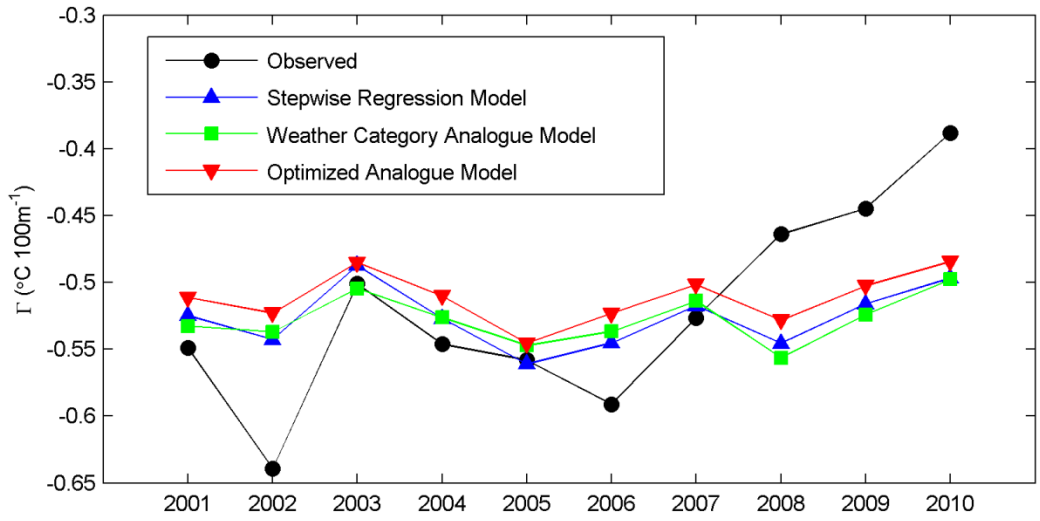

Figure 5.7. Interannual variability of observed and modelled lapse rates.

Table 5.5. PDD errors using lapse rates modelled through the cross-validation procedure. [a] 'Elevation' label indicates location (AWS station) to which temperatures were extrapolated (i.e. '500' indicates PDDs calculated by extrapolating 1100 m temperature to 500 m using modelled lapse rates).[b] Shows results from using temperature as the only predictor in a regression model, following the method of Hodgkins et al. (2012a), but employing 2 m reanalysis air temperature, which correlates more strongly with the lapse rate than 750 hPa air temperatures.

Model	**[a]Elevation (m)**	**Error (%)**
Stepwise Regression	500	0.0
	1100	-0.7
Weather Category Analogue	500	0.2
	1100	-1.0
Optimized Analogue	500	-1.9
	1100	-2.8
[b]Temperature Regression	500	6.7
	1100	-1.9
ELR	500	15.1
	1100	-38.0

5.5. Discussion

5.5.1. Meteorological controls on the lapse rate

With regards to the correlation between the lapse rate and the reanalysis meteorology, there are two particularly noteworthy relationships that emerge. The first of these is that the strongest correlation is found with the wind speed. Such an association is particularly interesting because it is in contrast with the conclusions of Gardner et al. (2009), who found no correlation between reanalysis wind speed and lapse rates on the Prince of Wales icefield, but may qualitatively agree with the study of Petersen and Pellicciotti (2011), which reported a steepening lapse rate as the valley wind strengthened at Juncal Norte Glacier, Chile.

It is suggested that the physical mechanism behind the observed correlation between the lapse rate and the wind speed may be attributed to the greater mixing of near surface air and entrainment that can be achieved when winds are vigorous (Stull, 1988; Pepin et al., 1999; Pepin, 2001; Barry, 2008). This is illustrated in Figure 5.8, which shows that the directional constancy of the glacier wind regime steadily declines as synoptic wind speeds increase, indicating that stronger synoptic winds have the potential to disrupt katabatic drainage.

Enhanced mechanical mixing driven by strong synoptic winds and the disruption of downhill drainage can then alter flow path lengths over the glacier and affect the temperature field. For example, without downhill drainage, the cumulative cooling effect of the glacier on the overlying air during its passage downhill is no longer felt at lower elevations (Greuell et al., 1997; Greuell and Böhm, 1998). In fact, depending on the resulting wind direction (which affects flow path length), it is possible that in some instances (e.g. upslope airflow), the cooling effect of the glacier may be greater at the higher elevation station, due to larger upwind sensible heat losses.

If strong synoptic wind speeds act to erode the katabatic boundary layer, then the contrasting results found in this study, compared to Gardner et al. (2009), may be explained by the lack of well-defined glacier winds that the authors noted were absent from their region of study. That is, it is suggested that the relationship between the lapse rate and the synoptic wind speed will only endure if there is a katabatic wind to erode.

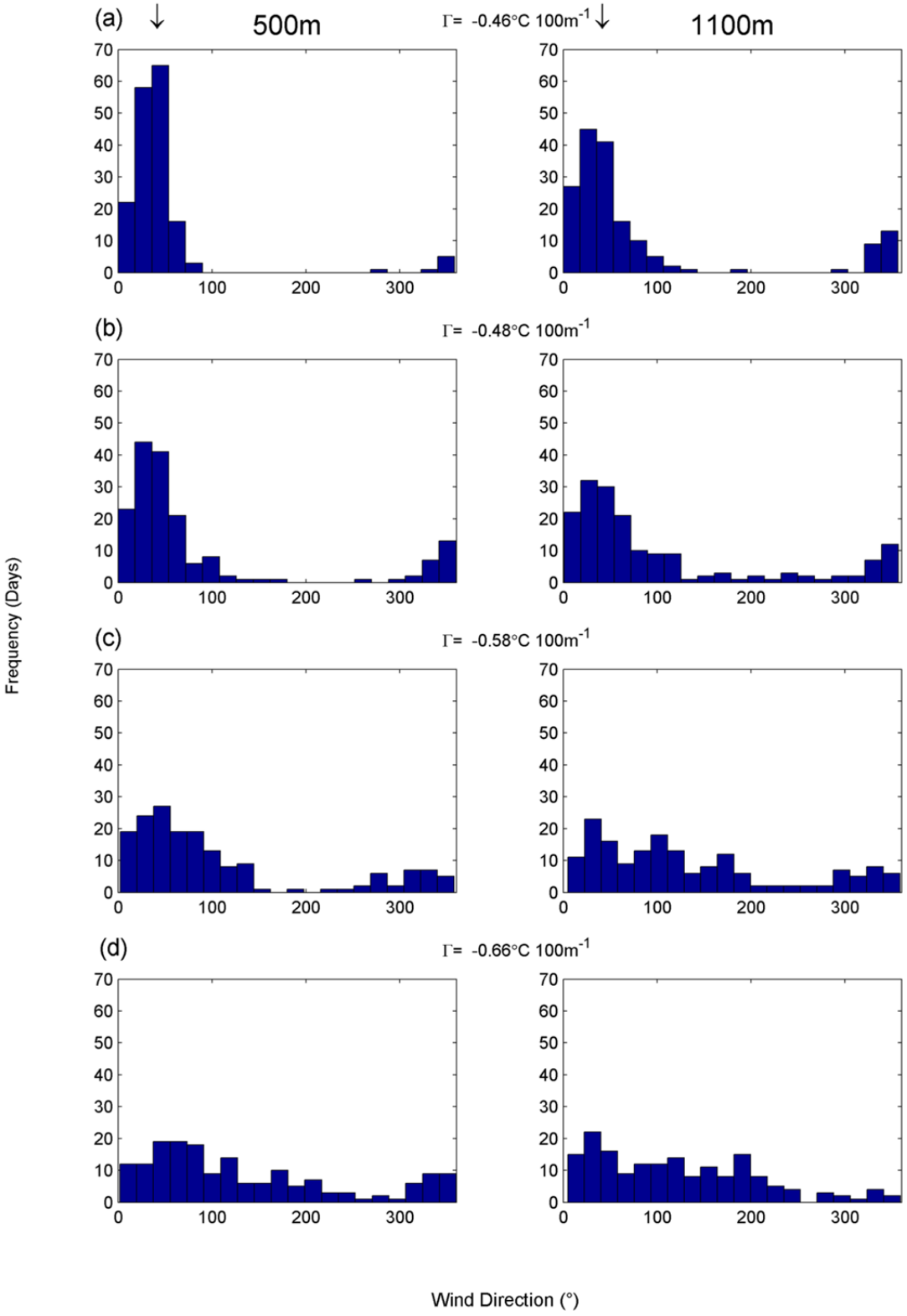

Figure 5.8. Histograms of wind direction recorded on the glacier at 500 m and 1100 m, as stratified by regional reanalysis wind speed quartiles (a-d). Arrows indicate approximate down-glacier direction. Lapse rates for each quartile are shown above each pair of histograms. The values of the wind-speed quartile boundaries, in order (first to third), are: 1.61 m s^{-1}, 2.65 m s^{-1}, and 3.85 m s^{-1}.

Because the katabatic wind is density driven and only occurs when the air overlying the glacier is chilled relative to the ambient atmosphere, katabatic drainage is unlikely to persist where this temperature deficit is low. It is therefore probable that in such environments, the association between the synoptic wind speed and the lapse rate which was observed in this study, may be greatly diminished or absent entirely. Moreover, it must also be considered that even where katabatic drainage is well established, the regional wind speed may be a poor indicator of its erosion if terrain is complex and the wind field is substantially modified by channelling/sheltering effects (e.g. Pepin and Norris, 2005).

With consideration of wider scale synoptic circulation, analyses indicated that strong winds and steep lapse rates were associated with low pressure and cyclonic curvature; shallow lapse rates were observed when gradient winds are weak, which often occurs during periods of higher air pressure. These results broadly agree with Marshall et al. (2007) who found an inverse relationship between the lapse rate and atmospheric pressure anomalies, and also confirms the suspicions of Hodgkins et al. (2012b) who speculated that shallow lapse rates at Vestari Hagafellsjökull were connected to periods of higher atmospheric pressure prevailing.

In contrast to the present study are the results of Braun and Hock (2004), who observed shallow lapse rates during warm air advection, forced by the passage of low-pressure systems on King George Island. This led the authors to conclude that air mass source area was a significant control on the lapse rate. The absence of this observation at Vestari Hagafellsjökull may well be attributed to the different climatological settings of these studies, and in particular, the rarity of air masses associated with freezing temperatures within the summer months (temperature data are presented in Section 5.4.1 and the relationship between temperature and the lapse rate is also discussed below). These differences serve to highlight the caution which should be applied in attempting to generalize the effect of synoptic circulation on the lapse rate to different climatological settings.

The second notable relationship with the reanalysis climatology uncovered in this study is the low correlation observed between the lapse rate and temperature, which is in contrast to the findings of Gardner et al. (2009) and Hodgkins et al. (2012a). It is argued that the reason for these differing results can be attributed to the spatial and

temporal differences of the present study: Hodgkins et al. (2012a) used data from April the 25th to the end of May, 2003 to calibrate a regression model that predicted lapse-rate variability from temperature at the 750 hPa surface, and recorded a much higher daily correlation than was observed in the present study (0.56). Although this may appear to contradict the results presented in this chapter, a similar figure is obtained if lapse rates from May (2001-2010) are analysed (r = 0.57 when correlated with reanalysis temperatures from the 750 hPa surface, and r = 0.64 if 2 m reanalysis temperatures are used; n = 267, p <0.01). This correlation is much higher than is observed in June, July or August (correlation coefficients of 0.3, 0.28 and 0.28, respectively) and indicates a temporal dependence on the strength of the relationship between temperature and the lapse rate.

It is suggested that the cause of this behaviour may be attributed to the thermal regime over the glacier. May is the coldest of the 4 months (May-August), with temperatures averaging -2.1°C at 1100 m and 1.7°C at 500 m over the period 2001-2010. Thus, the freezing line is typically situated between the two elevations during this month. Such a temperature field results in the glacier exerting a cooling influence at the lower elevation, which is absent higher on the glacier. The reason for this is that a melting surface is limited to a maximum of 0°C. Consequently, the positive air temperatures recorded at the lower elevation result in a sensible heat flux into the glacier and cooling of the overlying air. If temperatures are below 0°C at the higher elevation station, sensible heat exchange with the glacier surface will be minimal and no such cooling occurs (Denby et al., 2002; Gardner et al., 2009; Hodgkins et al., 2012b). Lapse rates will co-vary with air temperature when these conditions arise, because sensible heat losses at low elevations will increase as temperatures rise. This results in a larger relative cooling effect and a shallowing of the lapse rate. Conversely, when the 0°C isotherm is located above 1100 m, sensible heat losses are likely to occur at both elevations. In this situation, the effect of free-air temperature on the lapse rate is more ambiguous to define.

The data analysed in this study support this explanation: if the lapse rate is stratified based on occurrences where temperatures at both elevations are >0°C and correlations are performed between the lapse rate and reanalysis temperature (2 m), correlation is greatly reduced, even if May is included (r = 0.06, p = 0.09, n = 871). During periods when the freezing line is between these two stations, the correlation is appreciably

higher ($r = 0.45$, $p < 0.01$, $n = 125$). This mechanism may also explain why the correlations observed by Gardner et al. (2009) were substantially higher than those obtained in this study: the authors reported that higher elevations on the ice field experienced sub-zero temperatures throughout much of their investigation.

5.5.2. Empirical parameterization of the lapse rate

The regression and weather-category analogue models presented in this chapter aimed to capture lapse-rate variability, and their skill was assessed through a cross-validation procedure. The results of this process showed that both approaches performed similarly, and simulated the lapse rates at a daily time scale so that moderate-to-good agreement was achieved between observed and modelled series (correlation coefficients for the simulated and observed series ranging between 0.51 and 0.62). It was also found that the synoptic analogue technique could be improved if weather-category memberships were ignored, and instead, the lapse rate prescribed as the mean of the most synoptically similar days to have previously occurred. Experimentation with this procedure suggested that lapse rates were predicted best when the 15 most synoptically similar days were used as analogues. This variant of the analogue approach should be considered as an optimized version of the weather-category model, as by preferentially choosing the most similar days in this way, meteorological variability between the analogue days and the day to be simulated is minimized. In turn, this enables improved forecasting of the lapse rate.

The degree of spatial transferability of the regression or analogue models to either location on Langjökull, or to other glaciers within different topographic/climatic settings, remains to be determined. In this regard, however, it is considered that in general, an analogue-type approach may be more portable for lapse-rate parameterization. At Vestari Hagafellsjökull, for example, the wind speed was found to be a critical control on the lapse rate; if the same is true elsewhere, then model performance would be compromised should regional-scale wind speed data be too coarse to represent local wind conditions. Such limitations may occur if topography introduced a strong directional dependency on the form of the relationship between synoptic and local wind speed (e.g. preferential lee effects during certain wind directions). This complexity would challenge regression-based approaches because this would need to be addressed explicitly, but is implicitly included when analogues

are used to investigate lapse-rate variability. The analogue technique is indeed an elegant approach to forecasting lapse rates: the form of individual relationships between meteorological parameters and the lapse rate does not need to be determined, as the net effect of the prevailing meteorology is captured. This makes a strong case for such a holistic consideration of synoptic conditions for glacier-melt studies where lapse-rate parameterization is required.

The empirical models tested in this chapter indicate that regional-scale data can be employed usefully to constrain daily lapse-rate variability and demonstrated the importance of this for melt simulations by extrapolating PDDs up/down glacier. However, a notable limitation of all models was their failure to capture interannual variability adequately. Although the reason for this is unclear, a potential source of variability that is not considered in either of the models is the effect of local modification of the climate, which may vary from year-to-year and would not be captured by the reanalysis data. For example, differences in the extent and duration of snow cover on the forelands surrounding the glacier may affect local heat advection which in turn could influence the lapse rate; or changes in the surface roughness of the glacier could introduce variability into its cooling effect on the overlying air. It is also possible that subtle, interannual changes of the synoptic weather conditions may occur, that have non-linear effects on the lapse rate: Greater atmospheric moisture content, slight changes of wind direction or interactive effects resulting from particular weather category sequence (i.e. antecedent conditions), for example, might affect the lapse rate in ways which are not captured by either the analogue of regression approaches.

Attributing the cause of the pronounced interannual lapse-rate variability (which is not captured by the any of the models) is problematic: the effect of snow cover on the glacier forelands cannot be directly quantified, and even the presence/absence of snow cannot be ascertained with any confidence (glacier AWSs may provide a guide, though). Furthermore, the ratio of season length (92 days) to the number of weather categories (30) precludes a detailed analysis of any subtle changes that have occurred within the weather types. There is, however, at least the possibility of approximating the effect of variable surface roughness. Although this can only be speculative, it is considered useful to illustrate the potential effects that may result from variation of this parameter.

If all other things are equal, then a rougher surface will increase the sensible heat exchange between the glacier and the overlying air. This would lead to an increase in down-slope cooling and a shallower lapse rate that is more sensitive to changes in air temperature. To estimate the extent to which this may affect the lapse rate at Vestari Hagafellsjökull, the model of Greuell and Böhm (1998) may be applied.

The physically-based thermodynamic lapse-rate model of Greuell and Böhm assumes that two processes affect the lapse rate: sensible heat exchange with the glacier, and adiabatic contraction during descent. Temporally, such treatment assumes the lapse rate varies as a function of air temperature only, and katabatic drainage is also presumed to be continuous when melting conditions persists. These equations are therefore a simplification of the empirical models presented in this chapter. In only recognizing air temperature as a control on the lapse rate, the Greuell and Böhm model bares some conceptual similarity to a temperature-based regression model. But, because it adopts a physical perspective, it enables a first-order approximation of the importance of glacier surface roughness for cumulative downslope heat transfer and lapse-rate variability. Application of Greuell and Böhm's (1998) expressions to the data in this study is described in the following section.

5.5.3. Sensitivity of lapse rates to glacier surface roughness

The Greuell and Böhm (1998) model parameterizes air temperature within the glacier boundary layer as a function of the horizontal distance along the flow-line (x):

$$\boldsymbol{T(x) = (T_0 - T_{eq}) \exp\left(-\frac{x}{L_R}\right) + T_{eq}} \ , \qquad 5.9$$

where T_0 is the temperature at the top of the glacier flow-line. By setting T_0 to be the air temperature recorded at 1100 m, it is possible to determine the air temperature $T(x)$ at the 500 m AWS. The difference between T_0 and $T(x)$, when divided by the vertical elevation change, yields the lapse rate. The remaining parameters in Equation 5.9 to be defined are:

$$L_R = \frac{H \cos(\alpha)}{cH} \ , \qquad 5.10$$

$$T_{eq} = bL_R \ , \qquad 5.11$$

in which H gives the depth of the cooled layer overlying the glacier; α is the glacier's surface slope; cH is the bulk heat transfer coefficient, which incorporates the effects of atmospheric stability and surface roughness; and b is provided by:

$$b = \Gamma \tan(\alpha) \ , \qquad 5.12$$

with Γ as the dry adiabatic lapse rate (0.98°C 100 m^{-1}). To determine the effect of changing the surface roughness (z_{0w}) on the lapse rate, is to perturb the value cH, which is defined, e.g. Stull, (1988) as:

$$cH = k^2 \left[\ln\left(\frac{z}{z_{0w}}\right) - \Psi_M\left(\frac{z}{L}\right)\right]^{-1} \left[\ln\left(\frac{z}{z_{0T}}\right) - \Psi_H\left(\frac{z}{L}\right)\right]^{-1} . \qquad 5.13$$

All of these terms were explained in Chapter 2. Before the effect of varying z_{0w} may be investigated, it is necessary to obtain an estimate for H. This was achieved by using the mean cH obtained from both AWSs in Chapter 2's SEB investigations, and then, tuning the model until the mean modelled and observed lapse rates agreed. Tuning is performed by using air temperature measured at the 1100 m AWS as T_0 and

applying Equation 5.9 to calculate air temperature at the 500 m AWS. The slope is assumed constant between AWSs and is taken to be (3°) as obtained from the DEM presented in Chapter 2.

During this fitting procedure, and subsequent modelling of lapse rate's sensitivity to surface roughness, the following conditions are applied:

a) If air temperatures at both AWSs are below freezing, the mean lapse rate during such conditions (-0.71°C 100 m^{-1}, Γ_c) is applied to simulate air temperature at the 500 m AWS. This condition is required because the model assumes sensible heat losses to the glacier surface, which are unlikely when air temperatures are below the melting point.
b) If air temperature is above zero at the 500 m station, but freezing at 1100 m, then the 0°C isotherm is between these elevations. The location of this level is estimated using Γ_c, and the air temperature at 1100 m (T_{1100}); the Greuell and Böhm model is applied below this altitude. This information is also used to adjust the flow path length of air over the melting glacier, such that x in Equation 5.9 is replaced with the reduced distance that the 500 m station is now found along the flow line, x_corr:

$$x\_corr = x - \frac{T_{1100}\,{\Gamma_c}^{-1}}{\tan(\alpha)}\ . \qquad 5.14$$

c) When positive temperatures are observed at both AWS, the Greuell and Böhm model is assumed valid over the entire altitudinal range between AWS, and the flow-path length over the melting glacier (x) is simply the horizontal distance between these locations (11208 m).

Applying this model, and iteratively incrementing H, suggested a cooled layer thickness of 29 m (Figure 5.9a), and it is interesting to observe that this physical model actually captures daily lapse-rate variability reasonably well (Figure 5.9b). Although this performance is no better than the multiple regression or either of the analogue methods (the weather category, or optimized analogue technique) described in Section 5.4, it is considerably more skilful than simply using regression of free-air temperatures to predict the lapse rate (see correlations in Section 5.4 and Figure 5.4).

This demonstrates lapse rates may be predicted better from temperature variations alone if a physical, rather than empirical treatment is applied.

Having obtained estimates for all parameters in Equation 5.9, the effect of varying the surface roughness could be assessed. This was pursued by investigating two end-member scenarios: 1) that the surface roughness from the 1100 m station is valid for the entire flow-path length between stations, and 2) the 500 m surface roughness length is applicable over this distance. Physically, this translates to investigating the effect of whether melting snow or ice constitutes the glacier surface between AWSs, and is motivated by the fact that interannual changes in the position of the snowline will affect the glacier surface roughness, and hence the rate of sensible heat exchange between the glacier and air draining down-slope. These experiments were implemented by running the lapse rate model with the mean cH obtained from 1100 m (to simulate 1), and with the mean cH from 500 m (to simulate 2). Although this treatment also includes the effect of different stability corrections between locations (Equation 5.13), the relative effect on the value of cH is small compared to the difference in roughness lengths (Munro, 1989).

Whilst the results of this investigation only serve as a guide, the magnitude of the change in the lapse rate effected by these variations in cH, suggests that glacier surface roughness is unlikely to be responsible for the pronounced interannual variability observed (Figure 5.9c, red patch). Even if more extreme scenarios are considered, in which the roughness lengths are assumed to be ± an order of magnitude larger at the 500 m and 1100 m AWSs, respectively (and scenarios 1 and 2 applied with the value of cH adjusted in the lapse rate model accordingly), the observed lapse-rate variability is still not entirely accounted for (Figure 5.9c, blue patch). Thus, although variation of the surface roughness does have a non-negligible effect on the lapse rate, its required perturbation to account for the observed lapse-rate variability is considered unrealistic.

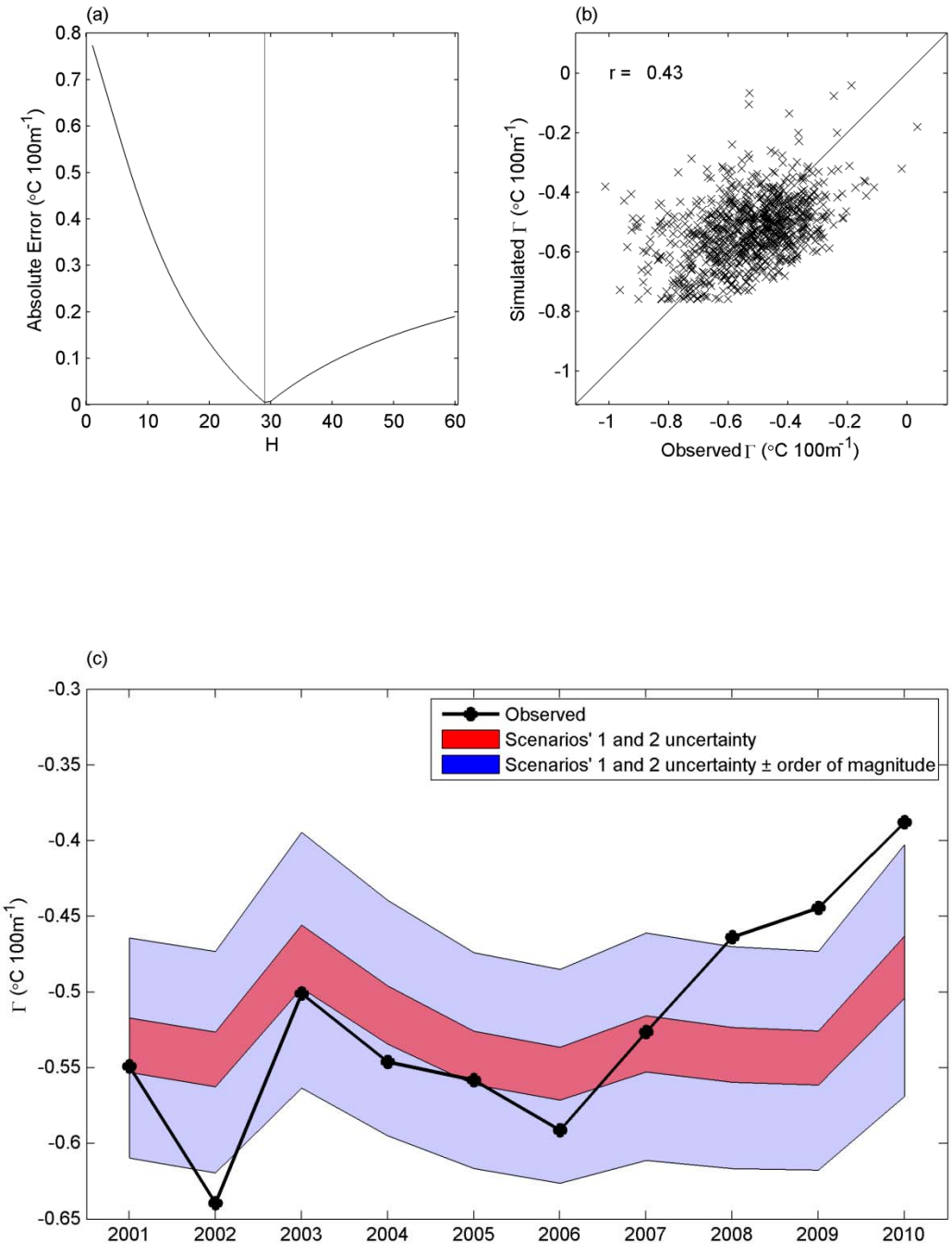

Figure 5.9. Results from applying the Greuell and Böhm model. (a) shows the tuning of H in Equation 5.9; the absolute error is defined as the absolute difference between mean simulated and observed lapse rates, and the vertical grey line shows the optimum solution (H = 29 m). (b) compares simulated and observed lapse rates at daily resolution, and r is the correlation coefficient between series. (c) provides the results from perturbing the roughness lengths. Scenario 1 assumes cH from the 500 m station is valid for the entire flow-path length between AWSs, and scenario 2 assumes cH from 1100 m is valid over this distance. The area spanned by the red coloured patch indicates uncertainty associated with the choice of cH: the lower and upper boundaries mark Equation 5.9's predictions using cH from 1100 m and 500 m, respectively. The blue patch shows the same as the red patch, but the respective cH values are calculated with z_{0w} values one order of magnitude greater at 500 m, and one order of magnitude smaller at 1100 m. See text for further explanation.

5.6. Synthesis and Conclusions

The aim of this chapter was to investigate synoptic controls on lapse-rate variability at Vestari Hagafellsjökull during the ablation season. This was pursued because temperature is a driving variable in nearly all melt models—whether physically- or empirically-based—and must invariably be spatially interpolated or extrapolated for distributed studies aiming to quantify glacier mass or energy balances. Specifically, a synoptic approach to the analyses was favoured because this holistic framework is well suited to tackling the complex synergy between meteorological elements which ultimately determines the lapse rate. It should also be considered that developing predictive models to constrain lapse-rate variability using synoptic climatological information has immediate, practical benefit for glacier-climate studies, as this limits the need for direct observations within the glacier boundary layer, which may be logistically challenging to obtain.

The synoptic investigation was pursued by assessing lapse rates' linear dependency on elements of synoptic meteorology and through exploring their relationship with weather types. From the synoptic meteorological variables, the strongest relation with the lapse rate was observed for the synoptic wind speed: steeper lapse rates (greater air temperature reduction with elevation) were observed as velocity increased. The synoptic weather categories also emphasised the importance of the wind field, as strong winds were observed in weather categories characterised by steep lapse rates. Examination of wider-scale circulation showed that this was often the result of cyclonic conditions prevailing. Shallow lapse rates, on the other hand, were found in weather categories which were characterised by generally warm, cloud-free weather and slack winds. Observations of the wider-scale flow indicated that this usually coincided with periods of high atmospheric pressure over Iceland.

To investigate whether this information may be used for predictive purposes, a regression model was developed to exploit the observed linear associations with synoptic meteorological variables, and an analogue model was devised that used the prevailing weather type to forecast the lapse rate. The skill of these techniques was assessed in a cross-validation scheme, and results were encouraging for both models: mean annual correlations were 0.51 and 0.62 and RMSEs were 0.133 °C 100 m^{-1} and 0.129 °C 100 m^{-1} for the weather category and regression models, respectively.

Further improvement of the analogue model was achieved by using the mean of the 15 most synoptically similar days as an analogue, rather than weather-category membership; this yielded a mean annual correlation of 0.58 and a mean annual RMSE of 0.127 °C 100 m^{-1}

The performance of these models is better than if air temperature alone is used as a predictor in a regression equation (Gardner et al., 2009; Hodgkins et al., 2012a, b), and the level of predictive skill they provide substantially reduced errors in PDDs calculated by extrapolating air temperature up/down glacier. Whilst this demonstrates a clear benefit of the research in this chapter, deficiencies in the models' ability to capture low frequency, interannual lapse-rate variability were noted. Although the reason for this cannot be ascertained with any certainty, it was speculated that changing glacier surface roughness could be responsible, and the physically-based lapse-rate model of Greuell and Böhm (1998) was applied to explore this possibility. The results from the model runs indicate that even if the glacier surface between AWSs oscillated from snow- to ice-covered on an interannual basis (which must be considered as unlikely), it would not explain the variability observed. Indeed, even if this oscillation occurred with the roughness length for ice an order of magnitude greater, and for snow an order of magnitude smaller, it would still not fully account for the observed interannual lapse-rate variability. The Greuell and Böhm model therefore indicates that although variable surface roughness may contribute to the interannual lapse-rate variability, it is unlikely to be responsible for the magnitude of the changes observed. Hence, the reason for the failure of the empirical models to adequately capture this variability remains somewhat unknown.

This limitation notwithstanding, the empirical, synoptic lapse-rate models developed in this chapter achieved a level of predictive skill which resulted in tangible improvements of PDD estimates when air temperatures were extrapolated up/down glacier. In turn, this could be of substantial practical benefit for distributed glacier mass and energy balance modelling, for which the robust and accurate distribution of near surface air temperatures is essential.

6. Climatological Controls on Degree-Day Factor Variability

6.1. Introduction

Snow- and ice-melt on glaciers is determined by the SEB, and may be simulated physically if sufficient information regarding the boundary-layer meteorology and the glacier surface (ice/snow surface temperature, roughness and albedo) is available. However, these data demands can rarely be satisfied fully, as prolonged in-situ meteorological monitoring on glaciers is logistically challenging (Van den Broeke et al., 2010). Furthermore, small-scale meteorological variability of the fields required to evaluate the SEB can be considerable, which limits the possibility of interpolating/extrapolating data from long-term records observed at off-glacier locations, or obtained from gridded climate products (e.g. reanalysis products, or forecasts of future climates provided by GCMs). For these reasons, empirical approaches to melt modelling are often pursued, which seek to integrate the effects of changing meteorology on the SEB implicitly. Such techniques may not only be more parsimonious and less computationally demanding, but can also eliminate the need for microclimatic information (i.e. downscaling) if empirical relations are sought between ablation and synoptic-scale meteorological variables.

In this regard, models which couple surface ablation with air temperature are particularly popular. This is because air temperature has been observed to correlate well with glacier ablation (discussed below), and also, because horizontal gradients of this variable in the atmosphere are usually slight (Barry and Chorley, 2009). Thus, air temperature remains largely homogeneous over synoptic scales, and is therefore amenable to both spatial interpolation and forecasting (Hock, 2003). These attributes have resulted in so-called 'temperature-index' models being applied widely for forecasting ablation under future scenarios of climate (e.g. Radić and Hock, 2006; Raper and Braithwaite, 2006; Hock et al., 2007; Radić and Hock, 2011 Marzeion et al., 2012), and have even been described as the *standard* approach for quantifying

ablation over both the Greenland ice sheet and mountain glaciers (Tarasov and Peltier, 1997; Braithwaite and Zhang, 1999).

In their most basic form, temperature-index melt models typically take the form (e.g. Van de Wal, 1996; Hock, 2003; Van den Broeke et al., 2010):

$$\sum_{i=1}^{n} M = DDF_{i,s} \sum_{i=1}^{n} T^{+} \Delta t \ . \qquad 6.1$$

Melt (M) is therefore calculated as the sum of positive temperatures (T^{+}) accumulated during the period Δt (usually one day), summed over n days and multiplied by the degree day factor ($DDF_{i,s}$) for snow or ice (subscripts s and i, respectively). These surface types are often differentiated because snow and ice vary in terms of their physical properties. This affects turbulent and radiative energy transfer between the glacier and the atmosphere, which in turn results in variability of the temperature-ablation relationship.

The ability of temperature-index approaches to simulate the complex processes which drive glacier melt accurately therefore rests upon its correlation with air temperature, which has been observed frequently (e.g. Braithwaite, 1981; Braithwaite and Olesen, 1990; Sicart et al., 2008). The physical basis of this correlation has largely been attributed to the integrating effect of air temperature, which to some extent implicitly includes information on both the radiative and turbulent heat fluxes (Braithwaite, 1981; Kuhn, 1993; Ohmura, 2001).

However, a caveat of the simplicity of temperature-index methods is the necessary assumptions which accompany their implementation. Because the DDF must account for all terms within the SEB, changes in the relative partitioning of the energy components will affect its value and therefore render a constant DDF implausible (Braithwaite, 1981). For example, low DDFs have broadly been acknowledged to result from high shares of the sensible heat flux within the SEB; higher DDFs typically prevail when this flux is subdued and the shortwave radiative flux increases its contribution towards surface ablation (Ambach, 1988a, b; Hock, 2003). This dependency on the partitioning within the SEB means that the DDF varies in both space and time, due to changes in the glacier surface (e.g. albedo or surface roughness) and the prevailing meteorology (Figure 6.1).

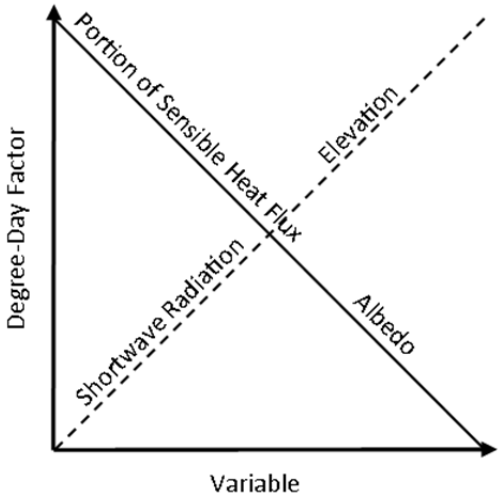

Figure 6.1 Schematic illustration of factors affecting the degree-day factor: its value increases with solar radiation and elevation and decreases as albedo increases and as the fraction of the sensible heat flux's share in the SEB rises. Modified from Hock (2003).

Whilst theoretical controls on the coupling of the DDF and the SEB are relatively well documented (e.g. Braithwaite 1995b), uncertainty regarding the spatial variability of the DDF is reflected in the tables of compiled DDFs from various studies around the world (e.g. Braithwaite and Zhang, 2000; Hock, 2003). The causes of observed differences have not been immediately evident (Braithwaite and Zhang, 2000), and compiled DDFs have shown little evidence of regional structure (Hock, 2003). Relatively small-scale variability of the DDF has also been reported. For example, within the Swiss Alps, Huss and Bauder (2009) noted appreciable differences in the factors observed for snow surfaces: from a sample of four locations on three glaciers, the highest DDF exceeded the lowest by more than a third. Similarly, Laumann and Reeh (1993) observed a gradual decline in DDFs for both snow and ice on a west-east transect of three glaciers in close proximity within southern Norway (factors for snow and ice declined by ~30% and 10%, respectively, with distance moved east). At a smaller scale still, Braithwaite et al. (1998b) found DDFs varied by ± 10% within a few metres during an ablation experiment in northern Greenland.

Such uncertainties as to how DDFs vary through space are a significant challenge to temperature-index modelling studies which seek to quantify global glacier wastage

(e.g. Raper and Braithwaite, 2006), especially so as attempts to provision for this variability explicitly have met with limited success: in possibly the most sophisticated globally applied temperature-index study to date, Radić and Hock (2011) could only account for around one third of the variance in tuned DDFs using multiple regressions of climatic regime indices (continentality and mass balance sensitivities to climate change) as predictors.

The complexities surrounding temporal change of the DDF can be considered as analogous to those that affect it spatially, as variables which affect its value vary through both space and time (Figure 6.1). Considering this non-stationarity of the DDF, and its dependence on the SEB, some authors have sought to introduce additional meteorological variables into temperature-index models (e.g. Lang, 1968; Pellicciotti et al., 2005). Whilst these adaptations can produce substantial improvements in melt forecasts, the additional demand for data recorded in-situ (or interpolated/extrapolated from other sources) can limit the advantage of applying these modifications where data are sparse. Such limitations are particularly apparent when forecasting ablation for likely future climates, as GCM output is spatially coarse and cannot resolve microclimatic variability in mountainous terrain. Many authors tasked with applying temperature-index models to such research have therefore chosen to neglect 'enhanced' versions and use air temperature as a solitary variable to infer ablation (Raper and Braithwaite, 2006; Radić and Hock, 2006; Radić and Hock, 2011).

The assumption of a temporally-constant DDF, even at interannual time scales, is not without risk however, as persistent changes in the SEB will affect the performance of temperature-index simulations. Such changes have indeed been noted by researchers studying multi-year DDF variability. Huss et al. (2009) reported a decline in DDFs in the Swiss Alps since a maximum during the 1940s, whilst Van den Broeke et al. (2010) observed an upward trend during the period 2003-2007 on the Greenland Ice Sheet. These changes can be attributed to variability of the prevailing weather characteristics and to variability of the surface albedo (Van den Broeke et al., 2010). It is therefore important to recognise that failure to incorporate this information into simulations may be a significant limitation of temperature-index methods, particularly for projections of future ablation, as climate change may manifest as variability in the

frequency and duration of particular weather types (e.g. Bárdossy and Caspary, 1990; Kalkstein et al., 1990).

6.2. Aims

Temperature-index models are therefore the primary approach for relating synoptic climatological processes to glacier surface melt, yet it is evident that the DDF, which is integral to their performance, changes through both space and time. Consequently, it is suggested that much can be gained in the field of glacier-climate interactions from a better understanding of how and why these changes manifest. Thus, investigating the spatial and temporal variability of the DDF is the aim of this chapter. Spatially, the data used in this thesis facilitates exploration of DDFs between locations on the same glacier (different elevations on Vestari Hagafellsjökull) and between glaciers (Vestari Hagafellsjökull and Storglaciären). Further, because a multi-year record of heat-budget data is available at these locations, a direct insight into the physical causes of the observed DDF variability may be provided. This is pursued to provide a better, process-based understanding of spatial controls of the DDF, which is much required in temperature-index modelling.

With regards to temporal variability, the aim of this chapter is to assess the effect of changes in the prevailing weather on the DDF. This is required to investigate the possible implications of assuming this parameter is constant in time.

6.3. Data and Methods

6.3.1. Data sources

To examine the association between DDF variability and the prevailing meteorology, the boundary-layer meteorology and the calculated SEB data presented in Chapters 2 and 3 are employed. For Vestari Hagafellsjökull, this data spans the period 2001-2007 at the 500 m elevation station and 2001-2010 at 1100 m. At both elevations the record from June-August is analysed. This interval corresponds to the main summer months when melting conditions persist at the higher and lower stations (see Chapter 2, Section 2.5 for further information regarding the ice cap's climatology).

For Storglaciären, data are used from the period 2005-2011, July-August. These data constitute a mix of meteorological data and SEB calculations determined from direct

AWS measurements (2010-2011), and from a synthetic series (2005-2009) generated by empirical transfer functions applied to off-glacier climate data (see Chapter 3 for details). Importantly, there are no albedo observations prior to 2010, hence the SEB was calculated for this period using a fixed value for albedo (0.38), corresponding to the median ice albedo obtained from the AWS measurements during fieldwork in 2010 and 2011.

To examine changes in synoptic-scale climatology, the weather categories identified for Vestari Hagafellsjökull and Storglaciären are utilised. Although 21 and 30 categories were differentiated in Chapter 4, only those consisting of 5 or more days are considered in this chapter's analyses. This decision is taken because the statistical approach used to explore DDF variability (described below) is challenged by such small sample sizes. Little is lost from truncating the analyses based on group size: the 17 (Storglaciären) and 25 categories (Vestari Hagafellsjökull) consisting of more than 5 days, which are examined for DDF variability in this chapter, hold >97% and >98% of all days, respectively.

6.3.2. Methodology

6.3.2.1. Degree-day factors

DDFs are calculated in this study according to:

$$DDF = \frac{M}{PDDs} \,, \tag{6.2}$$

where M is daily ablation, determined from the energy balance calculations, and PDD denotes 'positive degree-days', defined as:

$$PDDs = \frac{1}{n}\sum_{i=1}^{i=n} H(T)\, T_i \,, \tag{6.3}$$

in which, T_i is hourly air temperature, and $H(T)$ is a Heaviside function, which takes a value of zero when the temperature is at or below the melting point (assumed to be 0°C), and a value of 1 when temperatures are positive (e.g. Zhang et al., 2006; Marshall and Sharp, 2009). Hourly temperatures are preferred over daily means because the latter can be misleading when temperatures fluctuate around the melting

point (Hock, 2003). For example, it is quite possible for daily mean temperatures to be freezing (or slightly below), but for melting conditions to have persisted for periods during the day. This would introduce a bias towards higher DDFs because during such conditions, there is likely to still be surface melting, but there will be no contribution to $PDDs$ (Braithwaite, 1995b). $PDDs$ and DDFs are calculated at daily resolution (i.e. n = 24 in Equation 6.2); the units of the DDF are therefore mm. w.e. d^{-1} $°C^{-1}$.

When reporting DDFs for each location, different surface types are differentiated to facilitate comparison to previous studies. This is achieved by examining daily albedo recorded at the AWSs on Vestari Hagafellsjökull and Storglaciären. At Vestari Hagafellsjökull, there is a difference in summer surface types between the upper and lower AWSs. At the lower site, once snow cover has ablated away, glacier ice is exposed; at the upper site (which is approximately at the elevation of the equilibrium line altitude), firn underlies the snowpack (Guðmundsson et al., 2009). DDFs at Vestari Hagafellsjökull are therefore presented for snow and firn at 1100 m, and snow and ice at 500 m. At Storglaciären, DDFs are calculated for snow and ice, as at this elevation, glacier ice is revealed when snow cover is absent. It is important to note, however, that the SEB record prior to 2010 was generated with synthetic climate data and a prescribed, constant albedo. Calculations of the DDF for snow are therefore limited to 2010-2011.

6.3.2.2. Regression analysis of degree-day factors

To elucidate the relationship between the derived DDF, SEB and the prevailing meteorology—both between locations, and as a function of weather category—the treatment outlined by Braithwaite and Olesen (1990) and Braithwaite (1995b) is applied. This builds upon the fact that the DDF may be expressed:

$$DDF = \alpha(N^*/PDDs) + \beta\,, \tag{6.4}$$

where N^* is the number of days on which ablation occurs and α and β are regression parameters which relate $PDDs$ to the rate of snow and ice ablation:

$$M = \alpha + \beta PDDs + \varepsilon\,, \tag{6.5}$$

in which ε is the random error term (Braithwaite, 1995b). The advantage of using Equation 6.4 to analyse DDF variability, is that the physical processes which contribute to its variance can be addressed readily: the α term represents the amount of ablation at 0°C, and β gives the sensitivity of ablation to changes in $PDDs$. In consideration of Equation 6.4, it is also useful to observe that α and β may be related to the individual (m) energy fluxes:

$$\alpha = \frac{1}{L}\sum_{i=1}^{i=m} \alpha_i \ , \qquad 6.6$$

$$\beta = \frac{1}{L}\sum_{i=1}^{i=m} \beta_i \ , \qquad 6.7$$

where L is the latent heat of fusion (334 kJ kg^{-1}) and α_i and β_i are the intercept and gradient terms from regression of $PDDs$ upon each of the individual energy fluxes: net shortwave radiation; net longwave radiation; and the sensible and latent heat fluxes. These regression analyses provide a useful approach for investigating the driving factors which affect DDFs between different locations and weather categories: Equation 6.4 provides a clear breakdown as to the different contributions to the DDF, and equations 6.5 to 6.7 allow the physical causes of these of these differences to be evaluated.

For the regression, surface types (snow/ice/firn) are not differentiated. This decision is taken because at Storglaciären and at 500 m on Vestari Hagafellsjökull, snow cover is rare (Section 6.3). These small sample sizes challenge a statistical treatment, which is avoided by aggregating surface types. Although this is acknowledged as a simplification, the overall impact on the regression analyses is expected to be small, due to: i) the brevity of snow cover at the aforementioned sites; and ii) at 1100 m on Vestari Hagafellsjökull, where periods of snow and firn are more evenly shared (Section 6.4.1), the cut-off between surface types is relatively arbitrary because the physical properties of these surfaces (roughness lengths and albedo) are more similar than snow and ice. Indeed, DDFs for snow and firn are often not separated in temperature-index melt modelling studies (e.g. Hock, 1999).

6.4. Results

6.4.1. Observed degree-day factors

Observed DDFs for all locations are shown in Figure 6.2 and values of the DDF, as stratified by surface type, are provided in Table 6.1. Identification of the corresponding surface types for these factors was achieved using the daily albedo time series: as an objective rule, ice/firn was presumed for reflectivity <0.5 at 1100 m and <0.15 at 500 m at Vestari Hagafellsjökull; albedo <0.45 was taken as being indicative of an ice surface at Storglaciären. These subjectively-defined thresholds were selected based upon the evolution of surface reflectivity evident in Figure 6.3: the uncovering of the summer surface (ice or firn) is apparent from an abrupt reduction in albedo; the thresholds approximate the reflectivity when this transition occurs.

Table 6.1. Degree-day factors over the period of observation Note that the column labelled 'DDF' corresponds to the degree-day factor calculated irrespective of glacier surface type: summer (ice/firn) and winter (snow) surfaces are not differentiated. Units of the DDF are mm w.e. d^{-1} °C^{-1}.

Location	DDF	DDF_{snow}	$DDF_{ice/firn}$
Vestari Hagafellsjökull, 500 m	12.8	10.6	12.9
Vestari Hagafellsjökull, 1100 m	14.6	13.4	17.0
Storglaciären	6.8	5.2	6.9

DDFs from 500 m at Vestari Hagafellsjökull lay fairly centrally within the range reported for ice, and at the upper end of values typically given for snow (e.g. Table 1 in Hock (2003), in which reported values of the DDF range between 5.4 to 20 mm w.e. °C d^{-1} for ice and 2.5 to 11.6 mm w.e °C d^{-1} for snow); at 1100 m, DDFs are appreciably higher. Most notable is the high value observed for firn (17.0 mm w.e. $°C^{-1}$ d^{-1}); although this still falls within the values reported by Hock (2003), as both Ambach (1963) and Van de Wal (1992) obtained larger DDFs (~19 to 20 mm w.e. °C d^{-1}) at locations around the Greenland Ice Sheet. Also, elsewhere in Iceland, Guðmundsson et al. (2003) found a similar value (18.7 mm w.e. d^{-1}° C^{-1}) at approximately the same elevation (1200 m) on Brúarjökull, an outlet glacier of the Vatnajökull ice cap.

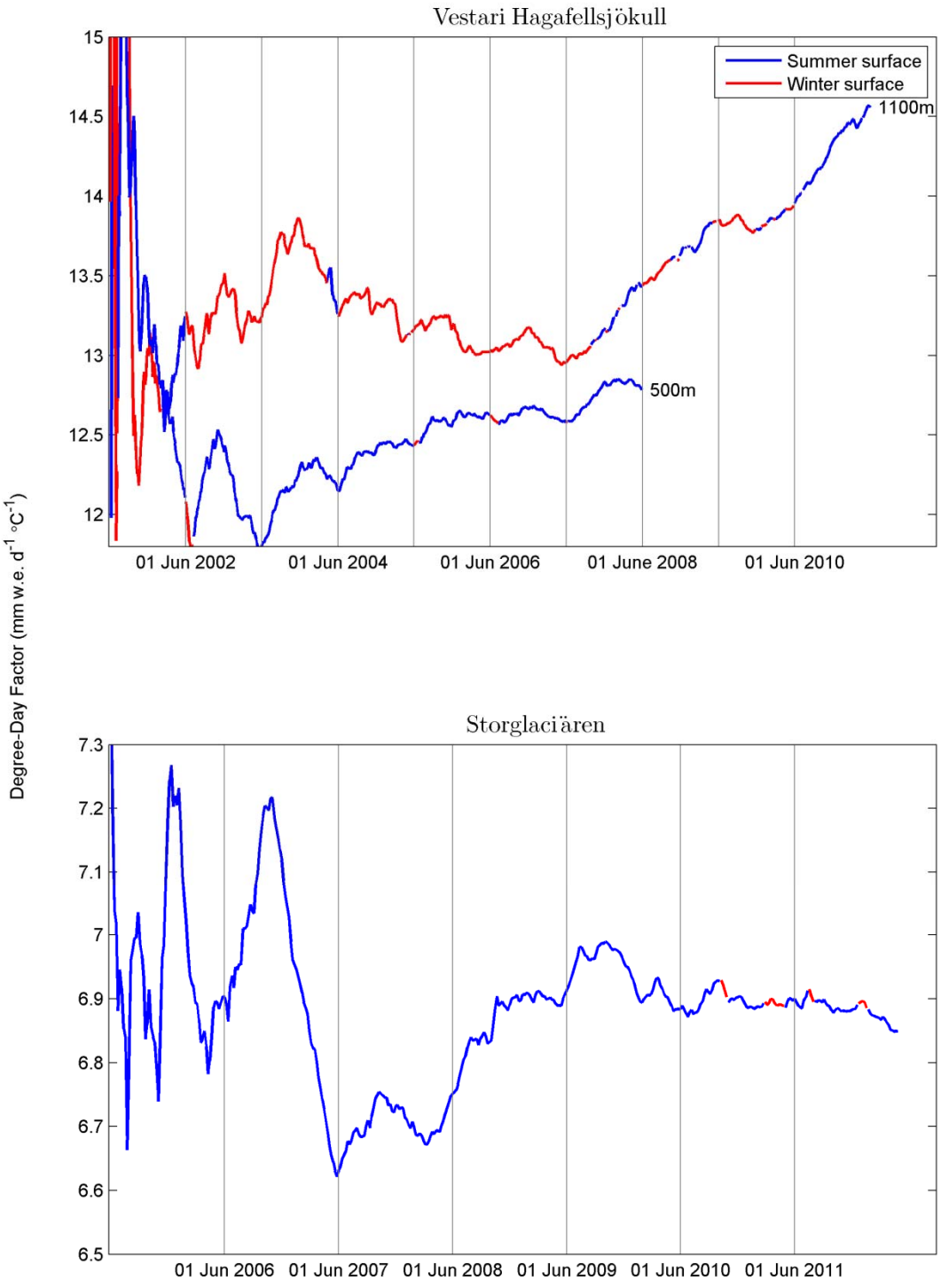

Figure 6.2. Observed degree-day factors. Values are calculated based on ablation and positive degree-days cumulated up to that point, which explains the decreasing variability with time (e.g. Van den Broeke et al., 2010). Vertical grey lines indicate the transition between successive JJA periods.

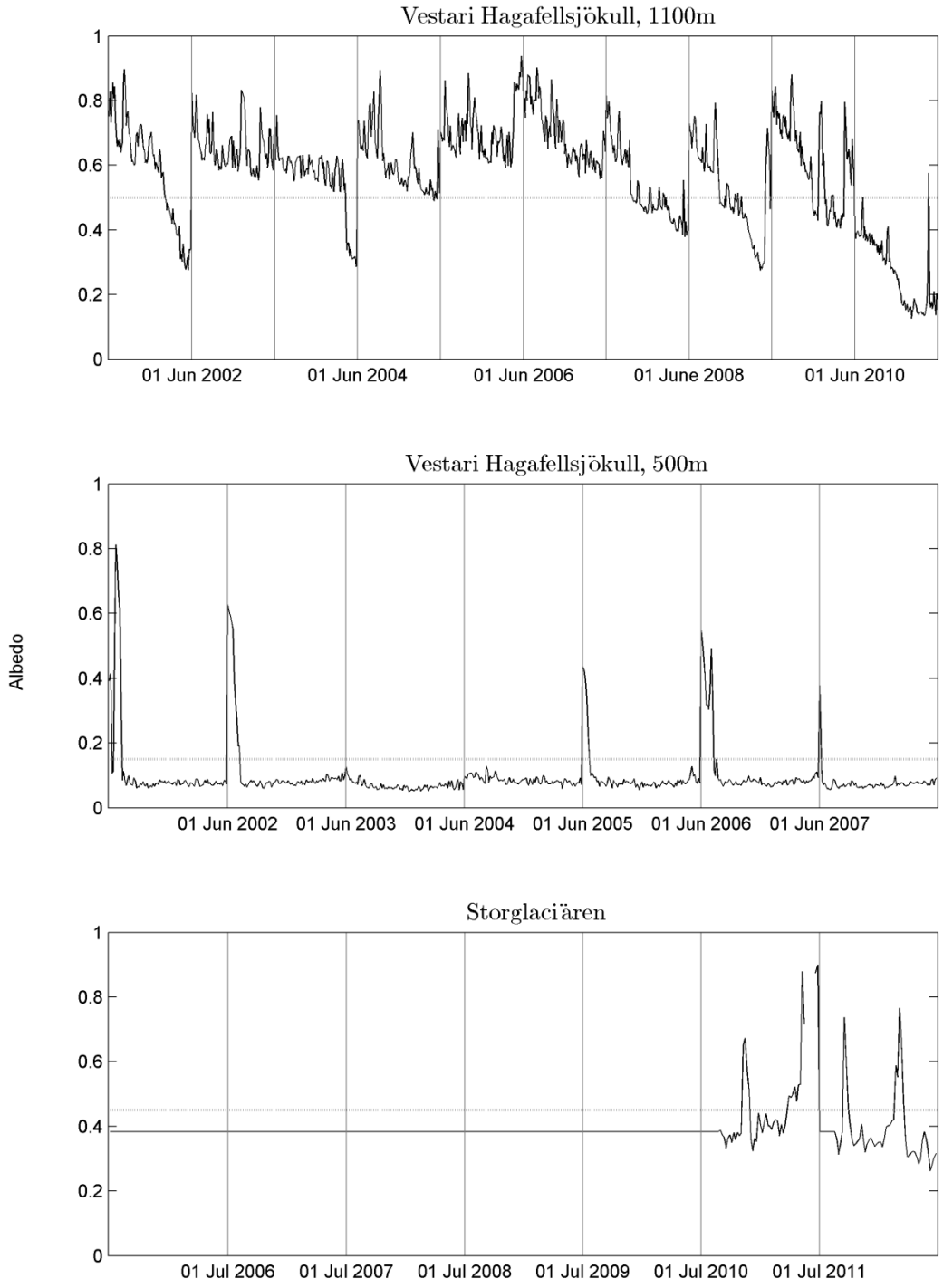

Figure 6.3. Time series of daily albedo. Dotted grey horizontal lines show the critical albedo values used to differentiate between snow and ice cover. Vertical grey lines have the same meaning as in Figure 6.2.Note that the albedo for Storglaciären is constant prior to the 11th of July 2010 because no in-situ observations are available prior to this date (see text in Section 6.3.1 for further details).

In comparison to previous DDFs obtained at Vestari Hagafellsjökull, the values found in this study are somewhat higher than those given by Guðmundsson et al. (2009) and Hodgkins et al. (2012a) (Table 6.2). This may be attributed partly to the slightly different methods of calculating DDFs in each study. Hodgkins et al. (2012a) used surface change measured by an acoustic sounder and estimates of snow/firn density to estimate mass lost to ablation, whilst Guðmundsson et al. (2009) used a combination of energy balance calculations and stake measurements. These differences might contribute to why the factors calculated in this study are slightly higher: DDFs derived from measurements of ablation can be affected by accumulation (i.e. energy which goes into melting summer snowfall will not be recognised); this does not occur when only modelled values are used (as is the case in the present study).

Table 6.2. Degree-day factors previously reported on Vestari Hagafellsjökull. The uncertainty (±) is the standard deviation; the large uncertainty reported by Hodgkins at al. (2012a) is a result of the short period of integration (daily). Units of the DDF are mm w.e. d^{-1} °C^{-1}.

Study	**Period**	$\boldsymbol{DDF_{snow}}$ 500 m	$\boldsymbol{DDF_{ice}}$ 500 m	$\boldsymbol{DDF_{snow}}$ 1100 m	$\boldsymbol{DDF_{firn}}$ 1100 m
Guðmundsson et al. (2009)	2001-2005 May-Sept	8.0 ± 1.6	11.1 ± 1.2	10.8 ± 0.9	11.5 ± 0.4
Hodgkins et al. (2012a)	2003 May-Aug	11.1 ± 5.4	11.8 ± 3.5	12.8 ± 4.5	10.8 ± 6.1

The timing of observations within the melt season is also likely to affect the derived DDFs because there is distinct seasonality of the energy fluxes at Vestari Hagafellsjökull (Guðmundsson et al., 2009). Furthermore, because the DDF is particularly sensitive to changes in surface albedo (Arendt and Sharp, 1999; Hodgkins et al., 2012a), interannual variability of this parameter will influence its value. This may explain the increasing trend of the DDF found at 1100 m on Vestari Hagafellsjökull observed during recent years (Figure 6.2), as the albedo of the summer surface has shown a marked decline, reaching a decadal low in 2010. Decreasing reflectivity of the glacier surface will provide additional melt energy, in the form of greater receipts of absorbed shortwave radiation, which would be independent of air temperature. Consequently, if the partitioning of other terms within the SEB remained constant, this would result in an increase of the DDF required to

relate air temperature to the ablation rate, and would explain the positive trend observed at 1100 m in Figure 6.2.

At Storglaciären, DDFs for both snow and ice found in this study are considerably lower than those at Vestari Hagafellsjökull and fall within the narrower range of DDFs given by Braithwaite (1995b, Table 2; DDF_{snow}: 3 to 5.7 mm w.e. d^{-1} °C^{-1}, and DDF_{ice}: 5.5 to 13.8 mm w.e. d^{-1} °C^{-1}). The values found in this study are also in very close agreement with those given by Hock (1999) for Storglaciären, obtained from air temperature/ablation stake measurements and the tuning of a spatially distributed temperature-index model (Table 6.3). This indicates that temporal variability of the DDFs may possibly be more muted at Storglaciären than at Vestari Hagafellsjökull, as the observed similarity is despite over a decade of separation between the two studies.

Table 6.3 Degree-day factors previously reported on Storglaciären. Units of the DDF are mm w.e. d^{-1} °C^{-1}.

Study	Period	Elevation (m.a.s.l.)	DDF_{snow}	DDF_{ice}
Hock (1999)	5th Jul-7th Sept, 1993	1550	3.2	-
	5th Aug-12 Aug, 1993	1370	-	6.0
	19th Jul-27th Aug, 1994	1370	-	6.4
	9th Jul- 4th Sep, 1994	1250	-	5.4

6.4.2. Regression analysis: spatial variability of the relationship between positive degree-days and energy balance components

Having obtained DDFs for the three locations, the differences in their values could be probed through the regression approach described in Section 6.3.2.2. By regressing PDDs upon ablation and examining the β, α and $N^*/PDDs$ parameters, it is possible to attribute the cause of the different DDFs observed between locations. The individual contributions of each of the energy fluxes to the difference in regression parameters (and therefore the DDF) then helps to provide a physical explanation as to why these differences arise. The results of these regression analyses are communicated in Figure 6.4 and Table 6.4.

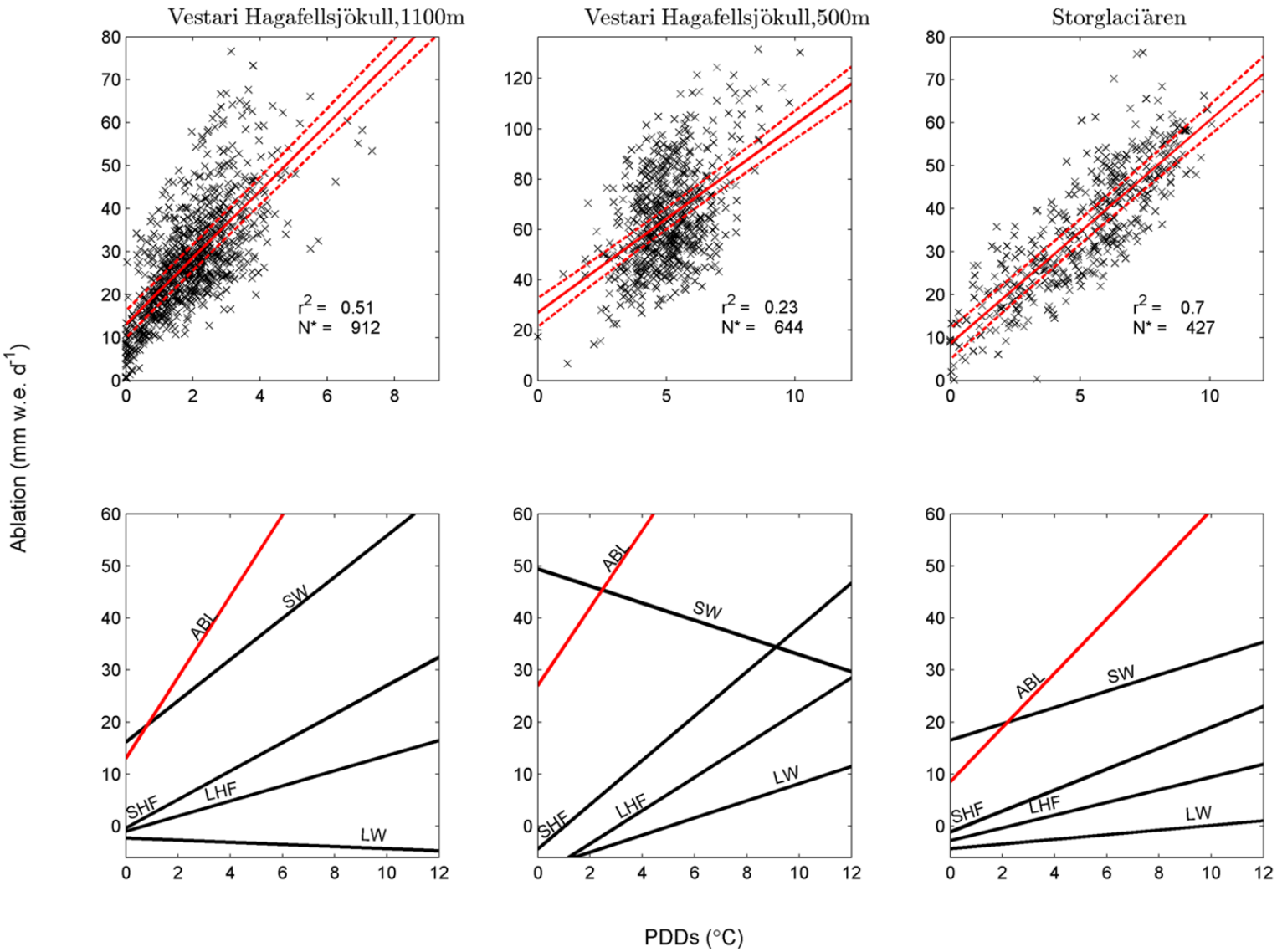

Figure 6.4. Top row: Regression lines relating positive degree days to ablation. The dotted lines give the standard error of the forecast. Bottom row: regressions relating positive degree days to each of the energy fluxes: SHF is the sensible heat flux, LHF is the latent heat flux, SW is shortwave radiation, LW is longwave radiation, and ABL is ablation.

Although DDFs, rather than slope and intercept parameters are usually reported, the values obtained for β and α relating PDDs to ablation itself (i.e. the row labelled 'ablation' in Table 6.4) can be compared to those obtained by Braithwaite and Olesen (1990) who gave regression parameters relating air temperature to ablation on Qamanârssûp and Norbogletscher, Greenland: they found slopes of ~5 to 8.5 mm w.e. d^{-1} $°C^{-1}$ and intercepts ranging between ~2 and ~ 9 mm w.e. d^{-1}. The slopes (β) obtained in the present study are therefore consistent with these values, but the intercepts (α) found for Qamanârssûp and Norbogletscher are somewhat lower than observed at Vestari Hagafellsjökull.

Table 6.4. Regression parameters relating positive degree-days to ablation and energy fluxes. Units of β are mm w.e. d^{-1} $°C^{-1}$ and units of α are mm w.e. d^{-1}.

	Vestari Hagafellsjökull, 1100 m			**Vestari Hagafellsjökull, 500 m**			**Storglaciären**		
	β (slope)	α (intercept)	$(N^*/PDDs)$	β	α	$(N^*/PDDs)$	β	α	$(N^*/PDDs)$
Ablation	8.0	12.6	0.52	7.4	27.0	0.20	5.3	8.3	0.19
SHF	2.7	-0.4	-	4.3	-4.4	-	2.0	-1.1	-
LHF	1.5	-1.0	-	3.2	-9.7	-	1.2	-2.8	-
SW	4.0	16.2	-	-1.6	49.4	-	1.6	16.5	-
LW	-0.2[a]	-2.3	-	1.6	-8.3	-	0.4	-4.3	-

With regards to the variability of the DDF found between different elevations on the ice cap, it is evident that the higher value obtained at the upper station can mainly be attributed to the ratio of $N^*/PDDs$: the term $\alpha(N^*/PDDs)$ accounts for ~66% of the difference between the DDFs, and is caused by the effect of the larger ratio $N^*/PDDs$ at 1100 m (2.6 times larger) outweighing the larger α at 500 m (2.1 times larger). This finding is in agreement with Ambach (1988a), Braithwaite (1995b), and Zhang et al. (2006) who outline the decrease of DDFs that occur as temperatures decrease. Braithwaite (1995b) explains this behaviour as being attributable to the fact that the ratio $(N^*/PDDs)$ decreases as temperatures rise, leaving the effect of α on the DDF to diminish progressively. The substantially lower DDF found for Storglaciären can be explained by a lower α term, which only reaches 66% and 30% of the values found at 1100 m and 500 m on Vestari Hagafellsjökull, respectively. In addition, the ratio $N^*/PDDs$ is much lower on Storglaciären than at the higher elevation station on Vestari Hagafellsjökull (only reaching 37% of its value). Although contributing to the

difference in DDFs to a lesser extent between glaciers, the temperature sensitivity to ablation (β) is also universally higher on the ice cap.

Exploring the physical explanation for the difference in the α and β regression parameters on Vestari Hagafellsjökull through examining the individual contributions from each energy flux, shows that slightly different regimes operate at these two elevations. For the turbulent heat fluxes (SHF and LHF), it is clear that there is greater sensitivity to air temperature (i.e. larger β) at the lower elevation AWS. Braithwaite and Olesen (1990) found a similar difference between the sensitivity of the sensible heat flux to temperature at Qamanârssûp and Norbogletscher, Greenland. The authors attributed this difference to greater wind speeds at Qamanârssûp, which increased the sensitivity of the sensible heat flux to temperature. The same explanation does not appear to be suitable at Vestari Hagafellsjökull, because differences between wind speeds at these two elevations are equal (5.46 m s^{-1}: see Chapter 2, Section 2.5.1).

An alternative explanation may be the different surface roughness lengths used to evaluate the turbulent heat fluxes between sites. At 500 m, the glacier surface is invariably ice, which has a greater roughness length than for the snow and firn that cover the glacier at 1100 m (Chapter 2, Section 2.4). The effect of this is to increase the exchange coefficient relating temperature to sensible heat exchange, making this flux more sensitive to $PDDs$ at 500 m. Latent heat transfer is similarly affected by the larger exchange coefficient, and because the partial pressure of water vapour is strongly collinear with temperature, its sensitivity to $PDDs$ is also higher at the lower elevation station.

The relationship between the radiative fluxes and temperature also varies between the two elevations, and perhaps most notable is the difference in the sensitivity of the shortwave radiative flux to temperature. A positive relation is found at 1100 m, whereas a slightly negative association prevails at the lower station. It is this difference which actually contributes most to the overall greater temperature sensitivity (i.e. the global β parameter) of ablation at 1100 m. At the higher station, the positive gradient can mainly be attributed to the relationship between reflected shortwave radiation and temperature, as albedo at 1100 m is correlated with PDDs (r = -0.38, p <0.01, n = 920). This correlation is partly due to the seasonality of albedo: June is the coldest month and has the highest albedo (mean albedos are 0.66, 0.56 and

0.49 for June, July and August, respectively) because the winter snowpack is generally still present in this month (Figure 6.3). In addition, throughout the season, summer snowfalls are more likely to occur when temperatures are lower, which will contribute to the negative association between PDDs and albedo (Sicart et al., 2008). The relationship between albedo and temperature then propagates to net-shortwave radiation to explain the positive gradient observed at 1100 m in Table 6.4; there is no significant correlation between incident shortwave radiation and PDDs at 1100 m (r = 0.04, p = 0.19, n = 920).

The negative gradient of the regression slope for shortwave radiation at 500 m (Figure 6.4; Table 6.4) is a result of the incident flux being weakly negatively correlated with PDDs (r = -0.17, p <0.01, n = 644). This correlation—which is absent at the higher station—can most likely be explained by the role of katabatic drainage. The analysis in Chapter 5 illustrated how katabatic winds are enhanced when high pressure prevails, and during such conditions, it is likely that incident shortwave radiation will be increased, due to subsidence and adiabatic expansion of descending air (Einarsson, 1984). In the absence of a rise in ambient air temperatures to accompany periods of high pressure, lower elevations will cool as air flowing under katabatic drainage exchanges sensible heat with the melting glacier. This mechanism is sufficient to introduce a negative association between PDDs and net shortwave radiation, as albedo is largely invariant at this elevation (Figure 6.3).

The difference between the temperature-independent parameters for shortwave radiation (α) (which represent the contribution of these fluxes to ablation when PDDs are zero), simply reflects the higher net shortwave radiation at 500 m; although, it is interesting to observe that incident shortwave radiation is actually greater at 1100 m (means of 221 W m^{-2} and 177 W m^{-2} at 1100 and 500 m respectively—see Chapter 2, Section 2.5.1), but the much lower albedo at 500 m (~0.1, compared to ~0.57 at 1100 m) more than compensates for this difference.

The gradients and intercepts relating longwave radiation to PDDs are the most challenging to interpret physically at Vestari Hagafellsjökull, due to the complexity of processes that govern the incident longwave heat flux, which is affected by cloud cover, atmospheric moisture content and temperature in a non-linear way (Sedlar and Hock, 2009). The gradient found for 1100 m is insignificantly different from zero, and probably reflects the greater importance of cloud cover, rather than temperature, in modulating the longwave flux higher on the glacier, as clouds are more intermittent at 1100 m (Guðmundsson et al., 2009). The smaller intercept for 500 m can likely be explained by the lower humidity which prevails here (mean relative humidity of 0.84 at 500 m and 0.93 at 1100 m), which will reduce the transmissivity of the atmosphere and lower the incident longwave flux (Sedlar and Hock, 2009).

At Storglaciären, the sensitivity of the turbulent heat fluxes is somewhat lower than at Vestari Hagafellsjökull. Again, this is mainly due to a smaller roughness length for ice on Storglaciären (2.7 mm, compared to 10 mm on Vestari Hagafellsjökull). However, the slower wind speeds that persist here may also contribute to this lower temperature sensitivity (mean wind speed of 2.92 m s^{-1}). The turbulent heat fluxes depend on the *product* of the temperature/vapour pressure gradient *and* the wind speed; hence, lower wind speeds can have the same effect as a smaller roughness length, reducing the effective exchange coefficient relating the quantities' gradient (water vapour of temperature) to the surface flux.

Regressions at Storglaciären are also characterised by positive relationships between PDDs and both the longwave and shortwave radiative heat flux components. The positive gradient relating the shortwave radiative flux to temperature cannot be attributed to albedo variations; instead, this association is due to a significant correlation between PDDs and incident shortwave radiation ($r = 0.22$, $p < 0.01$, $n = 429$). These results are in agreement with Sicart et al. (2008) who reported positive correlation coefficients between temperature and the radiative energy components observed from field observations on Storglaciären.

6.4.3 Synoptic climatology and degree-day factors

Having assessed the causes of DDF variability between locations, temporal variability was addressed by exploring how the DDF changes as a function of the prevailing weather. To facilitate this, the same regression analyses used to explore spatial variability of the DDF in Section 6.4.2 were applied.

The resulting DDFs calculated for each of the weather categories are given in tables 6.5 to 6.7. These values reveal the DDF to be highly variable between synoptic weather types. With regards to Vestari Hagafellsjökull, this variability (as given by the standard deviation) is more pronounced at 1100 m. There is, however, appreciable coherence for weather categories' DDFs between elevations, as indicated by a statistically significant correlation between weather categories' DDFs observed at 500 m and 1100 m ($r = 0.59$, $p < 0.01$, $n = 23$). This agreement is in spite of the somewhat different relationships between PDDs and SEB components noted at these two locations (Section 6.4.2) and suggests that the synoptic control on the DDF is strong.

Observations of DDFs for each weather category at Storglaciären also exhibit pronounced variability, exceeding the standard deviation found at 1100 m on the ice cap; however, this is mainly the result of the very high DDF found for Category S10 (137 mm w.e. d^{-1} $°C^{-1}$). If the results from Category S10 are discounted, then the standard deviation falls to only 1 mm w.e. $°C^{-1}d^{-1}$ which is appreciably lower than at either site on Vestari Hagafellsjökull.

The reason for the conspicuously high DDF found for Category S10 can be attributed to the low temperatures associated with this weather type, as less than one PDD was cumulated through the five days in this category. Yet despite these cool temperatures, the SEB calculations predict that positive receipts of net radiation caused some melting to occur on each day (~9 mm w.e to 13 mm w.e.). The result of this melting in the presence of low temperatures, means that the ratio of days on which melting occurs, to the cumulative positive degree-day total ($N^*/PDDs$) becomes large. This subsequently increases the DDF considerably by amplifying the contribution of the temperature independent component (α) to the DDF (Equation 6.4).

Table 6.5. Weather categories' regression parameters for Vestari Hagafellsjökull, 1100 m. *Indicates regression parameter is significantly different from zero at p = 0.05.[a] Gives the percentage of the degree day factor contributed by the term $\alpha(N^*/PDDs)$. Note that 'r' in column two is the Pearson's product-moment correlation coefficient. Units of the DDF are mm w.e. d^{-1} °C^{-1}.

Weather Category	r	β (mm w.e.°$C^{-1}d^{-1}$)	α (mm w.e. d^{-1})	$N^*/PDDs$	DDF	[a]% $\alpha(N^*/PDDs)$	n
V1	0.9	**9.2***	**7.5***	1.1	17.8	46.3	36
V2	-	-	-	-	-	-	<5
V3	0.61	**18.1***	**7.1***	8.1	76	75.7	32
V4	0.66	**6.5***	**11.2***	0.7	14.8	53	57
V5	0.44	**2.2***	**41.8***	0.2	10.9	76.7	21
V6	-	-	-	-	-	-	<5
V7	0.37	**5.5***	**18.7***	0.4	13.4	55.8	89
V8	0.28	**2.6***	**19.0***	0.5	11.5	82.6	64
V9	0.69	**7.0***	**11.5***	0.7	15.1	53.3	24
V10	0.52	**6.8***	**14.7***	0.6	15.2	58	99
V11	0.16	4.1	35.9	0.3	14.9	72.3	9
V12	0.41	5.8*	22.5	0.4	14.2	63.4	92
V13	-	-	-	-	-	-	<5
V14	0.71	**16.1***	6.5	0.6	20.2	19.3	8
V15	0.22	3.5	**21.9***	0.8	21.6	81.1	54
V16	0.5	**8.6***	**14.6***	0.7	18.4	55.5	70
V17	-0.06	-0.9	**38.5***	0.3	9.6	120.3	14
V18	0.12	1.8	**20.3***	0.9	20.7	88.3	24
V19	0.73	**13.6***	6	1.7	24.1	42.3	12
V20	0.79	**7.9***	**9.1***	0.9	15.8	51.8	17
V21	0.97	**13.2***	1.9	0.4	13.9	5.5	6
V22	0.94	**11.7***	**5.3***	0.6	14.6	21.8	21
V23	0.16	2.1	**30.9***	0.3	12	77.3	64
V24	0.59	**11.9***	6.7	0.5	15	22.3	22
V25	0.2	2.2	**21.1***	1.2	26.7	94.8	9
V26	0.76	**7.7***	**9.5***	1	17.2	55.2	34
V27	0.92	**10.5***	**8.9***	0.5	15.2	29.3	24
V28	0.79	10.4	5.3	0.3	12	13.3	6
V29	-	-	-	-	-	-	<5
V30	-	-	-	-	-	-	<5
Mean	0.53	7.5	15.9	0.9	18.4	56.6	-
Stdv.	0.52	7.5	16.2	0.9	12.7	27.9	-

Table 6.6. Weather categories' regression parameters for Vestari Hagafellsjökull, 500 m. See Table 6.5 caption for further information and details of * and [a] symbols.

Weather Category	r	β (mm w.e.°C^{-1}d^{-1})	α (mm w.e. d^{-1})	$N^*/PDDs$	DDF	[a]% $\alpha(N^*/PDDs)$	n
V1	0.75	**10.7***	0.3	0.2	10.7	0.6	29
V2	-	-	-	-	-	-	<5
V3	0.4	8.2	**25.2***	0.4	18.3	55.1	21
V4	0.55	**10.0***	**22.3***	0.2	15.2	29.3	44
V5	0.13	1.5	**100.7***	0.1	13.7	73.5	12
V6	-	-	-	-	-	-	<5
V7	0.31	**4.8***	**37.0***	0.2	11.4	64.9	67
V8	0.4	**5.0***	**25.3***	0.2	9.4	53.8	55
V9	0.42	6.4	22.2	0.2	10.9	40.7	16
V10	-0.13	-2.2	**66.8***	0.2	12.3	108.6	59
V11	0.53	10.1	33.5	0.2	15.4	43.5	6
V12	0.37	**6.5***	**48.2***	0.2	15.2	63.4	64
V13	-	-	-	-	-	-	<5
V14	0.49	15.4	3	0.2	16	3.8	5
V15	0.02	0.4	**64.5***	0.2	15.3	84.3	39
V16	0.09	2	**55.2***	0.2	13.6	81.2	55
V17	-0.19	-4.4	109.1	0.2	12.8	170.5	9
V18	0.06	1.5	42.4	0.3	12.9	98.6	16
V19	0.44	14.8	9.3	0.3	17.5	15.9	8
V20	0.75	**9.4***	12.1	0.2	12.3	19.7	13
V21	-	-	-	-	-	-	<5
V22	0.8	**11.3***	3.5	0.2	11.9	5.9	16
V23	-0.22	-4.9	**98.3***	0.2	12.1	162.5	34
V24	-0.19	-3.4	**83.6***	0.2	12.7	131.7	15
V25	-0.04	-0.8	70.5	0.2	15.1	93.4	6
V26	0.42	**5.9***	22.5	0.2	10.8	41.7	26
V27	0.84	**11.2***	4.6	0.2	12	7.7	17
V28	-	-	-	-	-	-	<5
V29	-	-	-	-	-	-	<5
V30	-	-	-	-	-	-	<5
Mean	0.30	5.2	41.7	0.2	13.4	63.1	-
Stdv.	0.33	6.0	33.7	0.1	2.3	48.5	-

Table 6.7. Weather categories' regression parameters for Storglaciären. See Table 6.5 caption for further information and details of * and [a] symbols.

Weather Category	r	β (mm w.e.°C^{-1}d^{-1})	α (mm w.e. d^{-1})	$N^*/PDDs$	DDF	[a]% $\alpha(N^*/PDDs)$	n
S1	-	-	-	-	-	-	<5
S2	0.44	4.5	16.5	0.3	8.7	56.9	15
S3	0.38	**3.5***	20.2	0.1	6.3	32.1	30
S4	0.76	**6.4***	-1	0.1	6.3	-1.6	65
S5	0.51	3.2	**22.9***	0.2	7.4	61.9	13
S6	0.69	**5.5***	**10.9***	0.2	7.9	27.6	48
S7	0.78	**5.3***	2.5	0.2	5.7	8.8	32
S8	0.7	**9.5***	-19.4	0.2	6.4	-60.6	33
S9	0.88	**5.4***	3.4	0.2	6.2	11	46
S10	0.68	12.9	**9.0***	13.8	137.1	90.6	5
S11	0.7	**4.3***	**12.6***	0.4	9	56	46
S12	0.88	**8.7***	-19	0.1	6.1	-31.1	10
S13	0.89	**6.4***	5.3	0.3	8.1	19.6	11
S14	-	-	-	-	-	-	<5
S15	0.43	2.1	37.1	0.1	6.7	55.4	19
S16	0.87	9.2	-7.5	0.2	7.9	-19	5
S17	0.69	**4.6***	**8.5***	0.4	8.2	41.5	22
S18	-	-	-	-	-	-	<5
S19	0.6	6.7	-1.5	0.2	6.5	-4.6	5
S20	-	-	-	-	-	-	<5
S21	-0.12	-1.4	**61.0***	0.1	6.8	89.7	15
Mean	0.63	5.70	9.50	1.01	14.8	25.5	-
Stdv.	0.25	3.25	19.42	3.29	31.5	41.5	-

Although the contribution of the ratio $N^*/PDDs$ to Category S10's DDF is considerable, it is not unprecedented: ratios exceeding unity are also found at 1100 m on Vestari Hagafellsjökull. When multiplied by the temperature-independent component of the regression equation (α in Equation 6.4), this term contributes to more than 100% of the DDF's value in some weather categories at both elevations on the ice cap (tables 6.5 and 6.6).

Considering the widespread use of temperature-index models, and in particular, their previous application to both Vestari Hagafellsjökull and Storglaciären (e.g. Guðmundsson et al., 2009; Hodgkins et al., 2012a; Hock, 1999; Radić and Hock, 2006; Radić and Hock, 2011), perhaps one of the most striking results in tables 6.5 to 6.7 is the considerable spread of correlation coefficients that is observed for all locations (Figure 6.5, top). Indeed, temperature is not significantly correlated with ablation (at p = 0.05) in ~28% and ~61% of weather categories at 1100 m and 500 m on Vestari Hagafellsjökull, and is similarly absent in ~41% of weather categories at Storglaciären—these categories account for ~20%, 47% and 15% of all days, at the respective glaciers. Whilst some of this variability in correlation may be the result of variable glacier surface conditions, particularly albedo at 1100 m on Vestari Hagafellsjökull (which will affect the SEB independently of weather type), this will not affect the correlation coefficients observed for the other two locations, as ice exposure is almost continuous and albedo nearly invariant at these places (Figure 6.3).

Examining the variability of regression parameters between elevations on Vestari Hagafellsjökull, illustrates that the coherence found between weather categories' DDFs is observed similarly for the regression parameters (Figure 6.5, bottom). This correlation is unsurprising, considering the relationship between the DDF and the intercept/gradient terms (Equation 6.4), and the correlations reported between DDFs; however, it is important to note that α and β are both correlated more strongly between locations than DDFs are. The relatively good agreement between these regression parameters therefore reinforces the statement that synoptic climatic variability is an important control on the energy partitioning within the SEB and thus the relationship between temperature and ablation.

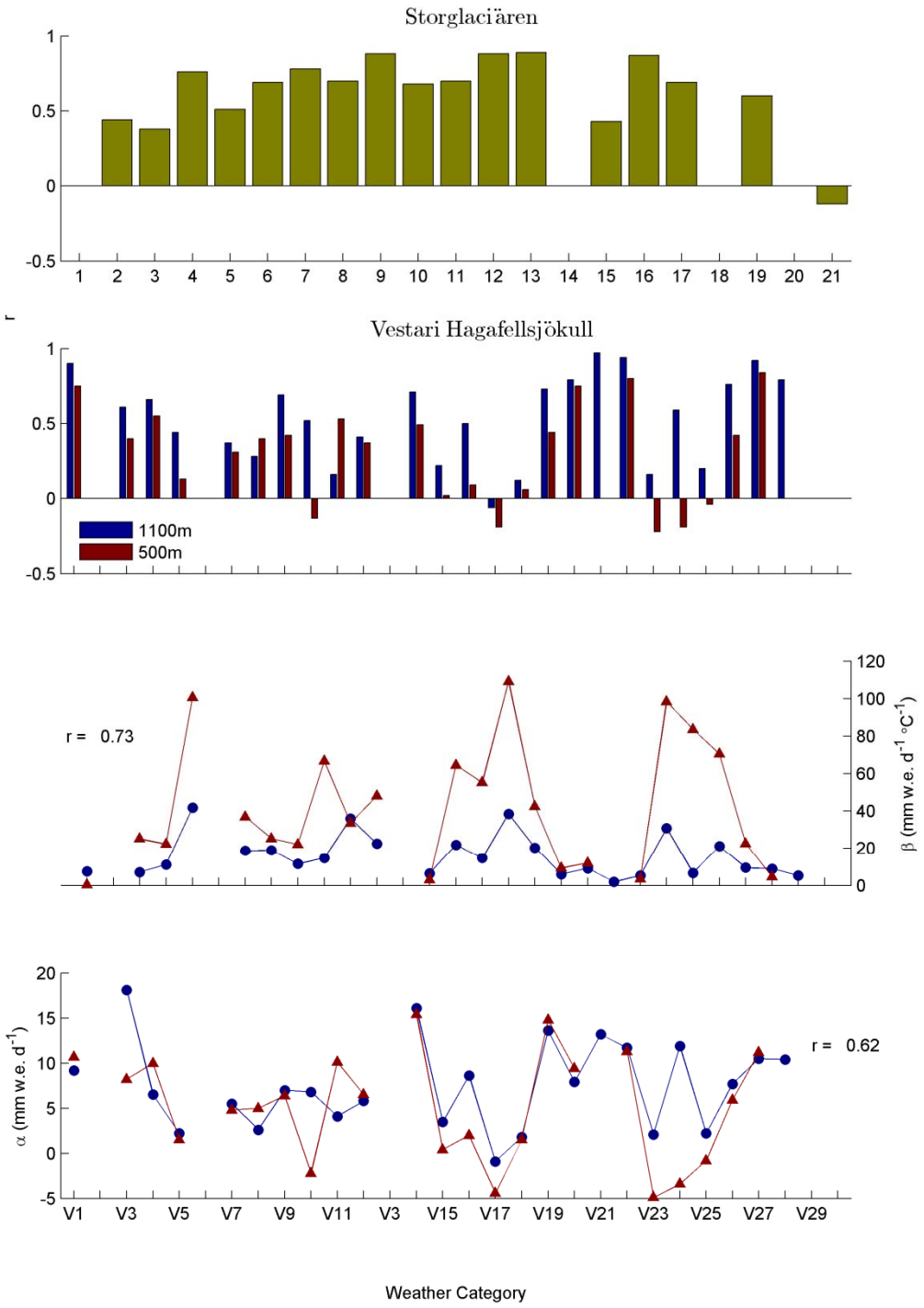

Figure 6.5. Pearson's product-moment correlation coefficients (r) between *PDDs* and ablation (top) and comparison of regression parameters relating *PDDs* to ablation at 1100 m and 500 m on Vestari Hagafellsjökull (bottom). Note that the colours used to identify the 1100 m and 500 m stations are the same in the bar and line plots.

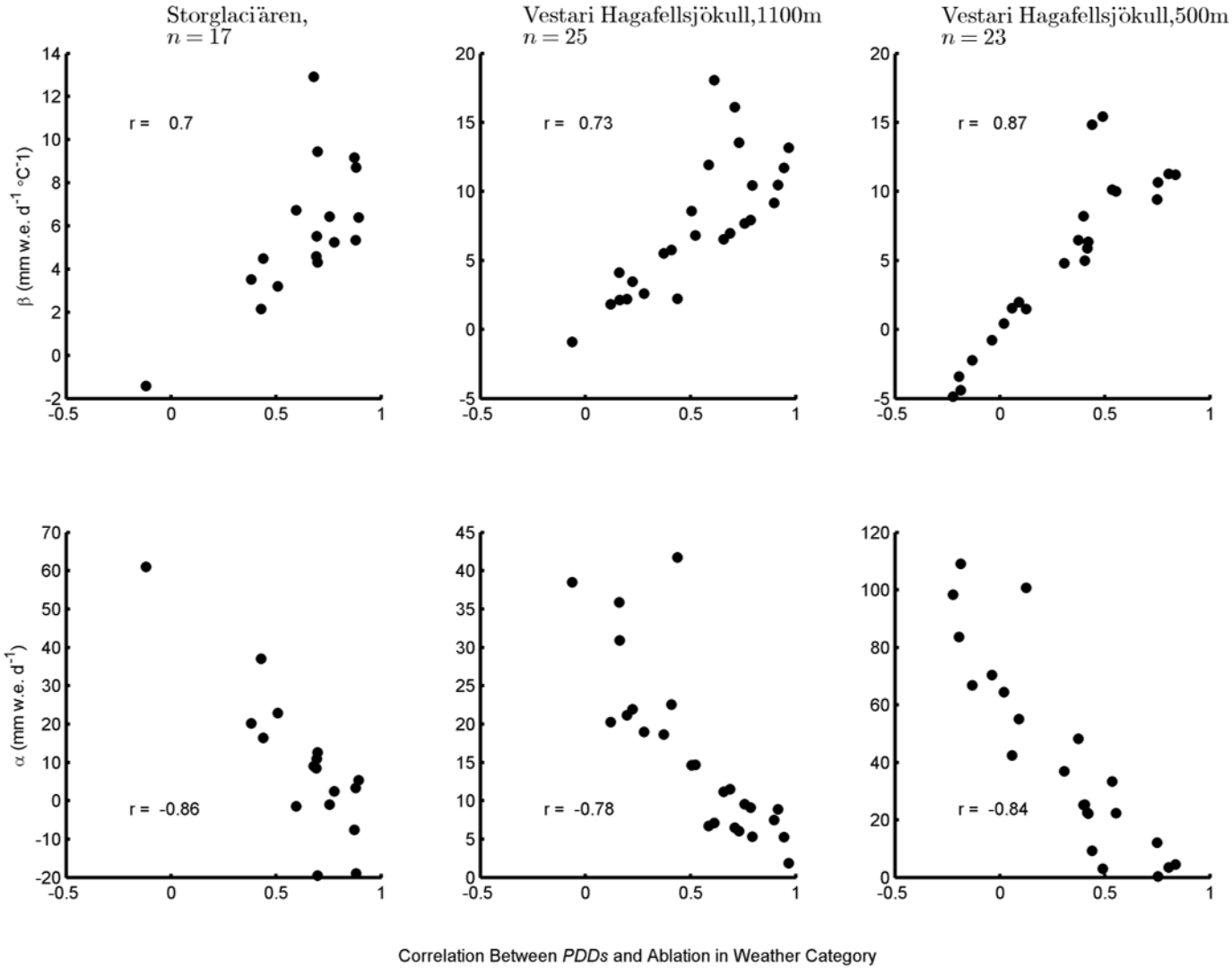

Figure 6.6. Bivariate scatter plots illustrating the relationship between regression parameters and the Pearson's product-moment coefficient (describing the correlation between *PDD*s and ablation) for each weather category. The coefficients (r) indicated in text on each graph show the correlation between regression parameters and the Pearson's coefficients for each location.

Closer examination of tables 6.5 to 6.7 also indicates that the correlation between ablation and $PDDs$ is dependent on the gradient of the slope parameter for each weather category (Figure 6.6, top). In addition, the intercept term is inversely related to the correlation coefficient (and therefore the gradient; Figure 6.6, bottom). This tendency was also noted by Braithwaite (2011) and seems to reflect mainly the fact that regression lines approach horizontal when correlation is diminished. Under these conditions, the intercept term approaches the value of the mean ablation during the weather category. It should also be acknowledged that Braithwaite (2011) suggested changes in the prevailing weather were likely to be responsible for variations of the regression parameters relating ablation to positive air temperatures.

Because the slope parameter quantifies the sensitivity of ablation to a change in temperature, and because it is also positively related to the ability of temperature to explain ablation (i.e. the correlation coefficient), its value is particularly important with regards to simulating the response of glacier ablation to a warming climate. For this reason, variability of β values between weather categories was explored in greater detail by examining the wider-scale synoptic circulation and SEB characteristics of weather categories identified by contrasting values of this parameter. To facilitate this further examination, only 'frequent' types were considered. This decision was taken because it is considered important to understand variability of the sensitivity of temperature to ablation within weather categories that occur more often, as these types have a greater overall effect on ablation. Frequent types were defined as those categories which contained more than n/N days at each location, where n is the number of days categorized, and N is the total number of weather categories (note that weather categories consisting of <5 days were excluded when calculating this ratio). Applying this rule resulted in the recognition of 7 'frequent' weather categories for Storglaciären and 8 categories for Vestari Hagafellsjökull. Contrasting β values within this subset of types were then identified statistically, by testing the significance of the difference between weather categories' β values; this was achieved by calculation of the test statistic, t:

$$t = \frac{\beta_i - \beta_j}{\sqrt{{SE_i}^2 + {SE_j}^2}}\ , \qquad 6.8$$

where i and j denote weather category, and take on 7 different values at Storglaciären, and 8 at Vestari Hagafellsjökull (corresponding to the number of frequent types at either location), and SE is the standard error of the β parameter in the regression equation relating $PDDs$ to ablation in the respective weather categories. t values of the difference in β values are therefore calculated for each possible pair of weather categories.

At Storglaciären, 5 of the 21 possible differences between β values yielded t values which were statistically significant (two-tailed test with n-4 degrees of freedom, and p = 0.05); at Vestari Hagafellsjökull, 6 (at 1100 m) and 10 (at 500 m) of the 28 possible comparisons produced t values which were statistically significant (tables 6.8 and 6.9). It is suggested that this larger contrast between weather categories' β values observed at 500 m on Vestari Hagafellsjökull than higher on the ice cap, may be related to the more changeable surface conditions at the higher elevation station. This is considered probable because the pronounced variability of albedo at this location (Figure 6.3) affects the temperature-ablation relationship independently of the prevailing weather, which in turn may reduce the signal to noise ratio examined by the Student's t-test. Further, it should be considered that the ice-surface at the 500 m station may be inherently more sensitive to changes in the SEB which occur as a function of prevailing weather categories, than the snow/firn surface found at higher elevations.

Acting on the information in tables 6.8 and 6.9, two contrasting weather categories were chosen for each location for detailed examination. At Storglaciären, categories S3 and S8 were selected, based on the fact that these frequent types had the largest significant difference in β values (tables 6.7 and 6.8); for Vestari Hagafellsjökull, V4 and V23 were chosen, because the difference in β between these categories was significant at both elevations, and the direction of this difference was also consistent (tables 6.5 to 6.6 and Table 6.9). In discussion of the comparisons, categories are denoted 'higher β' and 'lower β', in reference to the relative value of their respective β values.

Table 6.8. *t* values for the difference of weather categories' β values on Storglaciären. Asterisked values in bold are significant at $p = 0.05$.

Weather Category	S3	S4	S6	S7	S8	S9	S11
S3	-						
S4	1.66	-					
S6	1.10	0.82	-				
S7	0.97	1.13	0.25	-			
S8	**2.50***	1.61	2.03	**2.21***	-		
S9	1.09	1.31	0.19	0.11	**2.29***	-	
S11	0.45	**2.18***	1.13	0.92	**2.76***	1.30	-

Table 6.9. *t* values for the difference of weather categories' β values on Vestari Hagafellsjökull. Convention for indicating significant *t* values is the same as Table 6.8. Grey shading indicates values obtained for the 500 m station, and the section of table with no shading provides *t* values for the 1100 m station.

Weather Category	V4	V7	V8	V10	V12	V15	V16	V23
V4	-	1.75	1.80	**3.81***	1.14	**2.12***	**2.08***	**3.37***
V7	0.56	-	0.08	**2.43***	0.61	1.01	0.78	**2.31***
V8	**2.56***	1.55	-	**2.67***	0.58	1.09	0.87	**2.43***
V10	0.18	0.69	**2.60***	-	**2.88**	0.59	1.11	0.61
V12	0.45	0.12	1.77	0.59	-	1.38	1.21	**2.66***
V15	1.31	0.80	0.36	1.40	0.92	-	0.32	0.98
V16	1.00	1.32	**2.81***	0.84	1.26	1.85	-	1.42
V23	**2.27***	1.53	0.24	**2.34***	1.70	0.50	**2.65***	-

Figure 6.7 illustrates the different β values between the weather categories targeted for further examination. At the bottom of this figure, the contributions to these differences from the individual energy fluxes are also quantified (through application of Equation 6.7). It is evident from these data that the net shortwave radiation is largely responsible for the difference in β values at both locations, especially so at Vestari Hagafellsjökull, where the steeper regression line relating $PDDs$ to net shortwave radiation accounts for >100% of the difference in β. This can be explained by the significant correlation between incident shortwave radiation and $PDDs$ which is observed during Category V4 at both locations (r = 0.29, $p = 0.029$, and r = 0.35, $p = 0.02$ at 1100 m and 500 m, respectively); in Category V23, negative correlations are observed (r = -0.26, $p = 0.04$, and r = -0.34, $p = 0.05$ at 1100 m and 500 m, respectively).

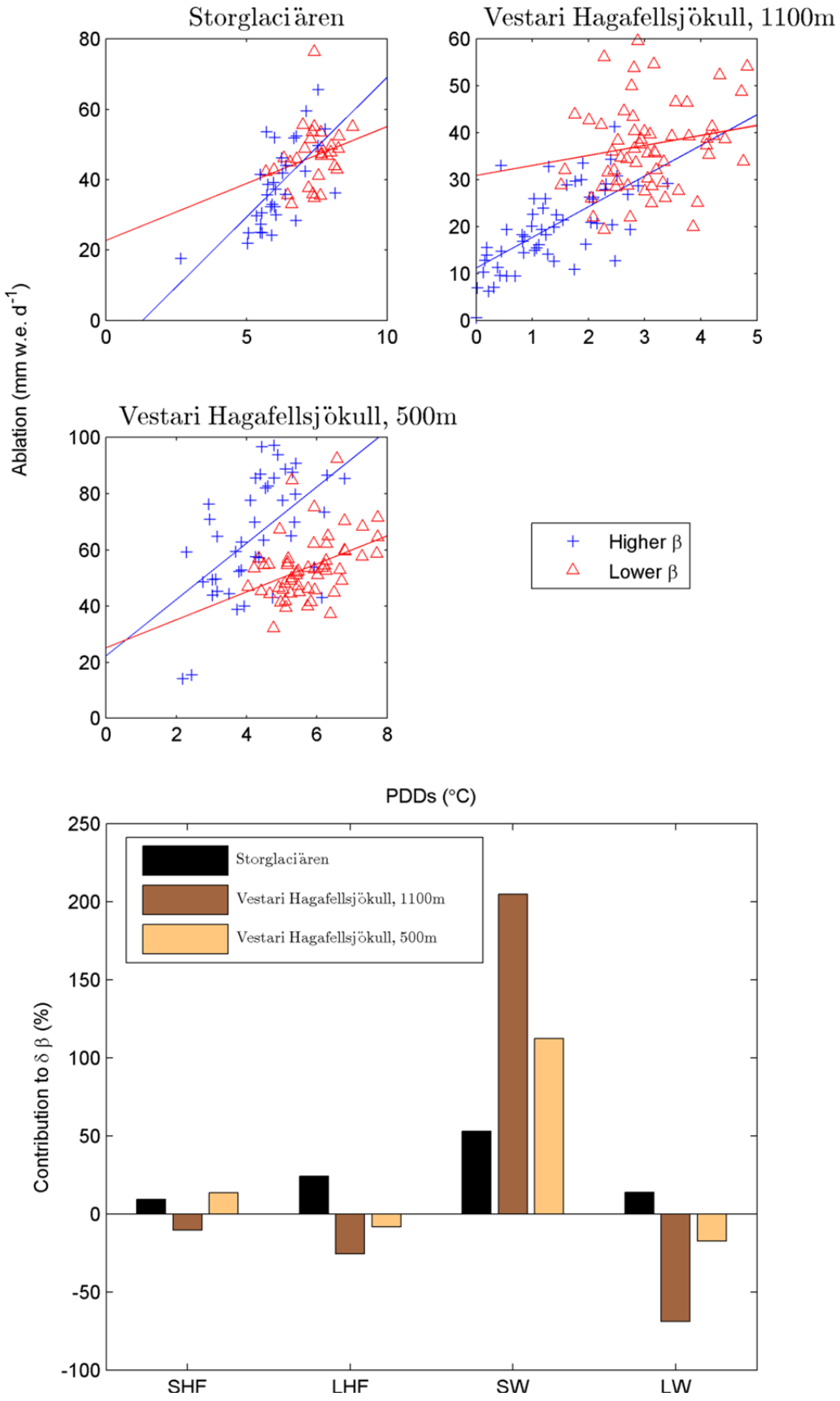

Figure 6.7. Top: regression of *PDDs* on ablation for those weather categories with contrasting β values (see text for details). Bottom: % contribution from each of the energy fluxes to the overall difference between β values (higher β – lower β; see Equation 6.7 for further details).

Air temperature effectively has a higher 'information content' during Category V4, as a consequence of acting as a partial index of shortwave radiation (e.g. Lang, 1968). Physically, this positive association between $PDDs$ and incident shortwave radiation is suggested to be the result of radiative heating of the glacier environs, and the subsequent advection of heat over the glacier. This explanation is supported by the fact that $PDDs$ are more strongly correlated with incident shortwave radiation during this category's occurrence at 500 m, which is closer to the glacier margin, and therefore more exposed to horizontal heat advection (e.g. Wendler, 1975; Hannah et al., 2000). Figure 6.8 shows that these conditions result from a ridge of high pressure extending over Iceland, producing clear skies, as indicated by the high and low receipts of short-and longwave radiation, respectively. Air temperatures are also relatively supressed during this category, owing to the north-westerly wind direction which occurs; a low over the British Isles also ensures these winds are quite brisk. Category V23, in which the correlation between $PDDs$ and incident shortwave radiation is negative, is characterised by contrasting conditions: mean air-flow is from the south west, which results in more humid air, and cloudier skies. Passage over the warm waters of the North Atlantic also ensures this weather category is associated with higher air temperatures than are observed in Category V4.

At Storglaciären, the reason for the difference in the contribution of the shortwave heat flux to β between the two categories targeted for further analysis (categories S3 and S8) is less evident. The high air pressures and clear skies associated with Category S3 do not result in a similar association between air temperature and shortwave radiation observed at Vestari Hagafellsjökull in Category V4 (correlation between air temperature and incident shortwave radiation in Category S3 = 0.03, p = 0.9). The role of the other energy fluxes in contributing to the difference of β between categories is also more pronounced at Storglaciären; the relatively low pressure and cyclonic curvature of Category S8 results in universally higher temperature sensitivities of all the energy fluxes.

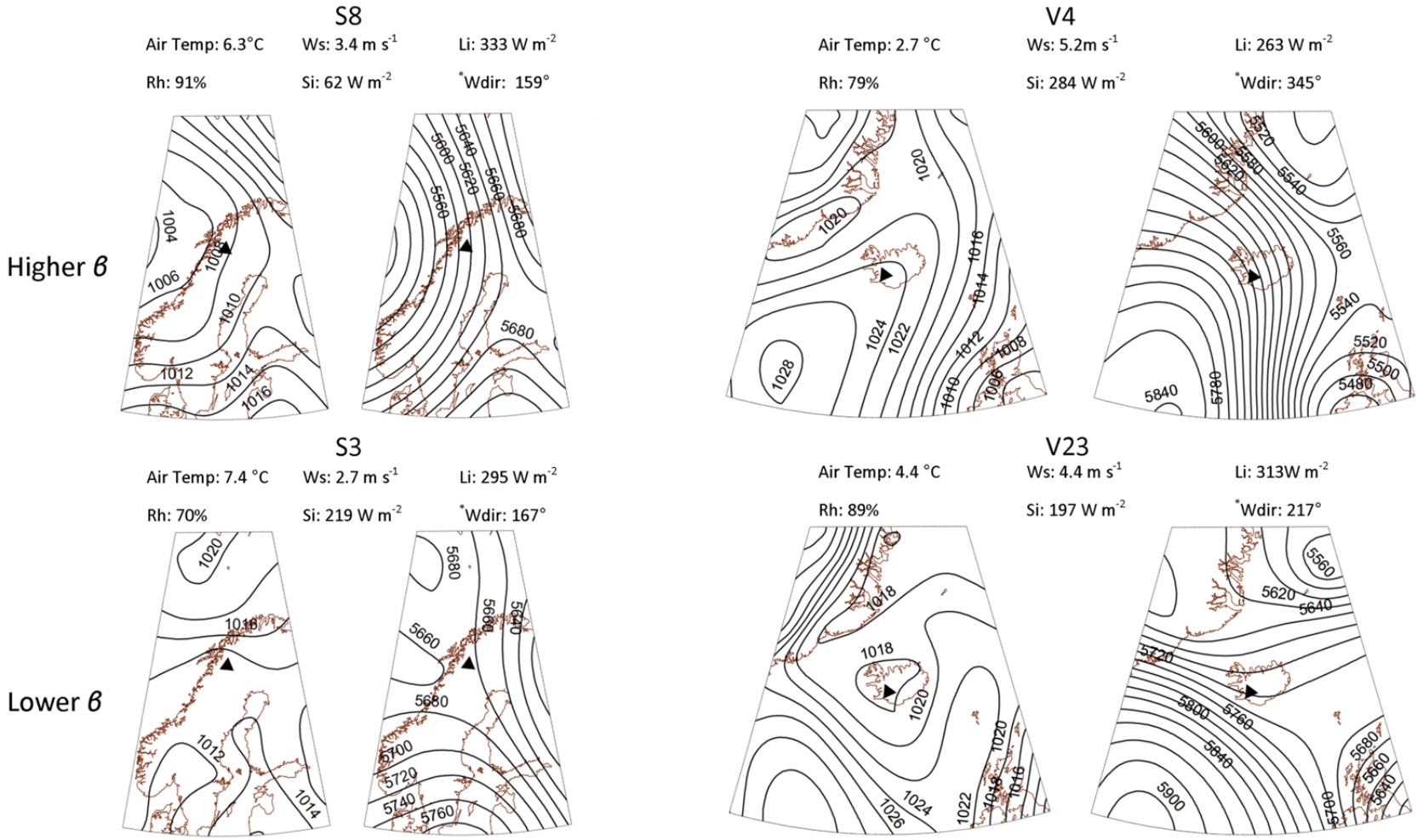

Figure 6.8. Synoptic plots of weather categories with contrasting β values (see Chapter 5, Figure 5.3 for an explanation of how plots are generated). For each weather category (labelled above charts), the left-hand side gives the mean sea level pressure (hPa), and the right-hand side provides the height of the500 hPa surface (metres). Annotations above plots provide the mean glacier meteorology (average of higher and lower AWS data at Vestari Hagafellsjökull): Rh is relative humidity, Ws is wind speed, Si and Li are incident shortwave and longwave radiation, respectively. *Wdir is 10m wind direction taken from the ERA interim data described in Chapter 4. Glacier locations are indicated by black triangles.

6.5. Discussion

6.5.1. Spatial variability of the degree-day factor

Spatial variability of the DDF has been acknowledged (Hock, 2003; Braithwaite and Zhang, 2000), and subsequently, better understanding and prediction of this parameter's geographical variation has been called for (Braithwaite, 2008). The present chapter makes a contribution in this regard by reporting DDFs at two sites on Vestari Hagafellsjökull and at one site on Storglaciären. These data therefore provide insight as to i) DDF variability on the same glacier, and ii) between glaciers, situated in different climatological and topographical settings.

DDFs for both snow and the summer surfaces (ice/firn) were found to increase with altitude on Vestari Hagafellsjökull. The sign of this elevational control on the DDF is in agreement with previous research (Hock, 2003; Zhang et al., 2006; Thibert et al., 2012). The reason for the greater DDF found higher on Vestari Hagafellsjökull was investigated through regression of $PDDs$ on ablation, and of $PDDs$ on the individual energy contributions to the SEB. For these analyses, surface types (ice/snow/firn) were not differentiated. The results showed that the majority of the difference between DDFs at these two elevations (~66%) could be attributed to the ratio $N^*/PDDs$, being substantially greater at 1100 m, due to melt conditions persisting in the presence of colder air temperatures. This tendency of DDFs to increase as temperatures decline has been referred to as the 'low-temperature effect' (Braithwaite, 1995b; Zhang et al., 2006), and has been explained by Zhang et al. (2006) as reflecting the fact that a greater proportion of melt energy is provided by global radiation (rather than the turbulent heat fluxes), as elevation increases. This interpretation is supported in the present study because the percentage of melt energy supplied by shortwave radiation is greater at 1100 m (94% and 64% of melt energy supplied by shortwave radiation at 1100 m and 500 m, respectively. Also see Chapter 2, Section 2.5.2.1 for further information regarding the partitioning of energy fluxes at Vestari Hagafellsjökull).

Other differences between the DDF observed on Vestari Hagafellsjökull were explained by the differing sensitivities of the individual energy balance components to $PDDs$ and their variable inputs to the SEB when $PDDs$ were zero (i.e. the β and α parameters, respectively). Notably, net shortwave radiation was found to contribute

most to the α parameter at both sites, and the low albedo surface at 500 m ensured that this parameter's value was greater at 500 m. These findings support those of Braithwaite and Olesen (1990) from Qamanârssûp and Norbogletscher, Greenland, who also reported shortwave radiation to be the solitary positive contributor to the value of α in a similar statistical analysis.

With regards to the sensitivity of ablation to temperature (β) at either site, the value of this parameter was found to be comparable between elevations. However, this similarity masks the fact that individual energy components displayed considerable differences in their temperature response to ablation at either elevation. In this regard, differences between contributions from net shortwave radiation and from the turbulent heat fluxes were particularly conspicuous. These differences were explained by the role of albedo and the surface roughness in modulating energy transfer between sites. The results obtained from comparing DDFs between elevations therefore support Zhang et al. (2006) who concluded that DDFs for a single glacier are prone to significant, small-scale variability.

Concerning DDF variability between locations, research to date has exhibited divergent conclusions. Hock (2003) suggests that warm maritime glaciers were likely to exhibit low DDFs. Similarly, Radić and Hock (2011) reported a positive correlation between increased continentality and the DDF, whereas Zhang et al. (2006) found the opposite to be true in western China. In the present study, Vestari Hagafellsjökull is regarded as maritime and Storglaciären is considered to be affected by both maritime and continental climates (Holmlund and Schneider, 1997). The smaller DDF found at Storglaciären (which is at least somewhat continental) therefore seems to support the findings of Zhang et al. (2006). However, this agreement does not extend to causation; the reasons for the higher DDF found at Vestari Hagafellsjökull contrast those suggested by Zhang et al. (2006), who attribute higher maritime DDFs to an increase in the turbulent heat fluxes: in the present study, the main causes of the lower DDFs on Storglaciären are a combination of a lower incident shortwave flux, higher albedo (than the lower elevation station on Vestari Hagafellsjökull) and the absence of the 'low-temperature effect'; it is only to a much lesser extent that the sensitivity of ablation to temperature (the β parameter) is a cause of the higher DDF found at Vestari Hagafellsjökull.

6.5.2. Synoptic climatology and the degree-day factor

Analysis of DDFs stratified by weather categories showed that at all locations, variability between these categories is apparent, and is appreciable on the ice cap, in particular. Moreover, on Vestari Hagafellsjökull, where measurements are available at two locations, there was significant agreement of DDFs between weather categories. This association occurs despite that, to some extent, the SEB at 1100 m can be expected to vary independently from that at 500 m, due to the pronounced variability of surface conditions, and specifically, of the albedo, which occurs at this altitude but is absent lower on the ice cap (Figure 6.3). That is, albedo variations introduce variability into the SEB between locations which is independent of the prevailing weather conditions. Thus, the fact that DDFs are significantly correlated between elevations suggests that the prevailing synoptic weather conditions exert a suitably strong control on the SEB at these locations.

The 'low-temperature effect' was also evident between weather categories at Storglaciären and at 1100 m on Vestari Hagafellsjökull, where ratios $N^*/PDDs$ exceeding unity were observed. On Storglaciären, this contributed to an implausibly high DDF being recorded in Weather Category S10 (137.1 mm w.e. d^{-1} $°C^{-1}$). This highlights the possibility of large discrepancies between β and the DDF occurring as a function of time (analogous to the spatial discrepancies reported in Section 6.5.1), and emphasises the need to consider the context of the prevailing weather conditions when interpreting the DDF.

Another interesting result to emerge from the regression analysis applied to the different weather categories was the variability of the correlation observed between air temperature and ablation. Similar findings were documented by Guðmundsson et al. (2009) when evaluating monthly degree-day melt model performance on Vestari Hagafellsjökull during the period 2001-2005. In this previous study, the authors attributed the variable correlation to the role of the turbulent heat fluxes—noting that correlations were higher when their share of the SEB increased. This explanation is, to some extent, in agreement with the present analyses: if the percentage share of the SEB held by the turbulent heat fluxes is correlated with the correlation coefficients quantifying the association between $PDDs$ and ablation in each weather category, then a significant relationship at the p = 0.1 level is found at 500 m but is absent at

1100 m (p = 0.17); better agreement is found if the percentage share of the SEB attributed to the sensible heat flux alone is correlated with the weather categories' correlation coefficients: significant positive associations are then found at the p = 0.05 level at 500 m and at the 0.1 level at 100 m. No significant associations at the p = 0.1 level between the percentage share of either the turbulent or sensible heat fluxes and weather categories' correlation coefficients are found for Storglaciären.

The variable correlation coefficients observed during different weather types, and, in particular, the lack of significant correlations within certain categories, can be considered as temporally analogous to the results of Sicart et al. (2008), who compared the temperature-ablation relationship on glaciers in contrasting climatic settings. The authors reported that on the tropical Zongo glacier, Bolivia, temperature is not well correlated with melt, due to the dominance of shortwave radiation in the SEB, which varied independently of air temperature. Consequently, it was suggested that temperature-index models would be unsuitable for the simulation of daily ablation in this environment. Considering these recommendations, the results from the present research suggest that temporal caution may also be warranted: the temperature-ablation correlation was observed to be absent at all locations during some weather categories. Failure to recognise this potential limitation could result in the overestimation of melt-model skill when applied in a forecasting capacity for future scenarios of climate, particularly so if there is an increase in the frequency of weather categories in which there is no significant association between temperature and ablation.

The correlation coefficients relating $PDDs$ to ablation for each weather category were also found to be related to the gradient of the regression line relating these variables (β). Due to this association, and because the β term quantifies the sensitivity of ablation to air temperature, specific attention was given to variation of this parameter between weather categories by closely examining two types with contrasting βs at each location. From these comparisons, the contrasts between categories at Vestari Hagafellsjökull gave results that were more physically interpretable, varying most in terms of the shortwave heat flux: the weather category with a greater sensitivity of ablation to temperature, and a higher correlation coefficient (Category V4), was characterised by anticyclonic curvature and the advection of north-westerly air. The steeper β parameter in this category was found to be the result of a large positive

contribution from the net shortwave flux, resulting from a significant correlation between the incident shortwave heat flux and $PDDs$ that occurred in Weather Category V4, but not in V23.

This positive correlation is inconsistent with the results reported in Section 6.4.2, which showed that for all days (irrespective of weather type), $PDDs$ have no significant relationship with the incident shortwave flux at 1100 m and a significantly negative association at 500 m. The reason for such apparently contradictory behaviour can be explained through examination of the synoptic climate regime at Vestari Hagafellsjökull. Figure 6.9 demonstrates that airflow from the south results in higher temperatures on the ice cap and lower receipts of incident shortwave radiation, whilst northerly airflow results in contrasting conditions. The cooler, sunnier weather and northerly airflow of Category V4, and the warmer, overcast conditions of Category V6 brought by south-westerly flow are therefore consistent with this system. It is therefore evident that this overall synoptic regime, in which temperature and shortwave radiation are negatively related, conceals the positive association that prevails *within* Category V4. The contrast between these categories thus provides a clear, physically interpretable example to support the variability of DDFs and regression parameters reported in Section 6.4.3.

With these considerations in mind, it is suggested that a weather-category conditioned regression model may be a useful alternative to traditional temperature-index formulations (e.g. Equation 6.1):

$$M_{i,j} = PDDs_i \, \beta_j + \alpha_j \ , \qquad 6.9$$

where ablation (M) on day i in weather category j is modelled with regression parameters (β and α) calibrated specifically for the prevailing weather type. By simulating ablation in this way, the variability of the DDF resulting from changing synoptic type is provisioned for directly. Moreover, separation of the temperature sensitivity (β) from the temperature-independent regression parameter (α) provides a more appropriate framework for addressing the effect of climatic warming within weather categories. Otherwise, erroneous sensitivities of ablation to air temperature, resulting from discrepancies between the DDF and β parameters, may provide unsuitable predictions of ablation for a warming climate.

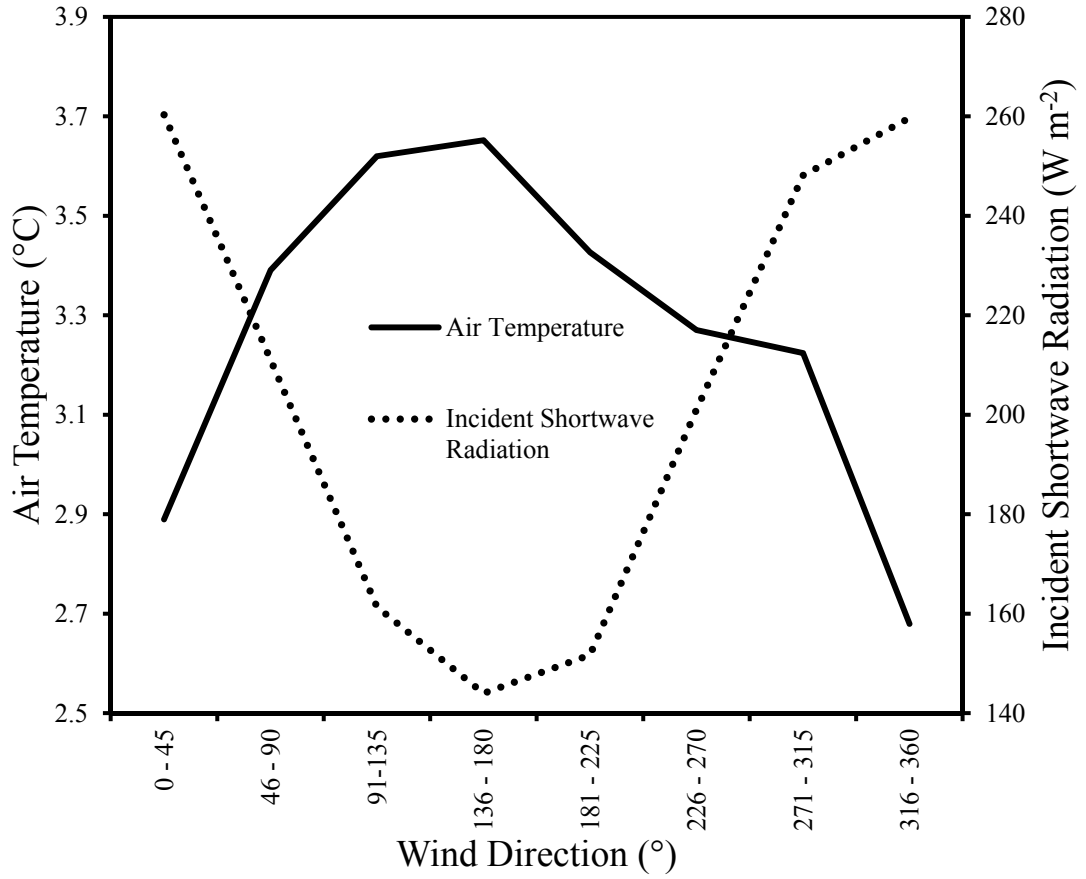

Figure 6.9. Mean air temperature and incident shortwave radiation (average of observations at 500 m and 1100 m AWSs on Vestari Hagafellsjökull) per 45° bins. Wind direction was taken from the ERA interim 10m wind direction field used and described in Chapter 4.

Although this proposed treatment offers a conceptual improvement in temperature-index modelling—through attempting to capture DDF resulting from variation of the prevailing weather conditions—it neglects the fact that during some weather categories, $PDDs$ are poorly correlated with ablation. During such conditions, it would seem that application of any temperature-based index model would therefore be inappropriate. As a consequence, it is suggested that alternative approaches, which integrate the effect of synoptic climatological variability on ablation without relying on the temperature-ablation relationship, should also be explored. This possibility is addressed in Chapter 7.

6.6. Synthesis and Conclusions

Despite the fact that glacier ablation is a function of the SEB, simplifying models which aim to simulate this process empirically, as a function of positive air temperatures, remain popular. Such popularity can be attributed to the generally good performance of these approaches, and to air temperature's robust nature to both forecasting and spatial interpolation. This latter quality is particularly desirable because glaciers are often located in remote areas where meteorological measurements are sparse. Temperature-index models therefore provide a practical framework for relating glacier ablation to synoptic climatological processes. The DDF, relating $PDDs$ to the rate of ablation, is a critical parameter in such approaches. The aim of this chapter was therefore to explore controls on its spatial variability, and its dependency on the prevailing weather conditions. This was pursued by adopting a regression-based approach to the analyses.

Spatially, DDFs were found to be higher on Vestari Hagafellsjökull, which was mainly a result of a higher value for the term $\alpha(N^*/PDDs)$, caused by a greater net-shortwave radiative flux, and the 'low-temperature effect' that is particularly apparent at 1100 m on the ice cap. The sensitivity of ablation to air temperature (β) was more comparable between glaciers, and between elevations on Vestari Hagafellsjökull; although, the contribution from individual energy terms to this sensitivity was variable.

Importantly, it was observed that the temperature sensitivity to ablation is erroneously overestimated where there is a large discrepancy between the DDF and the β parameter. Spatially, this difference between terms is greatest on the ice cap, but was also found to be considerable during certain weather types for all locations. This is pertinent with regards to simulating ablation in a warming climate, as forecasts may be compromised if the DDF is wrongly assumed to represent the sensitivity of ablation to air temperature.

The regression analysis applied to examine change of the DDF between weather categories, showed both slopes and intercepts to be non-stationary. Variability of the DDF between elevations on Vestari Hagafellsjökull was also observed to be coherent, despite neglecting the effect of the (pronounced) albedo variations at 1100 m which

independently affects the SEB and therefore suggests that the prevailing synoptic weather conditions are an important control on the DDF.

The β parameter, quantifying the sensitivity of ablation to temperature, was found to be related to the power of temperature to 'explain' ablation at all locations. Close examination of frequent weather categories with contrasting β values was undertaken to explore the conditions that produce these different temperature sensitivities. At Vestari Hagafellsjökull, the incident shortwave radiative flux was found to correlate with temperature during weather conditions associated with a higher ablation sensitivity to temperature. This was interpreted as being the result of incident solar radiation heating the glacier environs and the subsequent advection of heat on to the glacier. Thus, during this category, temperature also acted as an index of the shortwave heat flux—an association that is hidden by the overall synoptic regime at Vestari Hagafellsjökull, where warmer air temperatures are associated with southerly airflow and cloudy conditions. At Storglaciären, the higher sensitivity of ablation to air temperature in the category selected for further analysis, resulted from a slightly higher sensitivity of all the energy fluxes to air temperature.

Considering the pronounced variability of DDFs and regression terms between weather categories, a weather-category conditioned regression model was suggested as an empirical alternative to the traditional temperature-index model. The possibility of applying this model to simulate ablation will be explored in the following chapter. Furthermore, because $PDDs$ and ablation were sometimes only weakly correlated, the forthcoming analyses will also consider alternative means of integrating synoptic climatological information into simulations of glacier ablation.

7. Glacier Ablation Modelling Using Spatially-Coarse Reanalysis Data: An Inter-Comparison of Methods

7.1. Introduction

Numerical melt models, whether physically- or empirically-based, have traditionally been forced with in-situ boundary-layer meteorological data, from weather stations either in close proximity to glacier termini, or, located on-glacier (e.g. Arnold et al., 1996; Hock and Noetzli, 1997; Hock, 1999; Braithewaite and Zhang, 2000; Brock and Arnold, 2000; Hock and Holmgren, 2005; Pellicciotti et al., 2005; Jonsell et al., 2012). However, these in-situ data requirements limit the possibility of applying such models in space and time: spatially, the remote location of mountain glaciers means that in-situ data collection is impractical for all but a handful of locations; and temporally, future projections of glacier ablation are compromised by the 'mismatch of scale' (Machguth et al., 2009; Kotlarski et al., 2010; Mölg and Kaser, 2011) that exists between GCM output and the (sub) basin-scale required for melt modelling.

Whilst these limitations are evident for all numerical models, air temperature is more agreeable to spatial interpolation and forecasting, which means that empirical temperature-index approaches are more suited to making the transition from reliance on in-situ data, to utilizing coarse-scale climate information. These attributes have contributed to temperature-index models being the method of choice for simulating future glacier melt from climate model output (e.g. Radić and Hock, 2006; Raper and Braithwaite, 2006; Radić and Hock, 2011). However, the caveat to this portability is the simplification of complex climatic processes which ultimately govern the SEB and determine ablation. This warrants particular caution when forecasting glacier response to future climates, as the empirical temperature-ablation relationship may be non-stationary if climate warming manifests as changes in synoptic circulation (see Chapter 6, Section 6.5.2). Hence, physical energy balance approaches should be

preferred due to their explicit treatment of individual energy fluxes, yet the aforementioned scale-mismatch is currently a limiting factor.

With these considerations in mind, some recent research has addressed the possibility of applying spatially-coarse, gridded climate data to the problem of evaluating the energy (and mass) balance of glaciers explicitly. For example, Reichert et al. (2001) achieved promising results using statistically downscaled reanalysis data to drive energy balance models at Nigardsbreen, Norway and Rhonegletscher, Switzerland; and similarly positive results were recorded by Rye et al. (2010) at Midre Lovénbreen, Spitsbergen. Hock et al. (2007) also applied a reanalysis-driven energy-balance model to Storglaciären, Sweden, but found its performance was actually exceeded by temperature-index methods. The authors reported that inadequacies of the reanalysis data to simulate the dynamical, radiative and moisture properties of Storglaciären's local climate contributed to this under-achievement.

Results from attempting to apply spatially-coarse reanalysis data to evaluate the energy balance have therefore been limited, and the results mixed, and so there is a need for increased study in this area. Before researchers can demonstrate the improvement supplied by energy balance methods, over simpler temperature-index approaches when applied to spatially-coarse data, there would seem to be little gain from the use of computationally more demanding approaches. It should also be noted, however, that temperature-index and energy-balance models are but two, polarized approaches to melt modelling, and so alternative methods should be explored. In this regard, it is suggested that empirical approaches which integrate synoptic climatological information to simulate glacier surface ablation should be pursued.

7.2. Aims and Objectives

With these considerations in mind, the main aim of this chapter is to investigate the utility of applying gridded reanalysis data to drive physical and empirical melt models at Vestari Hagafellsjökull and Storglaciären. Specifically, the possibility of developing alternative empirical melt models which include information of synoptic climatological variability is addressed. This aim is pursued because 1) an appraisal of the utility of regional-scale data for melt modelling is desirable to ascertain the suitability of such data for simulating contemporary ablation in remote locations; and 2) the similarity in spatial resolution between reanalysis and GCM output means that

conceptually, these data are closely related (Hofer et al., 2010), hence an insight into the applicability of modelling approaches for simulating future ablation may also be provided.

In addition to examining the performance of different empirical and physical melt models, specific research questions relating to the reanalysis climatology are addressed: i) how well do the reanalysis data represent the observed glacier meteorology, and is this spatially variable (i.e. between locations)? ii) Which meteorological variables are captured best by the reanalysis data? And iii) how does this affect the different ablation simulations?

7.2.1. Ablation models

In total, four models are considered in this chapter. Each is conceptually different, but all are similar in their use of spatially-coarse reanalysis data. In this section, these four models are briefly introduced. For convenience in subsequent discussions, each model is given an acronym (indicated in brackets, below).

*Model 1(**R**eanalysis **S**urface **E**nergy **B**alance Model, 'RSEB')*

The first model considered is a surface energy-balance model, which takes a fully-physical approach to simulating ablation. The strength of this model is the fact that no assumptions need to be made regarding stationarity of empirical relationships between climatic variables and ablation, as instead, each of the energy fluxes is evaluated explicitly. This model is, however, heavily reliant on the glacier climate being reproduced accurately by the reanalysis data. Indeed, this demand may be challenging to satisfy, considering the coarse spatial scale of the reanalysis data, the complex topography in which the glaciers reside, and the development of the glacier boundary layer. Thus, whilst an explicit evaluation of each of the energy fluxes is physically desirable, the results from this model will provide a much needed insight as to the practicality of applying such an approach to regional-scale data.

*Model 2 (**T**emperature **In**dex model, 'TIn')*

The second model tested is a traditional temperature-index approach, whereby ablation (M) on day i is simply calculated as a linear function of positive air temperatures (T^+):

$$M_i = DDF_{ice/snow} T_i^+ \ , \qquad 7.1$$

in which $DDF_{ice/snow}$ is the 'degree-day factor', relating T^+ to the rate of glacier ablation (mm w.e. °C d^{-1}). The subscripts indicate that different factors are applicable, dependent on whether the melting glacier surface constitutes snow or ice. This basic formulation of the temperature-index model represents the most widely-used empirical approach to simulate ablation (Braithwaite and Zhang, 1999) and owes its popularity to simplicity and generally good performance (Hock, 2003). The use of temperature as a reliable index of ablation relies upon the integrating effect of this variable to quantify the contribution of all the energy fluxes. That is, whilst air temperature only directly contributes to the longwave and sensible heat flux, it is also generally considered as a good proxy for the remaining energy fluxes (Ohmura, 2001; Hock, 2003; see Chapter 6, Section 6.1 for further discussion). This model therefore relies on the relationship between temperature and ablation remaining constant in time—a reliance which is especially vulnerable to changes in synoptic circulation (Chapter 6).

*Model 3 (**W**eather **C**ategory **A**nalogue model 'WCA')*

The third model prescribes ablation based on the prevailing synoptic weather type:

$$M_{ij} = \overline{M_j} \ . \qquad 7.2$$

Ablation on day i, which belongs to weather category j, is therefore modelled as the mean observed during weather category j. The weather categories are adopted from the categorization scheme outlined in Chapter 4, and thus the same categories are used in this chapter as were employed in Chapter 5 (to investigate lapse rates), and Chapter 6 (to investigate variability of the degree-day factor). The nomenclature for weather categories is the same as in Chapter 6: categories are prefixed with 'S' or 'V' (for Storglaciären and Vestari Hagafellsjökull, respectively) to differentiate between locations.

This method of parameterizing ablation is similar to the analogue method applied in Chapter 5 to model lapse rates at Vestari Hagafellsjökull, and to the technique used by Brazel et al. (1992) to investigate ablation variability at West Gulkana Glacier, Alaska (see Chapter 4, Section 4.2.4.). The development of the WCA model builds upon the findings in Chapter 6, which highlighted the fact that during some weather categories,

the correlation between positive air temperatures and ablation was observed to be weak. By forecasting ablation as a function of weather-category membership, this model considers the net effect of the prevailing meteorology and does not assume that air temperature variations alone may be used as a proxy for the rate of ablation. Indeed, the WCA model does not assume linearity between ablation and *any* index of climate. It is believed that this 'holistic' approach may be particularly suitable for capturing the development of the glacier boundary layer, which can be expected to develop in a non-linear way, and has the potential to greatly affect surface energy exchange. Furthermore this model's use of nominal categories to quantify ablation rates provides a useful framework for elucidating linkages between surface ablation and synoptic-climatological processes.

*Model 4 (**W**eather **C**ategory **C**onditioned **T**emperature **In**dex Model 'WCCTIn')*

Finally, the fourth model considered is a hybrid of the TIn and WCA models, in which a temperature-index model is conditioned based on weather-category membership:

$$M_{ij} = {T_{ij}}^{+} \beta_j + \alpha_j \ . \qquad 7.3$$

The relationship between ablation and positive air temperatures is thus treated as a regression problem: the slopes and intercept terms (see Chapter 6, Section 6.3.2.2) vary as a function of weather-category membership. If the traditional temperature-index approach is regarded as a 'black-box' model (i.e. where temperature implicitly integrates all the processes which affect ablation; Kuhn, 1993), then the WCCTIn model can be considered as a set of black boxes, between which the temperature-ablation relationship varies. Physically, this model builds upon the WCA model by assuming that if the net effect of regional-scale weather determines ablation, then a within weather-category temperature change will have an additional effect. This model therefore specifically addresses the effect of variability in the frequency of weather categories, and the effect of within-type temperature change—a focus which is warranted given that both of these factors have proven to be temporally variable (e.g. Bárdossy and Caspary, 1990; Kalkstein et al., 1990). The WCCTIn model is a development of the concept introduced in Chapter 6 (Equation 6.9).

7.3. Data and Methodology

This section summarises the data required and the methodology pursued in this chapter. The specific data requirements of each of the four models employed in this chapter are given in Table 7.1. Below, aspects of the methodology relating to data preparation and the modelling procedure are discussed.

Table 7.1. Data requirements of the ablation models.

Model	Reanalysis Data Required	Additional Information Required
RSEB	Air temperature, vapour pressure, wind speed, incident shortwave radiation, incident longwave radiation	Surface temperature, ground heat flux, albedo
TIn	Air temperature	Surface-type (ice/firn/snow)
WCA	Variables used in the classification of weather categories (Chapter 4, Section 4.4): air temperature, dewpoint air temperature, wind speed, wind direction, cloud cover, and air pressure	-
WCCTIn	The same variables as those required in the TIn and WCA models	-

7.3.1. Meteorological data

The source of all the reanalysis meteorological data is the ERA-interim ECMWF archive (full details in Chapter 4, Section 4.4). All data required for analysis in this chapter were obtained at 6-hourly resolution before being post-processed to daily means. Of those models which require knowledge of the glacier-surface meteorology (air temperature, for the temperature-index methods, or the suite of variables required for the RSEB model—Table 7.1), all models are alike in their requirement that the reanalysis data should reproduce the glacier meteorology as closely as possible in order to accurately simulate ablation. However, this is challenged by the presence of considerable bias observed in the reanalysis data, relative to the AWS observations (Figure 7.1). Such bias is common in climate simulations, and may result from the quality of input data, or the simplification of parameterization schemes (Hashino et al., 2007; Rye et al., 2010). For example, the elevation of the ERA reanalysis grid-cells in which Vestari Hagafellsjökull and Storglaciären are located in show little coherence with the AWS elevations (~307 and ~753 m.a.s.l., respectively).

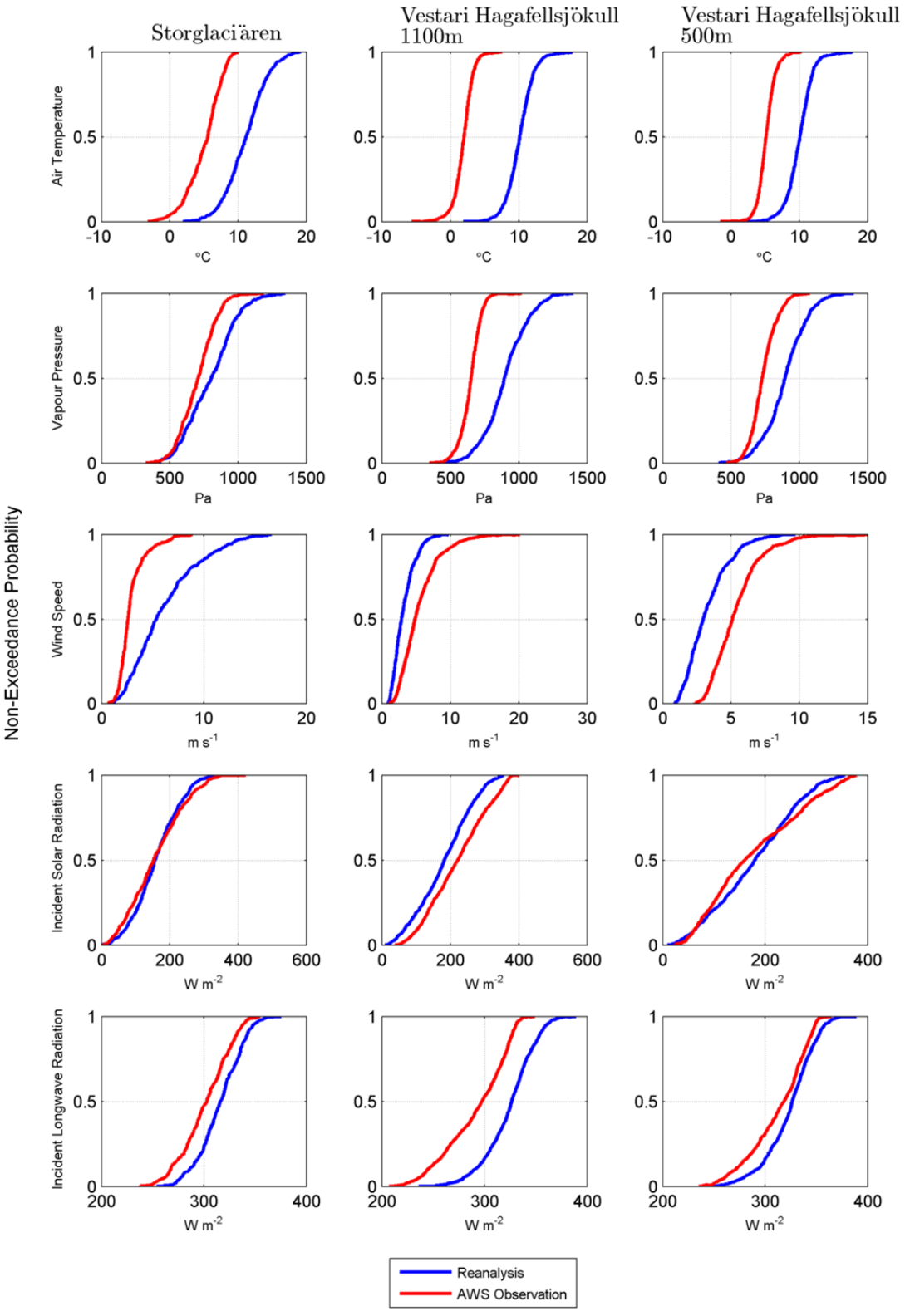

Figure 7.1. Empirical cumulative distributions for the reanalysis and AWS data.

It is therefore likely that some of the observed bias is a consequence of these elevation differences. Radić and Hock (2006) noted similar bias when comparing seasonal temperatures at Tarfala Research Station (close proximity to Storglaciären; Chapter 3) to ERA-40 reanalysis climate data; and, Rye et al. (2010) also observed substantial biases for precipitation, wind speed, temperature and humidity when simulating Midre Lovénbreen's mass balance with ERA-40 data.

Before the reanalysis data may be used to simulate ablation, it is necessary to correct for these systematic errors, and to accomplish this, the method of quantile mapping is applied (Panofsky and Brier, 1968). This technique involves re-scaling the mean and variance through the use of empirical cumulative distribution functions: the reanalysis data are replaced by the observed values of the same quantile (i.e. the observed values with the same non-exceedance probability). This technique is illustrated in Figure 7.2. A substantial benefit of this approach is that bias may be corrected without the need to make assumptions as to the distributions of either the reanalysis or the observed data (Guðmundsson et al., 2012). Quantile mapping has been used to correct ERA-40 reanalysis bias in glacier-climate studies before (Rye et al., 2010), and has also been applied frequently to correct both regional and general circulation model output (e.g. Wood et al., 2004; Ines and Hansen, 2006; Hashino et al., 2007; Ashfaq et al., 2010; Sunyer et al., 2012; Guðmundsson et al., 2012).

The bias correction does not, however, affect the temporal coherence between the reanalysis data and the glacier-based observations, which is required for the accurate simulation of surface ablation. Hence, the degree to which the gridded climate data capture this variability needs to be ascertained. This is explored through the calculation of Pearson's product-moment correlation coefficients between the reanalysis data and that recorded by the in-situ AWSs (described in Chapters 2 and 3). Prior to the correlation analysis, the reanalysis and AWS data are de-trended by subtraction of the respective monthly means for each meteorological variable. This is performed to remove any red noise (seasonal cycle) that may still be present within the two- and three-month summer periods at Storglaciären and Vestari Hagafellsjökull, respectively (cf. Gardner et al., 2009).

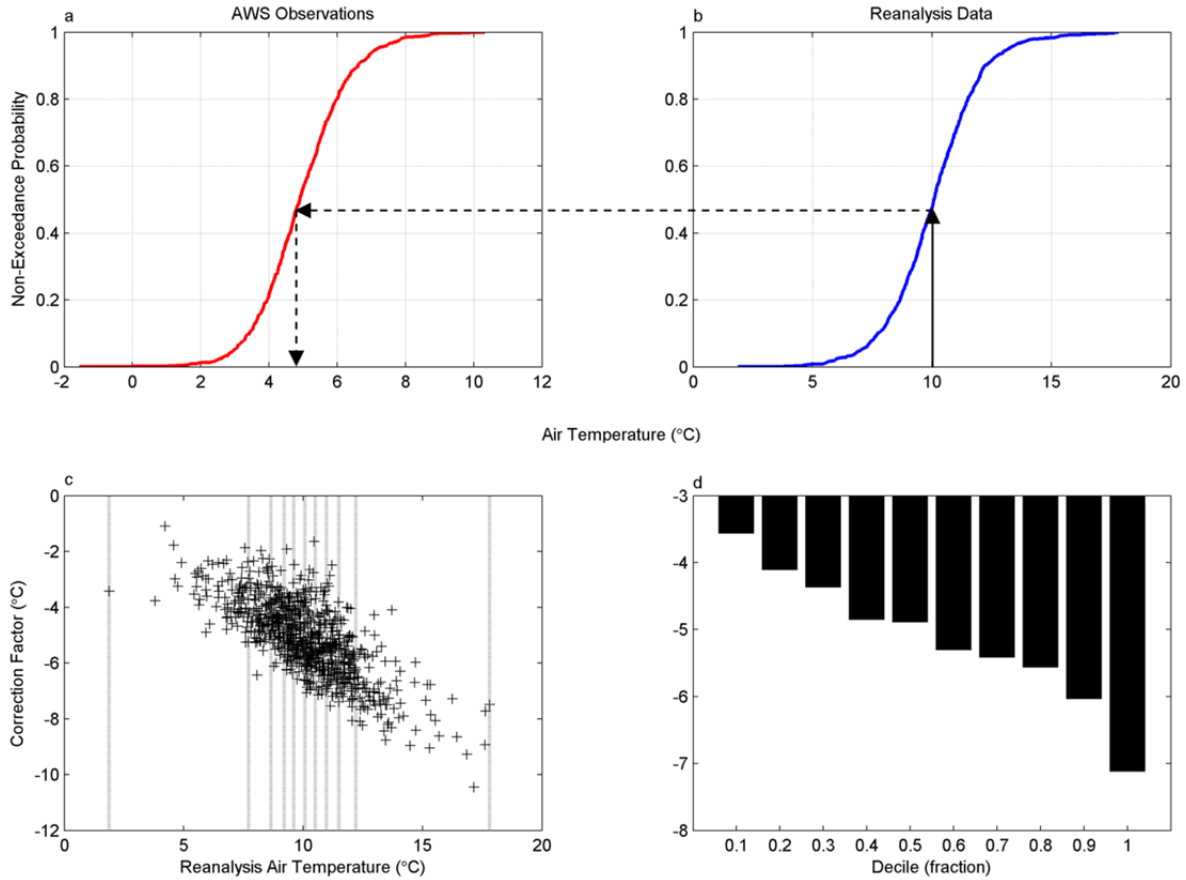

Figure 7.2. Example of the quantile-mapping procedure for air temperature at 500 m on Vestari Hagafellsjökull. The 10 °C reanalysis observation (b) has a non-exceedance probability of ~0.48 and this value is corrected by replacing the reanalysis observation with the AWS observation with the same non-exceedance probability, indicated by the arrows leading to 'a'. Hence, the 10 °C is remapped to a value of ~4.8 °C $^{-1}$. This process is analogous to adding a correction factor to each of the reanalysis observations, defined as the difference between the rank-ordered reanalysis and AWS air temperatures; these correction factors (which must be added to the reanalysis data) are shown in 'c'. The dotted lines in 'c' indicate deciles—the average correction factors for which are given in 'd'. Thus, in this example, the reanalysis data systematically overestimates air temperature, and the mean correction factor decreases monotonically as the reanalysis air temperature increases. Note that the upper limit of the y-axis in d is non-zero.

7.3.2. Modelling procedure

RSEB is distinct from the other models in that it is physically- rather than empirically-based, and its treatment in the modelling procedure is therefore somewhat different. The philosophy behind applying RSEB to reanalysis data was that the effect of coarse-scale meteorological input data on the accuracy of ablation simulations should be isolated. Consequently, no optimization or tuning of model parameters was considered. All model options (e.g. roughness lengths, treatment of the ground heat flux) were therefore treated as they were when the simulations driven by in-situ data were performed (chapters 2 and 3). This information is summarised in Table 7.2.

For the remaining models, which use empirical associations to simulate ablation, a cross-validation procedure is applied. This involves estimating parameters in each year being modelled (and then simulating ablation), based on observational data in all other years; validation and calibration are therefore never performed on the same data. This helps to ensure a realistic representation of model skill (Elsner and Schertmann, 1994). A cross-validation technique was also applied in Chapter 5's investigation into lapse-rate simulations at Vestari Hagafellsjökull. For the TIn model, cross validation simply involves calibrating $DDF_{ice/snow}$, and subsequent application of these values to the year being simulated. The relevant surface type (snow or ice) in both the calibration years, and the year being simulated, is identified with the aid of the in-situ albedo measurements: the threshold value of albedo for differentiating snow from the summer surface was 0.45 at Storglaciären, 0.5 at 1100 m and 0.15 at 500 m on Vestari Hagafellsjökull (see Figure 6.3, Section 6.4.1. in Chapter 6).

Simulating ablation in the cross-validation procedure for the WCA and WCCTIn models requires a two-step procedure. First, each day in the year being simulated must be assigned to a weather category. This is achieved through a nearest-neighbour technique (e.g. Martin et al., 1996): days in the validation year are assigned to the weather category to which it is closest, as given by the squared Euclidean distance between each day's principal component score and the weather category centroids. The same technique was applied to associate days to weather categories in Chapter 5 (Section 5.3.4) where further details of this procedure are provided.

Table 7.2. Parameterizations for RSEB.

Model Parameter	**Vestari Hagafellsjökull**	**Storglaciären**
Roughness length of momentum	Ice: 10 mm Firn: 2 mm Snow: 0.1 mm	Ice: 2.7 mm Snow: 0.15 mm
Roughness lengths of water vapour and temperature	Modelled according to Andreas (1987)	Same as Vestari Hagafellsjökull
Stability corrections for turbulent heat flux calculations	Non-linear expressions of Beljaars and Holtslag (1991) used for stable conditions (glacier surface temperature below air temperature); equations of Paulson (1970) and Dyer (1974) applied for unstable cases.	Neutral equations applied; no stability corrections are used
Ground heat flux	Neglected	Linearly interpolated between -5 W m^{-2} minimum on the 1st of July, to 0 W m^{-2} maximum on the 31st of August
Glacier surface temperature	0°C when SEB is positive; iteratively lowered in 0.25°C increments until SEB is zero if negative balances are encountered	Same as Vestari Hagafellsjökull
Reflected shortwave radiation	Incident flux multiplied by observed albedo	Same as Vestari Hagafellsjökull
Emitted longwave radiation	Calculated as a function of surface temperature ($L\uparrow = \sigma Ts^4$) where σ is the Stefan Boltzmann constant	Same as Vestari Hagafellsjökull
Rain heat flux	Neglected	Same as Vestari Hagafellsjökull

The second stage requires calculating the mean ablation (WCA) and the regression parameters (WCCTIn) for each weather category, based on observations from the calibration years. These parameters are then used to simulate ablation in the validation year. However, for the regression model in particular, this is challenged by the sometimes few observations during the calibration years, which results from a relatively high ratio of weather categories to the total number of days (see Chapter 4, Section 4.5.1 for information regarding the partitioning of days between weather categories). Consequently, an agglomeration technique was used to reduce this ratio. This involved specifying an arbitrary threshold group size of 20 days, such that, if any weather category consisted of less than this many days, the group was merged with the weather category it was most similar to; similarity was again adjudged based on the squared Euclidean distance between centroids. Merging of groups in this way was performed prior to the cross-validation procedure.

All of the models simulate ablation daily, and model skill is assessed on the ability to reproduce both daily and annual ablation. Metrics to quantify model performance are the systematic error:

$$RMSE_s = \left[N^{-1} \sum_{i=1}^{i=N} (\widehat{P_i} - O_i)^2 \right]^{0.5} , \quad 7.4$$

and the unsystematic error:

$$RMSE_u = \left[N^{-1} \sum_{i=1}^{i=N} (\widehat{P_i} - P_i)^2 \right]^{0.5} , \quad 7.5$$

where N is the number of days on which ablation is simulated, O_i is the observed ablation, P_i is the ablation predicted by the model, and $\widehat{P_i}$ is the predicted value from regressing P_i upon O_i. Separating errors into these components provides a more complete appraisal of model performance, as the systematic error describes the model's tendency to under- or over-estimate ablation, whilst the unsystematic error quantifies 'random' error.

An assessment of the models' performance based on both criteria is summarised with Willmott's index of agreement, given by:

$$d^2 = 1 - \left[\sum_{i=1}^{i=N} \frac{(P_i - O_i)^2}{(|P_i - \bar{O}| + |O_i - \bar{O})^2} \right], \quad 7.6$$

in which $\bar{O}$ denotes the mean of the observed series; hence, d^2contains information on model bias, and the ability of the model to capture observed variance (Willmott, 1981). The often-used r^2 measure, which addresses the models' skill in simulating ablation variability, is also reported. All models are evaluated relative to the ablation series simulated by the SEB models described in chapters 2 and 3 for Vestari Hagafellsjökull, and Storglaciären, respectively.

7.4. Results

7.4.1. Reanalysis climatology

In order to remove systematic bias between reanalysis data and the observations recorded on-glacier, a quantile-mapping procedure was applied (Section 7.3.1). This technique corrected the reanalysis meteorology through replacing the reanalysis data with AWS observations corresponding to the same non-exceedance probability. This procedure does not, however, affect the skill of the reanalysis data to capture temporal variability of the glacier climate, which is required for accurate simulation of ablation. Consequently, Pearson's product-moment correlation coefficients were calculated to ascertain the correspondence between AWS observations and the reanalysis data (Table 7.3).

Table 7.3. Correlation coefficients between daily de-trended (monthly-mean subtracted) reanalysis and AWS meteorological variables.

Variable	Storglaciären	Vestari Hagafellsjökull, 1100 m	Vestari Hagafellsjökull, 500 m
2 m Air temperature	0.92	0.84	0.70
2 m Vapour Pressure	0.91	0.81	0.71
2 m Wind Speed	0.59	0.69	0.47
Incident Global Radiation	0.75	0.73	0.77
Incident Longwave Radiation	0.80	0.64	0.74
Mean	0.79	0.74	0.68

These correlations indicate that, in general, there is reasonably good agreement between the reanalysis and in-situ observations. Generally, the highest correlation coefficients are observed for the thermal and moisture variables; variability of temperature at Storglaciären is captured particularly well. Such strong correlations evident for vapour pressure and temperature are perhaps unsurprising, given the homogeneity of these variables within air masses over large spatial scales (Barry and Chorley, 2009). Nevertheless, it is notable that the agreement between the AWS observations and the reanalysis data endures, despite the presence of the melting glacier surface, which can be expected to exert a drying and cooling influence on the overlying air (Greuell and Böhm, 1998; Shea and Moore, 2010; Marshall et al., 2007).

The wind speed, which is the remaining meteorological variable required for evaluation of the turbulent heat fluxes, displays less agreement with observations on-glacier. However, considering that wind speed has previously been acknowledged as being highly spatially variable over complex terrain (Salameh et al., 2009; Winstral and Marks, 2002), particularly over melting glaciers (Strasser et al., 2004; Hock and Holmgren, 2005), the fact that moderate-to-good temporal agreement is obtained is encouraging.

For the incident radiative fluxes, correlation coefficients between 0.64 and 0.8 (longwave radiation at 1100 m on Vestari Hagafellsjökull and Storglaciären, respectively) are observed. These values are in the range of those recorded by Rye et al. (2010) who compared daily glacier-based AWS observations and ERA-40 reanalysis radiation fields at Midre Lovénbreen (incident global radiation: $r = 0.61$; incident longwave radiation: $r = 0.84$). At Vestari Hagafellsjökull, the agreement between the observed and reanalysis radiation fields is higher than noted for air temperature and vapour pressure. This is counter to the correlations for Storglaciären, and, notably, from 1100 m on the ice cap. Possible reasons for such behaviour are suggested in Section 7.5.1.

7.4.2. Ablation models

To compare models, a cross-validation procedure was applied. This process involved estimating empirical model parameters (for TIn, WCA and WCCTIn) based on a calibration data set consisting of k-1 years (where k is the number of years for which data are available at each location), and then simulating ablation for each year in turn. For the models which utilised weather-category membership to predict ablation (WCA and WCCTIn), practical considerations necessitated that this process was preceded by an aggregating scheme that joined weather categories consisting of less than 20 days, to the next most similar category. This resulted in 8, 11, and 17 weather categories being entered into the cross-validation scheme at Storglaciären, and at 1100 m and 500 m on Vestari Hagafellsjokull, respectively (new weather-category memberships are given in Appendix 1). The cross-validation procedure not only facilitates a realistic estimate of forecast skill, but also results in an ensemble of model estimates for each of the empirical approaches (tables 7.4 to 7.7).

Table 7.4. Mean degree-day factors from the cross-validation procedure. Bracketed numbers give the standard deviation. This format is also used for Tables 7.5-7.8. Units of the DDF are mm w.e. d^{-1} °C^{-1}.

Location	$\boldsymbol{DDF_{snow}}$	$\boldsymbol{DDF_{ice/firn}}$
Storglaciären, 1387 m	5.5 (0.34)	6.9 (0.06)
Vestari Hagafellsjökull,1100 m	14.3 (0.23)	17.0 (0.29)
Vestari Hagafellsjökull, 500 m	12.0 (0.21)	12.8 (0.09)

Whilst variability of degree-day factors has largely been addressed already (Chapter 6), the cross-validation process facilitated a more detailed insight into the holistic effect of weather categories' passage on ablation: the wider-scale synoptic circulation for examples of low- and high-ablation weather categories are shown for Storglaciären and Vestari Hagafellsjökull in figures 7.3 and 7.4, respectively. Specifically, these examples illustrate synoptic conditions in each of the 'sub-categories' that were merged during the cross-validation procedure, and resulted in the highest and lowest ablation at each location.

Table 7.5. Regression parameters for weather categories on Storglaciären. [a] Category numbers are the same used in previous chapters; but some categories have been merged with those listed below (see Appendix 1). [b]The DDF is calculated: $\beta + \alpha(N^*/PDDs)$ (Chapter 6, Equation 6.4). Note that this convention is also used for tables 7.6 and 7.7.

[a]Weather Category	β (mm w.e.°C^{-1} d^{-1})	α (mm w.e. d^{-1})	$N^*/PDDs$	[b]DDF (mm w.e. d^{-1} °C^{-1})	Ablation (mm w.e. d^{-1})	n
S3	4.5 (0.47)	14.2 (3.95)	0.13	5.0	49.5 (1.03)	56
S4	5.2 (0.42)	8.3 (3.18)	0.14	5.6	44.4 (0.51)	63
S6	5.2 (0.47)	13.8 (2.72)	0.25	5.9	33.3 (0.77)	74
S7	5.0 (0.49)	2.9 (3.01)	0.19	5.6	29.5 (0.73)	41
S8	7.6 (1.26)	-13.6 (8.68)	0.15	8.9	38.4 (0.94)	53
S9	5.9 (0.37)	-2.6 (1.33)	0.23	6.2	23.8 (2.21)	50
S11	4.7 (0.27)	11.5 (1.26)	0.31	5.1	25.1 (0.67)	68
S17	6.6 (1.10)	1.9 (3.28)	0.41	8.0	12.9 (3.19)	29

Table 7.6. Regression parameters for weather categories at 1100 m on Vestari Hagafellsjökull.

Weather Category	β (mm w.e.°C^{-1} d^{-1})	α (mm w.e. d^{-1})	$N^*/PDDs$	DDF (mm w.e. d^{-1} °C^{-1})	Ablation (mm w.e. d^{-1})	n
V1	7.2 (0.57)	8.0 (0.71)	0.89	14.4	15.4 (1.04)	36
V3	5.0 (9.13)	8.5 (1.06)	5.12	48.5	8.6 (0.98)	32
V4	7.1 (0.20)	13.0 (0.35)	0.72	16.4	20.4 (0.63)	41
V5	2.4 (0.58)	39.7 (2.57)	0.19	10.0	52.5 (0.49)	24
V7	7.7 (1.06)	12.7 (1.93)	0.41	12.9	31.3 (0.83)	85
V8	3.0 (0.44)	18.0 (1.11)	0.50	12.0	24.2 (0.45)	62
V9	5.2 (0.70)	15.9 (0.65)	0.91	19.7	21.5 (0.55)	36
V10	8.8 (0.73)	13.5 (0.50)	0.66	17.7	26.4 (0.98)	88
V12	5.7 (0.27)	22.0 (1.17)	0.35	13.3	38.5 (1.32)	110
V15	6.5 (0.46)	18.4 (1.03)	1.02	25.4	24.1 (0.77)	69
V16	7.9 (0.31)	15.0 (0.45)	0.68	18.1	25.8 (0.60)	81
V18	7.4 (2.22)	19.7 (1.68)	1.36	34.1	22.4 (1.14)	43
V22	6.5 (0.71)	12.8 (2.12)	0.44	12.1	27.4 (1.14)	36
V23	6.7 (0.49)	15.9 (1.44)	0.32	11.7	37.1 (1.14)	69
V24	8.2 (1.27)	14.9 (2.20)	0.44	14.8	33.5 (1.41)	35
V26	7.8 (0.53)	12.2 (0.21)	1.11	21.3	17.5 (0.39)	44
V27	11.1 (0.95)	5.8 (1.96)	0.50	14.0	27.9 (0.66)	29

Table 7.7. Regression parameters for weather categories at 500 m on Vestari Hagafellsjökull.

Weather Category	β (mm w.e.°C^{-1} d^{-1})	α (mm w.e. d^{-1})	$N^*/PDDs$	DDF (mm w.e. d^{-1} °C^{-1})	Ablation (mm w.e. d^{-1})	n
V1	10.0 (2.16)	12.0 (8.66)	0.23	12.8	55.5 (1.09)	36
V3	11.5 (2.26)	18.2 (5.16)	0.39	18.7	46.3 (2.27)	21
V4	16.4 (0.57)	-7.5 (2.58)	0.22	14.7	65.3 (1.95)	38
V7	8.7 (0.84)	16.2 (4.56)	0.17	11.6	66.2 (0.41)	99
V8	7.5 (0.76)	13.4 (3.72)	0.18	10.0	53.9 (0.59)	64
V10	6.6 (0.71)	24.3 (3.07)	0.22	11.9	54.5 (0.75)	84
V12	6.5 (1.17)	43.3 (7.48)	0.16	13.3	84.7 (1.72)	79
V15	7.9 (0.75)	31.9 (3.59)	0.23	15.4	65.7 (0.76)	52
V16	14.2 (1.06)	-4.2 (5.26)	0.21	13.3	64.6 (0.96)	81
V23	16.3 (0.67)	-36.6 (5.65)	0.14	11.3	81.3 (2.58)	52
V26	13.7 (1.51)	-4.8 (5.96)	0.25	12.6	51.3 (1.84)	38

At Storglaciären, the highest ablation was found for Category S3 (Table 7.5); and as a result of the merging procedure, this category also represents the net effect of categories S14, S15 and S16 (Appendix 1). Figure 7.3 indicates that high-ablation categories are typically associated with the low-level advection of easterly air, resulting in relatively clear skies and warm air temperatures. On-glacier, this results in high receipts of net shortwave radiation and an amplified sensible heat flux (Table 7.8). The orientation of the low-level flow for these high-ablation categories is similar to that described by Pohjola and Rogers (1997), who found high-ablation seasons at Storglaciären were characterised by the advection of east to south-easterly air, resulting from a trough of low pressure extending over the North Atlantic to the Gulf of Bothnia. The weather category with the lowest ablation at Storglaciären was Category S17 (to which no categories were merged). The low-level flow during this weather type is characterised by a north-easterly gradient wind orientated approximately parallel to the north-western Norwegian coast, which would advect cool air from the Barents Sea into northern Scandinavia. Relatively cold air temperatures are indeed observed on-glacier during this weather category, and the atmosphere is dry, resulting in somewhat suppressed turbulent heat fluxes. The net shortwave flux is also appreciably lower in this weather type than in the high-ablation categories, owing to the greater cloud cover that typically prevails (Table 7.8).

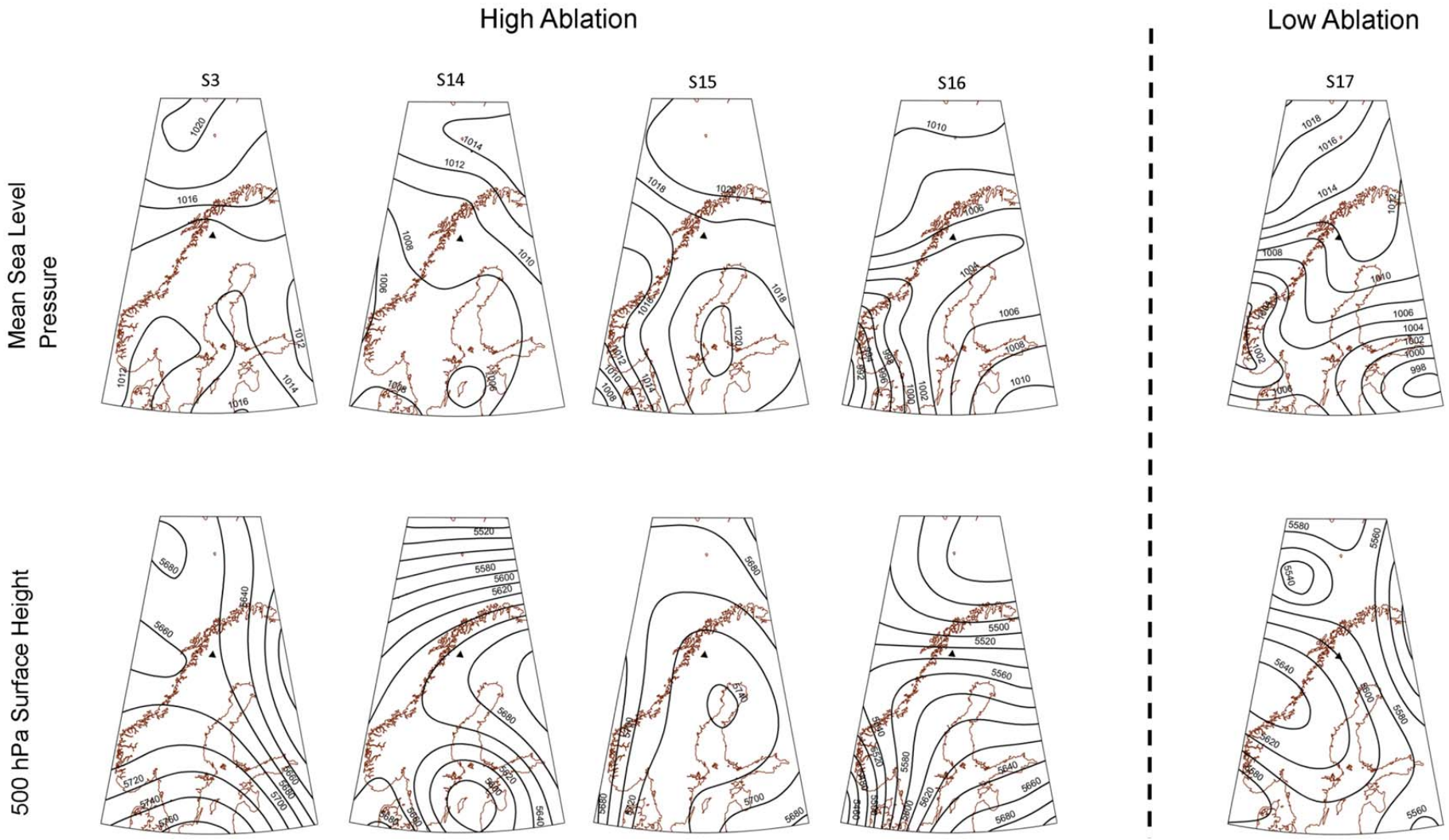

Figure 7.3. Mean sea level pressure (hPa) and height of the 500 hPa surface (metres) for the centroid days of 'high' and 'low' ablation weather categories at Storglaciären. Triangles indicate location of glacier.

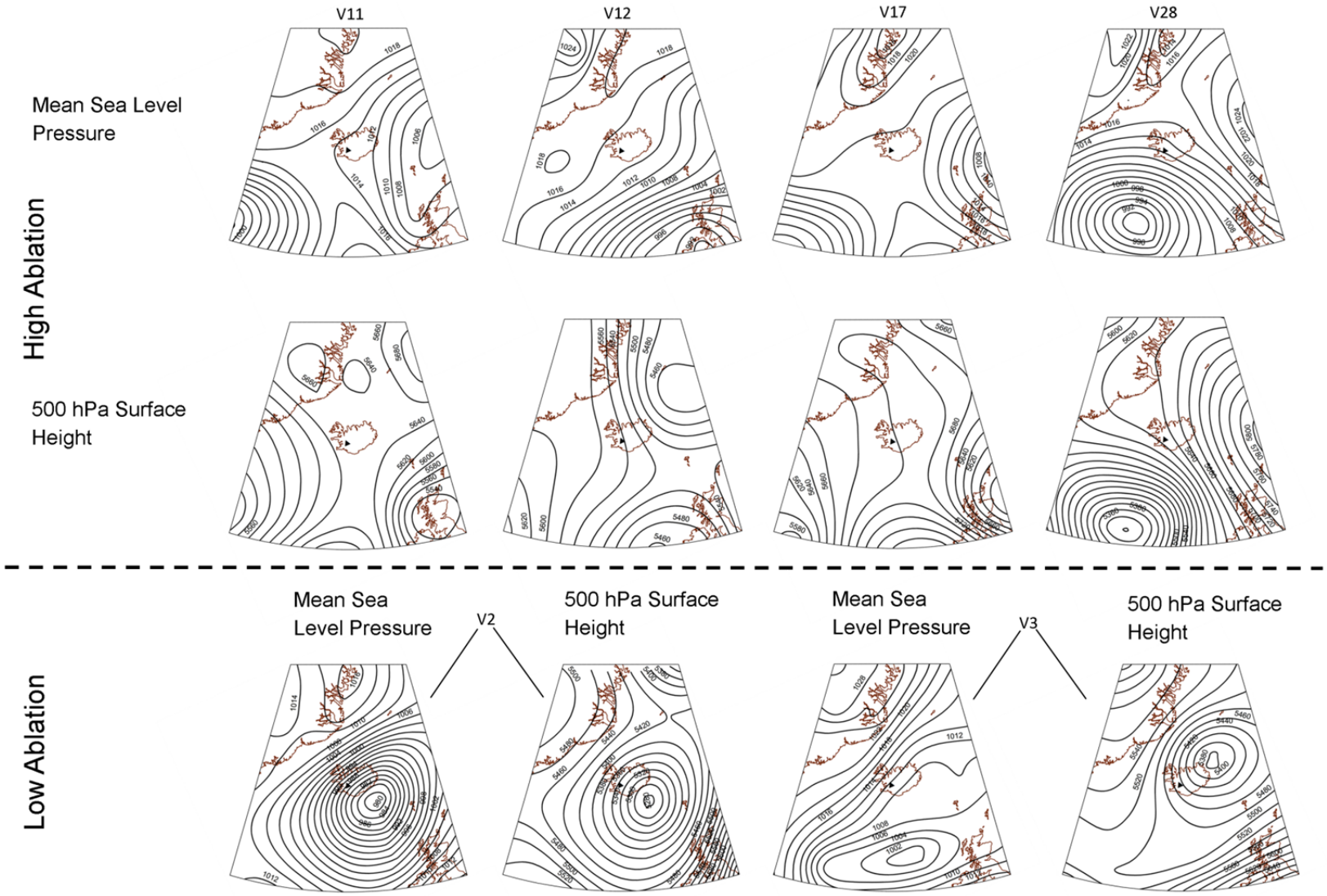

Figure 7.4. Same as Figure 7.3, but for Vestari Hagafellsjökull.

Table 7.8. Mean AWS meteorology and energy fluxes for 'low' and 'high' ablation weather categories. [a]Cloud cover calculated as the ratio of received to potential direct solar radiation (calculated from standard solar geometry after Iqbal, 1983).

	Weather Category	Air temperature (°C)	Vapour pressure (Pa)	Wind speed (m s^{-1})	[a]Cloud cover (fraction)	Sensible heat (W m^{-2})	Latent heat (W m^{-2})	Shortwave (W m^{-2})	Longwave (W m^{-2})	Melt energy (W m^{-2})	Ablation (mm w.e. d^{-1})
Storglaciären, 1387 m											
High	S3	7.4	718	2.7	0.45	54	14.4	135	-20	179	46
	S14	8.6	962	2.6	0.65	58	44.6	97	14	210	54
	S15	8.1	747	2.8	0.39	59	18.6	164	-27	211	55
	S16	5.9	600	2.5	0.31	43	0.2	185	-43	178	46
Low	S17	1.2	540	1.8	0.60	12	-0.2	65	-24	49	13
Vestari Hagafellsjökull, 1100 m											
High	V11	3.3	674	5.3	0.28	37	10.6	179	-41	188	49
	V12	2.6	640	4.9	0.32	28	3.5	148	-42	137	38
	V17	3.7	691	4.4	0.35	32	9.2	123	-34	132	35
	V28	3.4	699	7.3	0.57	51	19.8	86	-4	156	40
Low	V2	-1.1	571	19.0	0.62	-34	-25.2	44	-7	-28	8
	V3	-1.9	499	11.2	0.36	-45	-43.7	72	-41	-66	9
Vestari Hagafellsjökull, 500 m											
High	V11	6.4	730	6.1	0.32	91	22.7	287	-23	378	98
	V12	5.5	721	5.4	0.38	73	20.9	249	-19	324	84
	V17	6.3	798	4.7	0.46	74	33.6	210	-3	314	81
	V28	6.9	751	8.9	0.62	148	46.1	135	6	336	87
Low	V2	3.2	622	14.8	0.80	96	-0.2	86	-11	171	45
	V3	2.3	571	7.8	0.44	37	-16.6	175	-39	156	46

At Vestari Hagafellsjökull, Category V12 was chosen as an exemplar for high-ablation conditions, as this represented the highest ablation category at 500 m and the second highest at 1100 m. The aggregating procedure resulted in this category also representing categories V11, V17 and V28. Figure 7.4 illustrates that high-ablation conditions are typically associated with east-north-easterly flow at low levels, whilst northerly flow persists aloft. These conditions are similar to the 'Eastern' and 'Northeastern' types described by Einarsson (1984), during which fair weather in southern and western Iceland prevails. Measurements from the AWSs at both locations, show relatively warm air temperatures are found during such circumstances, and with the exception of Category V28, cloud cover is generally light. These conditions contribute to pronounced turbulent and radiative heat fluxes driving ablation (Table 7.8).

The lowest ablation category at Vestari Hagafellsjökull is Category V3, with which Category V2 had been merged. Both of these sub-types are characterised by cyclonic curvature and steep pressure gradients, resulting in high wind speeds on the ice cap. These types are also characterised by low temperatures and vapour pressure; the latter drives a latent heat loss at the glacier surface at both elevations, serving to further reduce available melt energy (Table 7.8). At 1100 m, where melt energy averages below zero, the minimal ablation observed during this category (<10 mm w.e. d^{-1}) is a result of sublimation.

7.4.3. Ablation-model performance

The daily and annual performance of each model is tabulated in Table 7.9 and summarised graphically in figures 7.5 and 7.6, respectively. At daily resolution, it is evident that RSEB is the best-performing ablation model at both elevations on the ice cap, recording the highest d^2 and r^2 values; at Storglaciären, WCCTIn proves to be most skilful. The same conclusions are drawn when the models are assessed annually: the only exception being that WCCTIn no longer performs best at Storglaciären; here the honours are shared between TIn and WCA, which achieve the highest d^2 and r^2 measures, respectively. The worst indicator of daily ablation is WCA, as this model is ranked lowest for all locations in Table 7.9. Graphically, the relatively poor correspondence with observations for WCA is also evident in Figure 7.5, which attests to considerable intra-category variability in ablation.

Table 7.9. Ablation model performance metrics. Red indicates the best performing model, and blue shows the worst. [a]Units of the systematic and unsystematic error components are mm w.e. d^{-1} when model performance is evaluated daily, and mm w.e. a^{-1} when assessed (inter-) annually.

	Storglaciären				Vestari Hagafellsjökull, 1100 m				Vestari Hagafellsjökull, 500 m			
	[a]$RMSE_s$	$RMSE_u$	d^2	r^2	$RMSE_s$	$RMSE_u$	d^2	r^2	RMSEs	RMSEu	d^2	r^2
						Daily						
RSEB	2.0	9.6	0.90	0.65	2.0	8.1	0.91	0.72	3.9	13.1	0.88	0.59
TIn	1.9	9.9	0.89	0.64	1.8	12.2	0.83	0.58	9.4	13.1	0.78	0.39
WCA	7.1	8.7	0.81	0.47	6.0	8.8	0.77	0.37	13.6	9.8	0.67	0.28
WCCTIn	3.9	7.5	0.91	0.69	4.6	8.6	0.82	0.47	9.8	10.4	0.81	0.48
						Annual						
RSEB	118	120	0.78	0.45	197	112	0.97	0.97	59	88	0.98	0.96
TIn	61	113	0.89	0.66	130	326	0.91	0.69	157	221	0.91	0.85
WCA	103	101	0.87	0.72	507	198	0.54	0.29	171	78	0.89	0.86
WCCTIn	82	94	0.89	0.70	447	238	0.63	0.36	32	99	0.98	0.94

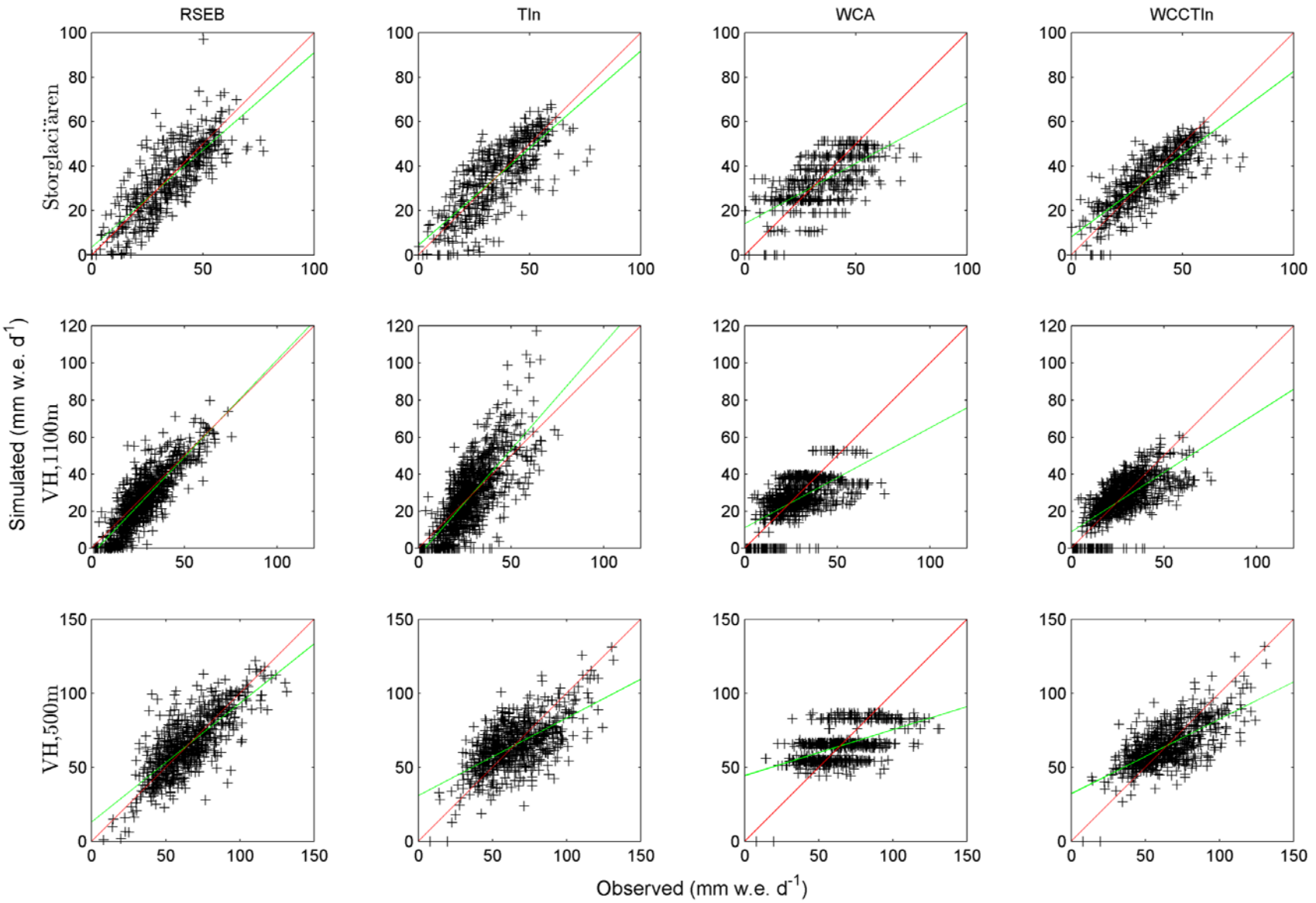

Figure 7.5. Performance of models evaluated daily. Red line gives the 1:1 relationship and the green line provides the best linear fit.

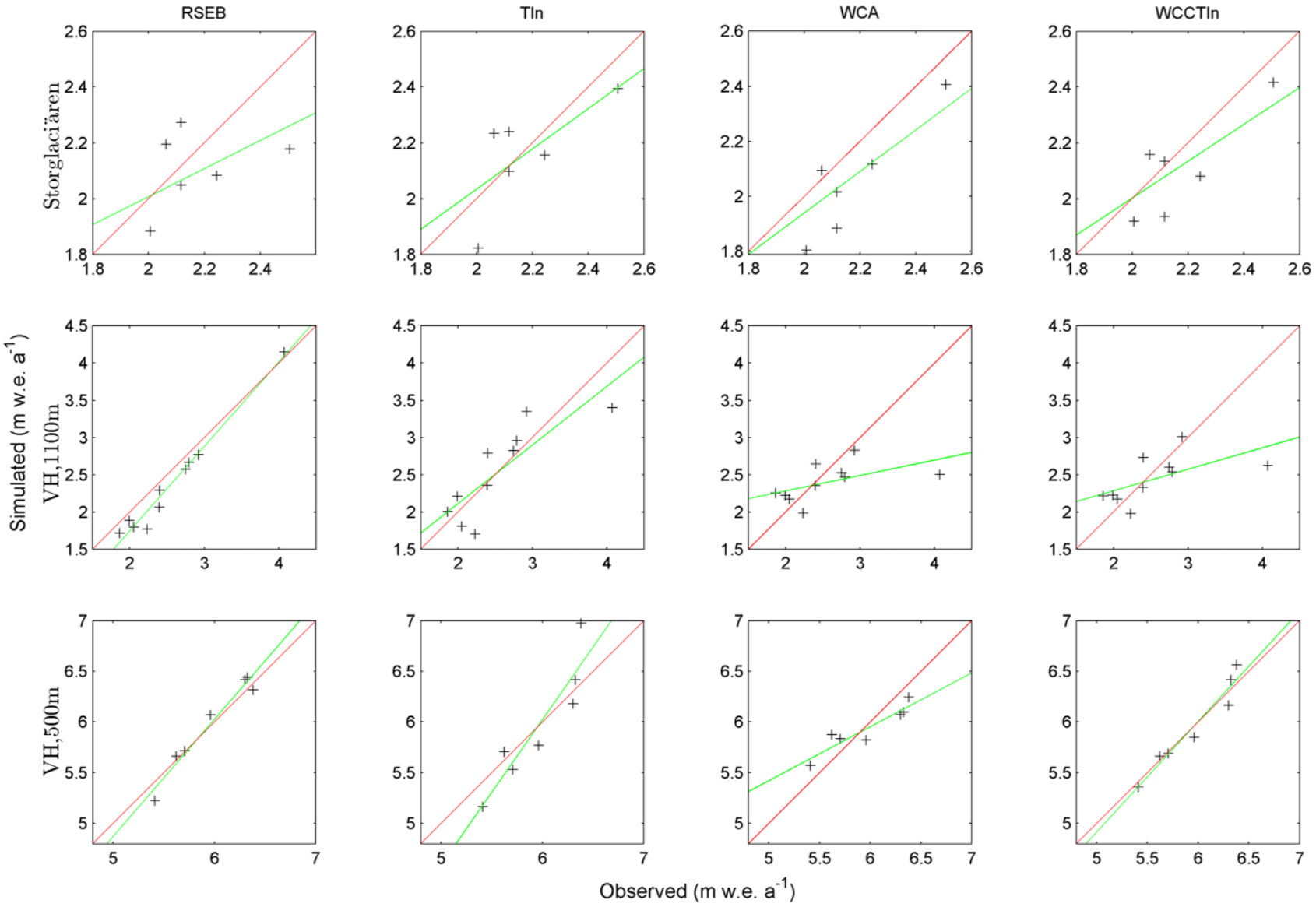

Figure 7.6. Interannual performance of models. Coloured lines have the same meaning as in Figure 7.5.

At annual resolution, with the exception of 1100m on Vestari Hagafellsjökull, the performance of WCA improves considerably: despite its simplicity, this model explains 72% and 86% of the interannual variation in ablation at Storglaciären and 500 m on Vestari Hagafellsjökull, respectively. It should be noted that this proportion of explained variance actually exceeds that provided by the frequently-used temperature-index model (TIn). The d^2 measure also increases for these locations, although, WCA still provides the worst performance at 500 on the ice cap according to this metric. It is interesting to observe that, despite the physical realism offered by RSEB, this method actually provides the worst indication of interannual ablation at Storglaciären.

Further insight regarding the performance of RSEB is facilitated through examination of the individual energy fluxes. The appropriate d^2 performance metrics are provided in Table 7.10 and the agreement between observed and simulated energetics is demonstrated visually in Figures 7.7 and 7.8. It is apparent that, averaged across all locations, the simulated sensible heat flux records the lowest agreement with observations for both daily and annual assessments, whilst the highest agreement is found for the shortwave heat flux. Aggregating the energy fluxes into the turbulent (sensible and latent heat) and radiative components (net shortwave and net longwave radiation), indicates that radiative heat energy is simulated with greater skill by RSEB at daily and annual resolution (d^2 values averaged across locations: 0.82 and 0.87 (daily), and 0.72 and 0.91 (yearly) for the turbulent and radiative heat flux components, respectively).

Table 7.10. Correspondence (d^2) between measured (i.e. simulated with the in-situ AWS data from chapters 2 and 3) and simulated energy fluxes (RSEB).

	Sensible heat		**Latent heat**		**Net Shortwave**		**Net Longwave**	
	daily	annual	daily	annual	daily	annual	daily	annual
Storglaciären, 1387m	0.80	0.46	0.93	0.87	0.89	0.92	0.88	0.87
Vestari Hagafellsjökull, 1100 m	0.67	0.67	0.81	0.64	0.93	1.00	0.80	0.79
Vestari Hagafellsjökull, 500 m	0.81	0.92	0.91	0.77	0.89	0.96	0.86	0.95
Mean	0.76	0.68	0.88	0.76	0.90	0.96	0.85	0.87

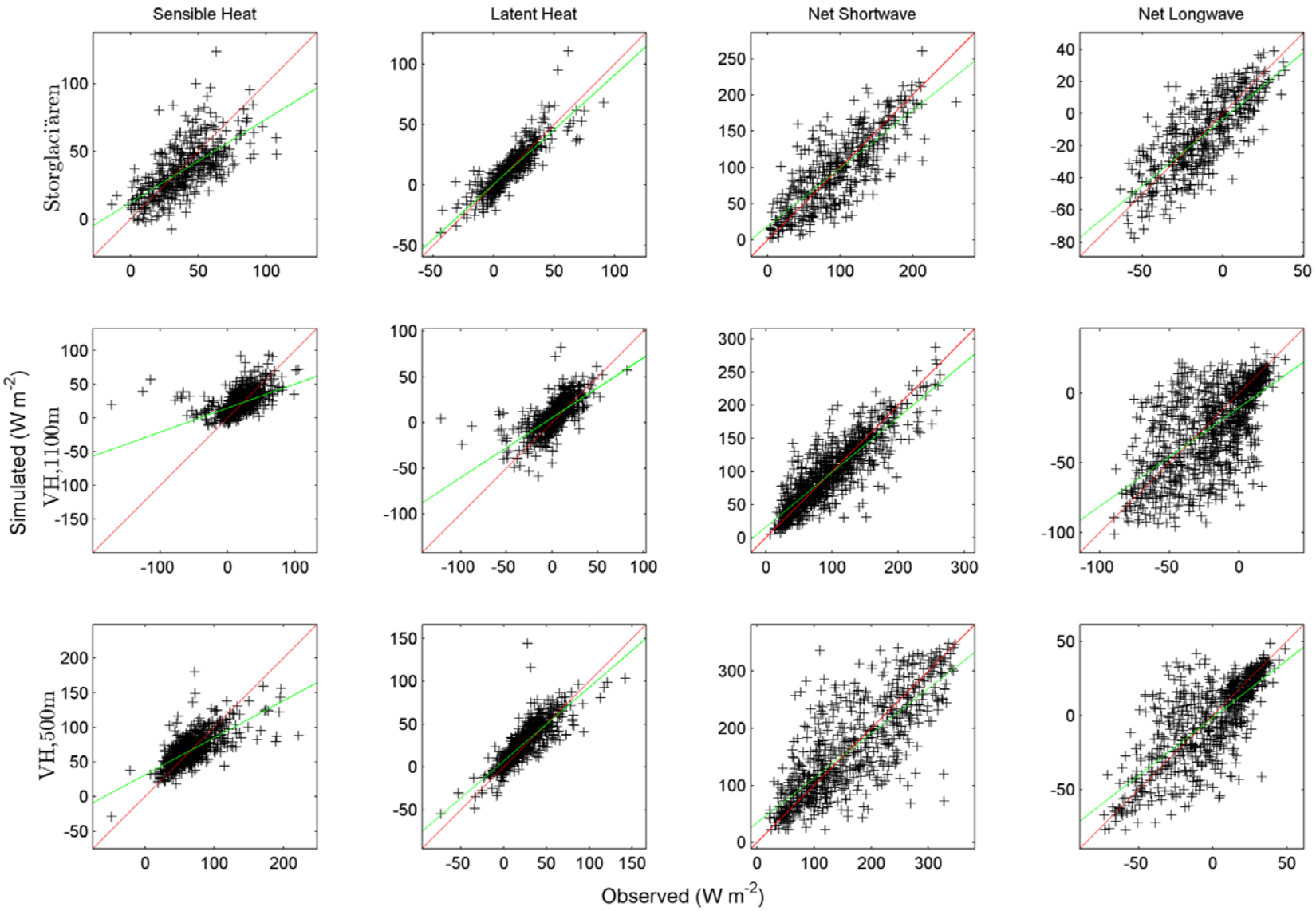

Figure 7.7. Daily summary of measured energy fluxes (i.e. modelled with in-situ AWS data—Chapters 2 and 3) and simulated energy fluxes (RSEB—driven by reanalysis data).

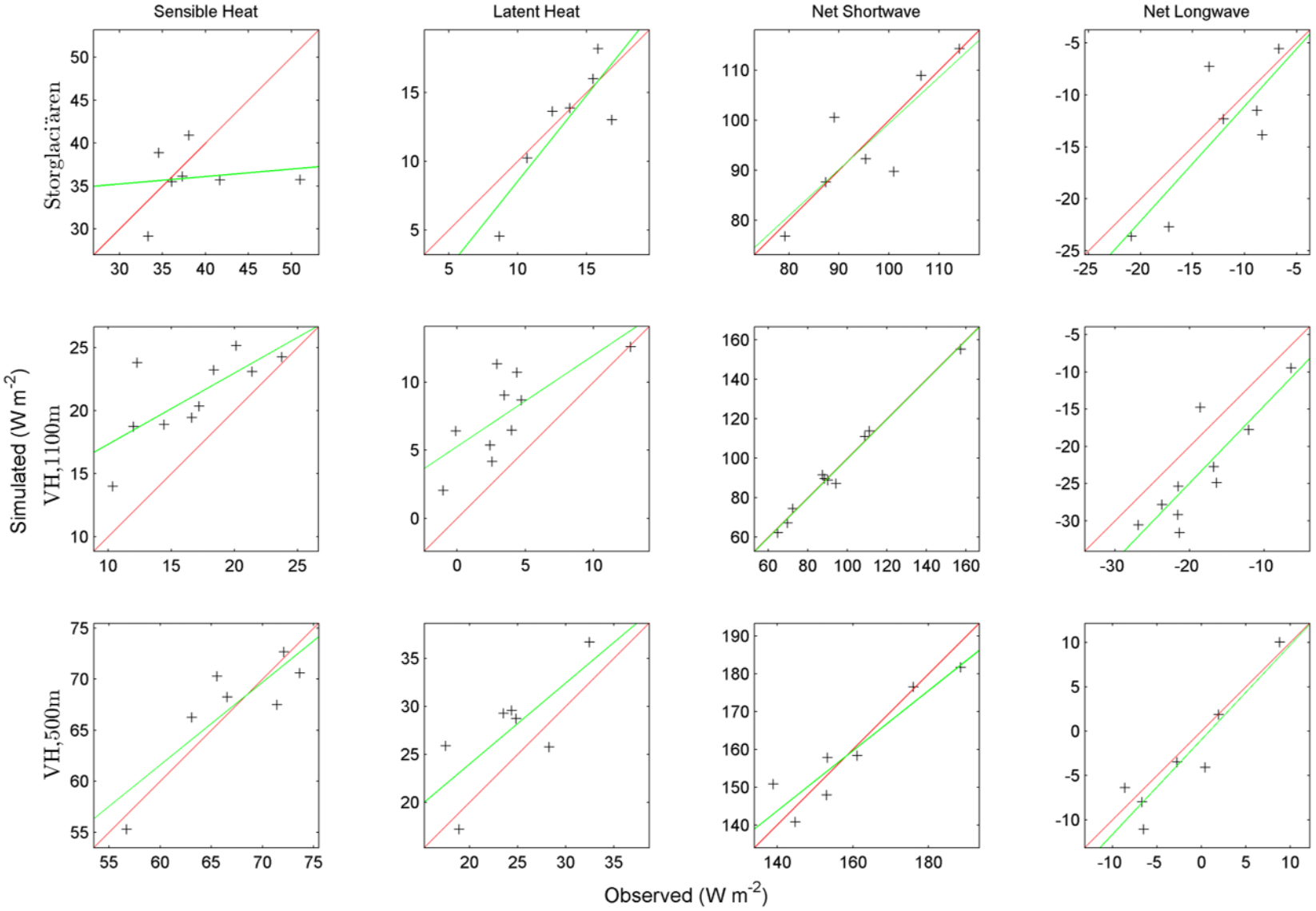

Figure 7.8. Annual summary of measured and simulated energy fluxes.

Integrating this examination of the individual energy fluxes into the assessment of ablation-model performance, it is evident that the limited skill of RSEB at annual resolution for Storglaciären can mainly be explained by the poor correspondence between the simulated and observed sensible heat transfer at this time scale: the annual mean sensible heat flux simulated by RSEB does not correlate significantly with the observed series at this location ($r = 0.14$, $p = 0.76$). This is largely a result of the failure of RSEB to simulate the pronounced sensible heat fluxes during 2006 (the year with the highest observed flux: Figure 7.8); during this year, sensible heat energy was underestimated by ~30% on Storglaciären.

The relative failure of RSEB to simulate sensible heat transfer adequately at Storglaciären is somewhat surprising, given that the interannual agreement between the glacier meteorology and reanalysis data is high for those variables needed to evaluate the sensible heat flux (the wind speed and air temperature: Table 7.11). However, it is important to note that this energy component depends on the product of the air temperature and the wind speed; it is therefore necessary to capture the covariance between these variables if the sensible flux is to be simulated accurately. This requirement is particularly pertinent because, through the katabatic wind, there is often a correlation between air temperatures and the wind speed recorded on glacier, and such a relation is indeed observed at Storglaciären (see Chapter 3, Section 3.4.3). Because katabatic drainage is a local micro-meteorological process at the scale of valley glaciers, it is not resolved explicitly by the spatially-coarse reanalysis data. Hence, failure to account for this process may result in systematic errors in the simulation of the sensible heat flux. The wind speed and temperature data from Storglaciären support this explanation: during 2006, the mean product of these two variables was underestimated significantly in the quantile-mapped reanalysis data (Figure 7.9: left). Indeed, it is apparent that much of the annual error in the simulated sensible heat flux at this location can be explained by discrepancies of this product (Figure 7.9: right).

Table 7.11. Annually-calculated Pearson's product-moment correlation coefficients between quantile-mapped reanalysis meteorological variables, and those recorded on-glacier.

Meteorological Variable	**Storglaciären**	**Vestari Hagafellsjökull, 1100 m**	**Vestari Hagafellsjökull, 500 m**
2 m Air Temperature	0.99	0.85	0.97
2 m Vapour Pressure	0.92	0.76	0.91
2 m Wind Speed	0.97	0.83	0.54
Incident Global Radiation	0.82	0.74	0.89
Incident Longwave Radiation	0.91	0.86	0.94
Mean	0.92	0.75	0.83

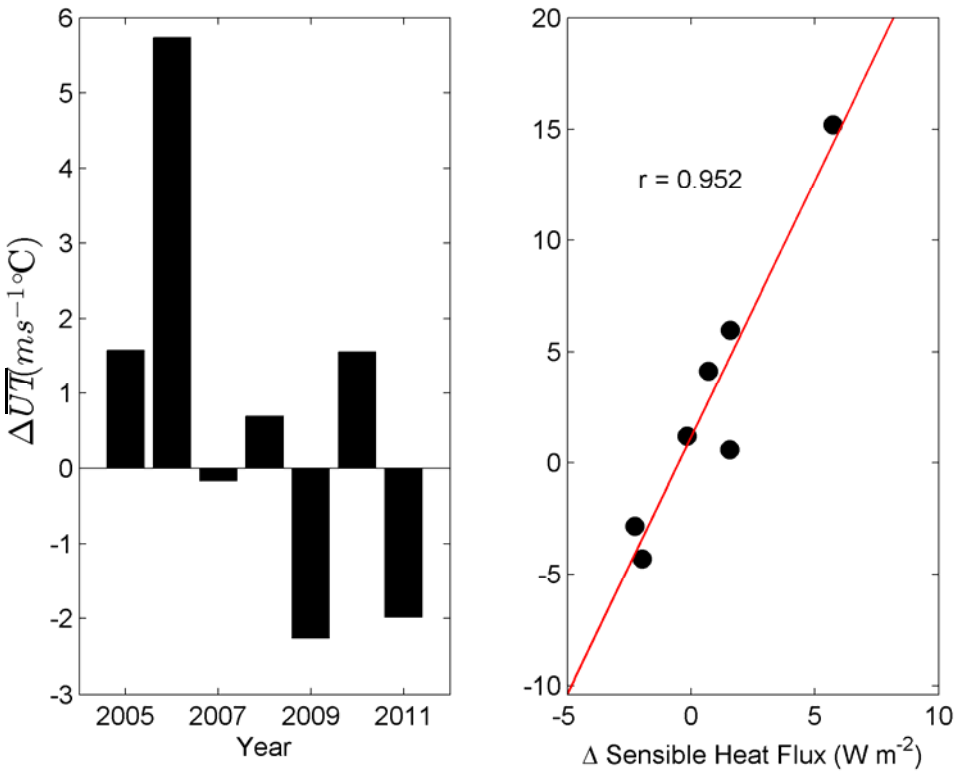

Figure 7.9. Differences in the annual-mean temperature-wind speed product (left-hand side) and their relationship with sensible heat flux residuals (right-hand side) at Storglaciären. The temperature-wind speed product (UT: where U is the wind speed and T is the air temperature) is defined as the mean daily wind speed multiplied by the mean daily air temperature. These products are calculated for both the quantile-mapped reanalysis data and the in-situ AWS observations. The resulting values are averaged to annual resolution ($\overline{UT}$) before the differences are calculated (observed $\overline{UT}$, minus $\overline{UT}$ calculated from the quantile-mapped reanalysis data). On the right-hand side, these differences are plotted against the difference in annual-mean sensible heat flux (observed minus that simulated by RSEB). Note that both graphs share the same y-axis label.

Further examination of the agreement between individual energy components also indicates the presence of appreciable biases, which are clearest at annual resolution for the higher elevation station on the ice cap (Figure 7.8). It is apparent, for example, that there is a tendency for the turbulent heat fluxes to be overestimated at 1100 m on Vestari Hagafellsjökull. However, it is suggested that this may be, in part, an artefact of the modelling procedure used in RSEB. In the absence of direct measurements, it is necessary to parameterize the emitted longwave flux as a function of the glacier surface temperature, which is achieved via an iterative procedure (Table 7.2). This contrasts with the analyses in chapters 2 and 3, in which the SEB is calculated mainly with the assumption of a 0°C surface (the synthesised Storglaciären series is an exception to this rule: Chapter 3, Section 3.5). Under this assumption, a glacier surface which is warmer than the air temperature is more likely to occur than when the surface temperature is lowered progressively (as in RSEB). In turn, this results in negative sensible heat fluxes being encountered less frequently in RSEB. The latent heat flux may also be biased by this different treatment, as the glacier surface temperature affects both the near-surface vapour-pressure gradient, and the latent heat of phase transition (Chapter 2; Section 2.4). Consequently, as the frequency of negative turbulent heat fluxes decreases, annual mean values of these energy components will increase.

The effect of the procedural difference is most likely to manifest at 1100 m on the ice cap, due to the cooler conditions and more frequent negative energy balances which persist here (Chapter 3, Section 3.7, Table 3.7). Stratifying the simulated energy fluxes as a function of the surface temperature simulated by RSEB supports this explanation, as both the daily and annual d^2 values for the turbulent heat fluxes improve at 1100 m if days with average surface temperatures below the melting point (~7% of the simulation) are excluded (d^2 values for the sensible heat flux of 0.80 and 0.75, and for the latent heat fluxes of 0.88 and 0.85 when assessed daily and annually, respectively). It is important to note that this process described, which introduces a positive bias in the turbulent heat fluxes, does not propagate to the ablation rate, as the surface temperature is only lowered when the SEB is negative; it does, however, suggest that caution is warranted when comparing the individual energy fluxes simulated by RSEB, with those generated by in-situ data.

7.5. Discussion

7.5.1. Reanalysis climatology

Critical to the physical simulation of glacier ablation is the ability of the reanalysis data to capture variability of the glacier boundary layer adequately. However, discrepancies between reanalysis data and the glacier climate are often observed (e.g. Hock et al., 2007; Rye et al., 2010), due to elevational differences between the grid and observed orography, and from biases that may result from simplifications within the reanalysis assimilation scheme. Such discrepancies were indeed evident when comparing reanalysis data with observations at all locations in this study, and these were corrected for with a quantile-mapping procedure (Section 7.3.1). The temporal coherence between the corrected reanalysis data and the glacier observations was then assessed through the calculation of Pearson's correlation coefficients.

The resulting agreement between glacier observations and the reanalysis climate data was found to vary between locations and the meteorological variable being assessed. Generally, reanalysis data correlated most strongly with air temperature and vapour pressure recorded on-glacier, and correlations were highest at Storglaciären. The wind speed generally exhibited the lowest correlations with the reanalysis data; and, overall, observations from the 500 m station on Vestari Hagafellsjökull exhibited the minimum correspondence with the quantile-mapped reanalysis variables. At this location, correlation coefficients for the air temperature, vapour pressure, and wind speed were appreciably lower than observed at the 1100 m station on Vestari Hagafellsjökull.

It is suggested that such elevational divergence in the agreement between reanalysis data and observations on the ice cap may be explained partly by the role of katabatic drainage. Katabatic flow has previously been observed to dry and cool air flowing downslope, due to cumulative sensible and latent heat exchange with the melting glacier surface (Greuell and Böhm, 1998; Shea and Moore, 2010; Chapter 5); this also causes the strength of the katabatic wind to increase downslope as the temperature deficit of the boundary layer is enhanced (Oerlemans and Grisogono, 2002). Hence, at low elevations on the ice cap, where katabatic flow is well developed, the thermodynamic state of the boundary layer will exhibit variations somewhat independently of the large-scale flow. This would explain the lower correlations for

air temperature, vapour pressure, and wind speed observed between the reanalysis data and observations lower on the glacier, and is consistent with Gardner et al. (2009) who found temperatures recorded at higher elevations in the Canadian High Arctic were in best agreement with reanalysis data.

Counter to the behaviour observed for air temperature, vapour pressure and wind speed, the on-glacier radiative fields exhibited greater agreement with the reanalysis data at the lower elevation station on Vestari Hagafellsjökull. This might be explained by the nature of the ERA reanalysis data. The long- and shortwave radiative fluxes are defined for the surface only, which is actually lower than even the 500 m station (ERA model surface is 307 m.a.s.l.). Consequently, it is likely that cloud cover will be poorly simulated for the higher altitude site. For example, low-level cloud cover (that *would* affect the surface radiation balance, and may be frequent at Icelandic glaciers Oerlemans et al. (1999), and see Chapter 2, Section 2.5.1), during otherwise clear-sky conditions, will also be erroneously assumed to affect incident receipts higher on the ice cap. This would compromise estimates of both longwave and shortwave radiation from the reanalysis data, as both are heavily affected by cloud cover (e.g. Sedlar and Hock, 2009; Klok and Oerlemans, 2002).

7.5.2. Ablation models

The utility of applying bias-corrected reanalysis data to forecast ablation was investigated with physically- and empirically-based techniques. A conceptual attraction of a physical treatment is that, because these approaches are founded on principles of energy transfer, they require little calibration and should therefore be portable in space and time. The performance of RSEB in this study was somewhat encouraging at Vestari Hagafellsjökull, achieving the most accurate simulation of ablation at both elevations on the ice cap in daily and yearly assessments. However, its success at Storglaciären was more modest: here, it performed worst at interannual resolution and it was out-performed by WCCTIn when assessed daily. This finding is consistent with Hock et al. (2007) who reported that temperature-index methods simulated the summer balance at Storglaciären more accurately than energy-balance approaches driven by ERA-40 reanalysis data.

It must also be considered that the appraisal of RSEB is optimistic for all locations. For example, the shortwave heat flux is afforded a very generous treatment in the model formulation, due to the fact that the reflected flux is determined with the measured albedo—a parameter which is not directly obtainable without in-situ measurements—and which may be challenging to determine empirically (Brock, 2004). Moreover, it is suggested that the quantile-mapping procedure contributes to a model performance which may be challenging to emulate in most practical applications. That is, pronounced biases were observed in the reanalysis data (see Section 7.3.1), and each of the meteorological variables was corrected using long series of the glacier meteorology for reference. These corrections are only possible where prolonged in-situ glacier observations are available, and this is certainly not the case for most glacierized areas worldwide (Jarosch et al., 2012).

Without such observations, reanalysis data must either be used unadjusted or corrected based on simplifying assumptions (e.g. static temperature lapse rates: Raper and Braithwaite, 2006; Paul and Kotlarski, 2010). In this regard it is worth noting the magnitude of some of the discrepancies between the reanalysis fields and the observations made on-glacier. For example, pronounced differences were observed for the wind speed (mean glacier wind speed underestimated by more than 40% at both elevations on the ice cap) and the incident shortwave flux (mean glacier shortwave incident flux underestimated by ~20% at 1100 m on the ice cap). If these data are applied without correction via the quantile-mapping procedure (i.e. if wind speed at 500 m and both wind speed and the incident shortwave flux at 1100 m on Vestari Hagafellsjökull are taken directly from the reanalysis data—without adjustment), RSEB no longer performs best out of the ablation models at these locations according to the d^2 measure (assessed daily: d^2= 0.77 and 0.79; assessed yearly: d^2 = 0.48 and 0.48, at 1100 m and 500 m, respectively; corresponding r^2 values of 0.70 and 0.52 (daily) and 0.80 and 0.94 (yearly)). Indeed, without correction of these variables, RSEB provides the worst estimate of ablation according to the d^2 metric at 1100 m for both annual and yearly assessments, and at 500 m when evaluated annually. Hence, it is evident that the absence of site-specific correction factors may be to the considerable detriment of RSEB's performance.

Whilst the empirical models explored in this study also require calibration of correction functions (to adjust air temperature to the glacier: TIn and WCCTIn), and the determination of site-specific model coefficients (TIn, WCCTIn, and WCA), the demands of these models are more easily satisfied than for RSEB: at most, only synchronous observations of air temperature and ablation are required. From a practical perspective, the merits of these empirical techniques for simulating ablation are therefore of particular interest.

TIn, a traditional temperature-index model, performed favourably at all locations, particularly at annual resolution: at this time-scale, the model explained 66% to 85% of variance in ablation. Daily ablation was also simulated reasonably well with this technique, although less so at 500 m on Vestari Hagafellsjökull, where performance metrics were somewhat modest ($d^2 = 0.78$; $r^2 = 0.39$). However, it is worth noting that the correspondence between temperature and ablation is actually greater at this location, and at 1100 m on Vestari Hagafellsjökull, when the reanalysis temperature data are used instead of the in-situ observations (according to the r^2 measure: see Chapter 6, Section 6.4.2, Figure 6.4). Importantly, this demonstrates that nothing is lost by using the spatially-coarser reanalysis air temperature data to determine estimates of ablation from the temperature-index method at the ice cap.

The inclusion of WCA in the analyses satisfied two purposes in this chapter: it acted as a method of forecasting ablation (Equation 7.2), and as a convenient framework to explore wider-scale processes driving ablation. At Storglaciären, high-ablation weather categories were found to be the result of pronounced sensible and shortwave heat fluxes, and examination of the synoptic pressure field showed that these conditions were the result of easterly air flow. The warm air temperatures observed during these conditions are consistent with the regime outlined by Chen and Hellström (1999), who report that air advected from the east is heated by its passage over a land surface warmed by summer insolation. The results from these analyses are also in agreement with the investigation performed by Fealy and Sweeney (2007), who observed a similar association between weather categories characterised by easterly air-flow, and enhanced summer ablation for a selection of Scandinavian glaciers (including Storglaciären). In addition, the authors reported that ablation was suppressed by weather categories characterised by the advection of northerly air; this also agrees with the present analyses, which found the lowest ablation resulted from

the advection of cold, polar air from the Barents Sea. During this type, the sensible and shortwave energy fluxes were particularly subdued.

At Vestari Hagafellsjökull, cold air temperatures were similarly associated with weather categories in which ablation was suppressed. However, these types were also characterised by cyclonic curvature and strong gradient winds. High-ablation weather categories at this location were typically the result of north-easterly flow prevailing; these conditions resulted in warmer air temperatures and clearer skies, the latter contributing to an amplified shortwave energy flux. The fact that these high-ablation conditions are associated with a northerly component of air-flow somewhat contrasts the results from Storglaciären, but is in agreement with the summary provided by Einarsson (1984), who states that 'favourable' weather in the south and west of Iceland results from such northerly air-flow.

Although WCA facilitated a useful insight into wider-scale processes governing ablation, its skill as a predictive model was limited at daily resolution. It was, however, more successful at simulating interannual variation in ablation: despite its simplicity, WCA accounted for 72% and 86% of its variance at Storglaciären, and at 500 m on Vestari Hagafellsjökull, respectively (corresponding d^2 values of 0.87 and 0.89). This ability to capture low-frequency changes in surface energetics is in agreement with regression-based studies which have successfully simulated components of glacier mass-balance from the annual frequency of specific weather types (e.g. Hoinkes, 1968; Yarnal, 1984a and Fealy and Sweeney, 2007).

The ability of WCA to capture interannual variability of ablation at the higher elevation station on Vestari Hagafellsjökull was less impressive ($d^2 = 0.54$, $r^2 = 0.29$), and it is argued that this failure is a result of the pronounced variability of albedo which occurs at this location (Chapter 6, Figure 6.3). This highlights an important limitation of using empirical methods to determine ablation rates: namely, that erroneous results will be obtained if non-stationarity exists between synoptic weather conditions and the SEB. Specifically, the pronounced change of albedo at 1100 m on Vestari Hagafellsjökull introduces variability into the SEB which is largely independent of the weather conditions. This can actively modify the relationship between weather categories and the SEB. Brazel et al. (1992) also noted that albedo variability challenged the coupling of synoptic weather types to the glacier ablation,

explaining that seasonal albedo trends at West Gulkana Glacier were critically important in determining the amount of ablation during specific weather types.

Albedo declines through time due to snow metamorphism (Brock, 2004; Hock, 2005). Thus, the timing of summer snowfalls within the ablation season will have an important effect on interannual albedo variations. Glacier albedo is also heavily affected by concentration of particulates, which may accumulate with time, and Hock (2005) states that deposits of sediment or rock debris can reduce albedo considerably. It is suggested that this process warrants particular consideration at 1100 m on Vestari Hagafellsjökull, where the 2010 eruption of the Eyjafjallajökull volcano deposited a tephra layer (Chapter 2, Section 2.4.). The effect which this had on the albedo is shown by the decadal-low of surface reflectivity observed in 2010; the tephra did not affect albedo at the 500 m station on Vestari Hagafellsjökull (Chapter 6, Figure 6.3; Guðmundsson, personal communication). If this effect on the albedo is considered as anomalous, there is perhaps justification for excluding 2010 from the analyses. If this year is omitted from the analyses and the cross-validation procedure re-run, the performance metrics of WCA do improve considerably (daily: $d^2 = 0.84$, $r^2 = 0.48$; annually: $d^2 = 0.74$, $r^2 = 0.50$).

WCCTIn built upon the analyses in Chapter 6 which noted that air temperature's role as an index of melt energy varied as a function of weather category. Thus, the effect of conditioning regression parameters relating positive air temperatures to ablation, as a function of weather-category membership was investigated with this approach. Applying this model in the cross-validation procedure yielded favourable results, as this method produced the highest d^2 (and r^2) values of the empirical models at Storglaciären and at 500 m on Vestari Hagafellsjökull when assessed daily. Indeed, at Storglaciären, WCCTIn even exceeded the performance of RSEB. The ability of WCCTIn to simulate interannual variability in ablation was also encouraging, although, its advantage over the other empirical techniques was less conclusive at this resolution. The performance of WCCTIn was also observed to be more modest at 1100 m on Vestari Hagafellsjökull for both daily and annual evaluations; however, it is apparent that this model is also affected by the tephra layer in 2010: if this year is similarly excluded, the performance metrics exhibit a comparable improvement to that

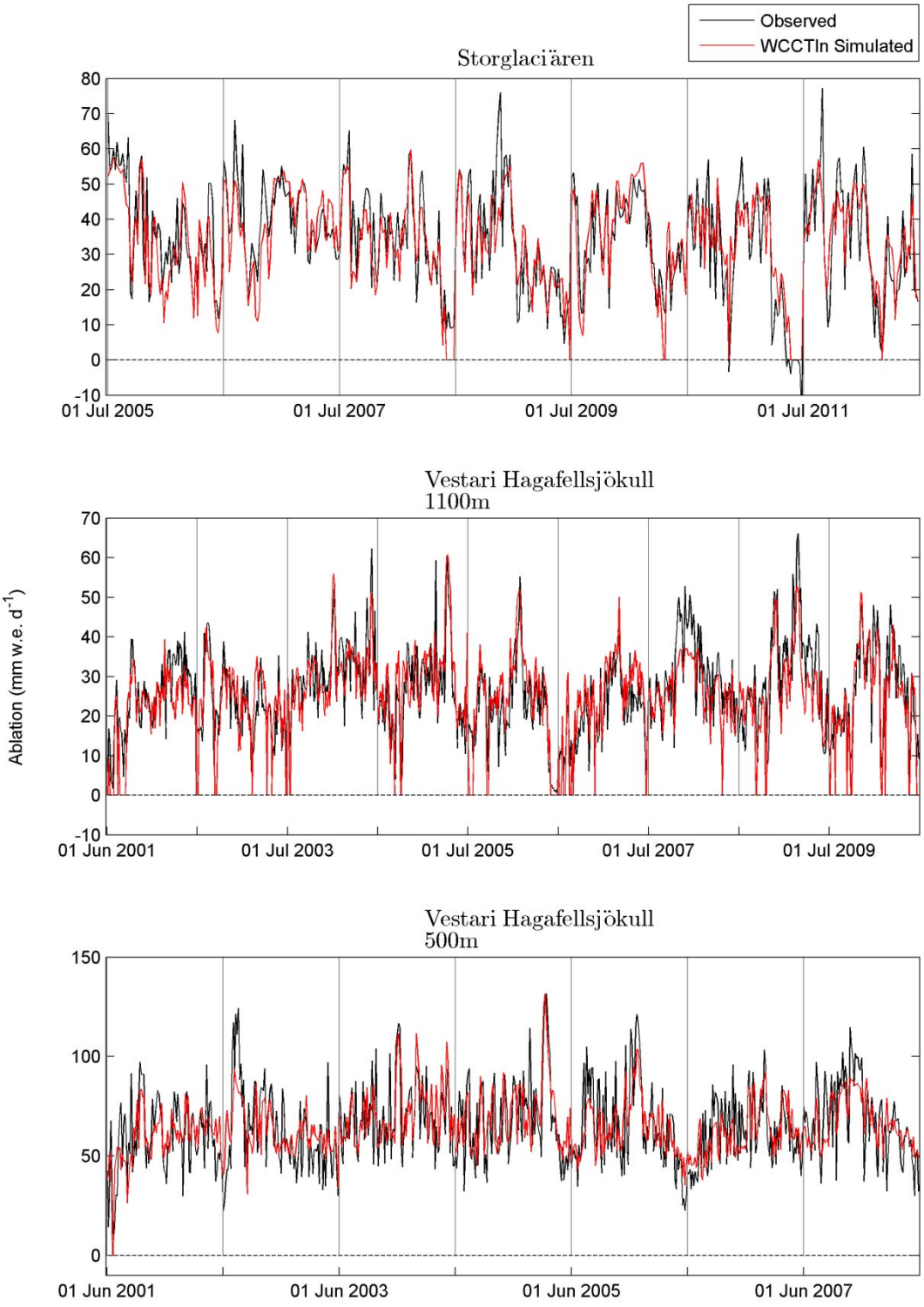

Figure 7.10. Observed ablation and that simulated by WCCTIn. Note that 2010 has been removed from the 1100 m station on Vestari Hagafellsjökull in this plot (see text for explanation).

witnessed for the WCA model (daily: d^2 = 0.87, r^2 = 0.59; annually: d^2 = 0.83, r^2 = 0.59). WCCTIn is then the best performing empirical model for all three locations when assessed daily with the d^2 measure, which evaluates the model's ability to capture variance and minimize bias (Figure 7.10). It should also be noted that this improved performance occurs despite the fact that snow and ice surfaces are not differentiated with this approach.

A useful illustration of using synoptically similar days to calibrate the regression equation relating $PDDs$ to ablation is shown in Figure 7.11. This demonstrates the ability of a modified form of WCCTIn to capture variance of ablation when applied in a cross-validation procedure. The modification is to relax weather-category membership and to calibrate regression parameters based on the n most synoptically similar days (according to the Euclidean distance between PC scores). Conceptually, this relaxation of weather-category membership is analogous to the 'optimized analogue' method used in Chapter 5 to model lapse-rate variability, and is considered to provide a useful demonstration of the benefits of the principle underlying WCCTIn. By iteratively incrementing n, it is apparent that model performance steadily declines as n increases. When n is at a maximum, the regression model is calibrated based on the entire dataset (excluding the year being simulated), and is therefore no different from a traditional temperature-index model (TIn).

The enhanced proportion of variance that can be explained when only synoptically-similar days are used to calibrate regression parameters—rather than using the whole data set—is appreciable: when n = 30, Figure 7.11 indicates that r^2 increases by 11% and 14% at Storglaciären and at 500 m on Vestari Hagafellsjökull, respectively, when compared to the performance when the regression is calibrated on the entire data set. The very limited improvement in performance at 1100 m on Vestari Hagafellsjökull (~4%) again underlines the importance of variable albedo at this location, which modifies the SEB somewhat independently of the prevailing weather.

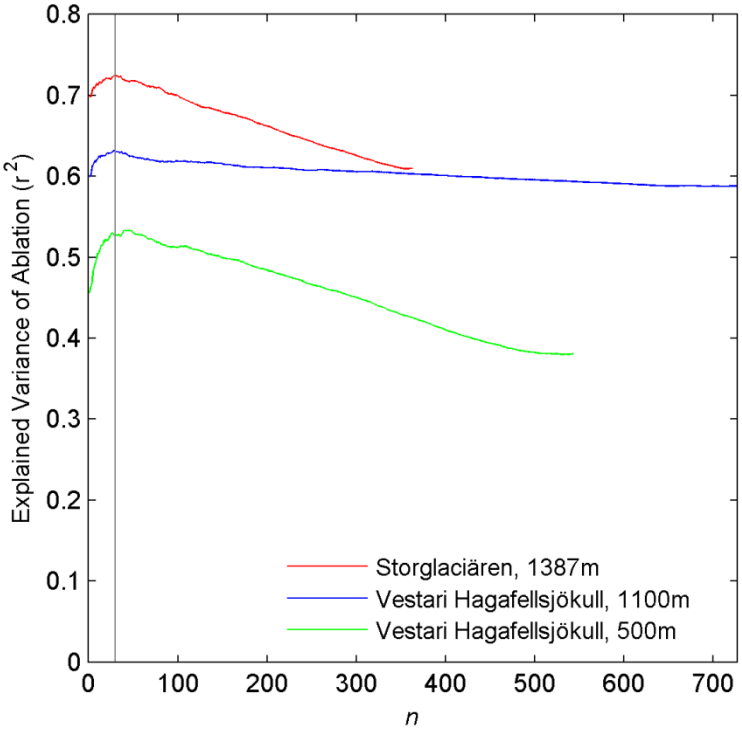

Figure 7.11. Change in the proportion of explained variance achieved by WCCTIn as a function of the number of most synoptically similar days the *PDDs*-ablation regression is calibrated with (n). The grey line shows the performance when n = 30.

It should also be highlighted that the maximum percentage of variance explained in Figure 7.11 is actually somewhat greater for all locations than is evident in Table 7.9; the same is true for the d^2 measure which reaches maximum values typically exceeding those attained by WCCTIn when n is in the region of 30-40 (maximum d^2 values of, 0.91, 0.87 and 0.83 at Storglaciären, 1100 m, and 500 m on Vestari Hagafellsjökull, respectively). These metrics indicate that the performance of WCCTIn can be improved by optimizing the synoptic-grouping procedure. This sensitivity of model performance to group sizes is addressed in Chapter 8 (Section 8.3).

7.6. Synthesis and Conclusions

Accurately simulating glacier-surface ablation from spatially-coarse climate data is desirable because it eliminates the need for recording logistically-intensive in-situ data. Similarly, because GCMs also provide future scenarios of climate at large horizontal resolutions, the ability to apply data skilfully at this scale to resolve processes within the glacier boundary layer, has significant temporal allure. However, glaciers are located in meteorologically complex environments: highly variable topography promotes micro-climatic variability, and katabatic winds cause

thermodynamic changes in the boundary layer which may be independent of the large-scale flow. These characteristics provide an appreciable challenge to researchers who seek to model the energy (and mass) balance of glaciers from such spatially-coarse data. This chapter examined these difficulties and investigated the relative skill of physical and empirical models in overcoming these challenges.

When compared to observations made on-glacier, the unadjusted reanalysis data exhibited considerable bias at all locations, which was corrected with a quantile-mapping procedure. This process recreates the observed statistical distributions of the different meteorological parameters exactly, but does not affect the temporal correspondence between the reanalysis data and the glacier meteorology, which was found to be variable between locations. Generally, the agreement between the bias-corrected reanalysis data and the glacier observations was best at Storglaciären; it was suggested that the lower correspondence at Vestari Hagafellsjökull may be due to the modifying effect—principally by katabatic forcing—which this ice-mass exerts on the local meteorology. However, despite the discordance between the reanalysis and observed meteorology, a physically-based model (RSEB) generally simulated ablation most accurately at all locations. It was emphasised, though, that the appraisal of RSEB was most likely optimistic, because albedo was prescribed with measurements in the model formulation. Moreover, it was argued that whilst the quantile-mapping procedure provides a simple-means by which to correct spatially-coarse climate information to the glacier boundary layer, such an approach demands extensive observations of glacier meteorology to determine suitable correction functions; this condition must be considered as challenging to satisfy for most applications which seek to drive simulations with spatially-coarse climate data.

Because the empirical ablation models investigated in this study have less-stringent data requirements than RSEB, it was suggested that the merits of these approaches are of particular interest from a practical perspective. The skill of applying the empirical techniques to forecast ablation was readily apparent from simulations applied in a cross-validation scheme. A temperature-index model (TIn) produced encouraging results, particularly at annual resolution, where it explained at least two-thirds of the observed variance in ablation at all locations. At daily resolution, it was also evident that driving TIn with reanalysis data, rather than air temperature recorded on-glacier (cf. Chapter 6), did not reduce its ability to simulate ablation. This demonstrates the

robust nature of temperature-index methods to transitioning from being forced with in-situ observations, to utilizing synoptic-scale data.

At daily resolution, WCA, which simply prescribed ablation as a function of weather-category occurrence, provided valuable insights into the coupling of ablation and wider-scale circulation, but heterogeneity of ablation within categories limited its predictive skill at this time-scale. Yet, despite its simplicity, the performance of this model was encouraging when evaluated annually, as it achieved levels of performance more comparable to the other empirical models at Storglaciären and at 500 m on Vestari Hagafellsjökull. It was, however, noted that albedo variability challenged WCA at 1100 m on Vestari Hagafellsjökull. This reflects a more general limitation of empirical models for simulating ablation: namely, if the relationship between surface energetics and synoptic climate is non-stationary, empirical techniques will be compromised by this behaviour.

The most encouraging results from the empirical ablation simulations were obtained when conditioning a temperature-index regression model as a function of weather-category membership (WCCTIn), which developed the principle introduced in Chapter 6 (Equation 6.9). If the anomalous albedo year of 2010 is discounted from observations at 1100 m on the ice cap, WCCTIn produced the best empirical estimate of daily ablation at all three locations according to the d^2 measure. This model also performed well at interannual resolution, although it offered no real advantage over TIn when assessed at this time-scale at 1100 m. Nevertheless, by recognising the fact that the temperature's role as an index of ablation is temporally variable—dependent on weather type—it is considered that WCCTIn provides a conceptually more robust approach to forecasting ablation for future climates, when persistent changes in the frequency and duration of weather types are likely. It is also important to note that the impressive performance of WCCTIn over daily time-scales demonstrates that traditional temperature-index models may be improved without additional demands for data recorded in situ. This benefit, combined with the simplicity with which WCCTIn can be implemented, provides a persuasive argument for examining this procedure of simulating ablation further.

8. Synthesis and Conclusions

8.1. Introduction

The aim of the thesis has been to contribute to an improved understanding of how synoptic climatological processes affect energy exchange and mass loss within the glacier boundary layer. This was pursued because there is a pressing need to determine the response of glaciers to a changing climate, which is hindered by a paucity of appropriately high-resolution meteorological data. For contemporary studies, the remote location of glaciers and ice caps provides the challenge—rendering prolonged, in-situ micrometeorological studies, impractical for all but a handful of the world's glaciers. Similarly, forecasting efforts are compromised by the coarse spatial resolution of GCMs, which do not resolve the local-micrometeorological variability required to accurately simulate processes of energy and mass exchange. It was argued, therefore, that much could be gained from establishing relations between synoptic-scale climate variability and processes within the glacier boundary layer. Specifically, it was suggested that coupling scales in this way provides a practical solution to simulating glacier surface energetics and ablation, and also contributes to the development of an enhanced understanding of how larger-scale climatic variability propagates to the meteorologically-complex glacier boundary layer.

Specific research objectives were formulated to realize this study's aim, these were to:

- gain insight into the variability of glacier surface meteorology and energy exchange at sub-daily to interannual time scales;
- explore how spatial variability of near-surface air temperature is related to synoptic climatic variability;
- investigate further the utility of using air temperature as a means of translating the effects of synoptic climate variability to the glacier boundary layer for purposes of quantifying ablation;
- examine the feasibility of developing practical, empirical models, which integrate synoptic climatological information to simulate ablation accurately.

In the next section (8.2), the findings of the research are summarised in relation to these objectives, before directions for future research are offered (Section 8.3), and concluding comments are given (Section 8.4).

8.2. Summary of Major Findings

8.2.1. Objective 1: Improved understanding of glacier meteorology and the SEB

The first objective sought to contribute to an enhanced understanding of glacier meteorology and energy exchange across a range of temporal scales. This objective was necessary to gain detailed insight into the processes driving ablation, which is required to understand the role of synoptic variability in modulating energy and mass exchange at the glacier surface. Chapters 2 and 3 addressed this objective by presenting meteorological data recorded at Vestari Hagafellsjökull and Storglaciären. These locations provided climatologically and glaciologically contrasting perspectives on the association between synoptic- and glacier-scale processes. Additional insights were obtained from observations at two locations on Vestari Hagafellsjökull, separated vertically by 600 m.

The meteorological record from Vestari Hagafellsjökull emphasised the distinct nature of the glacier boundary layer. Observations were available from May-October, and seasonality was observed during this period, which was in agreement with the climatology of Iceland outlined by Einarsson (1984). The period of June-August (JJA) was afforded explicit attention, as ablation rates are most rapid during this period, and on average, positive air temperatures persisted at the higher elevation station throughout these months. During JJA, air temperature variability was observed to be muted, and the wind was appreciably strong and consistent in direction. Such conditions are characteristic of katabatic boundary layers which have been observed over melting glaciers (Van den Broeke, 1997a; Oerlemans and Grisogono, 2002; Andreassen et al., 2008; Hodgkins et al., 2012b). The forcing which produces this distinct meteorology is heat exchange between the glacier and the atmosphere above, resulting in a cooling effect and a density gradient which drains air under gravity. It was suggested additionally that the longwave flux displayed characteristics that were the result of local modification of the boundary-layer meteorology by the proximate glacier surface: emissivities greater than unity were believed to be the result of

radiation emitted from above a near-surface temperature inversion (e.g. de Ruyter de Wildt et al., 2003; Björnsson et al., 2005).

The meteorology recorded at Storglaciären showed appreciable differences. The mean air temperature recorded at Storglaciären (1387m) was almost 3°C warmer than the higher elevation station on Vestari Hagafellsjökull; humidity was also greater at the valley glacier, whilst incident radiative fluxes and wind speed were subdued relative to the ice cap. Some of these observed differences may be attributed to the different climatologies of the regions in which these ice masses are located; potential air temperature elucidates this point well (Table 8.1).

Table 8.1. Mean potential air temperatures (θ) at off- and on-glacier locations during July and August. Locations of weather stations are abbreviated in brackets; these abbreviations are used in Equation 8.1.

	VH 500 m (VH)	**VH 1100 m (VH)**	**Storglaciären (1387 m) (Sg)**	**Hveravellir (641 m) (Hv)**	**TAWS (1135 m) (TS)**
θ (°C)	10.2	12.8	18.7	14.6	19.1

Utilising the off-glacier observations discussed from TAWS and Hveravellir (see Chapter 3, Section 3.7), facilitates separation of regional climatological influence (the 'regional effect') from boundary-layer modification (the 'glacier effect') by the respective ice masses. That is, if it assumed that the difference between potential temperatures from Hveravellir and TAWS constitutes the regional effect, then the glacier effect may be estimated from:

$$1 - \frac{TS - Hv}{Sg - VH_e}, \tag{8.1}$$

in which the mean potential temperatures at each station are abbreviated according to Table 8.1 and the subscript e denotes 500 m or 1100 m, as appropriate. Table 8.1 and Equation 8.1 therefore illustrate that, although the regional climate is cooler at Vestari Hagafellsjökull, 22% and 46% of the difference in air temperatures between Storglaciären and the AWSs at 1100 m and 500 m, respectively are attributable to the 'glacier effect'. The greater cooling at the lower elevation station on Vestari Hagafellsjökull is consistent with previous studies that have addressed spatial variability of glacier air temperatures, and emphasised the importance of flow-path length (Greuell et al., 1997; Shea and Moore, 2010). Enhanced cooling of the

overlying air is also likely to contribute to the greater wind speeds recorded on the ice cap, due to katabatic forcing.

In summarising the major findings from the meteorological observations at Vestari Hagafellsjökull and Storglaciären, it is important to stress this greater modification of the local climate by the larger ice cap. This was noted further when addressing Objective 4 in Chapter 7 (discussed in detail below), as agreement between reanalysis meteorology and glacier-based observations was lower at Vestari Hagafellsjökull—appreciably so at the 500 m station, in particular. Such information is relevant for research which seeks to interpolate or downscale climate data to the glacier scale. For example, studies which have projected global estimates of glacier wastage have downscaled air temperatures to the world's glaciers by applying standard atmospheric lapse rates (Raper and Braithwaite, 2006), through applying offsets (Radić and Hock, 2011), or by correcting gridded climatologies based on regression of gridded temperatures against elevation (Marzeion et al., 2012). None of these has considered glacier size as being an important factor affecting local climatology. Whilst the analyses in this thesis only compared two ice masses (which varied more than in terms of size alone), it is suggested that information regarding a size-dependency of the extent to which glaciers modify their climate, could possibly be integrated usefully into downscaling or interpolation routines to distribute meteorological fields more accurately in glacierized terrain (e.g. Jarosch et al., 2012). The glacier cooling effect observed at Vestari Hagafellsjökull is discussed in detail with regards to the second objective (Section 8.2.2).

Energy balance calculations were also performed to satisfy the first objective; and, using parameter values which had been obtained during previous investigations (Hock and Holmgren, 1996; Guðmundsson et al., 2009), surface ablation was modelled with good accuracy. At Storglaciären, the SEB was simulated using a combination of data recorded on- and off-glacier. Data recorded at TAWS was adjusted empirically to reproduce the glacier climate as closely as possible. Although the purpose of this exercise was mainly preparatory in the context of this thesis, the encouraging performance of the SEB model driven by off-glacier data (Chapter 3, Section 3.6.2) warrants mention in this summary. Prolonged in-situ meteorological monitoring in the glacier boundary layer is logistically challenging, and consequently, most SEB investigations have been of limited duration. This is problematic because significant

temporal variability of the SEB can occur, rendering brief studies possibly un-representative of glaciers' typical surface energetics (Hock, 2005; Andreassen et al., 2008). Weather stations located off-glacier are easier to maintain, and can therefore offer a solution, facilitating prolonged studies of glacier mass and energy exchange. However, direct substitution of such data in place of glacier-based observations is unsuitable, due to the modifying effect of the melting glacier surface, and small-scale meteorological variability caused by topographic influences (Munro, 2004). Thus, the results from Chapter 3, which showed that ablation (and the individual energy fluxes) could be simulated accurately using off-glacier meteorological data adjusted to the glacier boundary layer using simple empirical schemes, are particularly encouraging. Extending observations of glacier climate with the use of such techniques is highly desirable to monitor low-frequency changes in glacier meteorology, energy fluxes and ablation that may manifest as a result of a changing climate.

8.2.2. Objective 2: Synoptic controls on glacier lapse rates

The second objective was concerned with exploration of how synoptic-scale climatological variability affected near-surface air temperature, and was investigated by examining daily lapse-rate variability at Vestari Hagafellsjökull. This objective was motivated by the fact that air temperature is an essential driving variable in physical and empirical ablation models alike, and its spatial distribution over melting glaciers is complicated by shallow and temporally variable vertical gradients (e.g. Bøggild et al., 1994; Greuell et al., 1997; Hanna et al., 2005; Gardner et al., 2009; Hodgkins et al., 2012a, b). Furthermore, previous attempts to parameterize the lapse rate over melting glaciers have achieved mixed results. For example, Konya et al. (2007) found that lapse-rate variability was not simply associated with any meteorological variables recorded on Storglaciären; whereas, Gardner et al. (2009) achieved more success in the Canadian high Arctic, finding that free-atmosphere air temperatures were closely associated with lapse rates observed during the summer months. This relationship was demonstrated further by Hodgkins et al. (2012a, b) at Vestari Hagafellsjökull. Marshall et al. (2007) and Braun and Hock (2004) also found coherent relationships between lapse rates and synoptic circulation, in the Canadian high Arctic and Antarctic Peninsula, respectively.

The analyses in Chapter 5 contributed to this body of work by exploring and modelling daily lapse-rate variability using weather types and reanalysis climate data. The observations in this thesis emphasised the glacier's cooling effect at the 500 m station on Vestari Hagafellsjökull further (cf. Section 8.2.1), which resulted in mean lapse rates that were significantly shallower than the ELR. This was attributed to cumulative downslope sensible heat losses largely cancelling warming produced by adiabatic compression. Weather categories were then found to provide a useful framework for examining lapse-rate variability.

The steepest lapse rates were observed in weather categories characterised by strong gradient winds; this control was also identified through regression analysis, as the 10m reanalysis wind speed was found to correlate most strongly with the lapse rate. Reanalysis air temperature was of secondary importance. Using this information to forecast the lapse rate produced correlation coefficients approaching 0.6 between the simulated and observed series for the best performing models (Chapter 5, Section 5.4.4). This level of predictive skill was sufficient to reduce errors significantly in positive degree days calculated by extrapolating air temperatures up/down glacier, relative to application of the ELR. The synoptic lapse-rate models developed in this thesis also out-performed the regression model developed by Gardner et al. (2009). It was noted, however, that interannual lapse-rate variability was pronounced, and was not captured satisfactorily by any of the approaches investigated. A reason suggested for this relative failure was variability of the glacier surface characteristics, which could affect heat exchange with the boundary layer somewhat independently of the prevailing weather. Approximating part of this uncertainty by quantifying the effect of variable surface roughness with a physically-based lapse rate model after Greuell and Böhm (1998), suggested that variability of this parameter was unlikely to account fully for the low-frequency lapse-rate changes observed. Nevertheless, the physical simulation did reveal non-negligible effects of variable surface roughness. Hence, it is considered that lapse rate models may benefit from integrating such information into empirical schemes.

Although the spatial transferability of the regression or analogue models remains to be determined, it should be acknowledged that they were consistent in highlighting the importance of the synoptic wind field for modulating lapse-rate variability, and in this regard, there is coherence with research elsewhere. For example, Petersen and

Pellicciotti (2011) found that strengthening of the valley wind at Juncal Norte Glacier, Chile, also resulted in steeper lapse rates. Chapter 5 explained this, by demonstrating that stronger synoptic winds were capable of disrupting katabatic drainage; and, without downslope airflow, it was argued that sensible heat losses would no longer accumulate down-glacier. Additional studies from contrasting glacierized and climate regions are required to test the wider utility of the synoptic wind speed as an indicator of lapse rates. It is emphasised that such research is much required because, until the association between synoptic climate and the lapse rate is comprehended more fully, the possible effect of climate change upon this parameter will remain poorly understood.

8.2.3. Objective 3: Exploration of the temperature-index model

The third objective addressed the role of air temperature as an indicator of ablation. This work was undertaken because temperature-index methods are among the most common means of translating the effect of synoptic climate variability to the glacier-scale, and have been used widely to simulate the glaciological consequences of climate change (e.g. Braithwaite and Zhang, 1999). However, their performance is dependent on suitable parameterization of the DDF (the scalar which relates positive air temperatures to the rate of ablation) and observations have suggested that its value is spatially and temporally variable (Hock, 2003). Chapter 6 therefore explored variability of the DDF as a function of location, and of the prevailing weather conditions.

The analyses in this thesis found that the relationship between temperature and ablation varied considerably between locations. A particularly interesting observation was the dependency of the DDF on air temperature: cold conditions amplified the temperature-independent component (the intercept) of the temperature-ablation regression relationship, which explained the increasing DDFs found at higher elevation on the ice cap. These results were in agreement with previous observations that identified a general decline of DDFs with altitude (e.g. Hock, 2003), and with studies that have noted the 'low-temperature effect' (Braithwaite, 1995; Zhang et al., 2006; Van den Broeke, 2010). It was emphasised that consideration of such behaviour is highly important for temperature-index studies, as neglecting this effect would result in overestimating the sensitivity of ablation to air temperature. This finding

must be considered as especially pertinent for studies which address the glaciological consequences of climate warming.

In an attempt to explain air temperature's role as an index of ablation, the analyses in Chapter 6 also addressed the relationship between positive air temperatures and components of the SEB. The results illustrated appreciable differences in the individual energy fluxes' association with air temperature between locations. By recognising this spatial heterogeneity, these results agreed closely with Sicart et al. (2008), and stress the need to re-calibrate temperature-index for specific locations. Considering this spatial variability further, it is suggested that much can be gained from additional *observations* and *explanations* of temperature's association with the SEB in different climatic and glaciological environments. Such information is highly relevant for developing coherent strategies to distribute DDFs through space, which is a requisite for more robust temperature-index simulations of global extent (e.g. Raper and Braithwaite, 2006; Radić and Hock, 2011; Marzeion et al., 2012).

The temporal dimension to the analyses in Chapter 6 considered the effect of weather categories on the temperature-ablation relationship. This aspect of the research is considered to be an especially important contribution of the thesis because, although weather type has been acknowledged as an important control on the DDF (e.g. Lang and Braun, 1990; Hock, 2003), very few researchers have addressed this issue specifically. It was found that the correlation between air temperature and ablation varied as a function of weather category. Moreover, at all locations, weather categories in which air temperature explained less variance of ablation, were also found to be characterised by ablation amounts that were relatively insensitive to air temperature variability; this was illustrated quantitatively by the negative association between intercept and slope regression parameters. The sensitivity of ablation to positive air temperatures was assessed in detail by examining pairs of weather categories characterised by slope parameters which exhibited statistically significant differences. From these comparisons, the role of the net shortwave radiative flux emerged as being important, and this was particularly evident at Vestari Hagafellsjökull: during conditions typified by anticyclonic curvature and the advection of north-westerly air, it was observed that incident shortwave radiation correlated significantly with positive air temperatures—an association which was inconsistent with the general relation observed at this location (irrespective of weather

type). It was emphasised, therefore, that when this correlation endures, air temperature acts as a proxy for net shortwave radiation. The physical explanation suggested for this process was that the amplified insolation during anticyclonic conditions acted to warm the glacier environs and advect heat onto the glacier. Importantly, it was argued that this process remains hidden if weather types are not considered, as the climatology of Vestari Hagafellsjökull associates warmer air temperatures with the advection of moist southerly air masses, in which cloud cover is high.

These findings are considered as being highly relevant for temperature-index modelling. The dependency on prevailing weather category of both the amount of variation in ablation explained by air temperature, and the sensitivity of ablation to this parameter, demands that consideration of synoptic type be made when calibrating or applying temperature-index based methods. It is emphasised that because the association between air temperature and components of the SEB varies appreciably with weather type, the same caution that is afforded the spatial transferability of degree-day factors (Sicart et al., 2008), should be applied to their portability through time. This is especially true in the context of a changing climate: from the analyses undertaken, it is evident that persistent changes in the frequency or duration of weather types that may occur as the climate warms, would be likely to affect the skill and accuracy of temperature-index models calibrated without regard to the context of the weather types their parameters are calibrated for. In consideration of these results, it was suggested that utilising the weather-category memberships assigned in Chapter 4 to determine the temperature-ablation relationship would yield a more robust framework for assessing the effect of warmer air temperatures on ablation. This concept was explored in Chapter 7 with regards to Objective 4.

8.2.4. Objective 4: Examination of synoptically-based ablation models

The fourth objective sought to investigate the merits of forecasting ablation using spatially-coarse climate data. This was pursued because there is a need to appraise the utility of different approaches' ability to reconcile the scale mismatch between the typical resolution of gridded climate products, and that which is required to resolve processes of mass and energy exchange at the glacier surface. One physically-based SEB model was investigated, and three empirically-based techniques were explored; all were forced with reanalysis data. Conceptually, a physical simulation of the

ablation rate was regarded as the most attractive, due to absence of assumptions regarding the stationarity of empirical relationships between climate indices and ablation, and the minimal requirements for calibration. However, it was also considered that such an approach is heavily reliant on the glacier meteorology being represented well by the spatially-coarse data, and comparisons with in-situ observations indicated the presence of appreciable bias in the reanalysis meteorology. Temporal coherence was also observed to vary between locations and the meteorological variable being assessed. The lowest agreement with the reanalysis data was generally observed at the 500 m station on Vestari Hagafellsjökull. It was argued that this possibly resulted from the development of a distinct microclimate at this elevation on the ice cap, produced by thermodynamic forcing effected by sensible and latent heat exchange with the glacier's melting surface, which was independent of the large-scale flow. Such modification of the lower troposphere by glaciers has been noted previously from observations and regional climate modelling (Shea and Moore, 2010; Kotlarski et al., 2010).

The reanalyses variables for all locations were corrected through a quantile-mapping procedure. This technique proved sufficient to simulate ablation with reasonably good accuracy: with the exception of Storglaciären, it outperformed all empirical models investigated. However, it was emphasised that the derivation of empirical correction functions to adjust the reanalysis meteorology appropriately, demands extensive in-situ observations of the glacier climate; and, such requirements, it was suggested, are challenging to satisfy for most applications. In this regard, it is apparent that the development of parsimonious and spatially-transferable techniques to adjust spatially-coarse climate data to the glacier boundary layer would be to the practical benefit of simulating glacier-surface ablation with such gridded data products. For example, the work of Shea (2010) and Shea and Moore (2010), which has sought to integrate morphometric indices into the estimation of glacier boundary-layer meteorology from free-atmosphere observations holds promise. Yet, until such techniques are refined, it is suggested that simulating ablation physically using spatially-coarse data (e.g. reanalysis or GCM output), which does not account for the distinct glacier microclimate explicitly, will remain challenging.

The empirical techniques applied in Chapter 7 had less-stringent data demands, and were not dependent directly on the spatially-coarse reanalysis data capturing variability of the glacier-surface meteorology accurately; instead, their skill relied on establishing robust relationships between ablation and reanalysis parameters. The synoptic-analogue method of forecasting ablation (WCA) is considered to be an important contribution of the thesis, as very few researchers have employed such techniques to quantitatively forecast ablation; and, despite the simplicity of this method, it performed favourably at interannual resolution. The weather-type methodology also facilitated exploration of SEB components and ablation in the context of wider-scale circulation. The utility and importance of such insights are highlighted further in Section 8.3.

The most useful empirical methods for evaluating daily variability of ablation were provided by temperature-index approaches; the best performance was achieved when the results from Chapter 6 were developed, and the relationship between ablation and air temperature was varied as function of synoptic weather type (WCCTIn). This is an important finding of the research because it demonstrates that the often-used temperature-index model can be improved without the need for additional data recorded in-situ. Whilst it was noted that variability of the glacier albedo may limit the improvements provided by WCCTIn, it was suggested that the merits of this technique should be explored further. The need to consider weather type when applying temperature-index models to future climate scenarios was also stressed as being important. This is emphasised again here: climate change may manifest as variability of weather categories, imposed upon on a background warming signal (Kalkstein et al., 1990; Fettweis et al., 2013), and it is probable that the rate of warming between weather types will be variable. For example, those types characterised by arctic air masses are likely to warm faster than those associated with air masses originating from lower latitudes (cf. Serreze et al., 2009). Hence, failure to acknowledge differing sensitivities of ablation to changes in air temperatures could result in systematic forecasting errors which are concentrated in weather categories warming fastest.

Addressing Objective 4 therefore highlighted the utility of the temperature-index model to determine ablation empirically, and further emphasised the need to develop a thorough comprehension of the temperature-ablation relationship further, so that the limitations of this technique can be appreciated more fully, and reduced, where possible. The research in this thesis, has enhanced understanding in this regard, but given the ubiquity of temperature-index methods for forecasting ablation, it is argued that much could be gained from continued research into variability of the temperature-ablation relationship. This, along with suggested directions of future research is discussed in Section 8.3.

8.3. Future Research

The research in this thesis has helped reconcile the mismatch of scale between spatially-coarse climate data, and those which are required for understanding and simulating energetics and ablation within the glacier boundary layer. Through pursuit of this aim and the objectives identified, considerable scope for further research has been recognised.

The adoption of weather categories in the methodology proved to be a particularly useful approach for exploring glacier surface meteorology and energy exchange. In the research presented, the analyses were limited to point locations—both in terms of the classification (reanalysis data from a solitary grid cell)—and the information of glacier-surface processes (glacier AWS positions). It is considered that an interesting development of the research would be the up-scaling of the methodological principles to regional investigations. For example, the weather-typing procedure used in this thesis—developed to classify individual weather station output (Kalkstein and Corrigan, 1986)—has been adapted to catalogue weather types at the continental-scale (Kalkstein et al., 1996; Sheridan, 2002), and recent developments have seen this approach applied to western Europe (Bower et al., 2007). The latter contribution also identified climate regions through (semi-) objective grouping procedures (e.g. northern Scandinavia, central Europe). It is suggested that future research could benefit from addressing the response of glacier meteorology to synoptic forcing at much larger scales, and in a regionally-differentiated framework. This is perhaps communicated most readily with regards to the lapse-rate research: Chapter 5 identified the importance of weather types in determining this parameter at Vestari

Hagafellsjökull, and it is argued that this research could be developed greatly by assessing the extent to which lapse-rate response to weather types is consistent between proximate glaciers. It would be interesting, for example, to determine whether regionally-coherent responses to specific weather types could be identified. Such information could then be useful for developing typologies of glacier lapse-rate response to synoptic forcing as a function of climatological and glaciological setting. It is believed that this could be a very useful approach to structuring glacier lapse rate research.

Future research on DDF variability could benefit similarly from up-scaling in time as well as space. Spatially, coherence of the temperature-ablation relationship was observed at different locations on Vestari Hagafellsjökull, and analogously to the lapse rate example, it would be useful to explore whether this spatial correlation endured at larger scales. If it did, combining this information with regional- or continental-scale weather classifications (e.g. Bower et al., 2007) could facilitate suitable adjustment of DDFs over entire glacierized regions of the world, either for hindcasting applications, near real-time forecasting, or for simulations of future ablation if applied to GCM output.

Temporally, future research into the association between synoptic weather categories and DDFs could benefit from examination of decadal-scale trends. For example, Huss et al. (2009) examined a 94-year record of seasonal melt in the European Alps to explore low-frequency variability of the temperature-ablation relationship, and noted a gradual decline of degree-day factors, whereas Van den Broeke et al. (2010) observed an upward trend in western Greenland. Extending the methodology applied in this research to examine change of this parameter over prolonged timescales could be highly useful for examining such variability. It is observed, for example, that the period of high DDFs reported by Huss et al. (2009) (1940's), caused by enhanced solar radiation (which the authors attributed to 'solar brightening'), also coincided with an era of enhanced anticyclonic activity in the European Alps noted by Hoinkes (1968), which may provide a synoptic explanation. Changes of synoptic weather types might contribute similarly to the non-stationarity of the DDF reported by Van den Broeke et al. (2010), as recent years have seen almost unprecedented changes in atmospheric circulation over Greenland, manifesting as unusually high mid-

tropospheric pressure prevailing over the ice sheet (Fettweis et al., 2011; Hanna et al., 2012).

It should be noted that greater exploration of low-frequency DDF variability has been assisted by the recent work of Shea et al. (2009), who demonstrated a simple technique to extract snow and ice DDFs from specific mass balance measurements. As the number of years and glaciers for which mass balance measurements are available increases, there will consequently be greater scope for research into the coupling of synoptic climate variability and changes in the relationship between temperature and ablation. Such long-term investigations might also benefit from application of circulation-based synoptic classifications using air pressure fields (e.g. Fettweis et al., 2011), rather than the weather-typing procedure applied in this thesis, due to the long observational record of this parameter.

In this context, the suitability of different classification schemes for studies of glacier meteorology and the SEB could also be addressed in further research. The weather-category approach adopted in this thesis provided clear benefits and demonstrated proof of concept in the capacity it was employed; however, it was also evident that improvements could be realised in the lapse rate and ablation models if the grouping procedure was modified (Chapter 5, Section 5.4.4 and Chapter 7, Section 7.5.2, respectively). Considering the appreciable variety of algorithms, variables, and the number of groups identified in climate classifications (a comprehensive review can be found in Huth et al., 2008), it would be useful to explore the suitability of different techniques to the aspects of glacier-climate research investigated in this thesis.

Building on the examination of wider-scale circulation investigated briefly with the WCA model in Chapter 7, continued investigation of how different glacierized regions of the world respond to large-scale changes in atmospheric circulation, may also be a useful direction for future research. The North Atlantic Oscillation (NAO) and Greenland Blocking Index, for example, have been associated with the anomalous warming and melt observed on the Greenland Ice Sheet. It has also been suggested that the same atmospheric conditions have driven high melt rates in the Canadian Arctic Archipelago (Fisher et al., 2012; Hanna et al., 2012; Fettweis et al., 2013), but unremarkable melt rates in Svalbard (Moholdt et al., 2010). The explanation for this association is the difference in the direction of meridional airflow either side of the

Greenland Ice Sheet when Greenland anticyclones prevail (Fettweis et al., 2013). In this context, it is interesting to observe the statistically significant negative correlation (at p = 0.05) which exists between ablation on Vestari Hagafellsjökull and Storglaciären (Figure 8.1). This relationship is perhaps related to the dipole in air temperature response between Iceland and northwestern Europe discussed by Hanna et al. (2004) (and see Figure 8.1 caption), which has been associated similarly with the NAO. In light of the anomalous Greenland melt rates observed in the last years, and the possible role of the NAO in modulating ablation rates across the North Atlantic, it would therefore be interesting to investigate how Scandinavian glaciers are responding to the recent negative phase of the NAO, and to explore the extent to which coherent teleconnections exist between ablation rates either side of the North Atlantic.

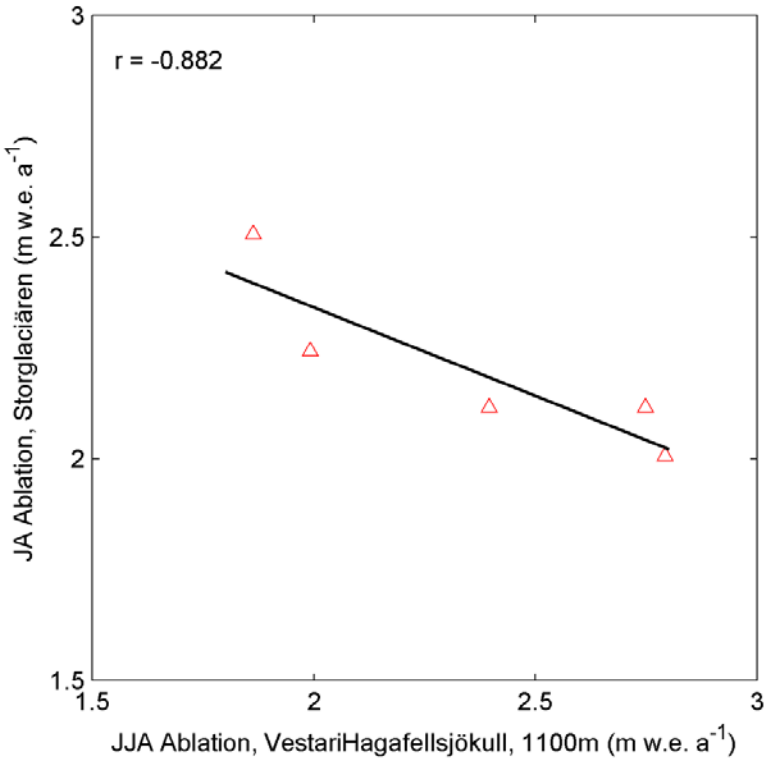

Figure 8.1. The relationship between ablation at Vestari Hagafellsjökull and Storglaciären. The 1100 m record is plotted rather than ablation observed at 500 m, because the latter only extends to 2007; annual ablation between elevations is generally well correlated, anyway (r = 0.75). Note the correlation shown is for years 2005 to 2009—2010 is omitted from Vestari Hagafellsjökull due to the anomalous ash cover on the glacier during this year. The correlation between annual air temperatures at 1100 m and Storglaciären is -0.77 for the corresponding years (p = 0.13); if 2010 is included, the correlation is -0.62 (p = 0.19).

Exploring synoptic aspects of glacier accumulation is also an area identified for further research. Precipitation in mountainous environments is determined by complex interactions between the large-scale flow and the underlying topography (Jiang, 2003; Mölg et al., 2009), and this challenges the accurate forecasting or precipitation in space and time (Rotunno and Houze, 2007). The holistic attributes of synoptic techniques make for a useful framework to reduce these complexities and integrate the net effect of large-scale climatic variability on precipitation, and hence processes that determine glacier accumulation. Indeed, synoptic approaches have been used successfully in this capacity before (e.g. Yarnal, 1984a; Stahl et al., 2006; Fealy and Sweeny, 2007; Schuenemann et al., 2009). Incorporating such techniques into mass-balance models driven by spatially-coarse climate data may therefore be a useful direction for future study.

Finally, it is suggested that the synoptic analogue approaches explored in the thesis to parameterize lapse rates and calibrate the temperature-index relationship are a simple, but powerful technique for investigating the effect of synoptic-scale climate variability on the glacier boundary layer. Because of these attributes, it is anticipated that such methods are well placed for a variety of downscaling-type applications. For example, in Chapter 7, the bias-corrected reanalysis metrological variables required to evaluate the SEB were correlated with glacier-based observations, and agreement was found to be limited. This was particularly evident at the ice cap, where it was argued that the glacier modified the local climate significantly. Consequently, until reanalysis products and GCMs consider glaciers and ice-caps explicitly in the physical simulation of near-surface meteorology, there will be considerable demand for techniques which can adjust such spatially-coarse data to the glacier boundary layer. The use of the analogue method in this regard is illustrated in Figure 8.2, in which it is evident that, despite its simplicity, this approach reproduces much of the observed meteorological variability. Further research may therefore build on this analogue technique for such downscaling purposes, as very few studies have applied such methods in a glaciological capacity.

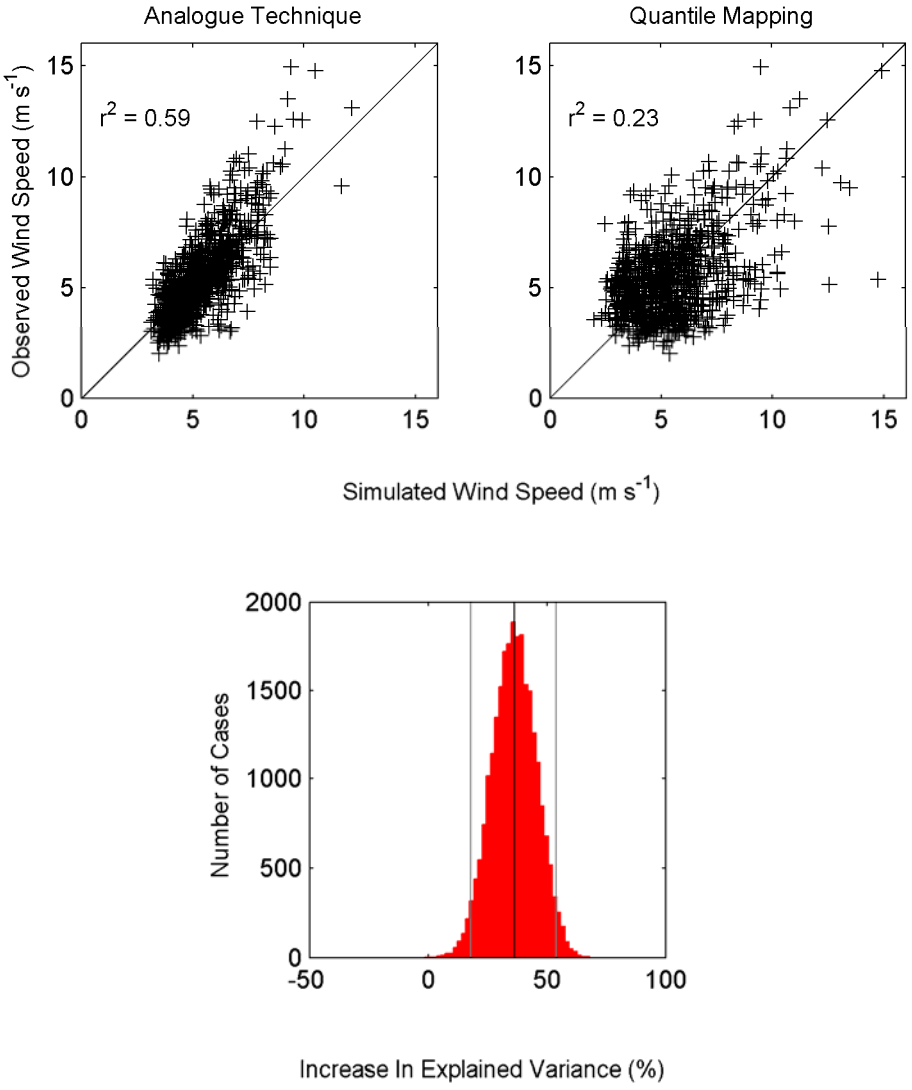

Figure 8.2. Example of the analogue downscaling technique applied to wind speed at 500 m on Vestari Hagafellsjökull. The analogue model is implemented in cross-validation scheme similar to the 'optimized analogue' lapse-rate model described in Chapter 5, Section 5.4.4. In this example, the wind speed is simulated as the mean observed at the 500 m AWS during the 5 most synoptically similar days to have occurred (excluding the year being simulated). Similarity is adjudged analogously to the technique described in Chapter 5, Section 5.4.4. The histogram shows the results of a bootstrapped simulation: the amount of variance explained in the observed meteorology by the quantile-mapped reanalysis data, and that simulated by the analogue model is calculated for 25000 random samples (with replacement) of 92 days in length (the span of JJA). The difference in r^2, expressed as a percentage, is calculated for each bootstrap sample ($r^2_{analogue}$ - r^2_{quant}) and plotted. The grey bars mark the two-tailed 95% confidence limits, and the black line gives the median.

8.4. Concluding Remarks

Mountain glaciers and ice caps are of the utmost hydrological importance, and quantifying their response to a changing climate is critical. However, the processes that drive glacier mass and energy transfer occur at a scale which challenges direct observation and prevents their explicit consideration in large-scale physical simulations. Methods that can extract information about these processes from spatially-coarse data are therefore required to develop a multi-scale understanding of glacier-climate interactions. Through applying techniques familiar to the field of synoptic climatology, the thesis made a contribution in this regard, and it has been demonstrated that meteorological data at the grid-scale may be integrated usefully into studies which address the glacier boundary-layer. It is therefore concluded that the methods explored in this research—and in particular, the use of weather categories—provide an appropriate framework for synthesising the cascade of complex physical processes which propagate the effects of coarse-scale meteorological variability to the glacier-scale. Exploring and refining these techniques further offers many opportunities for further research.

References Cited

ABATZOGLOU, J.T., and BROWN, T. J., 2012. A comparison of statistical downscaling methods suited for wildfire applications. *International Journal of Climatology*, **32**(5), pp. 772-780.

ACIA, 2005. Arctic Climate Impact Assessment, Cambridge University Press, 1042p.

ALDENDERFER, M.S. and BLASHFIELD, R.K., 1984. *Cluster Analysis.* 1st edn. USA: Sage Publications.

ALT, B.T., 1978. Synoptic climate controls of mass-balance variations on Devon Island ice cap. *Arctic and Alpine Research,* **10**(1), pp. 61-80.

AMBACH, W., 1998a. Heat balance characteristics and ice ablation, western EGIG-profile, Greenland, *Seventh Northern Research Basins Symposium/Workshop: Applied Hydrology in the Development of Northern Basins, Copenhagen Danish Society for Arctic Technology, Ililissat, Greenland.*, 25th May - 1st June 1998a, pp. 59-70.

AMBACH, W., 1988b. Interpretation of the positive-degree-days factor by heat balance characteristics - West Greenland. *Nordic Hydrology,* **19**(4), pp. 217-224.

AMBACH, W., 1963. Untersuchungen zum Encrgieumsatz in der Ablations zone des gronlandischen Inlandeises. (CAMP IV-EGIG.69°40'05" N, 49° 37'58" W). *Meddeleser om Grønland,* **174**(4).

AMBACH, W. and KIRCHLECHNER, P., 1986. Nomographs for the determination of meltwater from snow - and ice surfaces. *Wetter und Leben,* **38**(4), pp. 181-189.

ANDREAS, E.L., 1987. A theory for the scalar roughness and the scalar transfer coefficients over snow and sea ice. *Boundary-Layer Meteorology,* **38**(1), pp. 159-184.

ANDREASSEN, L.M., VAN DEN BROEKE, M.R, GIESEN, R.H. and OERLEMANS, J., 2008. A 5 year record of surface energy and mass balance from the ablation zone of Storbreen, Norway. *Journal of Glaciology,* **54**(185), pp. 245-258.

ARENDT, A. and SHARP, M.J., Energy balance measurements on a Canadian high arctic glacier and their implications for mass balance modeling. *IAHS Publication,* **256**, pp. 165-172.

ARNOLD, N.S., REES, W.G., HODSON, A.J. and KOHLER, J., 2006. Topographic controls on the surface energy balance of a high Arctic valley glacier. *Journal of Geophysical Research: Earth Surface,* **111**(F2).

ARNOLD, N.S. and REES, G.W., 2003. Self-similarity in glacier surface characteristics *Journal of Glaciology,* **49**(167), pp. 547-554.

ARNOLD, N., WILLIS, I., SHARP, M., RICHARDS, K. and LAWSON, W., 1996. A distributed surface energy-balance model for a small valley glacier. I. Development and testing for Haut Glacier d'Arolla, Valais, Switzerland. *Journal of Glaciology,* **42**(140), pp. 77-89.

ASHFAQ, M., BOWLING, L.C., CHERKAUER, K., PAL, J.S. and DIFFENBAUGH, N.S., 2010. Influence of climate model biases and daily-scale temperature and precipitation events on hydrological impacts assessment: A case study of the United States. *Journal of Geophysical Research: Atmospheres,* **115**(D14).

ASMEROM, Y., POLYAK, V.J. and BURNS, S.J., 2010. Variable winter moisture in the southwestern United States linked to rapid glacial climate shifts. *Nature Geoscience,* **3**(2), pp. 114-117.

BÁRDOSSY, A. and CASPARY, H., 1990. Detection of climate change in Europe by analyzing European atmospheric circulation patterns from 1881 to 1989. *Theoretical and Applied Climatology,* **42**(3), pp. 155-167.

BARRY, R.G., 2008. *Mountain Weather and Climate.* Third edn. Cambridge: Cambridge University Press.

BARRY, R.G. and CHORLEY, R.J., 2009. *Atmosphere, weather and climate.* Ninth edn. London: Routledge.

BARRY, R.G. and PERRY, A.H., 1973. *Synoptic climatology: Methods and applications.* First ed. London: Methuen and Co Ltd.

BAUR, F., HESS, P. and NAGEL, H., 1944. *Kalendar der Grosswetterlagen Europas 1881-1939.* Bad Hombourg, Germany.

BAXTER, M.J., 1994. *Exploratory Multivariate Analysis in Archaeology.* First edn. Edinburgh: Edinburgh University Press.

BEJARÁN, R.A. and CAMILLONI, I.A., 2003. Objective method for classifying air masses: an application to the analysis of the Buenos Aires' (Argentina) urban heat island intensity. *Theoretical Applied Climatology,* **74**(1-2), pp. 93-103.

BELJAARS, A.C.M. and HOLTSLAG, A.A.M., 1991. Flux parameterization over land surfaces for atmospheric models. *Journal of Applied Meteorology,* **30**(3), pp. 327-341.

BENN, D.I., WARREN, C.R. and MOTTRAM, R.H., 2007. Calving processes and the dynamics of calving glaciers. *Earth-Science Reviews,* **82**(3), pp. 143-179.

BERGER, A., 1978. Long-Term Variations of Daily Insolation and Quaternary Climatic Changes. *Journal of the Atmospheric Sciences,* **35**(12), pp. 2362-2367.

BINTANJA, R., and VAN DEN BROEKE, M. R., 1995. The surface energy balance of Antarctic snow and blue ice. *Journal of Applied Meteorology*, **34**(4), pp. 902-926.

BJÖRNSSON, H, 2006. Iceland. In: JANIA, J. and HAGEN, J.O. *Mass balance of Arctic Glaciers, IASC Report No. 5.* UNIVERSITY OF SILESIA, pp. 21-24.

BJÖRNSSON, H., and PÁLSSON, F., 2008. Icelandic glaciers. *Jökull*, **58**, pp. 365-386.

BJÖRNSSON, H., GUÐMUNDSSON, S. and PÁLSSON, F., 2005. Glacier winds on Vatnajökull ice cap, Iceland, and their relation to temperatures of its lowland environs. *Annals of Glaciology,* **42**, pp. 291-296.

BJORNSSON, H., PÁLSSON, F., SIGURETHSSON, O., and FLOWERS, G. E., 2003. Surges of glaciers in Iceland. *Annals of glaciology*, **36**, pp. 82-90.

BLANDFORD, T.R., HUMES, K.S., HARSHBURGER, B.J., MOORE, B.C., WALDEN, V.P. and YE, H., 2008. Seasonal and Synoptic Variations in Near-Surface Air Temperature Lapse Rates in a Mountainous Basin. *Journal of Applied Meteorology and Climatology,* **47**(1), pp. 249-261.

BØGGILD, C.E., REEH, N. and OERTER, H., 1994. Modelling ablation and mass-balance sensitivity to climate change of Storstrømmen, northeast Greenland. *Global and Planetary Change,* **9**(1), pp. 79-90.

BOLZ, H.M., 1949. Die Abhängigkeit der infraroten Gegenstrahlung von der Bewölkung. *Zeitschrift für Meteorologie,* **3**, pp. 201-203.

BOWER, D., MCGREGOR, G.R., HANNAH, D.M. and SHERIDAN, S.C., 2007. Development of a spatial synoptic classification scheme for Western Europe. *International Journal of Climatology,* **27**(15), pp. 2017-2040.

BRAITHWAITE, R.J., 2011. Why do we expect glacier melting to increase under global warming? In: J. BLANCO and H. KHERADMAND, eds, *Climate Change—Geophysical Foundations and Ecological Effects.* Intech, pp. 479-502.

BRAITHWAITE, R.J., 2008. Temperature and precipitation climate at the equilibrium-line altitude of glaciers expressed by the degree-day factor for melting snow. *Journal of Glaciology,* **54**(186), pp. 437-444.

BRAITHWAITE, R.J., 1995a. Aerodynamic stability and turbulent sensible-heat flux over a melting ice surface, the Greenland ice sheet. *Journal of Glaciology,* **41**(139), pp. 562-571.

BRAITHWAITE, R.J., 1995b. Positive degree-day factors for ablation on the Greenland ice sheet studied by energy balance modelling. *Journal of Glaciology,* **41**(137), pp. 153-160.

BRAITHWAITE, R.J., 1981. On glacier energy balance, ablation and air temperature. *Journal of Glaciology,* **27**(97), pp. 381-391.

BRAITHWAITE, R.J. and ZHANG, Y., 2000. Sensitivity of mass balance of five Swiss glaciers to temperature changes assessed by tuning a degree-day model. *Journal of Glaciology,* **46**(152), pp. 7-14.

BRAITHWAITE, R.J. and ZHANG, Y., 1999. Modelling Changes in Glacier Mass Balance that may Occur as a Result of Climate Changes. *Geografiska Annaler A,* **81**(4), pp. 489-496.

BRAITHWAITE, R.J., KONZELMANN, T., MARTY, C. and OLESEN, O.B.,1998a. Reconnaissance study of glacier energy balance in North Greenland, 1993 - 4. *Journal of Glaciology,* **44**(147), pp. 239-247.

BRAITHWAITE, R.J., KONZELMANN, T., MARTY, C. and OLESEN, O.B., 1998b. Errors in daily ablation measurements in northern Greenland, 1993-94, and their implications for glacier-climate studies. *Journal of Glaciology,* **44**(148), pp. 583-588.

BRAITHWAITE, R. J. and OLESEN, O. B., 1990. Response of the energy balance on the margin of the Greenland ice sheet to temperature changes. *Journal of glaciology*, **36**(123), pp. 217-221.

BRAUN, M. and HOCK, R., 2004. Spatially distributed surface energy balance and ablation modelling on the ice cap of King George Island (Antarctica). *Global and Planetary Change,* **42**(1), pp. 45-58.

BRAUN, M., SAURER, H., VOGT, S., SIMÕES, J.C. and GOBMANN, H., 2001. The influence of large-scale atmospheric circulation on the surface energy balance on the King George Island Ice Cap. *International Journal of Climatology,* **21**(1), pp. 21-36.

BRAZEL, A.J., CHAMBERS, F.B. and KALKSTEIN, L.S., 1992. Summer energy balance on West Gulkana Glacier, Alaska, and linkages to a temporal synoptic index. *Zeitschrift für Geomorphologie,* **86**, pp. 15-34.

BRIGGS, G.A., 1979: Analytical modeling of drainage flows, *draft document, Atmospheric Turbulence and Diffusion Laboratory*, NOAA.

BROCK, B.W., 2004. An analysis of short-term albedo variations at Haut Glacier D'Arolla, Switzerland. *Geografiska Annaler A,* **86**(1), pp. 53-65.

BROCK, B.W., MIHALCEA, C., KIRKBRIDE, M.P., DIOLAIUTI, G., CUTLER, M.E. and SMIRAGLIA, C., 2010. Meteorology and surface energy fluxes in the 2005-2007 ablation seasons at the Miage debris-covered glacier, Mont Blanc Massif, Italian Alps. *Journal of Geophysical Research: Atmospheres,* **115**(D9).

BROCK, B.W., WILLIS, I.C. and SHARP, M.J., 2006. Measurement and parameterization of aerodynamic roughness length variations at Haut Glacier d'Arolla, Switzerland. *Journal of Glaciology,* **52**(177), pp. 281-297.

BROCK, B.W. and ARNOLD, N.S., 2000. Technical communication: A spreadsheet - based (Microsoft Excel) point surface energy balance model for glacier and snow melt studies. *Earth Surface Preocesses and Landforms,* **25**(6), pp. 649-658.

BROCK, B.W., WILLIS, I.C., SHARP, M.J. and ARNOLD, N.S., 2000. Modelling seasonal and spatial variations in the surface energy balance of Haut Glacier d'Arolla, Switzerland. *Annals of Glaciology,* **31**, pp. 53-62.

BROHAN, P., KENNEDY, J.J., HARRIS, I., TETT, S.F.B. and JONES, P.D., 2006. Uncertainty estimates in regional and global observed temperature changes: A new data set from 1850. *Journal of Geophysical Research: Atmospheres,* **111**(D12).

BRUTSAERT, W., 1975. On a derivable formula for long-wave radiation from clear skies, *water resources research*, **11**(5), pp. 742-744.

BUSH, A.B. and PHILANDER, S.G.H., 1999. The climate of the Last Glacial Maximum: Results from a coupled atmosphere-ocean general circulation model. *Journal of Geophysical Research: Atmospheres,* **104**(D20).

CAREY, M., HUGGEL, C., BURY, J., PORTOCARRERO, C. and HAEBERLI, W., 2012. An integrated socio-environmental framework for glacier hazard management and climate change adaptation: lessons from Lake 513, Cordillera Blanca, Peru. *Climatic Change,* **112**(3-4), pp. 733-767.

CARRIVICK, J.L. and BROWN, I.A., 2001. The application of quicklook NOAA AVHRR satellite imagery in Northern Scandinavia for synoptic weather analyses. *Scottish Geographical Journal,* **117**(4), pp. 271-282.

CARRIVICK, J.L. and HOCK, R., 1999. *Measured and modelled melt and the surface energy balance on Storglaciären. In: Klingbjer, P. (ed): Tarfala Research Station Annual Report, 1998-1999.* Department of Physical Geography, Stockholm University, Research Report 111, pp. 28-33.

CHEN, D., and HELLSTRÖM, C., 1999. The influence of the North Atlantic Oscillation on the regional temperature variability in Sweden: spatial and temporal variations. *Tellus A*, **51**(4), pp. 505-516.

CHENG, S. and LAM, K.C., 2000. Synoptic typing and its application to the assessment of climatic impact on concentrations of sulphur dioxide and nitrogen oxides in Hong Kong. *Atmospheric Environment,* **34**(4), pp. 585--594.

CHOI, G., LEE, B., TENHUNEN, J., KANG, S., 2011. Intra-Annual variations in temperature lapse rate within a mountainous basin in Korea—a case study of the Punch Bowl, Yanggu. *Proceedings of the TERRECO Science Conference, October 2 - 7, 2011; Karlsruhe Institute of Technology, Garmisch-Partenkirchen, Germany*, pp. 71-76.

CULLEN, N.J., MOLG, T., KASER, G., STEFFEN, K. and HARDY, D.R., 2007. Energy-balance model validation on the top of Kilimanjaro, Tanzania, using eddy covariance data. *Annals of Glaciology,* **46**, pp. 227-233.

DE RUYTER DE WILDT, M.S., OERLEMANS, J. and BJÖRNSSON, H., 2003. A

calibrated mass balance model for Vatnajökull, Iceland. *Jökull,* **52**, pp. 1-20.

DE WOUL, M., HOCK, R., BRAUN, M., THORSTEINSSON, T., JÓHANNESSON, T. and HALLDÓRSDÓTTIR, S., 2006. Firn layer impact on glacial runoff: a case study at Hofsjökull, Iceland. *Hydrological Processes,* **20**(10), pp. 2171-2185.

DEE, D.P., UPPALA, S.M., SIMMONS, A.J., BERRISFORD, P., POLI, P.K., S., ANDRAE, U., BALMASEDA, M.A., BALSAMO, G., BAUER, P., BECHTOLD, P., BELJAARS, A.C.M., VAN DE BERG, L., BIDLOT, J., BORMANN, N., DELSOL, C., DRAGANI, R., FUENTES, M., GEER, A.J., HAIMBERGER, L., HEALY, S.B., HERSBACH, H., HÓLM, E.V., ISAKSEN, L., KÅLLBERG, P., KÖHLER1, M., MATRICARDI, M., MCNALLY, A.P., MONGE-SANZ, B.M., MORCRETTE, J.., PARK, B.., PEUBEY, C., DE ROSNAY, P., TAVOLATO, C., THÉPAUT, J. and VITART, F., 2011. The ERA-Interim reanalysis: configuration and performance of the data assimilation system. *Quarterly Journal of the Royal Meteorological Society,* **137**(656), pp. 553-597.

DENBY, B., GREUELL, W. and OERLEMANS, J., 2002. Simulating the Greenland atmospheric boundary layer. *Tellus A,* **54**(5), pp. 529-541.

DYER, A., 1974. A review of flux-profile relationships. *Boundary-Layer Meteorology,* **7**(3), pp. 363-372.

EASTERLING, D.R., 1990. Persistent patterns of thunderstorm activity in the central United States. *Journal of Climate,* **3**(12), pp. 1380-1389.

ECMWF, 2008. Newsletter No. 115—Spring 2008.

ECMWF, 2007. Newsletter No. 111—Spring 2007.

ECMWF, 2006. Newsletter No. 110—Winter 2006/07.

EINARSSON, M.Á., 1984. Climate of Iceland. In: VAN LOON.H., ed, *Climates of the Oceans*. First edn. Amsterdam: Elsevier, pp. 673-697.

ELSNER, J.B. and SCHMERTMANN, C.P., 1994. Assessing Forecast Skill through Cross Validation. *Weather and Forecasting,* **9**(4), pp. 619-624.

ESCHER-VETTER, H., 1985. Energy balance calculations for the ablation period 1982 at Vernagtferner, Oetztal Alps. *Annals of Glaciology,* **6**, pp. 158-160.

ESTEBAN, P., MARTIN-VIDE, J. and MASES, M., 2006. Daily atmospheric circulation catalogue for Western Europe using multivariate techniques. *International Journal of Climatology,* **26**(11), pp. 1501-1515.

EVERITT, B.S., LANDAU, S. and LEESE, M., 2001. *Cluster Analysis.* First edn. UK: Arnold Publishers.

FAVIER, V., WAGNON, P. and RIBSTEIN, P., 2004. Glaciers of the outer and inner tropics: A different behaviour but a common response to climatic forcing. *Geophysical Research Letters,* **31**(16).

FEALY, R., 2004. *An assessment of the Relationship between Glacier Mass Balance and Synoptic Climate in Norway: Likely future implications of climate change*, National University of Ireland, Maynooth.

FEALY, R. and SWEENEY, J., 2007. Identification of frequency changes in synoptic circulation types and consequences for glacier mass balance in Norway. *Norsk Geografisk Tidsskrift - Norweigan Journal of Geography,* **61**(2), pp. 76-91.

FEDEROV, E.E., 1927. Climate as totality of weather. *Monthly Weather Review,* **55**, pp. 401-403.

FERNAU, M.E. and SAMSON, P.J., 1990. Use of cluster analysis to define periods of similar meteorology and precipitation chemistry in eastern North America. Part II: Precipitation patterns and pollutant deposition. *Journal of Applied Meteorology,* **29**(8), pp. 751-761.

FETTWEIS, X., HANNA, E., LANG, C., BELLEFLAMME, A., ERPICUM, M. and GALLÉE, H., 2013. Brief communication: Important role of the mid-tropospheric atmospheric circulation in the recent surface melt increase over the Greenland ice sheet. *The Cryosphere,* **7**(1), pp. 241-248.

FETTWEIS, X., MABILLE, G., ERPICUM, M., NICOLAY, S. and BROEKE, M., 2011. The 1958-2009 Greenland ice sheet surface melt and the mid-tropospheric atmospheric circulation. *Climate Dynamics,* **36**(1-2), pp. 139-159.

FISHER, D., ZHENG, J., BURGESS, D., ZDANOWICZ, C., KINNARD, C., SHARP, M., and BOURGEOIS, J., 2012. Recent melt rates of Canadian arctic ice caps are the highest in four millennia. *Global and Planetary Change*, **84**(1), pp. 3-7.

FLOWERS, G.E. and CLARKE, G.K.C., 2002. A multicomponent coupled model of glacier hydrology 1. Theory and synthetic examples. *Journal of Geophysical Research: Solid Earth,* **107**(B11).

FÖHN, P., 1973. Short-term snow melt and ablation derived from heat-and mass-balance measurements. *Journal of Glaciology,* **12**(65), pp. 275-289.

FOUNTAIN, A. G., SCHLICHTING, R. B., JANSSON, P., and JACOBEL, R. W., 2005. Observations of englacial water passages: a fracture-dominated system. *Annals of Glaciology*, **40**, pp. 25-30

FRANCOU, B., VUILLE, M., FAVIER, V., and CÁCERES, B., 2004. New evidence for an ENSO impact on low-latitude glaciers: Antizana 15, Andes of Ecuador, 0 28′ S. *Journal of Geophysical Research*: Atmospheres **109**(D18).

GARDNER, A.S. and SHARP, M.S., 2009. Sensitivity of net mass balance estimates to near-surface temperature lapse rates when employing the degree-day method to estimate glacier melt. *Annals of Glaciology,* **50**, pp. 80-86.

GARDNER, A.S., SHARP, M.J., KOERNER, R.M., LABINE, C., BOON, S., MARSHALL, S.J., BURGESS, D.O. and LEWIS, D., 2009. Near-Surface Temperature Lapse Rates over Arctic Glaciers and Their Implications for Temperature Downscaling. *Journal of Climate,* **22**(16), pp. 4281-4298.

GEORGES, C. and KASER, G., 2002. Ventilated and unventilated air temperature measurements for glacier-climate studies on a tropical high mountain site. *Journal of Geophysical Research: Atmospheres,* **107** (D24).

GILLETT, N., ARORA, V., FLATO, G., SCINOCCA, J. and VON SALZEN, K., 2012. Improved constraints on 21st-century warming derived using 160 years of temperature observations. *Geophysical Research Letters,* **39**(1).

GILLETT, S. and CULLEN, N.J., 2011. Atmospheric controls on summer ablation over Brewster Glacier, New Zealand. *International Journal of Climatology,* **31**(13), pp. 2033-2048.

GOW, A.J., 1969. On the rates of growth of grains and crystals in South Polar firn. *Journal of Glaciology,* **8**(3)*,* pp. 241-252.

GRAINGER, M. and LISTER, H., 1966. Wind speed, stability and eddy viscosity over melting ice surfaces. *Journal of Glaciology,* **6**(43), pp. 101-127.

GRENFELL, T.C., 1979. The effect of ice thickness on the exchange of solar radiation over the polar oceans. *Journal of Glaciology,* **22**(87), pp. 305-320.

GREUELL, W. and BÖHM, R., 1998. 2 m temperatures along melting mid-latitude glaciers, and implications for the sensitivity of the mass balance to variations in temperature. *Journal of Glaciology,* **44**(146), pp. 9-20.

GREUELL, W., KNAP, W.H. and SMEETS, P.C., 1997. Elevational changes in meteorological variables along a midlatitude glacier during summer. *Journal of Geophysical Research: Atmospheres,* **102**(D22).

GREUELL, J.W. and KONZELMANN, T., 1994. Numerical modelling of the energy balance and the englacial temperature of the Greenland ice sheet: Calculation for the ETH-Camp location (1155m a.s.l.). *Global and Planetary Change,* **9**(1-2), pp. 91-114.

GREUELL, W. and SMEETS, P., 2001. Variations with elevation in the surface energy balance on the Pasterze (Austria). *Journal of Geophysical Research: Atmospheres,* **106**(D23).

GRUDD, H., and SCHNEIDER, T., 1996. Air temperature at Tarfala research station 1946-1995. *Geografiska Annaler A,* **78**(2-3), pp. 115-120.

GUÐMUNDSSON, S., BJÖRNSSON, H., PÁLSSON, F. and HARALDSSON, H.H., 2009. Comparison of energy balance and degree-day models of summer ablation on the Langjökull ice cap, SW-Iceland. *Jökull,* **59**, pp. 1-17.

GUÐMUNDSSON, S., BJÖRNSSON, H., PÁLSSON, F. and HARALDSSON, H.H., 2005. Energy balance of Brúarjökull and circumstances leading to the August 2004 floods in the river Jökla, N-Vatnajökull. *Jokull*, **55**, pp. 1-18

GUÐMUNDSSON, S., BJÖRNSSON, H., PÁLSSON, F. and HARALDSSON, H.H., 2003. *Comparison of physical and regression models of summer ablation on ice caps in Iceland.* RH-15-2003. Science Institue, University of Iceland/National Power Company of Iceland.

GUÐMUNDSSON, L., BREMNES, J.B., HAUGEN, J.E. and ENGEN SKAUGEN, T., 2012. Technical Note: Downscaling RCM precipitation to the station scale using quantile mapping - a comparison of methods. *Hydrology and Earth System Sciences Discussions,* **9**(5), pp. 6185-6201.

GUO, X., KUN, Y., LONG, Z., WEI, Y., SHENGHAI, L., MEILIN, Z., TANDONG, Y., and YINGYING, C.,2011. Critical evaluation of scalar roughness length parametrizations over a melting valley glacier. *Boundary-Layer Meteorology* **139**(2), pp. 307-332.

GUSMEROLI, A., JANSSON, P., PETTERSSON, R. and MURRAY, T., 2012. Twenty years of cold surface layer thinning at Storglaciären, sub-Arctic Sweden, 1989-2009 *Journal of Glaciology,* **58**(207), pp. 3-10.

GUTMANN, E.D., RASMUSSEN, R.M., LIU, C., IKEDA, K., GOCHIS, D.J., CLARK, M.P. and THOMPSON, G., 2012. A Comparison of Statistical and Dynamical Downscaling of Winter Precipitation over Complex Terrain. *Journal of Climate*, **25**(1), pp. 262-281.

HAGEN, J.O., MELVOLD, K., PINGLOT, F. and DOWDESWELL, J.A., 2003. On the net mass balance of the glaciers and ice caps in Svalbard, Norwegian Arctic. *Arctic, Antarctic, and Alpine Research,* **35**(2), pp. 264-270.

HANNA, E., JONES, J.M., CAPPELEN, J., MERNILD, S.H., WOOD, Land HUYBRECHTS, P., 2012. The influence of North Atlantic atmospheric and oceanic forcing effects on 1900-2010 Greenland summer climate and ice melt/runoff. *International Journal of Climatology* **33**(4), pp. 862-880.

HANNA, E., HUYBRECHTS, P., JANSSENS, I., CAPPELEN, J., STEFFEN, K. and STEPHENS, A., 2005. Runoff and mass balance of the Greenland ice sheet: 1958-2003. *Journal of Geophysical Research: Atmospheres,* **110**(D13).

HANNA, E., JÓNSSON, T. and BOX, J.E., 2004. An analysis of Icelandic climate since the nineteenth century. *International Journal of Climatology,* **24**(10), pp. 1193-1210.

HANNAH, D.M., GURNELL, A.M. and MCGREGOR, G.M., 2000. Spatio-temporal variation in microclimate, the surface energy balance and ablation over a cirque glacier. *International Journal of Climatology,* **20**(7), pp. 733-758.

HANNAH, D.M., GURNELL, A.M. and MCGREGOR, G.R., 1999. Identifying links between large-scale atmospheric circulation and local glacier ablation climates in the French Pyrenees, *Interactions between the cryosphere, climate and greenhouse gases (Proceedings of IUGG'99 Symposium HS2, Birmingham)*, July 1999, *IAHS Publication* **256**, pp. 155.

HANNAH, D.M. and MCGREGOR, G.M., 1997. Evaluating the impact of climate on snow- and ice-melt dynamics in the Taillon basin, French Pyrénées *Journal of Glaciology,* **43**(145), pp. 563-568.

HANSON, B., 1995. A fully three-dimensional finite-element model applied to velocities on Storglaciären, Sweden. *Journal of Glaciology*, **41**(137), pp. 91-102.

HASHINO, T., BRADLEY, A. and SCHWARTZ, S., 2007. Evaluation of bias-correction methods for ensemble streamflow volume forecasts. *Hydrology and Earth System Sciences Discussions,* **11**(2), pp. 939-950.

HAY, L.E., and CLARK, M.P., 2003. Use of statistically and dynamically downscaled atmospheric model output for hydrologic simulations in three

mountainous basins in the western United States. *Journal of Hydrology*, **282**(1), pp. 56-75.

HAY, J.E. and FITZHARRIS, B.B., 1988. A comparison of the energy balance and bulk - aerodynamic approaches for estimating glacier melt. *Journal of Glaciology,* **34**(117), pp. 144-153.

HAYS, J.D., IMBRIE, J., and SHACKLETON, N.J., 1976. Variations in the Earth's Orbit: Pacemaker of the Ice Ages. *Science*, **194(**4270), pp. 1121-1132.

HEALEY, J.F., 1993. *Statistics, a tool for social research.* Third edn. Belmont, California: Wadsworth Pub. Co.

HESS, P. and BREZOWSKY, H., 1952. Katalog der Grosswetterlagen Europas. *Berichte des Deutschen Wetterdienstes in der US-Zone,* **33**.

HIDALGO, H.G., DETTINGER, M.D., and CAYAN, D.R. 2008. Downscaling with constructed analogues: Daily precipitation and temperature fields over the United States. *California Energy Commission PIER Final Project Report CEC-500-2007-123*.

HOCK, R., 2005. Glacier melt: a review of processes and their modelling. *Progress in Physical Geography,* **29**(3), pp. 362-391.

HOCK, R., 2003. Temperature index melt modelling in mountain areas. *Journal of Hydrology,* **282**(1), pp. 104-115.

HOCK, R., 1999. A distributed temperature index ice and snow melt model including potential direct solar radiation. *Journal of Glaciology,* **45**(149), pp. 101-111.

HOCK, R., 1998. *Modelling of Glacier Melt and Discharge*, Department of Geography, University of Zurich.

HOCK, R., RADIC, V. and DE WOUL, M., 2007. Climate sensitivity of Storglaciären—An intercomparison of mass balance models using ERA-40 reanalysis and regional climate model data. *Annals of Glaciology,* **46**, pp. 342-348.

HOCK, R. and HOLMGREN, B., 2005. A distributed surface energy balance model for complex topography and its application to Storglaciären, Sweden. *Journal of Glaciology,* **51**(172), pp. 25-36.

HOCK, R. and NOETZLI, C., 1997. Areal melt and discharge modelling of Storglaciären, Sweden. *Annals of Glaciology,* **24**, pp. 211-216.

HOCK, R. and HOLMGREN, B., 1996. Some aspects of energy balance and ablation of Storglaciären, northern Sweden. *Geografiska Annaler A,* **78** (2-3), pp. 121-131.

HODGKINS, R., CARR, S., PÁLSSON, F., GUÐMUNDSSON, S. and BJÖRNSSON, H., 2012a. Sensitivity analysis of temperature-index melt simulations to near-surface lapse rates and degree-day factors at Vestari-Hagafellsjökull, Langjökull, Iceland *Hydrological Processes,* **26**(24), pp. 3736-3748.

HODGKINS, R., CARR, S., PÁLSSON, F., GUÐMUNDSSON, S. and BJÖRNSSON, H., 2012b. Modelling variable glacier lapse rates using ERA-Interim reanalysis climatology: an evaluation at Vestari-Hagafellsjökull, Langjökull, Iceland. *International Journal of Climatology,* **33**(2), pp. 410-421.

HODGKINS, R., COOPER, R., WADHAM, J., and TRANTER, M., 2005. Interannual variability in the spatial distribution of winter accumulation at a high-Arctic glacier (Finsterwalderbreen, Svalbard), and its relationship with topography. *Annals of Glaciology*, **42**, pp. 243-248.

HOFER, M., MÖLG, T., MARZEION, B. and KASER, G., 2010. Empirical-statistical downscaling of reanalysis data to high-resolution air temperature and specific humidity above a glacier surface (Cordillera Blanca, Peru). *Journal of Geophysical Research: Atmospheres,* **115**(D12).

HÖGSTROM, U., 1988. Nondimensional wind and temperature profiles in the atmospheric surface layer: a re-evaluation. *Boundary-Layer Meteorology,* **42**(1-2), pp. 55-78.

HOINKES, H.C., 1968. Glacier variation and weather. *Journal of Glaciology,* **7**(49), pp. 3-18.

HOLLAND, M.M. and BITZ, C.M., 2003. Polar amplification of climate change in coupled models. *Climate Dynamics,* **21**(3), pp. 221-232.

HOLMGREN, B., Climate and energy exchange on a sub - polar ice cap in summer. Arctic Institute of North America Devon Island Expedition, 1961 - 1963. Parts A:F. 1971. *Uppsala Universitet. Meteorologiska Institutionen. Meddelanden*

HOLMLUND, P., 1987: Mass balance of Storglaciären during the 20th century. *Geografiska Annaler A* **69**(3-4), pp. 439-447.

HOLMLUND, P. and JANSSON, P., 2005. A re-analysis of the 58-year mass balance record of Storglaciären, Sweden. *Annals of Glaciology* **42**, pp. 389-394.

HOLMLUND, H. JANSSON, P., 2002 Glaciological Research at Tarfala Research Station. Printed by Tryckindustri Information AB.

HOLMLUND, P. and JANSSON, P., 1999. The Tarfala mass balance programme. *Geografiska Annaler A,* **81**(4), pp. 621-631.

HOLMLUND, P. and SCHNEIDER, T., 1997. The effect of continentality on glacier response and mass balance. *Annals of Glaciology,* **24**, pp. 272-276.

HOLMLUND, P. and ERIKSSON, M., 1989: The cold surface layer on Storglaciären. *Geografiska Annaler A* **71**(3-4), pp. 241-244.

HOOKE, R.L. and POHJOLA, V.A., 1994. Hydrology of a segment of a glacier situated in an overdeepening, Storglaciaren, Sweden. *Journal of Glaciology*, **40**(134), pp. 140-148.

HOOKE, R.L., CALLA, P., HOLMLUND, P., NILSSON, M., and STROEVEN, A., 1989. A 3 year record of seasonal variations in surface velocity, Storglaciären, Sweden. *Journal of Glaciology*, **35**(120), pp. 235-247.

HUBERTY, C.J., 1994. *Applied Discriminant Analysis.* First edn. New York, United States: A Wiley-Interscience Publication.

HULTH, J., ROLSTAD, C., TRONDSEN, K., and RODBY, R. W., 2010. Surface mass and energy balance of Sorbreen, Jan Mayen, 2008. *Annals of Glaciology*, **51**(55), pp. 110-119.

HUSS, M. and BAUDER, A., 2009. 20th-century climate change inferred from four long-term point observations of seasonal mass balance. *Annals of Glaciology,* **50**, pp. 207-214.

HUSS, M., FUNK, M. and OHMURA, A., 2009. Strong Alpine glacier melt in the 1940s due to enhanced solar radiation. *Geophysical Research Letters,* **36**(23).

HUSS, M., FARINOTTI, D., BAUDER, A. and FUNK, M., 2008. Modelling runoff from highly glacierized alpine drainage basins in a changing climate. *Hydrological Processes,* **22**(19), pp. 3888-3902.

HUTH, R., BECK, C., PHILIPP, A., DEMUZERE, M., USTRNUL, Z., CAHYNOVÁ, M., KYSELÝ, J. and TVEITO, O.E., 2008. Classifications of atmospheric circulation patterns. *Annals of the New York Academy of Sciences,* **1146**(1), pp. 105-152.

HUTH, R., NEMEŠOVÁ, I. and KLIMPEROVÁ, N., 1993. Weather categorization based on the average linkage clustering technique: an application to European mid-latitudes. *International Journal of Climatology,* **13**(8), pp. 817-835.

IMBRIE, J., and IMBRIE, J., 1980. Modeling the climatic response to orbital variations. *Science*, **207**(4434), pp. 943-953.

IMMERZEEL, W.W., VAN BEEK, L.P. and BIERKENS, M.F., 2010. Climate change will affect the Asian water towers. *Science,* **328**(5984), pp. 1382-1385.

INES, A.V.M. and HANSEN, J.W., 2006. Bias correction of daily GCM rainfall for crop simulation studies. *Agricultural and Forest Meteorology,* **138**(1), pp. 44-53.

IPCC, 2007: Climate Change 2007: Synthesis Report. Contribution of Working Groups I, II and III to the Fourth Assessment Report of the Intergovernmental Panel

on Climate Change [Core Writing Team, PACHAURR, R.K and REISINGER, A.(eds.)]. IPCC, Geneva, Switzerland, 104 pp.

IQBAL, M., 1983. *An introduction to solar radiation.* First edn. London: Academic Press.

JACOB, T., WAHR, J., PFEFFER, W.T. and SWENSON, S., 2012. Recent contributions of glaciers and ice caps to sea level rise. *Nature,* **482**, pp. 514-518.

JACOBS, S., HELLMER, H., DOAKE, C., JENKINS, A. and FROLICH, R., 1992. Melting of ice shelves and the mass balance of Antarctica. *Journal of Glaciology,* **38**(130), pp. 375-387.

JANSSON, P., HOCK, R. and SCHNEIDER, T., 2003. The concept of glacier storage: a review. *Journal of Hydrology,* **282**(1), pp. 116-129.

JAROSCH, A.H., ANSLOW, F.S. and CLARKE, G.K., 2012. High-resolution precipitation and temperature downscaling for glacier models. *Climate Dynamics*, **38**(1-2) pp. 391-409.

JANSSON, P., 1996. Dynamics and hydrology of a small polythermal valley glacier. *Geografiska. Annaler A* **78** (2-3), pp. 171-180.

JIANG, N., 2011. A new objective procedure for classifying New Zealand synoptic weather types during 1958-2008. *International Journal of Climatology,* **31**(6), pp. 863-879

JIANG, N., 2011. A new objective procedure for classifying New Zealand synoptic weather types during 1958-2008. *International Journal of Climatology,* **31**(6), pp. 863-879

JÓHANNESSON, T., AÐALGEIRSDÓTTIR G., BJÖRNSSON, H., CROCHET, P., ELIASSON, E.B., GUÐMUNDSSON, S., JÓNSDÓTTIR, J.F., ÓLAFSSON, H., PÁLSSONn, F., RÖGNVALDSSON, Ó., SIGURÐSSON, O., SNORRASON, Á., SVEINSSON, Ó. G.B., and THORSTEINSSON, T.H. 2007, *Effect of climate change on hydrology and hydro-resources in Iceland*. Reykjavík, National Energy Authority, Report. OS-2007/011.

JÓHANNESSON, T., SIGURÐSSON, O., LAUMANN, T. and KENNETT, M., 1995. Degree-day glacier mass balance modelling with application to glaciers in Iceland, Norway and Greenland. *Journal of Glaciology,* **41**(138), pp. 345-358.

JOHNSON, R.J., 1991. *Multivariate Statistical Analysis in Geography.* Fourth (reprinted) edn. Hong Kong: Longman Scientific and Technical.

JOLIFFE, I.T. and PHILIPP, A., 2010. Some recent developments in cluster analysis. *Physics and Chemistry of the Earth,* **35**(9-12), pp. 411-421.

JONSELL, U.Y., NAVARRO, F.J., BAÑÓN, M., LAPAZARAN, J.J. and OTERO, J., 2012. Sensitivity of a distributed temperature-radiation index melt model based on AWS observations and surface energy balance fluxes, Hurd Peninsula glaciers, Livingston Island, Antarctica. *The Cryosphere,* **6**(3), pp. 539-552.

JUEN, I., KASER, G. and GEORGES, C., 2007. Modelling observed and future runoff from a glacierized tropical catchment (Cordillera Blanca, Perú). *Global and Planetary Change,* **59**(1), pp. 37-48.

KALKSTEIN, L.S., BARTHEL, C.D., GREENE, J.S. and NICHOLS, M.C., 1996. A new spatial synoptic classification: Application to air mass analysis. *International Journal of Climatology,* **16**(9), pp. 983-1004.

KALKSTEIN, L.S., DUNNE, P.C. and VOSE, R.S., 1990. Detection of climatic change in the western North American Arctic using a synoptic climatological approach. *American Meteorological Society,* **3**(10), pp. 1153-1167.

KALKSTEIN, L., TAN, G. and SKINDLOV, J.A., 1987. An evaluation of three clustering procedures for use in a synoptic climatological classification. *American Meteorological Society,* **26**(6), pp. 717-730.

KALKSTEIN, L. and CORRIGAN, P., 1986. A synoptic climatological approach for geographical analysis: Assessment of sulphur dioxide concentrations. *Annals of the Association of American Geographers,* **76**(3), pp. 381-395.

KASER, G., 1999. A review of the modern fluctuations of tropical glaciers. *Global and Planetary Change,* **22**(1), pp. 93-103.

KÄSMACHER, O. and SCHNEIDER, C., 2011. An objective circulation pattern classification for the region of Svalbard. *Geografiska Annaler A,* **93**(4), pp. 259-271.

KIPP and ZONEN, 2004. Instruction Manual: CM21 Precision Pyranometer, accessed via: http://www.kippzonen.com/?downloadcategory/991/Discontinued+Products.aspx

KIRCHOFER, W., 1973. Classification of European 500 mb patterns. *Arbeitsbericht der Schweizerischen Meteorologischen Zentralanstalt,* **43**.

KLOK, E.J. and OERLEMANS, J., 2002. Model study of the spatial distribution of the energy and mass balance of Morteratschgletscher, Switzerland. *Journal of Glaciology,* **48**(163), pp. 505-518.

KOBLET, T., GÄRTNER-ROER, I., ZEMP, M., JANSSON, P., THEE, P., HAEBERLI, W. and HOLMLUND, P., 2010. Reanalysis of multi-temporal aerial images of Storglaciären, Sweden (1959-99)—Part 1: Determination of length, area, and volume changes. *The Cryosphere,* **4**(3), pp. 333-343.

KONDRATYEV, K.Y., 1969. *Radiation in the atmosphere.* New York: Academic Press.

KÖNIG-LANGLO, G. and AUGSTEIN, F., 1994. Parameterization of the downward long-wave radiation at the Earth's surface in polar regions. *Meteorologische Zeitschrift,* **3**, pp. 343-347.

KONYA, K. and MATSUMOTO, T., 2010. Influence of weather conditions and spatial variability on glacier surface melt in Chilean Patagonia. *Theoretical Applied Climatology,* **102**(1), pp. 139-149.

KONYA, K., HOCK, R. and NARUSE, R., 2007. Temperature lapse rates and surface energy balance at Storglaciären, northern Sweden. *IAHS Publication,* **318**, pp. 186-194.

KONZELMANN, T., VAN DE WAL, R.S.W., GREUELL, W., BINTANJA, R., HENNEKEN, E.A.C. and ABE-OUCHI, A., 1994. Parameterization of global and longwave incoming radiation for the Greenland Ice Sheet. *Global and Planetary Change,* **9**(1), pp. 143-164.

KOTLARSKI, S., JACOB, D., PODZUN, R. and PAUL, F., 2010. Representing glaciers in a regional climate model. *Climate Dynamics,* **34**(1), pp. 27-46.

KUHN, M., 1993. Methods of assessing the effects of climatic changes on snow and glacier hydrology, *IAHS Publication*, **218**, pp. 135-144.

LA CHAPELLE, E., 1961. Energy exchange measurements on the Blue glacier, Washington.Glacier. *Journal of Geophysical Research,* **64**(4), pp. 443-449.

LAMB, H.H., 1972. British Isles weather types and a register of daily sequence of circulation patterns, 1861-1971. *Geophysical Memoir,* **16**, HM Stationary Office.

LANG, H. and BRAUN, L., 1990. On the information content of air temperature in the context of snow melt estimation. *IAHS Publication,* **190**, pp. 347-354.

LANG, H., 1968. Relations between glacier runoff and meteorological factors observed on and outside the glacier. *IAHS Publication,* **79**, pp. 429-439.

LAUMANN, T. and REEH, N., 1993. Sensitivity to climate change of the mass balance of glaciers in southern Norway. *Journal of Glaciology*, **39**(133), pp. 656-665.

LEMKE, P., REN, J., ALLEY, R.B. ALLISON, I., CARRASCO, J., FLATO, FUJII, G., KASER, G., MOTE, P., THOMAS, R.H. and ZHANG, T., 2007: Observations: Changes in Snow, Ice and Frozen Ground. In: Climate Change 2007: The Physical Science Basis. Contribution of Working Group I to the Fourth Assessment Report of the Intergovernmental Panel on Climate Change [Solomon, S., Qin, D., Manning, M., Chen, Z., Marquis, M., Averyt, K.B., Tignor, M., and Miller, H.L. (eds.)]. Cambridge University Press, Cambridge, United Kingdom and New York, NY, USA

LOCKWOOD, J.G., 1974. *World Climatology.* First edn. London: Edward Arnold.

LUND, I.A., 1963. Map-pattern classification by statistical methods. *Journal of Applied Meteorology,* **2**(1), pp. 56-65.

MACHGUTH, H., PAUL, F., KOTLARSKI, S. and HOELZLE, M., 2009. Calculating distributed glacier mass balance for the Swiss Alps from regional climate model output: A methodological description and interpretation of the results. *Journal of Geophysical Research: Atmospheres,* **114**(D19).

MACHGUTH, H., PAUL, F., HOELZLE, M., and HAEBERLI, W., 2006. Distributed glacier mass-balance modelling as an important component of modern multi-level glacier monitoring. *Annals of Glaciology*, **43**, pp. 335-343

MARSHALL, S.J. and SHARP, M.J., 2009. Temperature and Melt Modeling on the Prince of Wales Ice Field, Canadian High Arctic. *Journal of Climate,* **22**(6), pp. 1454-1468.

MARSHALL, S.J., SHARP, M.J., BURGESS, D.O. and ANSLOW, F.S., 2007. Near-surface-temperature lapse rates on the Prince of Wales Icefield, Ellesmere Island, Canada: implications for regional downscaling of temperature. *International Journal of Climatology,* **27**(3), pp. 385-398.

MARTIN, E., TIMBAL, B. and BRUN, E., 1996. Downscaling of general circulation model outputs: simulation of the snow climatology of the French Alps and sensitivity to climate change. *Climate Dynamics*, **13(**1), pp. 45-56.

MARZEION, B. and NESJE, A., 2012. Spatial patterns of North Atlantic Oscillation influence on mass balance variability of European glaciers. *The Cryosphere,* **6**(3), pp. 661-673.

MARZEION, B., JAROSCH, A.H. and HOFER, M., 2012. Past and future sea-level change from the surface mass balance of glaciers. *The Cryosphere,* **6**(6), pp. 1295-1322.

MATULLA, C., WATSON, E., WAGNER, S. and SCHÖNER, W., 2009. Downscaled GCM projections of winter and summer mass balance for Peyto Glacier,

Alberta, Canada (2000-2100) from ensemble simulations with ECHAM5-MPIOM. *International Journal of Climatology,* **29**(11), pp. 1550-1559.

MCKILLUP, S., 2005. *Statistics explained : an introductory guide for life sciences.* First edn. Cambridge: Cambridge University Press.

MEDINA, S., B.F. SMULL, R. A. HOUZE Jr., and M. STEINER, 2005. Crossbarrier flow during orographic precipitation events: Results from MAP and IMPROVE, *Journal of Atmospheric Science*, **62**(10), pp. 3580-3598,

MEIER, M.F., DYURGEROV, M.B., RICK, U.K., O'NEEL, S., PFEFFER, W.T., ANDERSON, R.S., ANDERSON, S.P. and GLAZOVSKY, A.F., 2007. Glaciers dominate eustatic sea-level rise in the 21st century. *Science,* **317**(5841), pp. 1064.

MEYERS, T. and DALE, R., 1983. Predicting Daily Insolation with Hourly Cloud Height and Coverage. *Journal of Applied Meteorology,* **22**(4), pp. 537-545.

MICHAELSEN, J., 1987. Cross validation in statistical climate forecast models. *Journal of Applied Meteorology,* **26**(11), pp. 1589-1600.

MICHALSKY, J.J., PEREZ, R., HARRISON, L. and LEBARON, A., 1991. Spectral and temperature correction of silicon photovoltaic solar radiation detectors. *Solar Energy,* **47**(4), pp. 229-305.

MITCHELL, T.D. and HULME, M., 1999. Predicting regional climate change: living with uncertainty. *Progress in Physical Geography,* **23**(1), pp. 57-78.

MOHOLDT, G., NUTH, C., HAGEN, J.O. and KOHLER, J., 2010. Recent elevation changes of Svalbard glaciers derived from ICESat laser altimetry. *Remote Sensing of Environment,* **114**(11), pp. 2756-2767.

MÖLG, T. and KASER, G., 2011. A new approach to resolving climate-cryosphere relations: Downscaling climate dynamics to glacier-scale mass and energy balance without statistical scale linking. *Journal of Geophysical Research: Atmospheres,* **116**(D16).

MÖLG, T., CULLEN, N.J. and KASER, G., 2009. Solar radiation, cloudiness and longwave radiation over low-latitude glaciers: implications for mass-balance modelling. *Journal of Glaciology,* **55**(190), pp. 292-302.

MOORE, R.D. 1983. On the use of bulk aerodynamic formulae over melting snow. *Nordic. Hydrology*, **14**(4), pp. 193-206.

MOTE, T.L., 1998a. Mid-tropospheric circulation and surface melt on the Greenland ice sheet. Part 1: Atmospheric teleconnections *International Journal of Climatology,* **18**(2), pp. 111-129.

MOTE, T.L., 1998b. Mid tropospheric circulation and surface melt on the Greenalnd ice sheet. Part II: Synoptic Climatology. *International Journal of Climatology,* **18**(2), pp. 131-145.

MÜLLER, H., 1985. On the radiation budget in the Alps. *Journal of climatology,* **5**(4), pp. 445-462.

MUNRO, D.S., 2004. Revisiting bulk heat transfer on Peyto Glacier, Alberta, Canada, in light of the OG parameterization. *Journal of Glaciology,* **50**(171), pp. 590-600.

MUNRO, D.S., 1991. A surface energy exchange model of glacier melt and net mass balance. *International Journal of Climatology,* **11**(6), pp. 689-700.

MUNRO, D.S., 1989. Surface roughness and bulk heat transfer on a glacier: comparison with eddy correlation. *Journal of Glaciology,* **35**(121), pp. 343-348.

OERLEMANS, J., 2000. Analysis of a 3 year meteorological record from the ablation zone of Morteratschgletscher, Switzerland: energy and mass balance. *Journal of Glaciology*, **46**(155), pp. 571-579.

OERLEMANS, J. and GRISOGONO, B., 2002. Glacier winds and parameterisation of the related surface heat fluxes. *Tellus,* **54A**(5), pp. 440-452.

OERLEMANS, J., BJÖRNSSON, H., KUHN, M., OBLEITNER, F., PÁLSSON, F. and SMEETS, C., 1999. Glacier-meteorological investigations on Vatnajökull, Iceland, summer 1996: An overview. *Boundary Layer Meteorology,* **92**(1), pp. 3-24.

OERLEMANS, J., ANDERSON, B., HUBBARD, A., HUYBRECHTS, P., JOHANNESSON, T., KNAP, W., SCHMEITS, M., VAN DE WAL, R. and WALLINGA, J., 1998. Modelling the response of glaciers to climate warming. *Climate Dynamics,* **14**(4), pp. 267-274.

OERLEMANS, J. and VUGTS, H., 1993. A meteorological experiment in the melting zone of the Greenland ice sheet. *Bulletin of the American Meteorological Society,* **74**, pp. 355-365.

OERLEMANS, J., and HOOGENDOORN, N. C., 1989. Mass balance gradients and climatic change. *Journal of Glaciology*, **35**(121), pp. 399-405.

OHATA, T., 1989. The effect of glacier wind on local climate, turbulent heat fluxes and ablation. *Zeitschrift für Gletscherkunde und Glazialgeologie,* **25**(1), pp. 49-68.

OHMURA, A., 2001. Physical basis for the temperature-based melt-index method. *American Meteorological Society,* **40**(4), pp. 753-761.

OKE, T.R., 1987. *Boundary layer climates.* Second edn. London: Routledge Press.

PANOFSKY, H.W. and BRIER, G.W., 1968. *Some Applications of Statistics to Meteorology.* First edn. Philadelphia: The Pennsylvania State University Press.

PARMHED, O., OERLEMANS, J. and GRISOGONO, B., 2004. Describing surface fluxes in katabatic flow on Breidamerkurjökull, Iceland. *Quarterly Journal of the Royal Meteorological Society,* **130**(598), pp. 1137-1151.

PATERSON, W.S.B., 1994. *The physics of glaciers.* Third edn. Oxford: Elsevier Science.

PAUL, F., and KOTLARSKI, S., 2010. Forcing a distributed glacier mass balance model with the regional climate model REMO. Part II: Downscaling strategy and results for two Swiss glaciers. *Journal of Climate*, **23**(6), pp. 1607-1620.

PAUL, F., ESCHER-VETTER, H., and MACHGUTH, H., 2009. Comparison of mass balances for Vernagtferner, Oetzal Alps, as obtained from direct measurements and distributed modeling. *Annals of Glaciology*, **50**, pp. 169-177.

PAULSON, C.A., 1970. The mathematical representation of wind speed and temperature profiles in the unstable atmospheric surface layer. *Journal of Applied Meteorology,* **9**(6), pp. 857-861.

PELLICCIOTTI, F., CARENZO, M., HELBING, J., RIMKUS, S. and BURLANDO, P., 2009. On the role of subsurface heat conduction in glacier energy-balance modelling. *Annals of Glaciology,* **50**, pp. 16-24.

PELLICCIOTTI, F., BROCK, B.W., STRASSER, U., BURLANDO, P., FUNK, M. and CORRIPIO, J., 2005. An enhanced temperature-index glacier melt model including the shortwave radiation balance: development and testing for Haut Glacier d' Arolla, Switzerland. *Journal of Glaciology,* **51**(175), pp. 573-587.

PEPIN, N., 2001. Lapse rate changes in northern England. *Theoretical and Applied Climatology,* **68**(1), pp. 1-16.

PEPIN, N. and KIDD, D., 2006. Spatial temperature variation in the Eastern Pyrenees. *Weather,* **61**(11), pp. 300-310.

PEPIN, N.C. and NORRIS, J.R., 2005. An examination of the differences between surface and free-air temperature trend at high-elevation sites: Relationships with cloud cover, snow cover, and wind. *Journal of Geophysical Research: Atmospheres,* **110**(D24).

PEPIN, N. and LOSLEBEN, M., 2002. Climate change in the Colorado Rocky Mountains: free air versus surface temperature trends. *International Journal of Climatology,* **22**(3), pp. 311-329.

PEPIN, N., BENHAM, D. and TAYLOR, K., 1999. Modeling Lapse Rates in the Maritime Uplands of Northern England: Implications for Climate Change. *Arctic, Antarctic, and Alpine Research,* **31**(2), pp. 151-164.

PETERSEN, L. and PELLICCIOTTI, F., 2011. Spatial and temporal variability of air temperature on a melting glacier: Atmospheric controls, extrapolation methods and their effect on modeling, Juncal Norte Glacier, Chile. *Journal of Geophysical Research: Atmospheres,* **116**(D23).

PETTERSSON, R., JANSSON, P. and HOLMLUND, P., 2003. Cold surface layer thinning on Storglaciären, Sweden, observed by repeated ground penetrating radar surveys. *Journal of Geophysical Research: Earth Surface*, **108**(F1).

PFEFFER, W.T., HARPER, J.T. and O'NEEL, S., 2008. Kinematic Constraints on Glacier Contributions to 21st-Century Sea-Level Rise. *Science,* **321**(5894), pp. 1340-1343.

PHILIPP, A., 2009. Comparison of principal component and cluster analysis for classifying circulation pattern sequences for the European domain. *Theoretical Applied Climatology,* **96**(1-2), pp. 31-41.

PHILIPP, A., BARTHOLY, J., BECK, C., ERPICUM, M., ESTEBAN, P., FETTWEIS, X., HUTH, R., JAMES, P., JOURDAIN, S., KREINKAMP, F., KRENNERT, T., LYKOUDIS, S., MICHALIDES, S.C., PIANKO-KLUCZYNSKA, K., POST, P. and ÁLVAREZ, D.R., 2010. Cost 733cat - A database of weather and circulation type classifications. *Physics and Chemistry of the Earth,* **35**(9-12), pp. 360-367.

POHJOLA, V.A. and ROGERS, J.C., 1997. Coupling between the atmospheric circulation and extremes of the mass balance of Storglaciären, northern Scandinavia. *Annals of Glaciology,* **24**, pp. 229-233.

PREISENDORFER, R.W. and MOBLEY, C.D., 1988. *Principal Components Analysis in Meteorology and Oceanography.* First edn. Amsterdam: Elsevier.

RABATEL, A., FRANCOU, B., SORUCO, A., GOMEZ, J., CÁCERES, B., CEBALLOS, J., BASANTES, R., VUILLE, M., SICART, J. and HUGGEL, C., 2013. Current state of glaciers in the tropical Andes: a multi-century perspective on glacier evolution and climate change. *The Cryosphere,* **7**(1), pp. 81-102.

RADIĆ, V. and HOCK, R., 2011. Regionally differentiated contribution of mountain glaciers and ice caps to future sea-level rise. *Nature Geoscience,* **4**(2), pp. 91-94.

RADIĆ, V. and HOCK, R., 2006. Modelling future glacier mass balance and volume changes using ERA-40 reanalysis and climate models: A sensitivity study at Storglaciären, Sweden, *Journal of Geophysical Research: Earth Surface,* **111**(F3).

RAPER, S.C.B. and BRAITHWAITE, R.J., 2006. Low sea level rise projections from mountain glaciers and icecaps under global warming. *Nature,* **439**(7074), pp. 311-313.

REICHERT, B.K., BENGTSSON, L. and OERLEMANS, J., 2001. Midlatitude forcing mechanisms for glacier mass balance investigated using general circulation models. *Journal of Climate,* **14**(17), pp. 3767-3784.

REICHERT, B.K., BENGTSSON, L., and AKESSON, O., 1999. A statistical modeling approach for the simulation of local paleoclimatic proxy records using general circulation model output. *Journal of geophysical research: Atmospheres*, **104**(D16).

REIJMER, C.H. and HOCK, R., 2008. Internal accumulation on Storglaciären, Sweden, in a multi-layer snow model coupled to a distributed energy and mass balance model. *Journal of Glaciology,* **54**(184), pp. 61-72.

RIGNOT, E., VELICOGNA, I., VAN DEN BROEKE, M., MONAGHAN, A. and LENAERTS, J., 2011. Acceleration of the contribution of the Greenland and Antarctic ice sheets to sea level rise. *Geophysical Research Letters,* **38**(5).

RIGNOT, E. and KANAGARATNAM, P., 2006. Changes in the velocity structure of the Greenland Ice Sheet. *Science,* **311**(5763), pp. 986-990.

ROBERTS, N., 1998. *The Holocene.* Second edn. Oxford: Blackwell-Wiley.

ROTUNNO, R. and HOUZE, R.A., 2007. Lessons on orographic precipitation from the Mesoscale Alpine Programme. *Quarterly Journal of the Royal Meteorological Society,* **133**(625), pp. 811-830.

RYE, C.J., ARNOLD, N.S., WILLIS, I.C. and KOHLER, J., 2010. Modeling the surface mass balance of a high Arctic glacier using the ERA-40 reanalysis. *Journal of Geophysical Research: Earth Surface,* **115**(F2).

SALAMEH, T., DROBINSKI, P., VRAC, M. and NAVEAU, P., 2009. Statistical downscaling of near-surface wind over complex terrain in southern France. *Meteorology and Atmospheric Physics,* **103**(1-4), pp. 253-265.

SCHUENEMANN, K.C., CASSANO, J.J. and FINNIS, J., 2009. Synoptic Forcing of Precipitation over Greenland: Climatology for 1961-99. *Journal of Hydrometeorology,* **10**(1), pp. 60-78.

SEDLAR, J. and HOCK, R., 2009. Testing longwave radiation parameterizations under clear and overcast skies at Storglaciären, Sweden. *The Cryosphere,* **3**(1), pp. 75-84.

SERREZE, M., BARRETT, A., STROEVE, J., KINDIG, D. and HOLLAND, M., 2009. The emergence of surface-based Arctic amplification. *Cryosphere,* **3**(1), pp. 11-19.

SERREZE, M.C., CARSE, F., BARRY, R.G. and ROGERS, J.C., 1997. Icelandic low cyclone activity: Climatological features, linkages with the NAO, and relationships with recent changes in the Northern Hemisphere circulation. *Journal of Climate,* **10**(3), pp. 453-464.

SHEA, J.M., 2010. *Regional-Scale Distributed Modelling of Glacier Meteorology and Melt, southern Coast Mountains, Canada*, University of British Columbia.

SHEA, J.M. and MOORE, R.D., 2010. Prediction of spatially distributed regional-scale fields of air temperature and vapour pressure over mountain glaciers. *Journal of Geophysical Research: Atmospheres,* **115**(D23).

SHEA, J.M., MOORE, R.D. and STAHL, K., 2009. Derivation of melt factors from glacier mass-balance records in western Canada. *Journal of Glaciology,* **55**(189), pp. 123-130.

SHEA, J.M. and MARSHALL, S.J., 2007. Atmospheric flow indices, regional climate, and glacier mass balance in the Canadian Rocky Mountains. *International Journal of Climatology,* **27**(2), pp. 233-247.

SHERIDAN, S.C., 2002. The redevelopment of a weather-type classification scheme for North America. *International Journal of Climatology,* **22**(1), pp. 51-68.

SICART, J.E., HOCK, R., RIBSTEIN, P. and CHAZARIN, J.P., 2010. Sky longwave radiation on Tropical Andean glaciers: parameterization and sensitivity to atmospheric variables. *Journal of Glaciology,* **57**(199), pp. 854-860.

SICART, J.E., HOCK, R., RIBSTEIN, P., LITT, M. and RAMIREZ, E., 2011. Analysis of seasonal variations in mass balance and meltwater discharge of the tropical Zongo Glacier by application of a distributed energy balance model. *Journal of Geophysical Research: Atmospheres,* **116**(D13).

SICART, J.E., HOCK, R. and SIX, D., 2008. Glacier melt, air temperature, and energy balance in different climates: The Bolivian Tropics, the French Alps, and northern Sweden. *Journal of Geophysical Research: Atmospheres,* **113**(D24)

SIGURDSSON, F., 1990. Groundwater from glacial areas in Iceland. *Jökull,* **40**, pp. 119-146.

SMEETS, C.J.P.P., DUYNKERKE, P.G. and VUGTS, H.F., 1999. Observed Wind Profiles and Turbulence Fluxes over an ice Surface with Changing Surface Roughness. *Boundary Layer Meteorology*, **92**(1), 99-121.

STAHL, K., MOORE, R.D. and MCKENDRY, I.G., 2006. The role of synoptic-scale circulation in the linkage between large-scale ocean-atmosphere indices and winter surface climate in British Columbia, Canada. *International Journal of Climatology,* **26**(4), pp. 541-560.

STAHL, K., MOORE, R.D., and MCKENDRY I.G. 2005. Lapse rates of climate variables for different atmospheric circulation conditions. *Headwater 2005*. Bergen, Norway. June 2005.

STEFFEN, K. and BOX, J., 2001. Surface climatology of the Greenland ice sheet: Greenland Climate Network 1995-1999. *Journal of Geophysical Research: Atmospheres,* **106**(D24).

STENNING, A.J., BANFIELD, C.E. and YOUNG, G.J., 1981. Synoptic controls over katabatic layer characteristics above a melting glacier. *Journal of Climatology,* **1**(4), pp. 309-324.

STEPHENSON, P., 1967. Some Considerations of Snow Metamorphism in the Antarctic Ice Sheet in the Light of Ice Crystal Studies. Physics of Snow and Ice, In: OURA, ed, *Proceedings of the International Conference of Low Temperature Sciences*, *14th-19th August, 1966, Sapporo, Japan,* pp. 725-740

STRASSER, U., CORRIPIO, J., PELLICCIOTTI, F., BURLANDO, P., BROCK, B. and FUNK, M., 2004. Spatial and temporal variability of meteorological variables at Haut Glacier d'Arolla (Switzerland) during the ablation season 2001: Measurements and simulations. *Journal of Geophysical Research: Atmospheres,* **109**(D3).

STULL, R.B., 2000. *Meteorology for scientists and engineers.* Second edn. Pacific Grove, USA: Brooks/Cole.

STULL, R.B., 1988. *An Introduction to Boundary Layer Meteorology.* First edn. Dordrecht, Netherlands: Kluwer Academic Publishers.

SUNYER, M., MADSEN, H. and ANG, P., 2012. A comparison of different regional climate models and statistical downscaling methods for extreme rainfall estimation under climate change. *Atmospheric Research,* **103**, pp. 119-128.

SWINBANK, W. C., 1963: Long-wave radiation from clear skies, *Quarterly Journal of the Royal Meteorological. Society*, **89**(381), pp. 330-348.

TANGBORN, W.V. 1984. Prediction of glacier derived runoff for hydro-electric development. *Geografiska Annaler A,* **66**(3), pp. 257-65.

TARASOV, L. and PELTIER, W.R., 1997. Terminating the 100 kyr ice age cycle. *Journal of Geophysical Research: Atmospheres,* **102**(D18).

THIBERT, E., ECKERT, N. and VINCENT, C., 2012. Climatic drivers of seasonal glacier mass balances: an analysis of 6 decades at Glacier de Sarennes (French Alps). *The Cryosphere,* **7**(1), pp. 47-66.

TEDESCO, M., SERREZE, M. and FETTWEIS, X., 2008. Diagnosing the extreme surface melt event over southwestern Greenland in 2007. *The Cryosphere* **2**(2), pp. 159-166.

VAN DE WAL, R., 1996. Mass-balance modelling of the Greenland ice sheet: A comparison of an energy balance model and a degree-day model. *Annals of Glaciology,* **23**, pp. 36-45.

VAN DE WAL, R., 1992. *Ice and Climate*, Utrecht.

VAN DE WAL, R. and WILD, M., 2001. Modelling the response of glaciers to climate change by applying volume-area scaling in combination with a high resolution GCM. *Climate Dynamics,* **18**(3), pp. 359-366.

VAN DE WAL, R. and OERLEMANS, J., 1994. An energy balance model for the Greenland ice sheet. *Global and Planetary Change,* **9**(1), pp. 115-131.

VAN DE WAL, R. and RUSSELL, A.J., 1994. A comparison of energy balance calculations, measured ablation and meltwater runoff near Søndre Strømfjord, West Greenland. *Global and Planetary Change,* **9**(1/2), pp. 19-38.

VAN DEN BROEKE, M., BUS, C., ETTEMA, J. and SMEETS, P., 2010. Temperature thresholds for degree-day modelling of Greenland ice sheet melt rates. *Geophysical Research Letters,* **37**(18)

VAN DEN BROEKE, M.R., 1997a. Structure and diurnal variation of the atmospheric boundary layer over a mid-latitude glacier in summer *Boundary-Layer Meteorology,* **83**(2), pp. 183-205.

VAN DEN BROEKE, M.R., 1997b. Momentum, Heat and Moisture Budgets of the Katabatic Wind Layer over a midlatitude Glacier in Summer. *Journal of Applied Meteorology,* **36**(6), pp. 763-774.

VAUGHAN, D.G., MARSHALL, G.J., CONNOLLEY, W.M., PARKINSON, C., MULVANEY, R., HODGSON, D.A., KING, J.C., PUDSEY, C.J. and TURNER, J., 2003. Recent rapid regional climate warming on the Antarctic Peninsula. *Climatic Change,* **60**(3), pp. 243-274.

VERGARA, W., DEEB, A., VALENCIA, A., BRADLEY, R., FRANCOU, B., ZARZAR, A., GRÜNWALDT, A. and HAEUSSLING, S., 2007. Economic impacts of rapid glacier retreat in the Andes. *Eos, Transactions American Geophysical Union,* **88**(25), pp. 261-264.

VIGNOLA, F., 1999. Solar cell based pyranometers: Evaluation of the diffuse responsivity, *Proceedings of the 1999 Annual Conference American Solar Energy Society*, June (1999), pp. 255-260.

VISBECK, M.H., HURRELL, J.W., POLVANI, L., and CULLEN, H.M., 2001. The North Atlantic Oscillation: past, present, and future. *Proceedings of the National Academy of Sciences*, **98**(23), pp. 12876-12877.

VUILLE, M., FRANCOU, B., WAGNON, P., JUEN, I., KASER, G., MARK, B.G. and BRADLEY, R.S., 2008a. Climate change and tropical Andean glaciers: Past, present and future. *Earth-Science Reviews,* **89**(3), pp. 79-96.

VUILLE, M., KASER, G. and JUEN, I., 2008b. Glacier mass balance variability in the Cordillera Blanca, Peru and its relationship with climate and large-scale circulation. *Global and Planetary Change,* **62**(1-2), pp. 14-28.

WAGNON, P., RIBSTEIN, P., KASER, G. and BERTON, P., 1999. Energy balance and runoff seasonality of a Bolivian glacier. *Global and Planetary Change,* **22**(1), pp. 49-58.

WALSH, J.E., CHAPMAN, W.L. and PORTIS, D.H., 2009. Arctic Cloud Fraction and Radiative Fluxes in Atmospheric Reanalyses. *Journal of Climate,* **22**(9), pp. 2316-2334.

WANG, X., AULER, A.S., EDWARDS, R., CHENG, H., ITO, E., WANG, Y., KONG, X. and SOLHEID, M., 2007. Millennial-scale precipitation changes in southern Brazil over the past 90,000 years. *Geophysical Research Letters,* **34**(23).

WANG, C. and ROGERS, J.C., 2001. A composite study of explosive cyclogenesis in different sectors of the North Atlantic. Part I: Cyclone structure and evolution. *Monthly Weather Review,* **129**(6), pp. 1481-1499.

WARREN, S.G. and WISCOMBE, W.J., 1980. A model for the spectral albedo of snow, II: Snow containing atmospheric aerosols. *Journal of the Atmospheric Sciences,* **37**(12), pp. 2734-2745.

WATSON, R.T., ZINYOWERA, M.C., MOSS, R.H., DOKKEN, D.J., eds. 1996, Climate Change 1995. Impacts, adaptations and mitigation of climate change: scientific-technical analysis contributions of Working Group II to the second assessment report of the International Panel of Climate Change, Cambridge University Press, Cambridge, United Kingdom and New York, NY, USA.

WENDLER, G., 1975. A note on the advection of warm air towards a glacier: A contribution to the IHD. *Zeitschrift für Gletscherkunde und Glazialgeologie,* **10**, pp. 199-205.

WHELER, B.A. and FLOWERS, G.A., 2011. Glacier subsurface heat-flux characterizations for energy-balance modelling in the Donjek Range, southwest Yukon, Canada. *Journal of Glaciology,* **57**(201), pp. 121-133.

WHITEMAN, C. D., and DORAN, J. C., 1993. The relationship between overlying synoptic-scale flows and winds within a valley. *Journal of Applied Meteorology*, **32**(11), pp. 1669-168

WILBY, R.L., WIGLEY, T., CONWAY, D., JONES, P., HEWITSON, B., MAIN, J. and WILKS, D., 1998. Statistical downscaling of general circulation model output: A comparison of methods. *Water Resources Research,* **34**(11), pp. 2995-3008.

WILBY, R.L. and WIGLEY, T., 1997. Downscaling general circulation model output: a review of methods and limitations. *Progress in Physical Geography,* **21**(4), pp. 530-548.

WILKS, D.S., 1995. *Statistical Methods in the Atmospheric Sciences*. First edn. London, England: Academic Press.

WILLIS, I.C., ARNOLD, N.S. and BROCK, B.W., 2002. Effect of snowpack removal on energy balance, melt and runoff in a small supraglacial catchment. *Hydrological Processes,* **16**(14), pp. 2721-2749.

WILLMOTT, C.J., 1981. On the validation of models. *Physical Geography,* **2**(2), pp. 184-194.

WISCOMBE, W.J. and WARREN, S.G., 1980. A Model for the Spectral Albedo of Snow. I: Pure Snow. *Journal of the Atmospheric Sciences,* **37**(12), pp. 2712-2733.

WINSTRAL, A. and MARKS, D., 2002. Simulating wind fields and snow redistribution using terrain-based parameters to model snow accumulation and melt over a semi-arid mountain catchment. *Hydrological Processes,* **16**(18), pp. 3585-3603.

WOOD, A.W., LEUNG, L.R., SRIDHAR, V. and LETTENMAIER, D.P., 2004. Hydrologic Implications of Dynamical and Statistical Approaches to Downscaling Climate Model Outputs. *Climatic Change,* **62**(1), pp. 189-216.

YANG, W., GUO, X., YAO, T., YANG, K., ZHAO, L., LI, S. and ZHU, M., 2011. Summertime surface energy budget and ablation modeling in the ablation zone of a maritime Tibetan glacier. *Journal of Geophysical Research: Atmospheres,* **116**(D14).

YARNAL, B., 1984a. Relationships between synoptic-scale atmospheric circulation and glacier mass balance in South-Western Canada. *Journal of Glaciology,* **30**(105), pp. 188-198.

YARNAL, B., 1984b. Synoptic-scale atmospheric circulation over British Columbia in relation to the mass balance of Sentinel Glacier. *Annals of the Association of American Geographers,* **74**(3), pp. 375-392.

ZHANG, Y., LIU, S. and DING, Y., 2006. Observed degree-day factors and their spatial variation on glaciers in western China. *Annals of Glaciology,* **43**, pp. 301-306.

ZORITA, E. and STORCH, H., 1999. The Analog Method as a Simple Statistical Downscaling Technique: Comparison with More Complicated Methods. *Journal of Climate,* **12**(8), pp. 2474-2489.

Appendix 1

Re-allocation of weather-category membership at 1100 m on Vestari Hagafellsjökull made prior to the cross-validation procedure (Chapter 7, Section 7.3.2).

Old Weather Category	New Weather Category
V2	V3
V6	V16
V11	V12
V13	V16
V14	V16
V17	V12
V19	V15
V20	V16
V21	V22
V24	V7
V25	V16
V28	V12
V29	V22
V30	V26

Same as above, for the 500 m station on Vestari Hagafellsjökull

Old Weather Category	New Weather Category
V2	V3
V5	V23
V9	V10
V11	V12
V13	V16
V14	V16
V17	V12
V18	V10
V19	V15
V20	V16
V21	V7
V22	V7
V24	V7
V25	V16
V27	V7
V28	V12
V30	V26

Same as above, for Storglaciären.

Old Weather Category	New Weather Category
S1	S6
S2	S6
S5	S11
S10	S11
S12	S8
S13	S11
S14	S3
S15	S3
S16	S3
S18	S6
S19	S11
S20	S9
S21	S4